Spin-Selective Chemical Reactions in Radical Pair Magnetoreception

by

Jason C. S. Lau

A thesis submitted to

University of Oxford

in partial fulfilment of the requirements for the degree of

Doctor of Philosophy

in

Physical and Theoretical Chemistry

Trinity Term 2013

Physical & Theoretical Chemistry Laboratory

and

Worcester College

Proletarier aller Lander, vereinigt euch!

Manifesto of the Communist Party, Karl Heinrich Marx, 1848

My logic is undeniable, my logic is undeniable, myyy looogic is unndeenniabble ...

I, Robot, V.I.K.I. (Virtual Interactive Kinetic Intelligence), 2004

Abstract

Spin-Selective Chemical Reactions in Radical Pair Magnetoreception

Jason C. S. Lau

A thesis submitted for the degree of Doctor of Philosophy

Trinity Term 2013

Physical & Theoretical Chemistry Laboratory and *Worcester College*

Many animals on earth need to navigate in their own environments for breeding and foraging. The ability to determine a correct heading and the current location for a migratory bird is critical for its survival. Animals that are sensitive to the Earth's magnetic field can use it to obtain their direction of travel.

In 2000, a paper suggested that radical pair reaction could form the basis for magnetoreception in migratory birds and a flavoprotein, cryptochrome, was proposed as the candidate for the radical pair precursor. Recent *in vivo* experimental results strongly support the hypothesis that radical pairs formed in the eyes of migratory birds are responsible for their magnetic compass sense. Cryptochrome has also been located in the UV-cones in the retinas of two different species of bird.

Radical pairs in living cells are influenced mainly by Zeeman interaction, hyperfine interaction, rotational modulation, etc., and together they influence the recombination reactions of the radical pairs. This thesis considers the possible role of radical pairs in avian magnetoreception, using computer simulations of the quantum mechanical evolution of a radical pair under a variety of conditions.

Chapter 1 contains the introductions to spin chemistry, avian magnetoreception, and the mathematical description of the quantum evolution of a radical pair.

Chapter 2 describes the four different theoretical models for a general non-diffusion-controlled radical pair reaction and the product yields of a radical pair reaction predicted by these four models are analysed and compared.

Chapter 3 introduces a model for avian magnetoreception that integrates photoselection with the radical pair reaction and the model is used to predict the retinal patterns that a bird may be able to use for magnetoreception. The anisotropic singlet product yields of a radical pair comprises the flavin chromophore and the tryptophan of a cryptochrome are also presented in this chapter. A paper based on some parts of this chapter is published[1] in the *Journal of The Royal Society Interface*.

Chapter 4 describes a modified version of an algorithm that is used to calculate the product yields detected in a reaction yield detected magnetic resonance (RYDMR) experiment. The new algorithm is used to analyse the results of two sets of RYDMR experiments in which two radical pair systems, pyrene/1,3-dicyanobenzene and chrysene/1,4-dicyanobenzene, were used. The modulated detection technique used in the RYDMR experiments is also discussed in this chapter. A section of this chapter is published[2] in a paper in the journal *Physical Chemistry Chemical Physics*.

[1] Lau, J.C.S.; Rodgers, C.T.; Hore, P.J., *J. R. Soc. Interface*, **9** (77): 3329–3337, 2012

[2] Wedge, C.J.; Lau, J.C.S.; Ferguson, K.-A.; Norman, S.A.; Hore, P.J.; Timmel, C.R. *Phys. Chem. Chem. Phys.*, **15** (38): 16043–16053, 2013

Acknowledgements

I would like to express my gratitude to my supervisor, Prof. Peter Hore, for his guidance and support in the past five years and for editing this thesis.

I would like to thank the following people for their valuable contributions to this thesis:

Chris Wedge: RYDMR data and γ-COMPUTE simulations,

Kelly-Anne Ferguson: rotary-RYDMR data,

Kiminori Maeda: explanations on Haberkorn and Jones-Hore models, and pyrene reaction schemes,

Kevin Henbest: discussion on pyrene reaction schemes and RYDMR experiments.

The Oxford Supercomputing Centre provided technical assistance and CPU-time on their supercomputers for some of the computer simulations in this thesis.

I also want to thank all past group members, especially Hannah, Till, Chris, and Jennifer. I have enjoyed our discussions on spin chemistry, MATLAB, politics, philosophy, the best day of the week, and other random mundane things.

Finally, thanks Mom and Dad. Although you are thousands of miles away, you gave me the opportunity to study abroad and I will always be grateful to you.

Jason Lau
October 2013

Contents

Chapter 1

Introduction

The two fundamental properties of an electron are its charge and its spin. The electronic charge was integral in the discovery of the electron in the late 19^{th} century. After J. J. Thomson's cathode ray experiments [1] in 1897 tested the 'electrified-particle' theory, Robert Millikan performed his famous oil drop experiment [2] to measure the elementary charge of an electron in 1911. However, the discovery of the electron spin would take longer.

In 1922, the Stern-Gerlach experiment [3], by Otto Stern and Walther Gerlach, demonstrated that a beam of silver atoms could be deflected by an inhomogeneous magnetic field and the beam was split into two discrete parts. Later scientists experimented with other atoms with one electron in their outer shell and also found that the beam would be split into two [4].

Pieter Zeeman discovered the Zeeman effect [5], which is the splitting of the atomic spectral lines by magnetic fields, in 1897 but nobody had an explanation. Various ideas were put forward but none was adequate. In 1925, George Uhlenbeck and Samuel Goudsmit published their explanation for the Zeeman effect [6]. In their paper, the authors wrote that the electron has one half unit of intrinsic angular momentum and the interaction between this angular momentum and the external magnetic field caused the Zeeman effect. This is the first time that the idea of a 'spinning' electron was suggested. Similarly, the spin angular momentum of the silver atoms also caused the beam to split in the Stern-Gerlach experiment.

Wolfgang Pauli further developed the idea of electron spin and incorporated his 'exclusion principle' into quantum mechanics [7]. He stated that any electron in an atom can be described

using four quantum numbers and no two electrons can be described by the same set of quantum numbers. Finally Paul Dirac proved the existence of the electron spin with his Dirac-equations in 1928 [8, 9] and provided the mathematics for spin quantum mechanics.

1.1 Spin

Two quantum numbers are needed to describe the interaction between an electron and a magnetic field, if there is no spin-orbit coupling. For an electron, the spin quantum number, s, is $1/2$ and the magnetic spin quantum number, m_s, is $\pm 1/2$. Since an electron has a half-integer spin number, it is a fermion. The $m_s = +1/2$ is known as the α-state and $m_s = -1/2$ is known as the β-state. The spin angular momentum, S, is related to the spin quantum number by

$$\hat{S}^2 \left| s, m_s \right\rangle = s(s+1)\hbar^2 \left| s, m_s \right\rangle \tag{1.1}$$

where $\hat{S}^2$ is the square of the spin angular momentum operator. The projection of the spin angular momentum in an arbitrary z-direction, $\hat{S}_z$, is given by

$$\hat{S}_z \left| s, m_s \right\rangle = m_s \hbar \left| s, m_s \right\rangle . \tag{1.2}$$

1.2 Radical Pair

Stern continued with the Stern-Gerlach experiment with molecules instead of atoms in the years after the first paper in 1922. He published results of the experiment with molecular hydrogen [10] in 1933 and he observed that the beam of hydrogen molecules was deflected by the magnetic field. Since there are no unpaired electrons, there is no contribution from the electron to the total spin angular momentum of the molecule. In fact, the deflection was due to the spin angular momentum of the nuclei in molecular hydrogen. In the paper, he calculated the magnetic moments of ortho-hydrogen and para-hydrogen from the results and this would lead to measurements of the magnetic moments of the proton, neutron, and other nuclei by other scientists.

Stern noted that it was difficult to improve the measurement of the magnetic moment of hydrogen from the deflection experiment more than several per cent [11] and other scientists then started to use other methods for the magnetic moment measurement. In 1939, Isidor Rabi

used electromagnetic radiation, oscillating at radio frequency (RF), that is in resonance with the energy gap of the nuclear spin of hydrogen in a magnetic field. This resonant frequency is known as the Larmor frequency. Rabi measured the Larmor frequencies at different field strengths and from the results he obtained the magnetic moment of the proton [12]. This was the beginning of nuclear magnetic resonance (NMR) spectroscopy, one of the most widely used spectroscopies by modern scientists to investigate molecular properties.

Rabi's experiments only applied to species that can be made into a molecular beam but the introduction of a new technique in 1946 expanded the scope of NMR. Edward Purcell reported the observed NMR signal of hydrogen in a solid, paraffin wax, [13] and Felix Bloch also observed the NMR signal of hydrogen in various liquids, such as water [14]. The two papers showed that NMR is applicable to both liquids and solids and provided a way to investigate molecular properties without destroying the sample.

By 1960's, NMR spectroscopy was becoming more widely used and in the second half of the decade, scientists published NMR spectra that showed enhanced absorption and emission involving radicals [15–17]. The effect was called chemically induced dynamic nuclear polarisation (CIDNP) as it was first thought the polarisation effect was purely due to radical chemistry. However it became clear later that the electron spins in the radicals are also involved. The CIDNP effect is due to the evolution of two correlated radicals, known as a radical pair, between the singlet and triplet states [18]. Depending on the precursor spin state, radical pair properties and the reaction scheme, the NMR signals of the products will be either absorptive or emissive [19]. A similar polarisation effect was also observed in the electron spin resonance (ESR) spectra of alkyl radicals measured by Fessenden and Schuler [20] in 1963. The electron polarisation effect is known as chemically induced dynamic electron polarisation (CIDEP) and it also arises from radical pairs [21].

1.2.1 Singlet and triplet radical pair

A radical is a molecule that has a single unpaired electron. A radical pair (RP) is two radicals that were created simultaneously with correlated spins. The correlated spins evolve coherently,

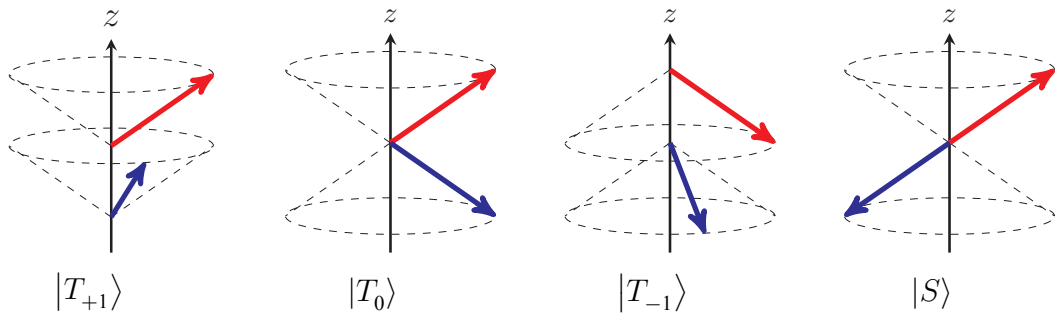

Figure 1.1: The vector model of a RP in triplet ($|T_{+1}\rangle, |T_0\rangle, |T_{-1}\rangle$) and singlet ($|S\rangle$) states. The red arrows denote the spin of radical 1 and the blue arrows denote the spin of radical 2. The spins that have a positive z-component are known as the α-state and the spins that have a negative z-component are known as the β-state. The spin vectors in the figure have z-projections of $\hbar/2$, however in the coupled angular momenta scheme of the singlet and triplet RPs, the z-projections of individual radical spins are not defined.

under the influence of other magnetic interactions, between the singlet and triplet states which are non-stationary states of the spin Hamiltonian.

In the vector model, a singlet RP has anti-parallel spins and a triplet RP has parallel spins (fig. 1.1). There are four spin wavefunctions in total; one wavefunction is the singlet and three wavefunctions are the triplets.

$$\text{Singlet } (S=0) \begin{cases} |S\rangle = \frac{1}{\sqrt{2}}\left(|\alpha_1\beta_2\rangle - |\beta_1\alpha_2\rangle\right) & (M_S = 0) \end{cases}$$

$$\text{Triplet } (S=1) \begin{cases} |T_{+1}\rangle = |\alpha_1\alpha_2\rangle & (M_S = 1) \\ |T_0\rangle = \frac{1}{\sqrt{2}}\left(|\alpha_1\beta_2\rangle + |\beta_1\alpha_2\rangle\right) & (M_S = 0) \\ |T_{-1}\rangle = |\beta_1\beta_2\rangle & (M_S = -1). \end{cases}$$

S is the total spin quantum number and M_S is the total magnetic spin quantum number. The spins in $|S\rangle$ and $|T_0\rangle$ precess around the arbitrary z-direction coherently; the spins are in phase in $|T_0\rangle$ and the spins are out of phase by π in $|S\rangle$ (fig. 1.1). On the other hand, the coherence between the spins in both $|T_{+1}\rangle$ and $|T_{-1}\rangle$ is not fixed. When an external magnetic field is present, the energies of $|S\rangle$ and $|T_0\rangle$ remain unchanged, the energy of $|T_{+1}\rangle$ increases, and the energy of $|T_{-1}\rangle$ decreases.

1.2.2 Radical pair reaction

In a general radical pair reaction (RPR), the first step is the generation of a spin-correlated RP from a precursor. There are a number of ways to generate the RP, all of which are described in an excellent review by Steiner and Ulrich [22]. The RPRs described in the later chapters are in liquid solution therefore this section will describe RPs formed in liquid solution (fig 1.2).

One convenient way of generating RPs is photoexcitation. The electron donor, D, is excited by a laser to an excited singlet state. This is followed by the rapid electron transfer from the donor to the electron acceptor, A.

Soon after the electron transfer, the radicals that have not recombine immediately are still within the same solvent cage and the distance between the radicals is governed by Brownian motion. The exchange energy between the radicals decreases as the distance increases. When the radicals diffuse apart sufficiently, the exchange energy becomes insignificant. Then the RP spin-state starts to evolve coherently under the influence of other magnetic interactions because the singlet and triplet states are non-stationary states of the spin Hamiltonian.

When the re-encounter of the radicals occurs, the RP undergoes a spin-selective reaction. If the RP is in the singlet state, the radicals recombine to form the cage products. However, if the RP is in a triplet state, no reaction occurs. If no reaction occurs within the solvent cage, the radicals may separate and react with scavengers in the solution to form the escape products. The re-encounter has to compete with the final separation of the radical pair.

The ratio of cage and escape products depends on the spin evolution of the RP therefore it depends on magnetic interactions, such as that with the external field. So the radical pair reaction is sensitive to a magnetic field.

The electron donor and acceptor are usually separate molecules, and their RPR is usually controlled by the rate of diffusion. In the special case that both the donor and acceptor are in the same molecule, a biradical is formed after photoexcitation. An example of a biradical is the carotenoid-porphyrin-fullerene (CPF) triad [23]. The porphyrin in the CPF triad adsorbs green light and is excited to a higher singlet state. Then two sequential electron transfers occur, from the porphyrin to the fullerene and from the carotenoid to the porphyrin. The spins centred at

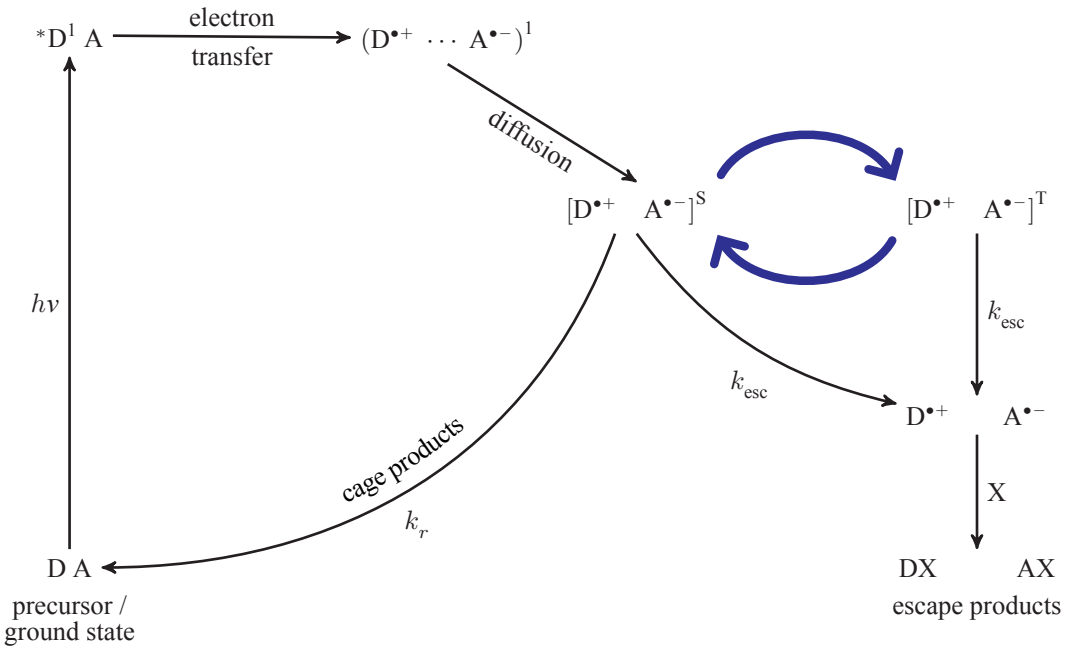

Figure 1.2: A generic radical pair reaction scheme. $\left(\mathrm{D}^{\bullet+} \cdots \mathrm{A}^{\bullet-}\right)^1$ is a species formed immediately after the electron transfer and it forms the singlet RP after the radicals diffuse apart such that the distance between them is large and the exchange energy is negligible. The blue arrows represent the singlet-triplet evolution of the RP. X is a scavenger molecule in the solution that reacts with the escaped free radical. k_r is the cage recombination rate and k_{esc} is the escape rate.

the carotenoid and the fullerene are correlated and form the biradical. The biradical will undergo singlet-triplet interconversion, and the singlet and triplet product ratio will depend on its magnetic interactions.

1.3 Magnetoreception

All animals on earth need to navigate in their own environments for breeding and foraging. Female loggerhead sea turtles in the Atlantic ocean swim back to the same beach every year to lay their eggs [24]. A species of migratory bird, the bar-tailed godwit, holds the record for the longest non-stop flight of any bird; it took a journey of over 10000 km from Alaska in the northern hemisphere to New Zealand in the southern hemisphere during the autumn migratory season [25]. Monarch butterflies make an annual migration from North America to Central America during the autumn and then make the reverse journey in the spring [26].

Two important pieces of information needed in navigation are the direction of travel and

the current position. Animals can identify their current location by either visual identification, olfactory cues or geomagnetic information. Natural landmarks and man-made structures can also help in identifying the current location. The intensity of the earth's magnetic field depends on the global position; the strength decreases from 65 μT at the poles to 25 μT at the equator, and there are local anomalies in the range of nT.

Animals can obtain their direction of travel from any of the three compasses: the sun compass, the celestial compass and the magnetic compass. The position of the sun in the sky changes during the year for locations away from the equator and the animals using the sun compass need to compensate for this effect [27]. The celestial compass can only be use for animals that are active at night and these animals navigate by looking at distant stars in the sky. The geomagnetic field can provide a magnetic compass sense and animals can obtain the direction relative to the magnetic north [28].

1.3.1 European robin and cryptochrome

The European robin (*Erithacus rubecula*) is a small, night-migrating passerine and the birds migrate from the north of Europe to the south of Europe during the autumn. The robin was one of the first avian species that was shown to have magnetoreception under laboratory conditions. In 1970, Wolfgang and Roswitha Wiltschko showed that the robins responded to both directional and intensity changes in the external magnetic field [29]. They also concluded that the biological magnetic compass is an inclination compass [30]; the robins cannot perceive the polarity of the magnetic field but can only perceive the angle of the field with respect to the horizontal.

The behavioural studies of robins coincided with the discovery of the RP in the CIDEP and CIDNP experiments, and a short time later, Klaus Schulten *et al.* made the link between magnetoreception and RP. In 1978, they published a paper describing a magnetic sensor based on a RP [31]. They showed that the product yield of a RPR depends on the direction and intensity of the external magnetic field, provided that there is an anisotropic magnetic interaction between the electron spins and their environment. Therefore in theory a RP can act as a magnetic compass for birds.

Schulten's paper was overlooked for more than 20 years because there was no suitable biomolecule as the RP precursor. The radical pair mechanism (RPM) was revived in a paper in 2000 that was co-authored by Schulten [32]. The authors again argued that the RP is the magnetic sensor in biology and the argument this time was stronger. Experiments on robins and Australian silvereyes in the 1990's showed that their magnetoreception is dependent on the wavelength of the ambient light [33,34] and this corresponded to the photoexcitation of the RP precursor in the RPM. The best evidence for the RPM is that the robins were disoriented when they were exposed to RF oscillating magnetic fields [35]. Out of all the potential mechanisms for magnetoreception, the RPM is the only one that is affected by RF fields. Specifically, the robins were disoriented by a RF field at 1.315 MHz, which is the Larmor frequency of the free electron spin at 47 μT. The strong and sharp resonance at the Larmor frequency suggests that the underlying RP may contain a radical that has no or very small hyperfine interactions.

In the 2000 Ritz *et al.* paper, the authors also suggested that a recently discovered class of photoreceptors, cryptochromes [36–38] could be the RP precursor. Cryptochrome (CRY) is a flavoprotein and its evolutionary predecessor is another flavoprotein, photolyase [38]. CRYs are found in most types of organisms, such as bacteria [39], plants [40], insects [41], mammals [42] and humans [43], and they show a variety of functions in different organisms. CRY1 was found to regulate plant growth in *Arabidopsis thaliana*, a small flowering plant [44]. CRY was also shown to have a role in circadian rhythms in mice [45] and fruitflies [41].

Fruitflies (*Drosophila melanogaster*) were also shown to be sensitive to a magnetic field in a paper by Gegear *et al.* in 2008 [46]. They trained wild-type and CRY-deficient fruitflies to respond to a magnetic field associated with a reward, and showed that only the wild-type, the flies that had CRY, would respond to a magnetic field. This was the first experiment that demonstrated the association between CRY and magnetoreception in any organism.

Efforts to locate CRY in avian species yielded some results during the past decade. CRY was found in the retina in chicken [47] and garden warbler [48], another migratory passerine. Further experiments on chicken and robin retinas found that there is co-localisation of CRY proteins and ultraviolet/violet cones [49] and the authors of the paper also suggested that CRYs are anchored

along the membrane-discs in the cones. This immobilisation may be important in preserving the anisotropic response of a CRY-RP in a magnetic field.

CRY has two cofactors, flavin adenine dinucleotide (FAD) and 5,10-methenyltetrahydrofolate (MTHF), buried inside the protein. After blue light photoexcitation of the FAD cofactor, a RP is formed between FAD and a surface tryptophan (Trp), and this RP was shown to have a lifetime of milliseconds *in vitro* [50]. The RP is formed via three sequential electron transfers along a chain of three Trps, leading to the surface of the protein [51, 52]. A H^+ abstraction may occur during the RP formation by $FAD^{\bullet -}$ to form the neutral $FADH^{\bullet}$. Although *in vitro* experiments showed that $FADH^{\bullet}$'s counter radical is $TrpH^{\bullet +}$, analysis of the *in vivo* experiments in robins shows that the counter radical appears to have no hyperfine interactions [53] and the superoxide radical was suggested as the counter radical [54,55]. However, it will be shown in chapter §3 that the identity of the counter radical does not affect the suitability of CRY as a magneto-directional sensor.

The Earth's magnetic field is only around 50 μT, which is very weak compared to the ~ 10 T fields that are routinely used in NMR. In this thesis, only RPR at low fields will be discussed because biological magnetoreception occurs at low fields. After the preliminary introduction to spin, RPs, and magnetoreception, the next sections contain details of the properties and interactions of a RPR, and the mathematics needed to calculate the product yields of a RPR.

1.4 Magnetic characteristics in radical pair reactions

There are a number of interactions that affect the singlet-triplet coherent evolution in a RPR. In this section some of these interactions are described but the RPR calculations in later chapters will only include the Zeeman and the hyperfine interactions, as other interactions are insignificant at low field and in biological conditions.

1.4.1 Zeeman interaction

The Zeeman interaction is named after Pieter Zeeman who discovered the effects of magnetic fields on atomic spectra in the late 19^{th} century. In classical physics, the energy of a magnetic

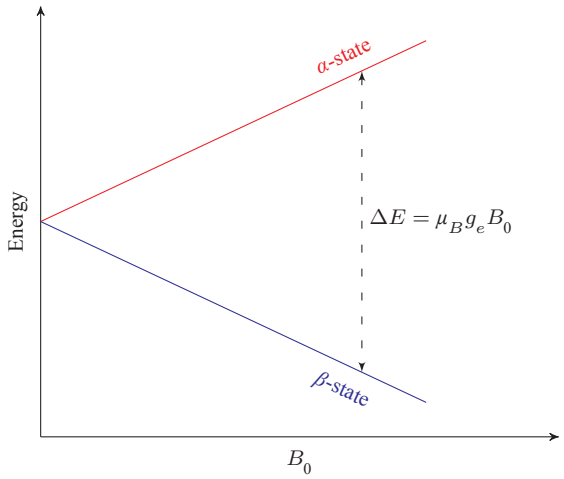

Figure 1.3: The energies of the α- and β-states in a magnetic field, B_0.

dipole in a magnetic field is

$$E = -\vec{\mu} \cdot \vec{B} \tag{1.3}$$

where $\vec{\mu}$ is the magnetic moment and $\vec{B}$ is the magnetic flux density (commonly know as the magnetic field) which is measured in Tesla. The magnetic moment is directly proportional to the angular momentum, $\vec{S}$, and it should not be confused with the magnetic quantum number, s (eq. 1.1).

$$\vec{\mu} = \gamma_e \vec{S} \tag{1.4}$$

where γ_e is the electron gyromagnetic ratio. When $\vec{B}$ points in the z-direction with strength, B_0,

$$\mu_z = \gamma_e S_z = \gamma_e \hbar m_s, \tag{1.5}$$

$$E = -\gamma_e \hbar m_s B_0. \tag{1.6}$$

γ_e is negative. Usually the energy is expressed in terms of the Bohr magneton, μ_B;

$$E = \mu_B g_e m_s B_0 \ , \ \mu_B = 9.274 \times 10^{-24}\,\mathrm{J\,T^{-1}} \quad [56], \tag{1.7}$$

where g_e is the electron g-factor and $g_e = 2.002$ [56] for a free electron. In contrast to nuclear spins, the electronic β-state is lower in energy than the α-state in a magnetic field. The energy difference (fig. 1.3) between the α-state and the β-state is

$$\Delta E = \mu_B g_e B_0. \tag{1.8}$$

The spin Hamiltonian for the Zeeman interaction is similar to equation 1.7;

$$\hat{H} = \frac{\mu_B}{\hbar}\hat{\vec{S}} \cdot \mathbf{g} \cdot \vec{B} \tag{1.9}$$

where $\hat{\vec{S}}$ is now a spin operator and will be defined in a later section. $\mathbf{g}$ is a tensor that describes the anisotropy in the g-factor. This anisotropy occurs because molecular orbitals are not spherically symmetric and spin-orbit coupling of electron angular momenta in molecular orbitals is complex. The g-factor anisotropy can be observed frequently in solid state ESR experiments but for the low fields and organic molecules that are considered in the later chapters, it is reasonable to assume that $\mathbf{g}$ is isotropic and to use the free electron g-factor, g_e. Therefore the Zeeman Hamiltonian for a B_0 field that points along the z-direction is

$$\hat{H} = \frac{\mu_B}{\hbar} g_e B_0 \hat{S}_z \tag{1.10}$$

where $\hat{S}_z$ is the spin operator in the z-direction. The characteristic resonance frequency of the electron in a magnetic field is know as the Larmor frequency, ω_0, and

$$\frac{\omega_0}{B_0} = |\gamma_e| = \frac{\mu_B g_e}{\hbar} = 1.761 \times 10^{11}\,\mathrm{rad\,s^{-1}\,T^{-1}}. \tag{1.11}$$

Magnetic nuclei also have Zeeman interactions in a magnetic field but their gyromagnetic ratios are small compared to the electron. Hydrogen has one of the largest nuclear gyromagnetic ratios ($\gamma_{^1\mathrm{H}} = 2.675 \times 10^8\,\mathrm{rad\,s^{-1}\,T^{-1}}$) and it is $\sim$600 times smaller than $|\gamma_e|$. Therefore the nuclear Zeeman interaction can be omitted in low field RPR calculations.

1.4.2 Hyperfine interaction

The hyperfine interaction (HFI) is the magnetic interaction between the electron spin and the nuclear spins in a radical. The Hamiltonian for the HFI is

$$\hat{H} = \hat{\vec{S}} \cdot \mathbf{A} \cdot \hat{\vec{I}} \tag{1.12}$$

where $\mathbf{A}$ is the HFI tensor. Usually $\mathbf{A}$ is quoted in its eigenframe, and equation 1.12 becomes

$$\hat{H} = A_{xx}\hat{S}_x\hat{I}_x + A_{yy}\hat{S}_y\hat{I}_y + A_{zz}\hat{S}_z\hat{I}_z \tag{1.13}$$

where A_{xx}, A_{yy}, A_{zz} are the eigenvalues of $\mathbf{A}$.

There are two main contributions to the HFI; one of the contributions is the Fermi contact interaction [57], which is

$$a_{\text{iso}} = \frac{2\mu_0}{3}\gamma_e\gamma_n|\Psi(r=0)|^2. \tag{1.14}$$

The Fermi contact interaction depends on the orbital wavefunction of the unpaired electron, the magnetic moment of the electron, and the magnetic moment of the nucleus. For a non-zero a_{iso}, the spin density function at the nuclear position, $|\Psi_0(r=0)|^2$, should be non-zero. This means that the wavefunction should have some atomic s-orbital character. The Fermi contact interaction remains constant during molecular rotation and it is the isotropic part of the HFI. The isotropic part of the HFI Hamiltonian is

$$\hat{H}_{\text{iso}} = a_{\text{iso}}\,\hat{\vec{S}}\cdot\hat{\vec{I}}, \text{ where } a_{\text{iso}} = \frac{1}{3}\text{Tr}[\mathbf{A}]. \tag{1.15}$$

The other contribution to the HFI is the electron-nucleus dipolar coupling. The Hamiltonian at $\vec{r}$ is similar to the classical dipolar coupling [57],

$$\hat{H}_{\text{dipolar}}(\vec{r}) = \frac{\mu_0}{4\pi}\,\gamma_e\gamma_n\left[\frac{\hat{\vec{S}}\cdot\hat{\vec{I}}}{|\vec{r}|^3} - \frac{3\left(\hat{\vec{S}}\cdot\vec{r}\right)\left(\hat{\vec{I}}\cdot\vec{r}\right)}{|\vec{r}|^5}\right]|\Psi(\vec{r})|^2. \tag{1.16}$$

The dipolar coupling depends on the magnetic moment of the electron and the nucleus, the distance, the orientation, and the spin density. The anisotropic part of the HFI Hamiltonian is found by integrating equation 1.16 over all space;

$$\hat{H}_{\text{aniso}} = \int_V \hat{H}_{\text{dipolar}}(\vec{r})\ \text{d}V. \tag{1.17}$$

$\hat{H}_{\text{aniso}}$ is usually expressed as

$$\hat{H}_{\text{aniso}} = \hat{\vec{S}}\cdot\mathbf{A}_{\text{aniso}}\cdot\hat{\vec{I}}\,, \quad \mathbf{A}_{\text{aniso}} \propto \left\langle\frac{3\cos^2\theta - 1}{r^3}\right\rangle. \tag{1.18}$$

$\mathbf{A}_{\text{aniso}}$ is traceless and is the anisotropic part of $\mathbf{A}$. The dipolar interaction averages to zero when the molecule is tumbling rapidly so anisotropic HFI usually is not considered in liquid phase RPR.

The unpaired electron in an aromatic radical, such as the pyrene radical (which will be described in section §4.1.1), is usually located in the excited conjugated π^*-orbital above and below

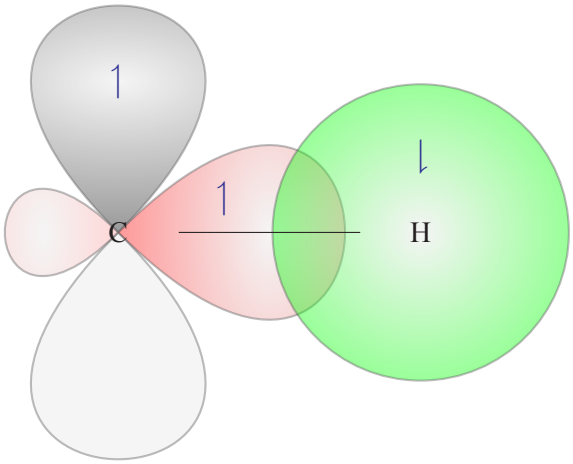

Figure 1.4: Schematic representation of the spin polarisation of the C-H bond in the plane of an aromatic molecule. The unpaired electron (↑) is localised in the π^*-orbital (black). The exchange interaction causes the electron localised in the sp_2 hybrid orbital (red) to have parallel spin and hence the electron (↓) localised in the s-orbital (green) has anti-parallel spin. The HFI between the unpaired electron and the hydrogen nucleus is mediated through the spin polarisation of the C-H bond, despite the fact that the unpaired electron is in an orthogonal orbital to the C-H bond.

the carbon ring. This π-orbital can be described by a linearly combination of the individual carbon p_z-orbitals in the aromatic ring. Although there is zero spin density at the hydrogen nucleus that lies in the plane of the aromatic ring, the electron still experiences a HFI with the hydrogen in solution (see section §4.1.1).

The isotropic HFI in aromatic radical arises from a mechanism called spin polarisation (fig. 1.4) [58]. The unpaired electron in the π^*-orbital can polarise the pair of electrons in the bonding molecular orbital of the C-H bond through the exchange interaction. The two electrons localised at the carbon atom, one in the p_z-orbital and one in the sp^2 hybrid orbital, have parallel spins due to the exchange interaction. Due to Pauli's exclusion principle, the electron localised at the hydrogen atom has anti-parallel spin and this electron interacts with the hydrogen nuclear spin via the Fermi contact interaction. Therefore the unpaired electron that is localised in the π^*-orbital is able to interact with the hydrogen nuclei in the plane of the aromatic ring.

1.4.3 Other magnetic characteristics

The Zeeman interaction and the HFI are the only two interactions under consideration in this thesis but the product yields of a RPR are under the influences of other interactions and processes. The effects of these interactions and processes are assumed to be negligible under the conditions that are considered in this thesis. In this subsection, these effects are discussed briefly before a detail description of the calculation of product yields in the next section.

Δg mechanism

As described in section §1.4.1, g depends on the orbital environment and the variation is small for organic molecules. However this small difference is important at high fields, $\sim$ 1 T (eq. 1.10), as the Zeeman interaction dominates the HFI. The small difference in g between the two radicals, known as the Δg mechanism, can drive singlet-triplet interconversion in a RPR. This is because the two electron spins are precessing at significantly different rates around the strong external field. Since the RPR considered in this thesis will be in the low field region, the difference in g values can be ignored and the Δg mechanism will not be considered.

Exchange interaction

When there is significant orbital overlap between the two unpaired electrons in the RP, the electrons experience an exchange interaction. The exchange interaction is a quantum mechanical energy and it is the non-classical part of the Coulomb interaction between the electrons that depends on their spins. The exchange interaction Hamiltonian is

$$\hat{H}_{\text{ex}} = -2J\hat{\vec{S}}_1 \cdot \hat{\vec{S}}_2. \tag{1.19}$$

J is the exchange integral and the energy gap between the singlet state and the triplet state of the RP is $2J$. The distance dependence of J in a RP can be approximated by a pair of hydrogen atoms approaching from infinite distance (fig. 1.5a). As the separation distance decreases, the atoms form a bonding orbital (S) and an anti-bonding orbital (T_0). This distance dependence is approximated by an exponential [59],

$$J(r) = J_0\, e^{-\frac{r}{r_j}}, \tag{1.20}$$

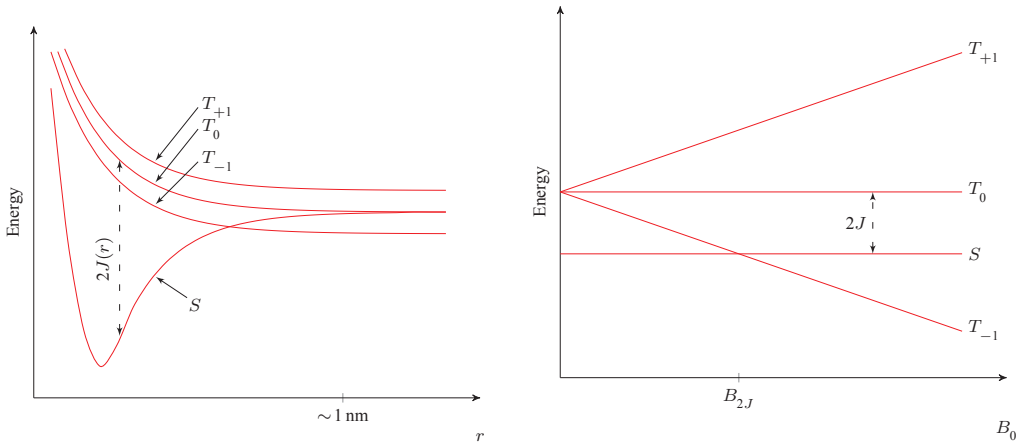

(a). The energies of the four RP states as a function of distance, as deduced from a simple model of the hydrogen atoms approaching from infinite radical separation. The energies of the three T-states are split by the Zeeman interaction with the external field. S is separated from T_0 by $2J(r)$ and this exchange energy depends on the separation, r, between the radicals. At distances larger than 1 nm, the exchange energy becomes negligible compared to other interactions.

(b). The energies of the four RP states as a function of the external field. T_{+1} and T_{-1} are dependent on the external field due to the Zeeman interaction. S is separated from T_0 by the exchange energy, $2J$. In the drawing, J is negative and therefore S is lower in energy. S and T_{-1} become degenerate at B_{2J}.

Figure 1.5: Two drawings of the energies of different RP states as a function of radical distance, r and as a function of external field, B_0.

where r is the radical separation. Typical values for J_0 and the range parameter, r_j, are 1.7×10^{17} rad s^{-1} and 0.049 nm respectively [60]. For a RPR in a weak field ($\sim$ 100 µT), J is of the same order of magnitude as the Larmor frequency when $r \approx 1.1$ nm. When the radical distance exceeds 1.1 nm (fig. 1.5a), the geminate RP is formed and spin mixing is allowed. However, when the radical distance decreases during re-encounter, the exchange energy dominates other interactions and spin mixing is blocked.

T_{+1} and T_{-1} states have non-zero magnetic spin angular momentum therefore their energies depend on the external magnetic field due to the Zeeman interaction. Depending on the sign of the exchange interaction, either T_{+1} or T_{-1} becomes degenerate with S at the field strength $B_0 = {}^{2J}/_{g_e \mu_B}$ (indicated as B_{2J} in fig. 1.5b) and singlet-triplet interconversion occurs.

Dipolar interaction

In addition to the dipolar interaction between the electron and the nuclei in a radical (§1.4.2), there is also a dipolar interaction between the two electrons in a RP. The Hamiltonian for this electron-electron dipolar interaction is similar to equation 1.16 (substitute the nuclear variables with electron variables) and its strength also decreases with increasing distance,

$$\hat{H}_{DD} \propto \frac{\gamma_e^2}{r^3}. \tag{1.21}$$

The separation between the two radicals ($\sim$ 1 nm) is bigger than intra-molecular electron-nucleus distance. Although the electron gyromagnetic ratio is bigger, the electron-electron dipolar interaction is usually negligible at typical inter-radical distances. This dipolar interaction is also averaged to zero by molecular rotational diffusion.

Relaxation

A RP is not an isolated system and in addition to the interactions described in the previous sections, it also interacts with its environment. This interaction between the electron spins in the RP and the environment causes the spin system to return to thermal equilibrium. This is called relaxation.

There are two main types of relaxation. Longitudinal relaxation (also known as spin-lattice relaxation) causes the spin populations to return to their thermal equilibrium values according to the Boltzmann distribution and this is characterised by the time constant, T_1. In NMR spectroscopy, this is the increase of the z-magnetisation after the initial RF pulse. However, in a low field RPR, the eigenaxis of the spin system does not coincide with the external field, and T_1 processes can be viewed as returning the populations of the eigenstates to equilibrium. Since longitudinal relaxation involves the redistribution of populations, energy is exchanged with the environment.

The second type of relaxation is transverse relaxation (also know as spin-spin relaxation) and it is characterised by the time constant, T_2. In NMR spectroscopy, after the initial RF pulse, all the spins are in phase and the resultant magnetisation precesses around the z-direction at a frequency dependent on the external field strength. Transverse relaxation decreases the precessing

magnetisation - causing the spins to 'fan-out' in the xy-plane - and randomises the phases of the spins. In a RPR, the same type of relaxation causes the dephasing of coherences between different eigenstates of the system. Therefore some time after the creation of the RP, all coherences will be lost and no more singlet-triplet interconversion will occur.

The main relaxation mechanism is the interaction of the spin system with random field fluctuations generated by the thermal motion of the surrounding molecules. Therefore the relaxation time scale of solids is longer than liquids and gases. The spin system interacts with the random fields via any anisotropic interaction, such as the dipole-dipole interaction. Although the tumbling motion of the molecules averages the anisotropic interaction to zero, the instantaneous field that the spin system experiences is non-zero. A detail description of various relaxation mechanisms can be found in various NMR textbooks, such as Levitt [61] and Slichter [62].

The most frequently used theoretical description of relaxation is Redfield theory. It treats the time-dependent field fluctuations as perturbations on the time-independent Hamiltonian. A detail derivation of Redfield theory can be found in the excellent review by Goldman [63]. Another frequently used formalism is the Lindblad equation [64] and it is a general Markovian master equation that describes non-coherent evolution of the density matrix. It is widely used to describe relaxation in open quantum systems.

Relaxation processes are assumed to be negligible in the RPR calculations in this thesis. For a RP to function as a magnetoreceptor, biological conditions may have evolved to suppress relaxation. A protein that is attached to a rigid structure within a cell would have limited motion thus the biradical created from such a protein would have a long relaxation time. It is also conceivable that the reaction kinetics of a RP is faster than relaxation. Magnetic field effects are routinely observed in RP systems in the liquid state and this shows that relaxation has minor effects on some RPRs.

1.4.4 Summary

In this thesis, RPRs in low fields in solution are considered. In solution, most of the magnetic interactions are averaged to zero or are negligible except the Zeeman interaction and the HFI. Relaxation is assumed to be operating at a slower rate than the recombination reaction and to

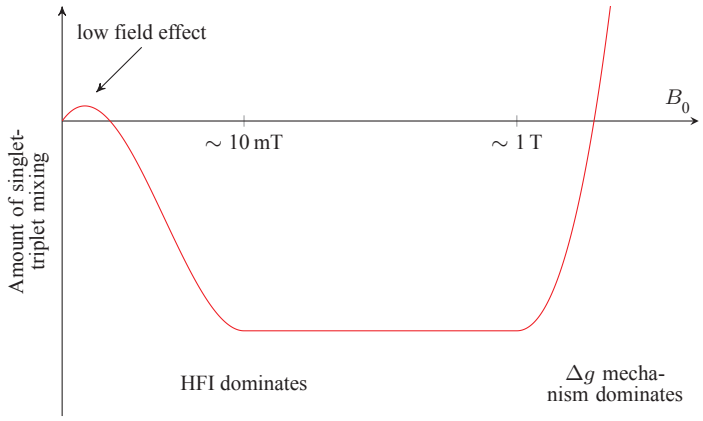

Figure 1.6: A drawing of the amount of singlet-triplet mixing as a function of the field strength, B_0. Adapted from McLauchlan & Steiner [60].

have no effect on the spin dynamics. At low fields, the Zeeman interaction and the HFI are the same order of magnitude and both affect the singlet-triplet interconversion. The HFI promotes interconversion at low fields and the Δg mechanism dominates at very high fields (fig. 1.6).

1.5 Spin operators

Quantum mechanical observables can be calculated using matrix representations. Spin operators corresponding to observables are represented by matrices and spin states are represented by vectors. The Pauli matrices are a set of three 2×2 complex matrices and they are the spin operators for a spin-$1/2$ particle. The matrices are Hermitian and unitary, and this implies that the eigenvalues of the Pauli matrices are real. Wolfgang Pauli used these matrices in his formulation of the Pauli-equation in 1927 hence the matrices are named after him. The spin-$1/2$ Pauli matrices are

$$\sigma_x = \begin{pmatrix} 0 & 1 \\ 1 & 0 \end{pmatrix} , \quad \sigma_y = \begin{pmatrix} 0 & \mathrm{i} \\ -\mathrm{i} & 0 \end{pmatrix} , \quad \sigma_z = \begin{pmatrix} 1 & 0 \\ 0 & -1 \end{pmatrix} . \tag{1.22}$$

The xyz spin operators are given by

$$\hat{S}_i = \frac{1}{2}\sigma_i \quad \text{where} \quad i = x, y, z \tag{1.23}$$

which are the normalised Pauli spin matrices. As it is customary in spin chemistry, the spin operators are expressed in units of rad s^{-1} therefore h is omitted. The eigenvectors for $\hat{S}_z$ are

$$|\alpha\rangle = \begin{pmatrix} 1 \\ 0 \end{pmatrix} , \; |\beta\rangle = \begin{pmatrix} 0 \\ 1 \end{pmatrix} , \tag{1.24}$$

with eigenvalues of $+1/2$ and $-1/2$ respectively. Usually the eigenvectors in equation 1.24 are used as the orthogonal basis for a spin-1/2 particle, hence the α, β designation. It is easy to see that $\hat{S}_z$, $|\alpha\rangle$ and $|\beta\rangle$ satisfy the relationship in equation 1.2;

$$\hat{S}_z |\alpha\rangle = \frac{1}{2} |\alpha\rangle \ , \quad \hat{S}_z |\beta\rangle = -\frac{1}{2} |\beta\rangle \, . \tag{1.25}$$

Product spin operators, such as $S_z I_z$ in equation 1.13 for the HFI, are constructed using Kronecker products. The order of the Kronecker products needs to be consistent for all spin operators. For example, the z-spin operator for a RP coupled to a proton is

$$S_{Az} I_{1z} = \hat{S}_z \otimes \hat{I}_z \otimes \mathbb{1}_B \tag{1.26}$$

where $\mathbb{1}$ is a 2×2 identity matrix and $\otimes$ denotes a Kronecker product. $\hat{I}_z$ is the z-spin operator for the nuclear spin, and in the case of a proton, $\hat{I}_z = \hat{S}_z$. Any particle that is not coupled in the spin operator, such as the electron B in equation 1.26, an identity matrix with the same dimension as the particle's spin space, $\mathbb{1}_B$, is used. The spin operators of a RP that has couplings to two or more nuclei can be constructed by adding more identity matrices to equation 1.26 in the correct places. For the j-th nucleus coupled to electron A in a RP with n nuclei, the spin operator is

$$S_{Ap} I_{jq} = \hat{S}_p \otimes \bigotimes_{1}^{j-1} \mathbb{1} \otimes \hat{I}_q \otimes \bigotimes_{1}^{n-j} \mathbb{1} \otimes \mathbb{1}_B \ , \quad \text{where } p, q = x, y, z. \tag{1.27}$$

Matrix representations of the angular momentum operator of larger spin quantum numbers can be calculated from the z-operator (eq. 1.2), the raising and lowering operators ($\sigma_\pm = \sigma_x \pm i\sigma_y$). For convenience, the matrix representations for a spin-1 particle are listed below:

$$\sigma_x = \frac{1}{\sqrt{2}} \begin{pmatrix} 0 & 1 & 0 \\ 1 & 0 & 1 \\ 0 & 1 & 0 \end{pmatrix} \ , \quad \sigma_y = \frac{i}{\sqrt{2}} \begin{pmatrix} 0 & -1 & 0 \\ 1 & 0 & -1 \\ 0 & 1 & 0 \end{pmatrix} \ , \quad \sigma_z = \begin{pmatrix} 1 & 0 & 0 \\ 0 & 0 & 0 \\ 0 & 0 & -1 \end{pmatrix} . \tag{1.28}$$

1.6 Theoretical description

In the next few sections, all the necessary mathematics to calculate the singlet product yield (SY) of a RPR is described. Usually, the matrix representation of quantum mechanics is used. First, the density matrix formalism in Hilbert space is described, then the transformation to Liouville space, which is necessary when complex kinetic and relaxation mechanism are involved, is described.

Dirac's bra-ket notation is used in this section; the ket, $|\psi\rangle$, represents a state vector and the bra, $\langle\psi|$ is the Hermitian conjugate (the complex conjugate transpose) of the ket. The superscript dagger, $A^{\dagger}$, denotes the Hermitian conjugate of a matrix and the superscript asterisk, A^{*} denotes the complex conjugate.

1.6.1 State vectors - representation of a wavefunction

A quantum system can be described by a wavefunction. Consider a system with n orthogonal basis states, $\left|\psi_1\right\rangle \cdots \left|\psi_n\right\rangle$, the wavefunction, $|\Psi\rangle$, can be written as a linear combination (also know as superposition) of the basis states;

$$|\Psi\rangle = c_1 \left|\psi_1\right\rangle + \cdots + c_n \left|\psi_n\right\rangle = \sum_{i=1}^{n} c_i \left|\psi_i\right\rangle . \tag{1.29}$$

The coefficients c_i describe the contributions of the $\left|\psi_i\right\rangle$ states to the wavefunction. The coefficients can be complex numbers therefore they also describe the relative phase of the states in the superposition. It is convenient to write the wavefunction ket as a column vector, with the coefficients in equation 1.29 as the vector elements;

$$|\Psi\rangle = \begin{pmatrix} c_1 \\ \vdots \\ c_n \end{pmatrix} . \tag{1.30}$$

The scalar product of the bra, $\langle\Psi|$ and the ket, $|\Psi\rangle$, is given by

$$\langle\Psi \mid \Psi\rangle = \sum_{i,j}^{n} c_i c_j^{*} \left\langle \psi_j \middle| \psi_i \right\rangle . \tag{1.31}$$

Since all the states are orthonormal, $\left\langle \psi_j \middle| \psi_i \right\rangle = \delta_{ij}$. All elements in equation 1.31 are zero except when $i = j$ and the scalar product simplifies to:

$$\langle\Psi \mid \Psi\rangle = \sum_{i}^{n} |c_i|^2 \tag{1.32}$$

The wavefunction is normalised so that equation 1.32 equals one. $|c_i|^2$ represents the probability of the system being in state $\left|\psi_i\right\rangle$. This scalar product can also be found by vector multiplication of $\langle\Psi|$ and $|\Psi\rangle$ using equation 1.30.

1.6.2 Operators

An operator, $\hat{A}$, acts on a wavefunction to give a new wavefunction. If the basis states are the eigenstates of the operator, then the action of an operator on a given state, $\left|\psi_i\right\rangle$, is

$$\hat{A}\left|\psi_i\right\rangle = a_i\left|\psi_i\right\rangle, \tag{1.33}$$

i.e. $\hat{A}$ simply scales $\left|\psi_i\right\rangle$. The effect of the operator on a wavefunction is

$$\hat{A}\left|\Psi\right\rangle = \sum_i^n a_i c_i\left|\psi_i\right\rangle. \tag{1.34}$$

For an experimental measurement, there is an operator, $\hat{A}$, that corresponds to the observable. The mean value of the observable is given by the expectation value of $\hat{A}$,

$$\left\langle\hat{A}\right\rangle = \left\langle\Psi\middle|\hat{A}\middle|\Psi\right\rangle. \tag{1.35}$$

Substituting results in equations 1.32 and 1.34 into equation 1.35, the expectation value simplifies to

$$\left\langle\hat{A}\right\rangle = \sum_i^n a_i|c_i|^2. \tag{1.36}$$

The observable is the weighted averaged of all the eigenvalues, a_i. Any single experimental measurement will result in obtaining one of the eigenvalues, with the probability of $|c_i|^2$.

In general, the basis states are not the eigenstates of the operator and the expectation value is

$$\left\langle\hat{A}\right\rangle = \sum_{i,j}^n c_i c_j^* A_{ji}\,, \quad \text{where } A_{ji} = \left\langle\psi_j\middle|\hat{A}\middle|\psi_i\right\rangle. \tag{1.37}$$

1.6.3 Density matrix

The density matrix, $\hat{\rho}$, comprises the product coefficients, $c_i c_j^*$, in equation 1.37, and the density matrix elements are

$$\rho_{ij} = c_i c_j^* = \left\langle\psi_i\middle|\hat{\rho}\middle|\psi_j\right\rangle. \tag{1.38}$$

The indices, i and j, correspond to the rows and columns of the density matrix. The density matrix is given by

$$\hat{\rho} = \left|\Psi\right\rangle\left\langle\Psi\right| = \begin{pmatrix} c_1 \\ c_2 \\ \vdots \\ c_n \end{pmatrix}\begin{pmatrix} c_1^* & c_2^* & \cdots & c_n^* \end{pmatrix} = \begin{pmatrix} c_1c_1^* & c_1c_2^* & \cdots & c_1c_n^* \\ c_2c_1^* & \ddots & & \vdots \\ \vdots & & \ddots & \vdots \\ c_nc_1^* & \cdots & \cdots & c_nc_n^* \end{pmatrix}. \tag{1.39}$$

The diagonal elements, ρ_{ii}, in the density matrix represent the populations of the states, $|\psi_i\rangle$, and the off-diagonal elements, ρ_{ij}, represent the coherences between two states, $|\psi_i\rangle$ and $|\psi_j\rangle$.

Substituting equation 1.38 into equation 1.37, the expectation value becomes

$$\left\langle \hat{A} \right\rangle = \sum_{i,j}^{n} \rho_{ij} A_{ji} = \sum_{i}^{n} \left(\hat{\rho}\hat{A} \right)_{ii} = \mathrm{Tr}\left[\hat{\rho}\hat{A} \right] = \mathrm{Tr}\left[\hat{A}\hat{\rho} \right]. \tag{1.40}$$

Therefore the expectation value of an operator, $\hat{A}$, is simply the trace of the product of the density matrix, $\hat{\rho}$, and the operator. The density matrix formalism allows the evaluation of the ensemble average and also allows the combination of coherent spin evolution and incoherent processes, such as reaction kinetics and spin relaxation, in the calculations.

1.6.4 Liouville-von Neumann equation

The time dependence of the density matrix under a given Hamiltonian is deduced from the time-dependent Schrödinger equation,

$$\mathrm{i}\frac{\mathrm{d}}{\mathrm{d}t} |\Psi\rangle = \hat{H} |\Psi\rangle . \tag{1.41}$$

$\hbar$ is omitted in equation 1.41 because the equation is expressed in units of rad s^{-1}. The differential of equation 1.39 with respect to time is

$$\frac{\mathrm{d}}{\mathrm{d}t}\hat{\rho} = \frac{\mathrm{d}}{\mathrm{d}t} |\Psi\rangle \langle\Psi| + |\Psi\rangle \frac{\mathrm{d}}{\mathrm{d}t} \langle\Psi| = -\mathrm{i}\hat{H} |\Psi\rangle \langle\Psi| + |\Psi\rangle \left(-\mathrm{i}\hat{H} |\Psi\rangle \right)^{\dagger}. \tag{1.42}$$

Using the Hermiticity of the Hamiltonian, equation 1.42 simplifies to

$$\frac{\mathrm{d}}{\mathrm{d}t}\hat{\rho} = -\mathrm{i}\hat{H} |\Psi\rangle \langle\Psi| + \mathrm{i} |\Psi\rangle \langle\Psi| \hat{H} = -\mathrm{i}\hat{H}\hat{\rho} + \mathrm{i}\hat{\rho}\hat{H} \tag{1.43}$$

$$\frac{\mathrm{d}}{\mathrm{d}t}\hat{\rho} = -\mathrm{i}\left[\hat{H}, \hat{\rho} \right] \tag{1.44}$$

where the square bracket denotes a commutator. Equation 1.44 is the Liouville-von Neumann equation which describes the time dependence of the density matrix and the Schrödinger equation (eq. 1.41) describes the time dependence of the wavefunction.

If the Hamiltonian is time-independent, the solution of the Liouville-von Neumann equation is given by

$$\hat{\rho}(t) = e^{-\mathrm{i}\hat{H}t}\, \hat{\rho}(0)\, e^{\mathrm{i}\hat{H}t} \tag{1.45}$$

where $\hat{\rho}(0)$ is the initial density matrix and $e^{\hat{X}}$ is a matrix exponential.

However, if the Hamiltonian is time-dependent, equation 1.45 does not hold. In this case, one way to solve the Liouville-von Neumann equation is to use a time-discretised Hamiltonian. Now if the Hamiltonian is approximately piece-wise constant, then the density matrix at t can be found by propagating the initial density matrix, $\hat{\rho}(0)$, via a series of small time-steps. This will be explained in detail in chapter §4.

Equation 1.44 only contains the coherent spin evolution and other incoherent processes, such as reaction kinetics and relaxation, are represented by other operators which are added to the time-dependence equation. The reaction kinetics operators will be the main focus of the chapter §2 where more details on incoherent processes will be presented.

1.6.5 Singlet yield in Hilbert space

To calculate the SY, the singlet projection operator, $\hat{P}_S$, is needed;

$$\hat{P}_S = |S\rangle \langle S| = \frac{1}{4}\mathbb{1} - \hat{\vec{S}}_A \cdot \hat{\vec{S}}_B. \tag{1.46}$$

The components of $\hat{\vec{S}}_A$ and $\hat{\vec{S}}_B$, which are the electron spin operators for A and B, are constructed from the Pauli spin matrices (eq. 1.22) using Kronecker products;

$$\hat{S}_{Ai} = \hat{S}_i \otimes \bigotimes_1^n \mathbb{1} \otimes \mathbb{1}_B \qquad \text{where } i = x, y, z \tag{1.47}$$

$$\hat{S}_B = \mathbb{1}_A \otimes \hat{S}_i \otimes \bigotimes_1^m \mathbb{1}. \tag{1.48}$$

Substituting $\hat{P}_S$ as the operator in equation 1.40, the singlet probability is

$$\left\langle \hat{P}_S(t) \right\rangle = \mathrm{Tr}\left[\hat{\rho}(t)\hat{P}_S\right]. \tag{1.49}$$

For a singlet born RP, the initial density matrix is

$$\hat{\rho}(0) = \frac{\hat{P}_S}{M} \tag{1.50}$$

where M is the nuclear spin multiplicity. If a RP is coupled to one spin-½ proton, then $M = 2$. Substituting equation 1.45 and 1.50 into equation 1.49 gives

$$\left\langle \hat{P}_S(t) \right\rangle = \frac{1}{M}\,\mathrm{Tr}\left[e^{-\mathrm{i}\hat{H}t}\,\hat{P}_S\,e^{i\hat{H}t}\,\hat{P}_S\right]. \tag{1.51}$$

The triplet projection operator, $\hat{P}_T$, is

$$\begin{aligned}\hat{P}_T &= |T_{+1}\rangle\langle T_{+1}| + |T_0\rangle\langle T_0| + |T_{-1}\rangle\langle T_{-1}| \\ &= \mathbb{1} - \hat{P}_S = \frac{3}{4}\mathbb{1} + \hat{\vec{S}}_A \cdot \hat{\vec{S}}_B.\end{aligned} \tag{1.52}$$

$\hat{P}_T$ includes all three triplet states. Both projection operators, $\hat{P}_S$ and $\hat{P}_T$, have the property that $\hat{P}_i^2 = \hat{P}_i$.

Dynamic probability factor

If the recombination rates of the singlet state and the triplet state are the same, it can be assumed that the spin evolution and radical recombination are two independent processes. At the creation of the RP, the radicals in the geminate RP are close together and the exchange energy between the two electrons is large, therefore the RP is locked in the initial precursor spin state. A short time later, the radicals diffuse apart to about 1 nm where the HFI and Zeeman interactions become dominant and the external field affects the singlet-triplet interconversion. The radicals will re-encounter some time later - the encounter rate is governed by the diffusion rate - and react to form the spin-selective products. A RP is assumed to re-encounter only once; RPs that re-encounter in the singlet state will recombine to form the ground state product and RPs that re-encounter in the triplet state will separate permanently to form the escape products.

The rate of RP recombination is

$$\frac{\mathrm{d}}{\mathrm{d}t}[\mathrm{RP}_S] = \left\langle \hat{P}_S(t) \right\rangle f(t). \tag{1.53}$$

The function, $f(t)$, is similar to a 'constant of proportionality' of the singlet recombination rate. $f(t)$ was termed the dynamic probability factor by Deutch [65] in 1972. This function includes several factors that affect the RPR: the diffusion rate, re-encounter statistics of the RPs, distance dependence of the recombination and separation rate of RPs, and the rate of competing radical reactions. The SY of the RPR then is the integral of equation 1.53 from $t = 0$ to $t = \infty$,

$$\Phi_S = \int_0^\infty \left\langle \hat{P}_S(t) \right\rangle f(t)\,\mathrm{d}t. \tag{1.54}$$

There are several mathematical forms of $f(t)$ and a short summary of the two most popular functions, the exponential model and the Noyes probability distribution of first re-encounter, can

be found in Steiner and Ulrich's review [22]. In the early RPR development, the exponential function was widely used. The exponential model is

$$f(t) = k\, e^{-kt} \tag{1.55}$$

where k is the rate constant. The model assumes that the RPs decay exponentially and the average re-encounter time, or the lifetime of the RP, is $1/k$. The exponential model is probably unrealistic but it is the simplest and the easiest to use compared to other models.

Using the exponential model, equation 1.54 can be simplified to [66]

$$\Phi_S = \frac{1}{M} \sum_{m=1}^{4M} \sum_{n=1}^{4M} |P^S_{mn}|^2 g(\omega_{mn}) \,, \tag{1.56}$$

$$g(x) = \frac{k^2}{k^2 + x^2} \,, \quad \omega_{mn} = \omega_m - \omega_n \,, \quad P^S_{mn} = \left\langle n \left| \hat{P}^S \right| m \right\rangle . \tag{1.57}$$

ω_m is the m-th eigenvalue of the Hamiltonian and $|m\rangle$ is the corresponding m-th eigenvector. The SY depends on the singlet character of the eigenstates of the Hamiltonian and the function $g(\omega_{mn})$. For significant singlet-triplet interconversion, the exponential rate, k, must be smaller than some of the frequencies, ω_{mn}, so that there is time for the coherences to evolve [66].

1.6.6 Singlet yield in Liouville space

The SY can be calculated in Liouville space. The Hilbert space density operator, $\hat{\rho}(t)$, is transformed to the Liouville density ket, $|\hat{\rho}(t)\rangle$, by 'flattening' the Hilbert space $n \times n$ indices, (i, j), into a single Liouville $n^2 \times 1$ index, k; the new index counts through all (i, j) sequentially as

$$(i,j) = \{(1,1),(1,2),\cdots,(1,n),(2,1),\cdots,(n,1),\cdots,(n,n)\} \Longleftrightarrow k = \{1,2,\cdots,n^2\}.$$

The elements in the density operator correspond to the elements in the Liouville density ket,

$$\hat{\rho}(t) \Longleftrightarrow |\hat{\rho}(t)\rangle \equiv \begin{pmatrix} \rho_{11} & \rho_{12} & \cdots & \rho_{1n} \\ \rho_{21} & \ddots & & \vdots \\ \vdots & & \ddots & \vdots \\ \rho_{n1} & \cdots & \cdots & \rho_{nn} \end{pmatrix} \Longleftrightarrow \begin{pmatrix} \rho_{11} \\ \rho_{12} \\ \vdots \\ \rho_{1n} \\ \rho_{21} \\ \vdots \\ \rho_{n1} \\ \vdots \\ \rho_{nn} \end{pmatrix} . \tag{1.58}$$

The row-wise flattening of $\hat{\rho}(t)$, described in equation 1.58, is not the only way of transforming Hilbert space operators to Liouville space vectors but it gives an easy way to form the Liouville space superoperators by calculating the Kronecker products of Hilbert space operators. In general, two Hilbert space operators, which operate on the Hilbert space density operator as $\hat{A}\,\hat{\rho}(t)\,\hat{B}$, have an equivalent Liouville space superoperator, $\hat{\hat{\Omega}}$;

$$\hat{A}\,\hat{\rho}(t)\,\hat{B} \Longleftrightarrow \hat{\hat{\Omega}}\,|\hat{\rho}(t)\rangle \quad \text{where } \hat{\hat{\Omega}} = \hat{A} \otimes \hat{B}^T. \tag{1.59}$$

The time-dependence of the Liouville density ket is given by the stochastic Liouville equation [67–70],

$$\frac{\mathrm{d}}{\mathrm{d}t}\,|\hat{\rho}(t)\rangle = \hat{\hat{L}}\,|\hat{\rho}(t)\rangle \tag{1.60}$$

where $\hat{\hat{L}}$ is the Liouvillian superoperator. Equation 1.60 is analogous to the Hilbert space equation (eq. 1.44). The Liouvillian includes both coherent and incoherent processes;

$$\hat{\hat{L}} = -\mathrm{i}\hat{\hat{H}} + \hat{\hat{K}} + \hat{\hat{W}} + \hat{\hat{\Gamma}} \tag{1.61}$$

where $\hat{\hat{H}}$ is the Hamiltonian superoperator, $\hat{\hat{K}}$ is the kinetic superoperator, $\hat{\hat{W}}$ is the relaxation superoperator, and $\hat{\hat{\Gamma}}$ is the stochastic superoperator which describes the random translational and rotational diffusion of the RP. $\hat{\hat{H}}$ describes the coherent spin evolution of the RP and

$$\hat{\hat{H}} = \hat{H} \otimes \mathbb{1} - \mathbb{1} \otimes \hat{H}^T. \tag{1.62}$$

If $\hat{\hat{L}}$ is time-independent, the solution to the differential equation 1.60 is

$$|\hat{\rho}(t)\rangle = e^{\hat{\hat{L}}t}\,|\hat{\rho}(0)\rangle \tag{1.63}$$

where $|\hat{\rho}(0)\rangle$ is the initial Liouville density ket.

Any Hilbert space operator can be written as a Liouville ket using equation 1.58 and the Liouville bra is the Hermitian conjugate of the ket:

$$\left|\hat{A}\right\rangle^{\dagger} = \left\langle\hat{A}\right|, \tag{1.64}$$

$$\left|\hat{A}\right\rangle^{T} = \left\langle\hat{A}^*\right|. \tag{1.65}$$

To find the expectation value of an operator in Liouville space, I can replace the Hilbert space indices, (i, j), in equation 1.40 with Liouville space index, k, in the same way as in equation

1.58;

$$\left\langle \hat{A} \right\rangle = \mathrm{Tr}\left[\hat{A}\hat{\rho}\right] = \sum_{i,j} \left(\hat{A}\right)_{ji} \rho_{ij} = \sum_{i,j} \left(\hat{A}^T\right)_{ij} \rho_{ij}$$
$$= \sum_{k} \left(\hat{A}^T\right)_{k} \rho_k. \tag{1.66}$$

Then I can transform equation 1.66 to a Liouville bra and ket, using equations 1.58 and 1.65 and the expectation value in Liouville space is

$$\left\langle \hat{A} \right\rangle = \left\langle \hat{A}^\dagger \middle| \hat{\rho} \right\rangle. \tag{1.67}$$

Therefore the expectation value is simply an inner product of a Liouville bra and a Liouville ket. Using the exponential model (eq. 1.55), the SY in Liouville space is

$$\Phi_S = k \int_0^\infty \left\langle \hat{P}_S \middle| \hat{\rho}(t) \right\rangle e^{-kt}\, \mathrm{d}t. \tag{1.68}$$

Substituting equation 1.63 into equation 1.68 gives

$$\Phi_S = k \int_0^\infty \left\langle \hat{P}_S \middle| e^{\hat{\hat{L}}t} \middle| \hat{\rho}(0) \right\rangle e^{-kt}\, \mathrm{d}t. \tag{1.69}$$

The integral in equation 1.69 simplifies to

$$\begin{aligned}
\Phi_S &= k \int_0^\infty \left\langle \hat{P}_S \middle| e^{-\left(-\hat{\hat{L}}+k\mathbb{1}\right)t} \middle| \hat{\rho}(0) \right\rangle \, \mathrm{d}t \\
&= k \left\langle \hat{P}_S \middle| -\left(-\hat{\hat{L}} + k\mathbb{1}\right)^{-1} \left[e^{-\left(-\hat{\hat{L}}+k\mathbb{1}\right)t} \right]_0^\infty \middle| \hat{\rho}(0) \right\rangle \\
&= k \left\langle \hat{P}_S \middle| -\left(-\hat{\hat{L}} + k\mathbb{1}\right)^{-1} \left[\overbrace{e^{-\left(-\hat{\hat{L}}+k\mathbb{1}\right)\cdot\infty}}^{0} - \overbrace{e^{-\left(-\hat{\hat{L}}+k\mathbb{1}\right)\cdot 0}}^{1} \right] \middle| \hat{\rho}(0) \right\rangle \\
&= k \left\langle \hat{P}_S \middle| \left(-\hat{\hat{L}} + k\mathbb{1}\right)^{-1} \middle| \hat{\rho}(0) \right\rangle.
\end{aligned} \tag{1.70}$$

Both equations 1.69 and 1.70 can be used to calculate the SY. The propagator, $e^{\hat{\hat{L}}t}$, in equation 1.69 is calculated for a small time-step and it is used to propagate the density ket, $|\hat{\rho}(t)\rangle$, successively for a sufficient number of time-steps. Then the SY is calculated using numerical integration. The matrix inverse in equation 1.70 is either calculated explicitly or calculated as a left-division problem (i.e. solving for $|b\rangle$ in $\hat{A}\,|b\rangle = |c\rangle$). The matrix size of the Liouvillian, which depends on the RP system, determines which equation, 1.69 or 1.70, is more efficient in computing the SY.

Although calculating the SY in Liouville space is generally slower than in Hilbert space, as the Liouville spin-space dimension is the square of the Hilbert spin-space dimension, complex incoherent processes, such as kinetics and relaxation, can be included in Liouville space. A recent paper by Hogben *et al.* [71] showed that the size of the Liouville spin-space can be reduced significantly, therefore computation of the SY in Liouville space can be dramatically improved.

Chapter 2

Spin-selective radical pair recombination reactions

The exponential model was described in section §1.6.5 and it is widely used to account for the radical recombination of the RPR. However, this model is only suitable when the reaction is diffusion-controlled and the rates of the spin-selective reactions are the same. Another theoretical description is needed to describe a RPR that has different rates of escape and recombination product formations or a general, non-diffusion-controlled RPR that has different singlet and triplet recombination rates.

The standard model for calculating the product yields of RPRs with different singlet and triplet rate constants is based on the phenomenological equations described by Haberkorn in 1976 [72]. Haberkorn's kinetic operator is widely used, however Haberkorn acknowledged that it is phenomenological. A question was raised in the 2009 Spin Chemistry conference and previously in two papers [73, 74] submitted to the e-archive, arXiv, about the validity of the phenomenological equations. At the conference, Kominis [75] stated that Haberkorn's equations could not describe all the quantum mechanical effects of the radical recombination reactions and a new approach based on quantum measurement theory was needed.

Kominis has published two papers [76, 77] on a new kinetic operator in 2009 and in 2011. The model published in the 2011 paper is a modified version of the one published in 2009. The modified model may have been prompted by email correspondence in 2009 between Kominis

and Hore, in which it was conveyed to Kominis that the original model generated incorrect results if mixed initial states were used (this will be discussed in more detail in section §2.6). However, the assertion made in the 2011 paper implied that Kominis considered that the original and the modified models are both valid, and Kominis has never stated, either in print or in person, that the modified model should replace the original model. Therefore the original and the modified models will both be examined and compared to the Haberkorn model in this chapter.

Jones and Hore [78] have also published a different kinetic operator in 2010. Although the two papers by Kominis and the paper by Jones-Hore all suggested that a new RPR model is needed, the Haberkorn model has been used successfully to analyse experimental results ever since its publication in 1976. There was no experimental evidence to challenge the validity and the applicability of the Haberkorn model in 2009, thus the current debate on the RPR model is a theoretical one.

In this chapter, the different kinetic operators are described first, and the differences in the calculated SYs between the four RPR models are compared in the later sections, using a simple RP system. In the next four sections, a minimal basis will be used for simplicity. Only the singlet S state and the triplet T_0 state will be considered, and the $T_{\pm1}$ states will be omitted. The characters S and T represent the S and the T_0 states respectively.

2.1 Haberkorn model

The kinetic operator in the Haberkorn model [72] is based on four phenomenological equations:

$$\frac{\mathrm{d}}{\mathrm{d}t}\rho_{SS} = -k_S\rho_{SS} \quad , \quad \frac{\mathrm{d}}{\mathrm{d}t}\rho_{TT} = -k_T\rho_{TT} \quad , \tag{2.1}$$

$$\frac{\mathrm{d}}{\mathrm{d}t}\rho_{ST} = -\frac{k_S + k_T}{2}\rho_{ST} \quad , \quad \frac{\mathrm{d}}{\mathrm{d}t}\rho_{TS} = -\frac{k_S + k_T}{2}\rho_{TS} \quad , \tag{2.2}$$

where $\rho_{AB} = \langle A|\hat{\rho}|B\rangle$.

The singlet population, ρ_{SS}, and the triplet population, ρ_{TT}, decay with first order rate constants, k_S and k_T respectively. As a result of the recombination (or escape) of the radicals, the coherences between the singlet and triplet states also decrease and the coherences decay with the average of the singlet and triplet rate constants, $1/2(k_S + k_T)$.

In Hilbert space, the time-dependence of the density operator is

$$\frac{\mathrm{d}}{\mathrm{d}t}\hat{\rho} = -\mathrm{i}\left[\hat{H},\hat{\rho}\right] - \frac{k_S}{2}\left(\hat{P}_S\,\hat{\rho} + \hat{\rho}\,\hat{P}_S\right) - \frac{k_T}{2}\left(\hat{P}_T\,\hat{\rho} + \hat{\rho}\,\hat{P}_T\right) \tag{2.3}$$

where $\hat{P}_S$ and $\hat{P}_T$ are the singlet and triplet projection operators, which are defined in §1.6.5. The first term in equation 2.3 is the commutator in the Liouville-von Neumann equation (c.f. eq. 1.44). The second and third terms are the operators that account for the recombination kinetics.

In Liouville space, the Liouvillian is

$$\hat{\hat{L}} = -\mathrm{i}\hat{\hat{H}} - \frac{1}{2}k_S\hat{\hat{P}}_S^{+} - \frac{1}{2}k_T\hat{\hat{P}}_T^{+} \tag{2.4}$$

where the commutator and anti-commutator superoperators are defined as

$$\hat{\hat{A}}^{\pm} = \hat{A}\otimes\mathbb{1} \pm \mathbb{1}\otimes\hat{A}^T. \tag{2.5}$$

The time dependence of the density operator can be solved either numerically in Hilbert space, or analytically in Liouville space (using eq. 1.61, if the spin Hamiltonian is time independent), when kinetic operators are included. The relative speed of SY computations in Hilbert space and Liouville space depends on the size of the spin system and the rate constants used.

The SY, with the Haberkorn kinetic terms, is the integral of the singlet probability and the singlet rate constant over all time;

$$\Phi_S = k_S\int_0^{\infty}\left\langle\hat{P}_S(t)\right\rangle\,\mathrm{d}t. \tag{2.6}$$

Similarly, the triplet product yield is calculated by replacing k_S and $\langle\hat{P}_S\rangle$ in equation 2.6 with k_T and $\langle\hat{P}_T\rangle$.

2.2 Kominis model

Old Kominis model

In his original 2009 paper [76, 79], Kominis stated that the phenomenological equations used in the Haberkorn model do not fully describe the quantum mechanical evolution of the radical pair recombination reaction. His reasoning was that the trace of the density matrix is not conserved

during the evolution in the Haberkorn model. This argument will be examined further in section §2.4.2.

Using quantum measurement theory to describe the recombination, Kominis formulated a new equation of motion for the density matrix,

$$\frac{\mathrm{d}}{\mathrm{d}t}\hat{\rho} = -\mathrm{i}\left[\hat{H},\hat{\rho}\right] - \frac{k_S + k_T}{2}(\hat{\rho}\,\hat{P}_S + \hat{P}_S\,\hat{\rho} - 2\hat{P}_S\,\hat{\rho}\,\hat{P}_S). \tag{2.7}$$

In Liouville space, the Liouvillian for equation 2.7 is

$$\hat{\hat{L}} = -\mathrm{i}\hat{\hat{H}} - \frac{k_S + k_T}{2}\hat{\hat{P}}_S^{+} + (k_S + k_T)\hat{\hat{P}}_{SS} \tag{2.8}$$
$$\text{where} \quad \hat{\hat{P}}_{ab} = \hat{P}_a \otimes \hat{P}_b.$$

The terms in the second bracket of equation 2.7 have the form of a Lindblad master equation [80], using the singlet projection operator as the Lindblad operator. Kominis's interpretation of equation 2.7 is that both singlet and triplet recombination channels essentially measure the same observable, $\hat{P}_S$, with a total measurement rate $1/2(k_S + k_T)$. The trace of the density matrix in equation 2.7 is conserved at all times, i.e.

$$\mathrm{Tr}\left[\hat{\rho}(t)\right] = \left\langle \hat{P}_S(t) \right\rangle + \left\langle \hat{P}_T(t) \right\rangle = 1. \tag{2.9}$$

The population of RPs in $\hat{\rho}$ stays constant at all times and separate 'quantum jump' equations are needed to account for the disappearance of RPs through singlet and triplet reaction channels. The equations[1] are given by the probabilities of a RP disappearing via the singlet channel, p_S, and the triplet channel, p_T, in the time interval $(t \to t + \mathrm{d}t)$:

$$\mathrm{d}p_S = k_S \left\langle \hat{P}_S(t) \right\rangle \mathrm{d}t, \tag{2.10}$$

$$\mathrm{d}p_T = k_T \left\langle \hat{P}_T(t) \right\rangle \mathrm{d}t. \tag{2.11}$$

The amount of RPs left, $n(t)$, in the time interval $(t \to t + \mathrm{d}t)$ is related to the quantum jump equations (eq. 2.10 and 2.11) by[2]

$$\mathrm{d}n = -n(t)\left[\mathrm{d}p_S + \mathrm{d}p_T\right]$$

[1] Equations 2.10 and 2.11 are adapted from equation (7) in Kominis's paper [76].

[2] Equation 2.12 is adapted from equation (9) in Kominis's paper [76].

$$\begin{aligned}
\mathrm{d}n &= -n(t)\left[k_S\langle\hat{P}_S\rangle + k_T\langle\hat{P}_T\rangle\right]\mathrm{d}t \\
\mathrm{d}n &= -n(t)\left[k_S\langle\hat{P}_S\rangle + k_T(1-\langle\hat{P}_S\rangle)\right]\mathrm{d}t \\
\frac{\mathrm{d}n}{\mathrm{d}t} &= -n(t)[(k_S-k_T)\langle\hat{P}_S\rangle + k_T]. \qquad (2.12)
\end{aligned}$$

Integrating equation 2.12 gives the RP population at time t:

$$n(t) = \exp\left[-(k_S-k_T)\int_0^t \left\langle\hat{P}_S(\tau)\right\rangle \,\mathrm{d}\tau - k_T t\right]. \qquad (2.13)$$

The singlet yield is the integral over all time of the RPs in the singlet state multiplied by the singlet rate constant,

$$\Phi_S = k_S\int_0^\infty \left\langle\hat{P}_S(t)\right\rangle n(t)\,\mathrm{d}t. \qquad (2.14)$$

New Kominis model

In 2011, Kominis published a modified version [77] of his original model and the new model retains the same trace-preserving equation of motion (eq. 2.7) that describes the density matrix until recombination occurs. However the description of the recombination is changed significantly. The recombination is no longer accounted for by the quantum jump equations but it is described by extra terms in the equation of motion of the density matrix:

$$\begin{aligned}
\frac{\partial}{\partial t}\hat{\rho} = &-\mathrm{i}\left[\hat{H},\hat{\rho}\right] - \frac{1}{2}(k_S+k_T)(\hat{\rho}\,\hat{P}_S + \hat{P}_S\,\hat{\rho} - 2\hat{P}_S\,\hat{\rho}\,\hat{P}_S) \\
&-(1-p_{\text{coh}})(k_S\hat{P}_S\,\hat{\rho}\,\hat{P}_S + k_T\hat{P}_T\,\hat{\rho}\,\hat{P}_T) \\
&-p_{\text{coh}}(k_S\,\mathrm{Tr}\left[\hat{P}_S\,\hat{\rho}\right] + k_T\,\mathrm{Tr}\left[\hat{P}_T\,\hat{\rho}\right])\frac{\hat{\rho}}{\mathrm{Tr}[\hat{\rho}]}. \qquad (2.15)
\end{aligned}$$

p_{coh} is a function that provides a measure of the coherence between the singlet and the triplet states, and it is defined as

$$\begin{aligned}
p_{\text{coh}} &= \frac{M\,\mathrm{Tr}\left[\hat{P}_S\,\hat{\rho}\,\hat{P}_T\cdot\hat{P}_T\,\hat{\rho}\,\hat{P}_S\right]}{\mathrm{Tr}\left[\hat{P}_S\,\hat{\rho}\,\hat{P}_S\right]\mathrm{Tr}\left[\hat{P}_T\,\hat{\rho}\,\hat{P}_T\right]} \\
&= \frac{M\,\mathrm{Tr}\left[\hat{P}_S\,\hat{\rho}\,\hat{P}_T\,\hat{\rho}\right]}{\mathrm{Tr}\left[\hat{P}_S\,\hat{\rho}\right]\mathrm{Tr}\left[\hat{P}_T\,\hat{\rho}\right]} \qquad (2.16)
\end{aligned}$$

where M is the nuclear spin multiplicity. According to Kominis's paper, a state that can be written as

$$\hat{\rho} = |\Psi\rangle\langle\Psi|,\ |\Psi\rangle = \alpha|S\rangle + \beta|T\rangle \qquad (2.17)$$

that is maximally coherent in the $\{S, T\}$ basis if $\alpha, \beta \neq 0$, and $p_{\text{coh}} = 1$ for this state. Such a state is also a pure state. On the other hand, the state

$$\hat{\rho} = \lambda_S |S\rangle \langle S| + \lambda_T |T\rangle \langle T| \tag{2.18}$$

is minimally coherent in the $\{S, T\}$ basis and $p_{\text{coh}} = 0$ for this state. Therefore p_{coh} is also zero for pure singlet and triplet states. If $\lambda_S > 0$ or $\lambda_T > 0$, the resultant density matrix describes a mixed state.

There are four main terms in Kominis's new equation of motion (eq. 2.15). The first term is the spin Hamiltonian commutator that describes the coherent evolution of the density matrix due to the magnetic interactions of the RP. The second term is the Lindblad term that decreases the coherence of the density matrix due to the 'quantum measurements' of the unsuccessful RP recombinations. The third and fourth terms decrease both the singlet-triplet coherence and the RP population of the density matrix, both of which are dependent on the coherence function, p_{coh}.

The time dependence of the density matrix in Kominis's new model can only be solved numerically in either Hilbert space or Liouville space. This is because equation 2.15 involves the expectation values of the singlet and triplet projections, the total population of the density matrix, and the coherence function, all of which are time-dependent. From the numerically calculated singlet projection, the SY can be found by numerically integrating equation 2.6.

For the rest of this chapter, equations 2.7, 2.13, and 2.14 are referred as the old Kominis model and equations 2.15, and 2.16 are referred as the new Kominis model. The new Kominis model is a modified version of the old Kominis model and it will be shown in a later section that the RPR product yields calculated using the two models are significantly different.

2.3 Jones-Hore model

After Kominis's 2009 paper, Jones and Hore published a separate model that describes that RP recombination reaction [78]. The Jones-Hore model is based on similar principles to the Haberkorn model; the singlet population, the triplet population and the singlet-triplet coherences decay at different rates, and the kinetic operator is found using four rate equations.

In a singlet recombination reaction that occurs at a rate of k_S, the wavefunction of a portion of the ensemble collapses to singlet during the time interval $(t \rightarrow t + \mathrm{d}t)$. Due to the wavefunction collapse, the reaction removes a portion, $k_S\,\mathrm{d}t$, of the singlet population, ρ_{SS}, and also removes the same portion, $k_S\,\mathrm{d}t$, of all singlet coherences (i.e. ρ_{ST} and ρ_{TS}). Similarly, when the wavefunction collapses to triplet during a triplet reaction, ρ_{TT}, ρ_{TS} and ρ_{ST} all decrease by a fraction $k_T\,\mathrm{d}t$. Therefore the four rate equations of the density matrix elements are:

$$\frac{\mathrm{d}}{\mathrm{d}t}\rho_{SS} = -k_S\rho_{SS} \quad , \quad \frac{\mathrm{d}}{\mathrm{d}t}\rho_{TT} = -k_T\rho_{TT} \quad , \tag{2.19}$$

$$\frac{\mathrm{d}}{\mathrm{d}t}\rho_{ST} = -(k_S + k_T)\rho_{ST} \quad , \quad \frac{\mathrm{d}}{\mathrm{d}t}\rho_{TS} = -(k_S + k_T)\rho_{TS} \quad . \tag{2.20}$$

Comparing equations 2.2 and 2.20, the rate of singlet-triplet decoherence in the Jones-Hore model is twice as much as in the Haberkorn model.

The density matrix elements in equations 2.19 and 2.20 need to be converted to Hilbert space operators. Remember $\hat{P}_a = |a\rangle\langle a|$, the operator $\hat{O}$ is defined as

$$\hat{O} = \hat{P}_a\,\hat{\rho}\,\hat{P}_b = |a\rangle\langle a|\,\hat{\rho}\,|b\rangle\langle b|\,. \tag{2.21}$$

Any element in the operator $\hat{O}$ can be found by:

$$O_{mn} = \langle m|a\rangle\langle a|\hat{\rho}|b\rangle\langle b|n\rangle = \delta_{ma}\delta_{bn}\langle a|\hat{\rho}|b\rangle \tag{2.22}$$

Therefore $\hat{O}$ is an operator with O_{ab} as the only non-zero element and O_{ab} equals to ρ_{ab}. Using operators with the same form as equation 2.21, the equation of motion in Hilbert space is

$$\begin{aligned}\frac{\mathrm{d}}{\mathrm{d}t}\hat{\rho} = -\mathrm{i}\left[\hat{H},\hat{\rho}\right] &- k_S\left(\hat{P}_S\,\hat{\rho}\,\hat{P}_S + \hat{P}_S\,\hat{\rho}\,\hat{P}_T + \hat{P}_T\,\hat{\rho}\,\hat{P}_S\right)\\ &- k_T\left(\hat{P}_T\,\hat{\rho}\,\hat{P}_T + \hat{P}_T\,\hat{\rho}\,\hat{P}_S + \hat{P}_S\,\hat{\rho}\,\hat{P}_T\right).\end{aligned} \tag{2.23}$$

Using the identity $\hat{P}_S + \hat{P}_T = \mathbb{1}$, equation 2.23 simplifies to

$$\frac{\mathrm{d}}{\mathrm{d}t}\hat{\rho} = -\mathrm{i}\left[\hat{H},\hat{\rho}\right] - k_S\left(\hat{\rho} - \hat{P}_T\,\hat{\rho}\,\hat{P}_T\right) - k_T\left(\hat{\rho} - \hat{P}_S\,\hat{\rho}\,\hat{P}_S\right). \tag{2.24}$$

The equivalent Liouvillian is

$$\hat{\hat{L}} = -\mathrm{i}\hat{\hat{H}} - (k_S + k_T)\mathbb{1} + k_S\hat{\hat{P}}_T^{+} + k_T\hat{\hat{P}}_S^{+}. \tag{2.25}$$

The SY is calculated in the same way as the Haberkorn model using equation 2.6.

2.4 Theoretical differences

2.4.1 Haberkorn and Jones-Hore models

Fundamentally the Haberkorn model and the Jones-Hore model are based on the same type of first order rate equations and the only difference between them is the rate of the decoherence due to the recombination reactions. Comparing equations 2.2 and 2.20, it is clear that the coherence between singlet and triplet decays at twice the rate in the Jones-Hore model compared to the Haberkorn model. This means that the singlet-triplet interconversion is depressed in the Jones-Hore model.

Quantum measurement theory is discussed in both papers by Kominis and Jones-Hore. A measurement of the observable, $\hat{O}$, causes the wavefunction of a quantum system to collapse into one of the eigenstates of $\hat{O}$, corresponding to n-eigenvalues, $o_1, o_2, \ldots, o_n$. The observable $\hat{O}$ is not the same as the spin Hamiltonian of the system, therefore $o_1, o_2, \ldots, o_n$ are not the same as the eigenstates of the spin Hamiltonian.

The RP recombination reaction can be interpreted as a hypothetical two-step process. The first step is a quantum measurement that causes a coherent RP to collapse to either an incoherent pure singlet state or triplet state and it removes all singlet-triplet coherences (fig. 2.1). After the measurement, the pure singlet and triplet decay from the excited state to the ground state and form the singlet and triplet products at different rates, k_S and k_T [81].

The rate of decoherence is the same as the rate of measurement, k_m, and the general rate equation of the coherence is

$$\frac{\mathrm{d}}{\mathrm{d}t}\rho_{ST} = -k_m \rho_{ST}. \tag{2.26}$$

The same equation applies to ρ_{TS}.

All eigenvalues of the density matrix are non-negative; the density operator is positive semi-definite [82]. One of the properties of a positive semi-definite matrix is that the determinant is also non-negative. This constraint gives a lower bound for the rate of decoherence. Given a density matrix in the $\{S, T\}$ basis,

$$\hat{\rho} = \begin{pmatrix} \rho_{SS} & \rho_{ST} \\ \rho_{TS} & \rho_{TT} \end{pmatrix},$$

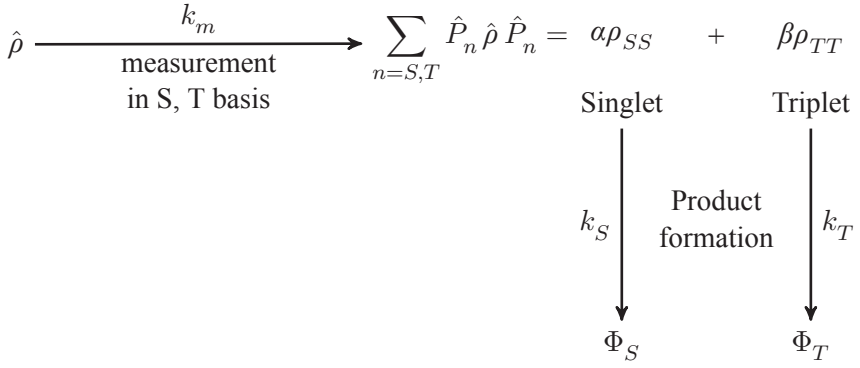

Figure 2.1: Quantum measurement in RPR. $\hat{\rho}$ is the density matrix for the ensemble. ρ_{SS} and ρ_{TT} are the singlet and triplet populations respectively. The RP recombination reaction is separated hypothetically into two steps, measurement and decay. A fraction, $k_m \mathrm{d}t$, of the ensemble is measured and the observable, $\hat{P}_n$, projects the density matrix onto the singlet or triplet subspace. Then the excited singlet and triplet states decay at rates k_S and k_T respectively. After a measurement, the singlet-triplet coherences are removed from the measured portion of the ensemble. $\alpha : \beta$ is the ratio of the singlet population to the triplet population which is dependent on the state of the density matrix.

its determinant is

$$\begin{aligned} |\hat{\rho}| &= \rho_{SS}\rho_{TT} - \rho_{ST}\rho_{TS} \geqslant 0 \\ &\Rightarrow \rho_{SS}\rho_{TT} \geqslant \rho_{ST}\rho_{TS}. \end{aligned} \tag{2.27}$$

During the RP recombination, all elements in the density matrix decay with first order rate constants (eq. 2.1 and 2.26). Effectively, the matrix elements of $\hat{\rho}$ decay exponentially and $\hat{\rho}$ has to satisfy the inequality equation (eq. 2.27) for all time. Therefore equation 2.27 becomes [83]

$$\rho_{SS}(t)\,\rho_{TT}(t) \cdot e^{-(k_S+k_T)t} \geqslant \left|\rho_{ST}(t)\right|^2 \cdot e^{-2k_m t} \tag{2.28}$$

$$\Rightarrow k_m \geqslant \frac{1}{2}(k_S + k_T) \tag{2.29}$$

where $\rho_{ab}(t)$ is the element ab of $\hat{\rho}$ evaluated at time t. Equation 2.28 is true for all time and all initial conditions. The Haberkorn model uses the average of the singlet and triplet recombination rates, which is the lower limit of the decoherence rate. It appears that, mathematically speaking, the decoherence rate can be higher than $1/2(k_S + k_T)$.

Recent papers have argued theoretically that the decoherence that accompanies the recombination of RPs should occur at a rate of $1/2(k_S + k_T)$ [81,83]. Higher rates of decoherence can be found in more complex recombination schemes. The recombination of RPs in the liquid phase

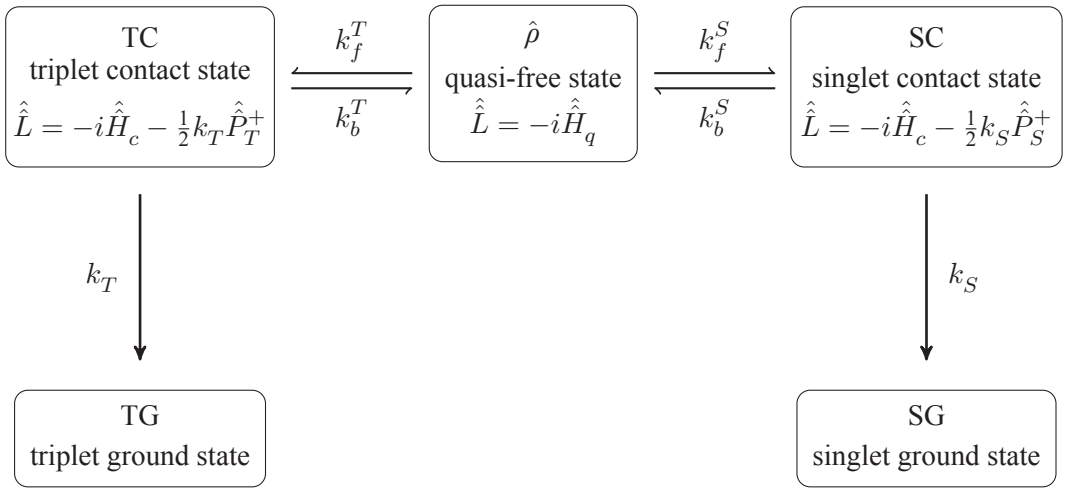

Figure 2.2: Reaction scheme for a two-site RP recombination. The quasi-free state and the contact state evolve under different spin Hamiltonians, $\hat{\hat{H}}_q$ and $\hat{\hat{H}}_c$ respectively. Only $\hat{\hat{H}}_c$ contains the exchange interaction.

can be viewed as a two-step process (fig. 2.2). The radicals are under the influence of the spin Hamiltonian when they are quasi-free, which means the radicals are well separated but within the same solvent cage. When the radicals diffuse close to each other in the contact state, then the RP evolves under a different spin Hamiltonian, with a large exchange interaction, and the kinetic superoperator.

This two-site model was proposed in a paper by Shushin in 1991 [84] and the Liouvillian for the contact state should include the exchange interaction. The contact state is formed reversibly from the quasi-free state and the RP will recombine irreversibly from the contact state to form the ground state product.

The rate equations for the singlet populations of the quasi-free, contact and singlet product states are:

$$\frac{\mathrm{d}}{\mathrm{d}t}\rho_{SS} = -k_f^S\rho_{SS} + k_b^S\rho_{SS}^{\mathrm{SC}}, \tag{2.30}$$

$$\frac{\mathrm{d}}{\mathrm{d}t}\rho_{SS}^{\mathrm{SC}} = k_f^S\rho_{SS} - (k_b^S + k_S)\rho_{SS}^{\mathrm{SC}}, \tag{2.31}$$

$$\frac{\mathrm{d}}{\mathrm{d}t}\rho_{SS}^{\mathrm{SG}} = k_S\rho_{SS}^{\mathrm{SC}}. \tag{2.32}$$

$\hat{\rho}$, $\hat{\rho}^{\mathrm{SC}}$, $\hat{\rho}^{\mathrm{SG}}$, $\hat{\rho}^{\mathrm{TC}}$, and $\hat{\rho}^{\mathrm{TG}}$ are the density matrices of the quasi free state, the singlet contact state, the singlet ground state, the triplet contact state, and the triplet ground state.

The contact state can be assumed to be a short-lived intermediate with a low concentration. One can apply the steady state approximation (SSA) to the contact state (eq. 2.31), hence

$$\rho_{SS}^{\mathrm{SC}} = \frac{k_f^S}{k_b^S + k_S}\rho_{SS}. \tag{2.33}$$

Substituting equation 2.33 into equations 2.30 and 2.32 gives

$$\frac{\mathrm{d}}{\mathrm{d}t}\rho_{SS} = -\frac{k_f^S k_S}{k_b^S + k_S}\rho_{SS}, \tag{2.34}$$

$$\frac{\mathrm{d}}{\mathrm{d}t}\rho_{SS}^{\mathrm{SG}} = \frac{k_f^S k_S}{k_b^S + k_S}\rho_{SS}. \tag{2.35}$$

The rate of singlet ground state formation is the same as the singlet population decay in the RP. Similarly, the triplet population in the RP decays as

$$\frac{\mathrm{d}}{\mathrm{d}t}\rho_{TT} = -\frac{k_f^T k_T}{k_b^T + k_T}\rho_{TT}. \tag{2.36}$$

The rate equations of the coherences between singlet and triplet are

$$\frac{\mathrm{d}}{\mathrm{d}t}\rho_{ST} = -(k_f^S + k_f^T)\rho_{ST} + k_b^S\rho_{ST}^{\mathrm{SC}} + k_b^T\rho_{ST}^{\mathrm{TC}}, \tag{2.37}$$

$$\frac{\mathrm{d}}{\mathrm{d}t}\rho_{ST}^{\mathrm{SC}} = k_f^S\rho_{ST} - (k_b^S + \frac{k_S}{2})\rho_{ST}^{\mathrm{SC}}, \tag{2.38}$$

$$\frac{\mathrm{d}}{\mathrm{d}t}\rho_{ST}^{\mathrm{TC}} = k_f^T\rho_{ST} - (k_b^T + \frac{k_T}{2})\rho_{ST}^{\mathrm{TC}}. \tag{2.39}$$

The decoherence rates due to radical recombination in equations 2.38 and 2.39 are $1/2\ k_S$ and $1/2\ k_T$ per equation 2.2. Similarly, equations 2.37, 2.38, and 2.39 also apply to ρ_{TS}, ρ_{TS}^{SC}, and ρ_{TS}^{TC}. The SSA can be applied to equations 2.38 and 2.39, hence

$$\rho_{ST}^{\mathrm{SC}} = \frac{k_f^S}{k_b^S + k_S/2}\,\rho_{ST}, \tag{2.40}$$

$$\rho_{ST}^{\mathrm{TC}} = \frac{k_f^T}{k_b^T + k_T/2}\,\rho_{ST}. \tag{2.41}$$

Substituting equations 2.40 and 2.41 into equation 2.37 gives the rate equation for ρ_{ST} and ρ_{TS};

$$\frac{\mathrm{d}}{\mathrm{d}t}\rho_{ST} = -\left(\frac{k_f^S k_S}{2\ \left(k_b^S + k_S/2\right)} + \frac{k_f^T k_T}{2\ \left(k_b^T + k_T/2\right)}\right)\rho_{ST}, \tag{2.42}$$

$$\frac{\mathrm{d}}{\mathrm{d}t}\rho_{TS} = -\left(\frac{k_f^S k_S}{2\ \left(k_b^S + k_S/2\right)} + \frac{k_f^T k_T}{2\ \left(k_b^T + k_T/2\right)}\right)\rho_{TS}. \tag{2.43}$$

When $k_b^S \gg k_S, k_b^T \gg k_T$, the rate equations resemble the Haberkorn model [85]:

$$\frac{\mathrm{d}}{\mathrm{d}t}\rho_{SS} = -\frac{k_f^S k_S}{k_b^S}\rho_{SS} = -k_S^{\text{eff}}\rho_{SS}, \tag{2.44}$$

$$\frac{\mathrm{d}}{\mathrm{d}t}\rho_{TT} = -\frac{k_f^T k_T}{k_b^T}\rho_{TT} = -k_T^{\text{eff}}\rho_{TT}, \tag{2.45}$$

$$\frac{\mathrm{d}}{\mathrm{d}t}\rho_{ST} = -\left(\frac{k_f^S k_S}{2\,k_b^S} + \frac{k_f^T k_T}{2\,k_b^T}\right)\rho_{ST} = -\frac{k_S^{\text{eff}} + k_T^{\text{eff}}}{2}\rho_{ST}, \tag{2.46}$$

$$\frac{\mathrm{d}}{\mathrm{d}t}\rho_{TS} = -\frac{k_S^{\text{eff}} + k_T^{\text{eff}}}{2}\rho_{TS}. \tag{2.47}$$

When $k_b^S \ll k_S, k_b^T \ll k_T$, the rate equations resemble the Jones-Hore model [85]:

$$\frac{\mathrm{d}}{\mathrm{d}t}\rho_{SS} = -k_f^S\rho_{SS}, \tag{2.48}$$

$$\frac{\mathrm{d}}{\mathrm{d}t}\rho_{TT} = -k_f^T\rho_{TT}, \tag{2.49}$$

$$\frac{\mathrm{d}}{\mathrm{d}t}\rho_{ST} = -\left(k_f^S + k_f^T\right)\rho_{ST}, \tag{2.50}$$

$$\frac{\mathrm{d}}{\mathrm{d}t}\rho_{TS} = -\left(k_f^S + k_f^T\right)\rho_{TS}. \tag{2.51}$$

Therefore the Haberkorn and Jones-Hore models are the limits of the two-site model. Depending on the RP system, the decoherence rate, $\eta(k_S + k_T)$, can be in the range of $1/2 \leqslant \eta \leqslant 1$ in this two-site model.

2.4.2 Old and new Kominis models

The old Kominis model is the only model that preserves the trace of the density operator. Kominis's original argument against the decay of the trace of the density operator is that this decay "eliminates the actual presence of quantum coherence effects" [76]. However the density operator can be easily expanded to include the product space and any decaying RP population can be added to the product space [83, 86].

In practice, the product space is omitted because it is assumed that there is no coherence between the RP states and product states, as any coherence between two different chemical species decays rapidly, and the product states are not involved in any coherent evolution. A smaller density operator, which does not have the unnecessary product space, is easier to use in calculations.

As $\mathrm{Tr}\,[\hat{\rho}(t)] = 1$ at all times for the old Kominis model, 'quantum jump' equations are needed to account for the recombination of the RP. These equations (eq. 2.10 and 2.11) are unique to this model and imply that the recombination has no effects on the density operator.

Expanding the kinetic terms in the old Kominis model, equation 2.7 becomes

$$\frac{\mathrm{d}}{\mathrm{d}t}\hat{\rho} = -\mathrm{i}\left[\hat{H},\hat{\rho}\right] - \frac{1}{2}(k_S + k_T)(\hat{P}_S\,\hat{\rho}\,\hat{P}_T + \hat{P}_T\,\hat{\rho}\,\hat{P}_S). \tag{2.52}$$

Compared to the Haberkorn model, the old Kominis model has the same rate of singlet-triplet decoherence, and the terms for the decay of singlet and triplet populations are omitted in order to preserve the trace of the density operator.

The new Kominis model has the same basic decoherence rate as the Haberkorn and old Kominis models (second term in eq. 2.15). However the trace of the density matrix is no longer conserved in the new Kominis model. The third and fourth terms in equation 2.15 reduce the diagonal elements of the density matrix as the RP evolves.

A new function, p_{coh} (eq. 2.16), is introduced in the new Kominis model and it is an attempt to describe the fraction of the RP population that is coherent. It is debatable whether equation 2.16 is an accurate description of the singlet-triplet coherence. The function has never been used before or tested experimentally in a Spin Chemistry context.

p_{coh} is used to account for the recombination of the coherent and incoherent parts of the population separately. The third term accounts for the incoherent part and it only reduces the singlet and triplet populations (diagonal elements of the density matrix). The fourth term reduces the whole density matrix (populations and coherences) that is proportional to the singlet and triplet probabilities, and it accounts for the recombination of the coherent part.

Therefore the new model has two separate sources of decoherence: the measurements of the RP (second term in eq. 2.15), and the recombination of the RP (fourth term in eq. 2.15). Close examination of p_{coh} shows that the sum of the separate dynamics of two pure states will be different from the dynamics of a mixed state of the same pure states. This point will be discussed further in section §2.6.

The two Kominis models are fundamentally different from the Haberkorn and Jones-Hore models in the description of the RP recombination reaction in the equation of motion of the

density matrix. All four models have their own theoretical underpinnings and it is difficult to ascertain which one is correct. In the next section, the calculated singlet yields of a simple RP system using all four models are presented. Different external fields and reaction rates will be used in order to find the conditions under which it may be possible to distinguish the four models in an experiment.

2.5 Differences in simulation

It is useful to compare the simulations of the time evolution and the SY of a simple spin-$1/2$ RP system using the four models. Different singlet and triplet rate constants are used in the simulations and the rate constants that produce the biggest distinction between the four models can be found. The simulations can be used to devise a suitable experiment that will distinguish the four models and assess the validity of each model.

The RP system used in the simulations in this section is coupled to one spin-$1/2$ nucleus with an isotropic hyperfine coupling constant. No spin-relaxation is included in the simulations so that the only source of singlet-triplet decoherence is the RP recombination reaction. The lack of spin-relaxation will demonstrate the differences in the simulations due to the different kinetic operators used in the four RPR models. All four RP states, S, T_{+1}, T_0, and T_{+1}, are included in the simulations in this section.

2.5.1 Time evolution simulation

The singlet population of a singlet-born RP is calculated at 1 mT using the four models (fig. 2.3a). The singlet populations of the first 5 µs are different for the four models. After $t = 5$ µs, the time evolutions of the Haberkorn and new Kominis models become very similar, and separately, the Jones-Hore and the old Kominis models are also very similar.

The oscillation in the time evolution of the singlet population is caused by the singlet-triplet interconversion which is driven by the spin Hamiltonian. Therefore the amplitude of the oscillation is an indication of the amount of singlet-triplet coherence in the system. From the amplitude of the oscillations, the rates of singlet-triplet decoherence can be ranked in descending order: Jones-Hore, Old Kominis, New Kominis, Haberkorn. The order of decoherence rates is con-

sistent with the differences of the decoherence operators in the four models. After $t = 5\,\mu s$, the oscillations have disappeared in the Jones-Hore and the old Kominis models, whereas the Haberkorn and the new Kominis models still have significant oscillations.

The triplet population of a triplet-born RP is calculated at 1 T using the four models (fig. 2.3b). 1 T is a high field compared to the hyperfine coupling used in the simulations, therefore the T_{+1} and T_{-1} states are not accessible from the T_0 state. Although the Jones-Hore model has a smaller oscillation amplitude, which is a result of the higher decoherence rate, the overall triplet population decay is similar to the Haberkorn and new Kominis models. The triplet populations of the three models all decay to around $2/3$ because of the high field and the slow triplet reaction rate. The triplet population decay rate of the old Kominis model is significantly higher than the other models. It appears that the T_{+1} and T_{-1} states in the old Kominis model react at a faster rate compared to the other three models.

2.5.2 Quantum Zeno effect

The quantum Zeno effect is an effect in which the decay of an unstable particle is hindered by continuously observing the quantum state of the particle [87]. Effectively, the evolution of the particle is stopped by the frequent measurement of the particle's quantum state and the particle remains in its initial state. In Kominis's 2009 paper, he argued that Haberkorn's phenomenological equations are inadequate to describe all quantum mechanical effects, and that the quantum Zeno effect, which is shown to its full extent using the Kominis model, is fundamental and essential to the RPR.

It was discussed in section §2.4.1 that the singlet reaction and the triplet reaction can be interpreted as quantum measurements of the RP system. The quantum Zeno effect occurs when the triplet rate constant is sufficiently larger than the singlet rate constant for a singlet-born RP and vice versa for a triplet-born RP.

Under the condition $k_T \gg a \gg k_S$, the singlet-triplet coherence decays at a faster rate than the hyperfine coupling frequency. Although the HFI induces coherent evolution between $\rho_{SS} \leftrightarrow \rho_{ST}$ and $\rho_{SS} \leftrightarrow \rho_{TT}$, any coherence ($\rho_{ST}$) accumulated from the singlet population (ρ_{SS}) is quickly removed before it evolves into the triplet population (ρ_{TT}). Therefore the RP

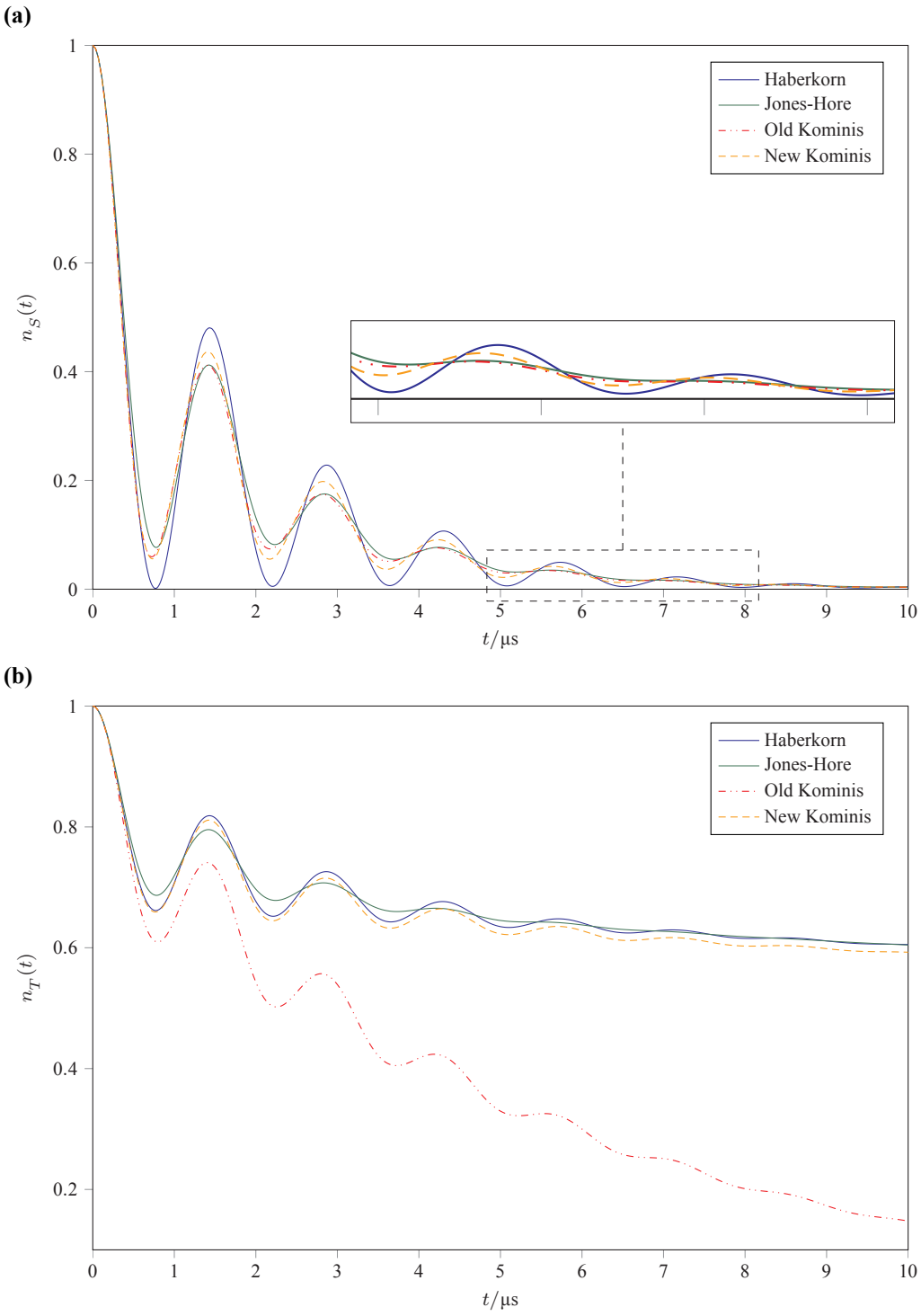

Figure 2.3: Time evolution of a RP which contains a spin-1/2 nucleus is calculated using the four different models. (a) is the singlet population and (b) is the triplet population as a function of time. The conditions of the simulation are as follows: (a) $B_0 = 1\,\mathrm{mT}$, $k_S = 0.01\,\mu\mathrm{s}^{-1}$, $k_T = 1\,\mu\mathrm{s}^{-1}$, the initial state is singlet and (b) $B_0 = 1\,\mathrm{T}$, $k_S = 1\,\mu\mathrm{s}^{-1}$, $k_T = 0.01\,\mu\mathrm{s}^{-1}$, the initial state is triplet. The hyperfine coupling of the single nucleus is isotropic, $a = 0.05\,\mathrm{mT}$, in both simulations.

is effectively 'locked' in the initial singlet state and no triplet product is produced under the quantum Zeno condition.

Singlet-born RP

The time evolution of a singlet-born RP with a single spin-1/2 nucleus with $k_S = 0$ is calculated for a range of k_T values in a 1 mT external field (fig. 2.4). The quantum Zeno effect can be seen for the Haberkorn, the Jones-Hore, and the new Kominis models at $k_T > 10\,\mu s^{-1}$ and the singlet population decay rates of the three models in this quantum Zeno region are different: when $k_T = 100\,\mu s^{-1}$, the Jones-Hore model has the slowest decay rate and the new Kominis model has the fastest decay rate. However, the old Kominis model lacks any quantum Zeno effect at the same region; the whole RP population is predicted to react very quickly via the triplet channel for $k_T > 1\,\mu s^{-1}$.

Triplet-born RP

The time evolution of a triplet-born RP with one spin-1/2 nucleus and $k_T = 0$ is also calculated for a range of k_S values in a 1 T field (fig. 2.5). As discussed in the previous subsection, at such a high field, only interconversion between $T_0 \leftrightarrow S$ occurs. Since the triplet channel is non-reactive, only 1/3 of the RP population will decay via the singlet channel and 2/3 of the RP population will remain in the $T_\pm$ states.

The triplet populations calculated using the Haberkorn and the Jones-Hore models of a triplet-born RP are very similar and there are minor differences in the population decay rate in the quantum Zeno region, $k_S > 10\,\mu s^{-1}$. These two models both correctly predict that the triplet population does not decay below 2/3 at any time.

Contrary to the other three models, the old Kominis model predicts that the whole RP population will react via the singlet channel and no quantum Zeno effect is shown (fig. 2.5c and 2.6). The old Kominis model fails to account for the unreactive $T_\pm$ states and the reason for this failure will be discussed in the next section. The new Kominis model simulation may appear to be similar to the Haberkorn and the Jones-Hore model, however closer examination of the triplet

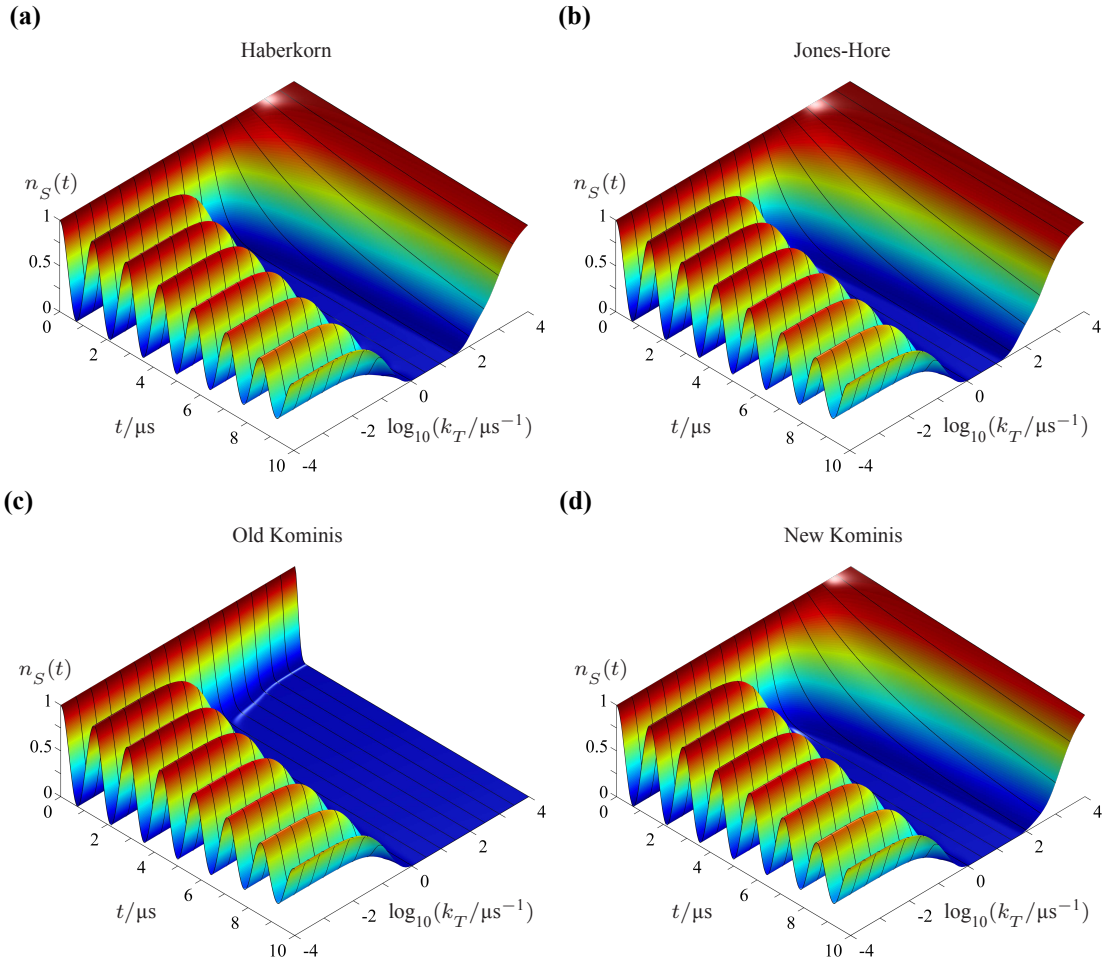

Figure 2.4: Time evolution of the singlet population of a RP which contains a spin-1/2 nucleus is calculated using the four different models for a range of k_T values. The conditions of the simulation are as follows: $B_0 = 1$ mT, $k_S = 0$, $a = 0.05$ mT, the RP is singlet-born. The model used is stated at the top of each subfigure. In (c), the old Kominis predicts no quantum Zeno effect for $k_T > 100\ \mu s^{-1}$, contrary to the other three models.

population calculated using the new Kominis model at long time shows that the terminal triplet population is less than 2/3 (fig. 2.6).

2.5.3 Singlet yield simulation

SYs are calculated using the four different models with different values of k_S, k_T, and B_0 (fig. 2.7). The RP used has a single spin-1/2 nucleus ($a = 1$ mT) and is singlet-born. The plots in figure 2.7 can be divided into five sections, as shown in figure 2.8.

Section (i) is a region where the SY is varying from 0 to 1 as the reaction rates are similar in magnitude ($k_S \approx k_T \leqslant a$) and products are formed via the completing singlet and triplet

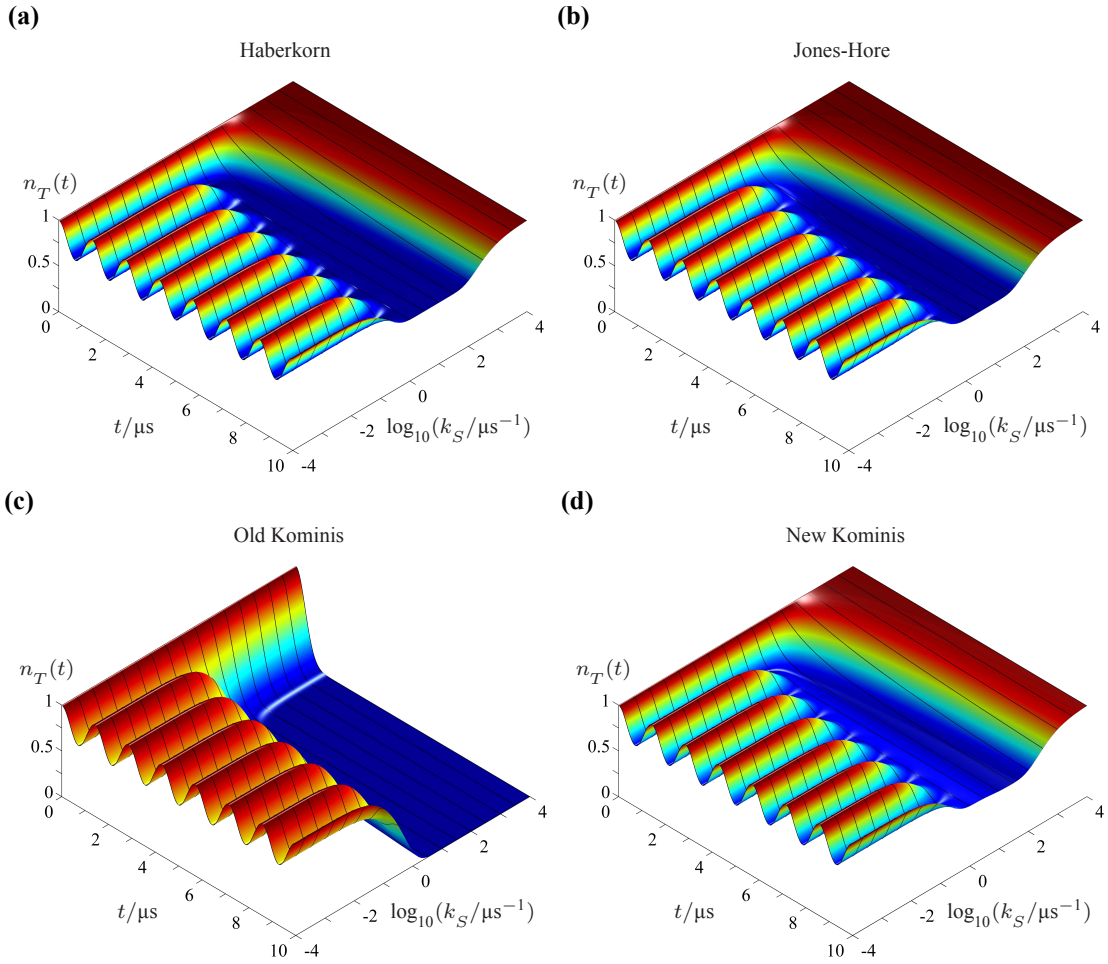

Figure 2.5: Time evolution of the triplet population of a RP which contains a spin-1/2 nucleus is calculated using the four different models for a range of k_T values. The conditions of the simulation are as follows: $B_0 = 1\,\mathrm{T}$, $k_T = 0$, $a = 0.05\,\mathrm{mT}$, the RP is triplet-born. The model used is stated at the top of each subfigure. In (c), the old Kominis model predicts that all of the RP population would decay for $k_T > 1\ \mu s^{-1}$, which is unexpected.

channels. In section (ii), $\Phi_S = 1$ because $k_S \gg k_T$ and all RPs recombine via the singlet channel before any singlet-triplet interconversion occurs.

In section (iii), $k_T > k_S$ but $k_S < a$, so a large proportion of RPs evolved into the triplet state and reacts via the triplet channel, hence $\Phi_S \approx 0$. Section (iv) is the quantum Zeno region where the triplet rate constant is significantly faster than the rate of singlet-triplet interconversion. Any coherences built up by the coherent evolution is quickly removed due to $k_T \gg a$ and only singlet product is formed. Section (v) is the boundary between section (iii) and (iv), and the parameters used are in-between those in section (iii) and (iv), therefore $0 < \Phi_S < 1$.

The SY dependence on k_S, k_T, and B_0 is very similar for the Haberkorn, the Jones-Hore, and

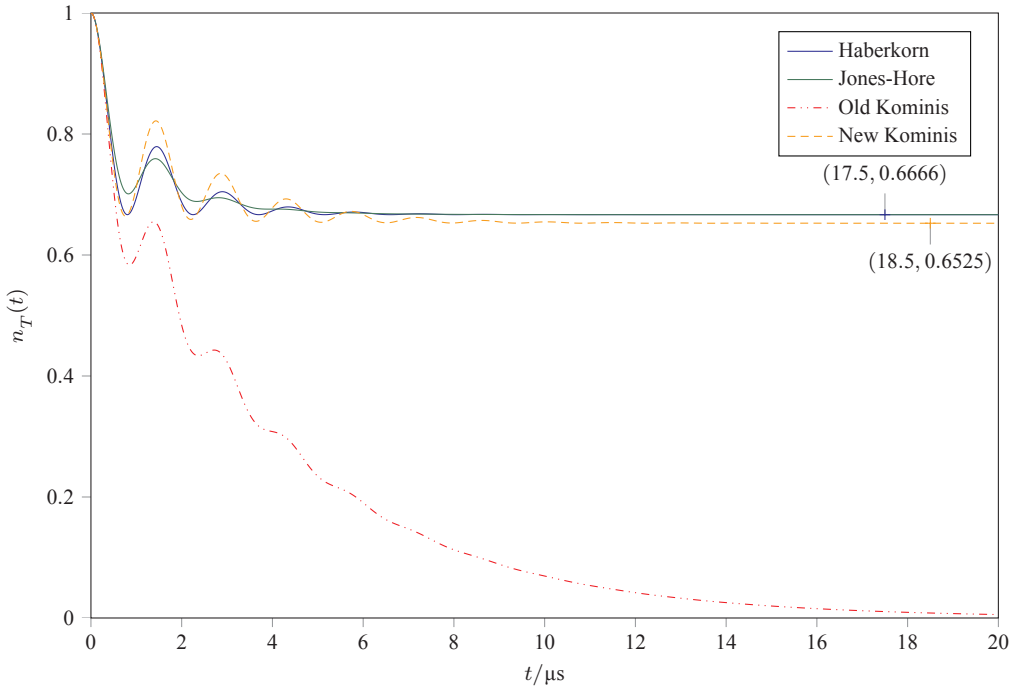

Figure 2.6: Time evolution of the triplet population of a RP which contains a spin-1/2 nucleus is calculated using the four different models. The conditions of the simulation are as follows: $B_0 = 1\,\mathrm{T}$, $k_S = 1\,\mu\mathrm{s}^{-1}$, $k_T = 0$, the initial state is triplet. The hyperfine coupling constant of the single nucleus is isotropic, $a = 0.05\,\mathrm{mT}$. The triplet populations for the old Kominis and the new Kominis models at $t = 20\,\mu\mathrm{s}$ are less than 2/3.

the new Kominis models. However, the old Kominis model predicts very different SY dependence compared to the other three models, especially in the quantum Zeno region ($k_T > 10^3\ \mu\mathrm{s}^{-1}$ and $1\ \mu\mathrm{s}^{-1} < k_S < 10^2\ \mu\mathrm{s}^{-1}$, *i.e.* section (iv) in fig. 2.8). This is due to the absence of the quantum Zeno effect in the old Kominis model (see fig. 2.4).

Singlet yield difference

The root mean squared difference of the SYs calculated over 9 field strengths, with a particular set of k_S and k_T rate constants, between any two models is

$$\Delta\Phi_S^{\mathrm{rms}}(X,Y) = \sqrt{\frac{1}{9}\sum_{i=1}^{9}\left[\Phi_S(X,B_{0,i}) - \Phi_S(Y,B_{0,i})\right]^2} \tag{2.53}$$

$$\text{where } X,Y = \begin{matrix}\mathrm{H\,(Haberkorn),\ JH\,(Jones\text{-}Hore)}\\ \mathrm{OK\,(Old\ Kominis),\ NK\,(New\ Kominis)}\end{matrix}\text{, and}$$

$$B_{0,i} = \{0.01, 0.02, 0.05, 0.1, 0.2, 0.5, 1, 2, 5\}\,\mathrm{mT}.$$

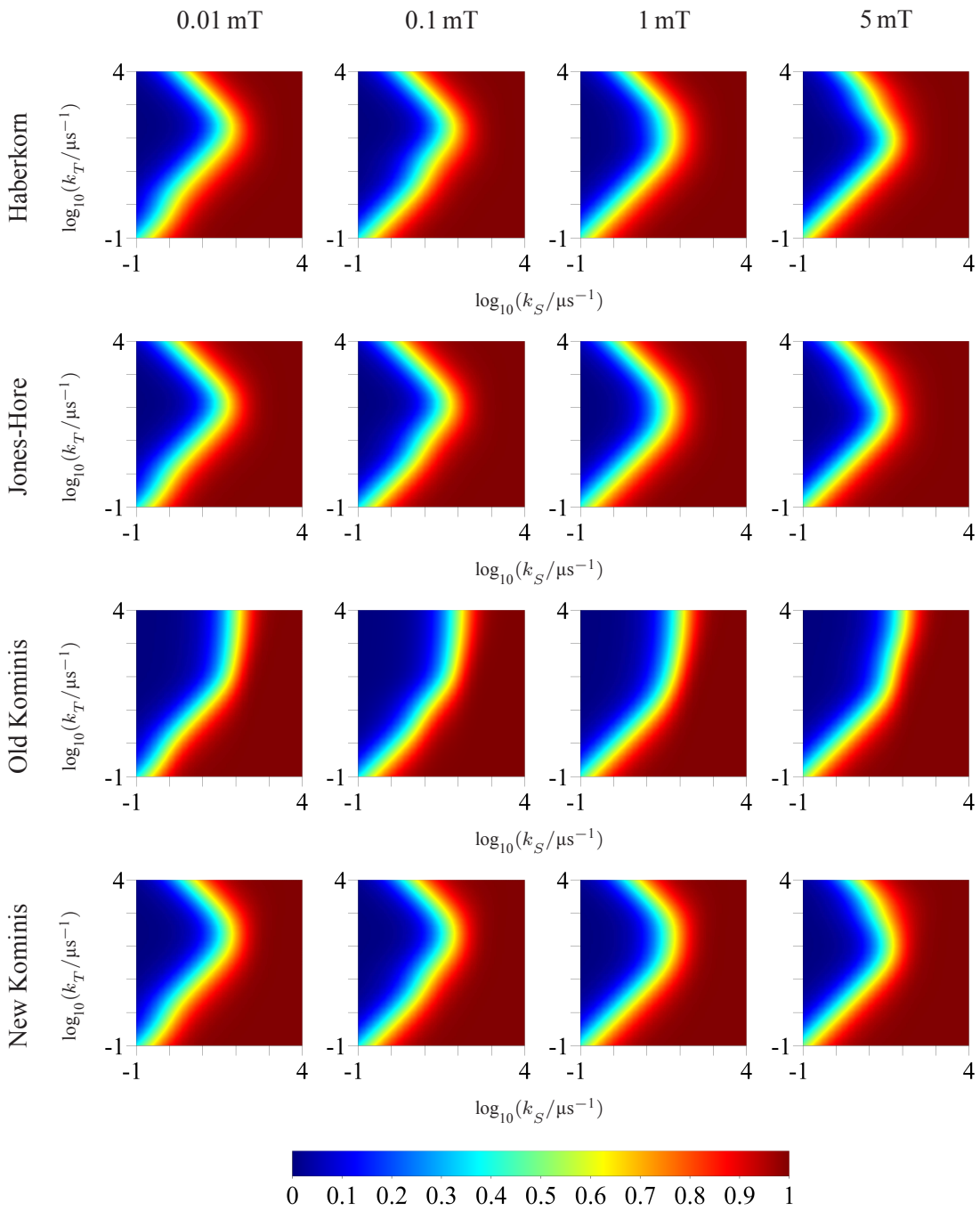

Figure 2.7: Four different RPR models, Haberkorn, Jones-Hore, old Kominis, and new Kominis, are used to calculate the SYs of a singlet-born RP with one spin-1/2 nucleus, $a = 1\,\text{mT}$. The colour of the plot represents the SY, blue = 0 and red = 1. Four different B_0 field strengths, 0.01 mT, 0.1 mT, 1 mT, and 5 mT, are used. The values of the singlet rate constant, k_S, and the triplet rate constant, k_T, vary between 0.1 μs^{-1} and 10, 000 μs^{-1}.

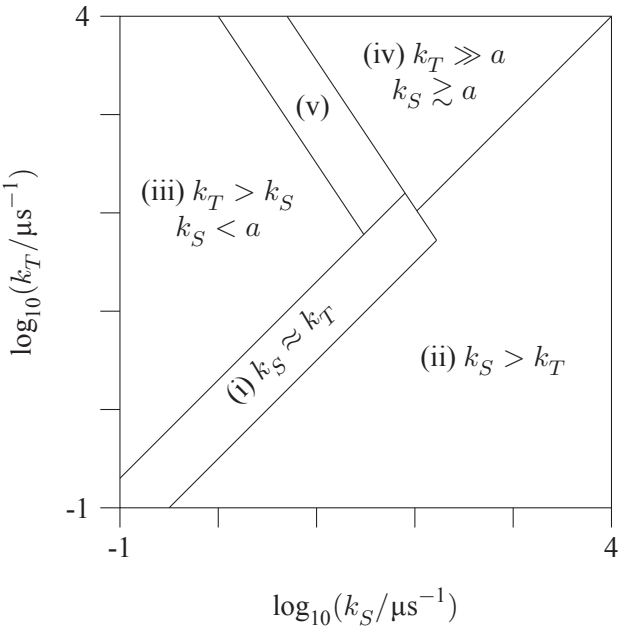

Figure 2.8: The SY plots in figure 2.7 is simplified into five sections as indicated. The description of the five sections is in the main text.

The largest difference (fig. 2.9) between the Haberkorn, the Jones-Hore, and the new Kominis models occurs in the quantum Zeno region where the different amount of singlet-triplet decoherence has the largest influence on the SY. The difference outside of the Zeno region is very small; for a large range of k_S and k_T values, $\Delta\Phi_S^{\text{rms}}$ is smaller than 0.04 which may not be experimentally measurable. The difference between the old Kominis and the other three models is significantly bigger in the Zeno region because the old Kominis model incorrectly predicts a larger proportion of RPs will react via the singlet channel.

In a typical experiment on RPs, the signal detected depends on the experimental conditions and the sensitivity of the detectors, and usually a multiple of the absolute value of the SY is detected. It is therefore difficult to examine the validity of the four models using the SY alone.

Difference in the low field effect

A widely used RP experiment is magnetic field modulation of reaction yields (MARY) spectra, in which the RP product yield is recorded at different B_0 fields. The experiment is usually carried out under a sinusoidally modulated B_0 field and the output signal equates to the first derivative of the SY function, $\Phi_S(B_0)$.

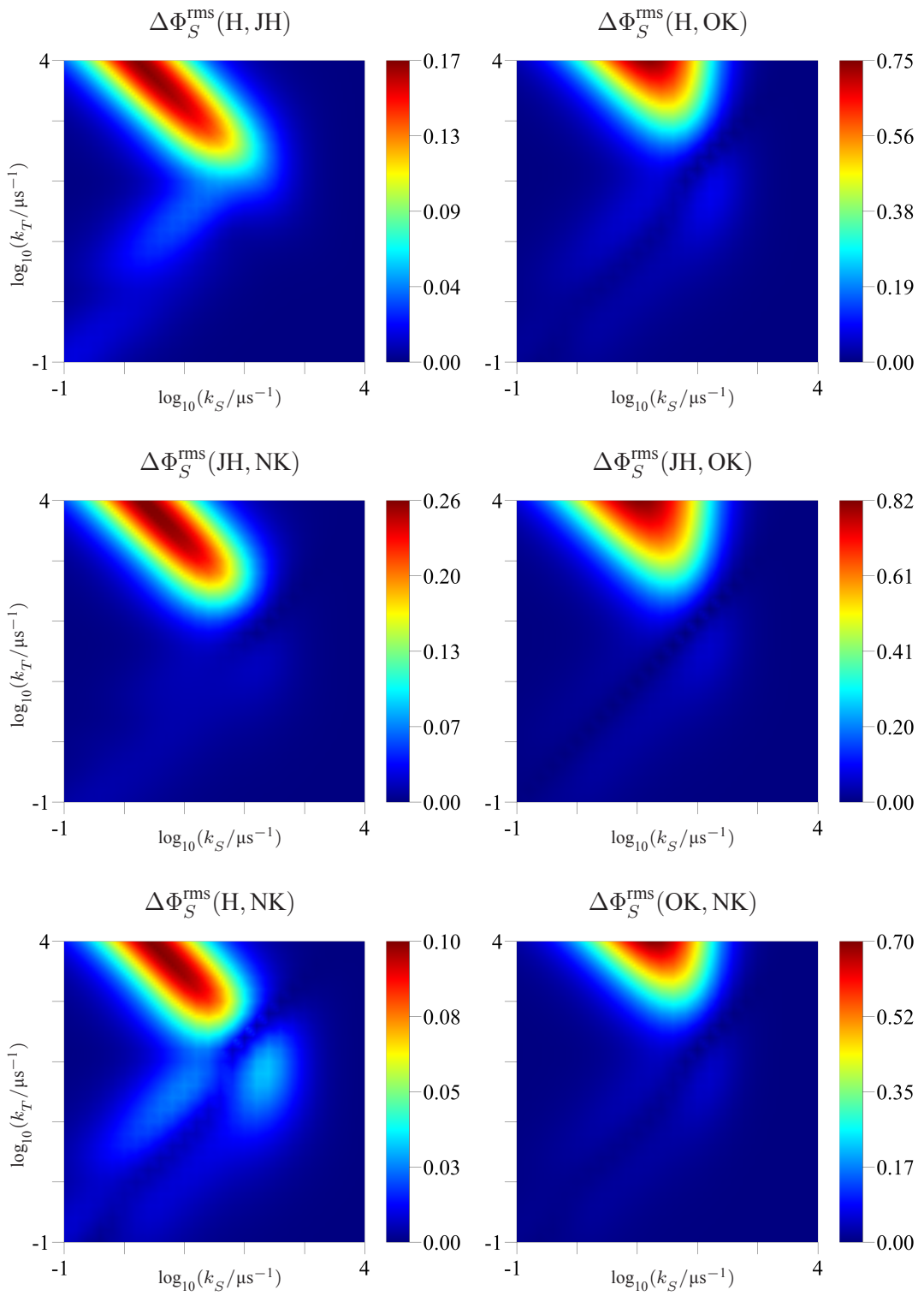

Figure 2.9: Root mean squared difference in the calculated SYs between the four RPR models, the Haberkorn (H), the Jones-Hore (JH), the old Kominis (OK), and the new Kominis (NK) models. The colour of the plot represents the magnitude of $\Delta\Phi_S^{\mathrm{rms}}(X,Y)$ and the colour axis for each plot is different. The difference is averaged over 9 B_0 strengths, $\{0.01, 0.02, 0.05, 0.1, 0.2, 0.5, 1, 2, 5\}$ mT.

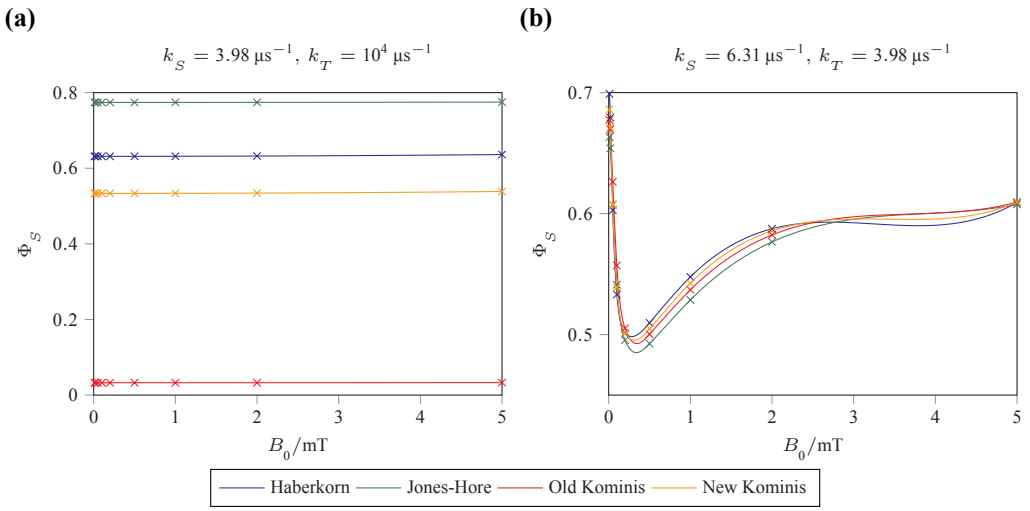

Figure 2.10: The MARY curve of a RP with one spin-1/2 nucleus ($a = 1\,\text{mT}$) for two sets of singlet and triplet rate constants. In (a) and (b), the crosses are the calculated SYs at specific field strengths and the lines are the cubic spline interpolation to those points. The low field effects, $\Delta\Phi_S^{\text{LFE}}$, in (b) for the four models are, Haberkorn: 0.23, Jones-Hore: 0.18, old Kominis: 0.17 and new Kominis: 0.20.

The largest SY difference is found at $k_S = 3.98\,\mu s^{-1}$ and $k_T = 10^4\,\mu s^{-1}$. At these rate constants, the predicted SYs are different in magnitude for each model but the shape of the SY functions against B_0 are the same for each of the four models(fig. 2.10a). Therefore it is difficult to assign a model to the experimental MARY data if the first derivative of $\Phi_S(B_0)$ is similar for the four models.

When the rate constants are similar in magnitude to the HFI, the low field effect (LFE) appears [66]. The LFE, $\Delta\Phi_S^{\text{LFE}}$, is the decrease in the SY when a weak field is applied compared to the zero field SY;

$$\Delta\Phi_S^{\text{LFE}} = \Phi_S(B_0 = 0) - \min\left[\Phi_S(B_0)\right]. \tag{2.54}$$

$\Delta\Phi_S^{\text{LFE}}$ is one of the empirical quantities that can be obtained from a MARY spectrum. The size of the LFE is dependent on the singlet-triplet coherence, therefore the four RPR models predict different LFEs (fig. 2.10b) and $\Delta\Phi_S^{\text{LFE}}$ can be used to distinguish the four models.

From the SYs previously calculated (fig. 2.9) at the nine B_0 field strengths (eq. 2.53), the $\Delta\Phi_S^{\text{LFE}}$ for each RPR model is calculated from a cubic spline interpolation to the nine points.

The square-rooted, averaged sum of the difference of the LFE is defined as

$$\overline{\Delta\Delta\Phi_S^{\mathrm{LFE}}} = \sqrt{\frac{1}{12}\sum_{X,Y}\left[\Delta\Phi_S^{\mathrm{LFE}}(X) - \Delta\Phi_S^{\mathrm{LFE}}(Y)\right]^2} \tag{2.55}$$

$$\text{where } X, Y = \mathrm{H}, \mathrm{JH}, \mathrm{OK}, \mathrm{NK}.$$

The factor $1/12$ is used to average the 12 possible combinations of choosing a pair of RPR models out of 4.

When the singlet and triplet rate constants are significantly larger than the hyperfine coupling constant ($k_S, k_T > 100\,\mu\mathrm{s}^{-1}$ in fig. 2.11), the singlet-triplet coherence decays quickly and no LFE is observed. In this case, there is no difference in the LFE predictions of the four models. Differences in the LFE are found when k_T is slightly larger than k_S and both rate constants are smaller than the hyperfine coupling constant ($1\,\mu\mathrm{s}^{-1} < k_S < 3\,\mu\mathrm{s}^{-1}$ and $3\,\mu\mathrm{s}^{-1} < k_T < 10\,\mu\mathrm{s}^{-1}$ in fig. 2.11).

2.6 Kominis models and mixed states

It was shown in section §2.5.2 that the old Kominis model fails to account the unreactive $T_{\pm}$ states in a high field (fig. 2.5c and 2.6) and this failure is caused by the mixed initial state. First, it is necessary to define a pure quantum state and a mixed quantum state.

A pure quantum state is a state that can be described by a ket vector $\left|\Psi_i\right\rangle$, i.e. $\hat{\rho} = \left|\Psi_i\right\rangle\left\langle\Psi_i\right|$, and a mixed quantum state is a state that cannot be described by a single ket vector in any basis set, i.e. $\hat{\rho} = \sum_i c_i \left|\Psi_i\right\rangle\left\langle\Psi_i\right|$. A mixed quantum state can be written as an ensemble of pure states;

$$\hat{\rho} = \sum_i p_i \hat{\rho}_i \tag{2.56}$$

where p_i is the fraction of the mixed state, $\hat{\rho}$, that contains the pure state, $\hat{\rho}_i$. The triplet RP is a mixed state; the triplet contains three equal proportion of pure states, T_{+1}, T_0, and T_{-1}. A pure state satisfies the following relation:

$$\mathrm{Tr}\left[\hat{\rho}^2\right] = 1. \tag{2.57}$$

If the initial state of a two-level quantum system is a simple mixed state, i.e.

$$\hat{\rho}(0) = c_1\hat{\rho}_1 + c_2\hat{\rho}_2,$$

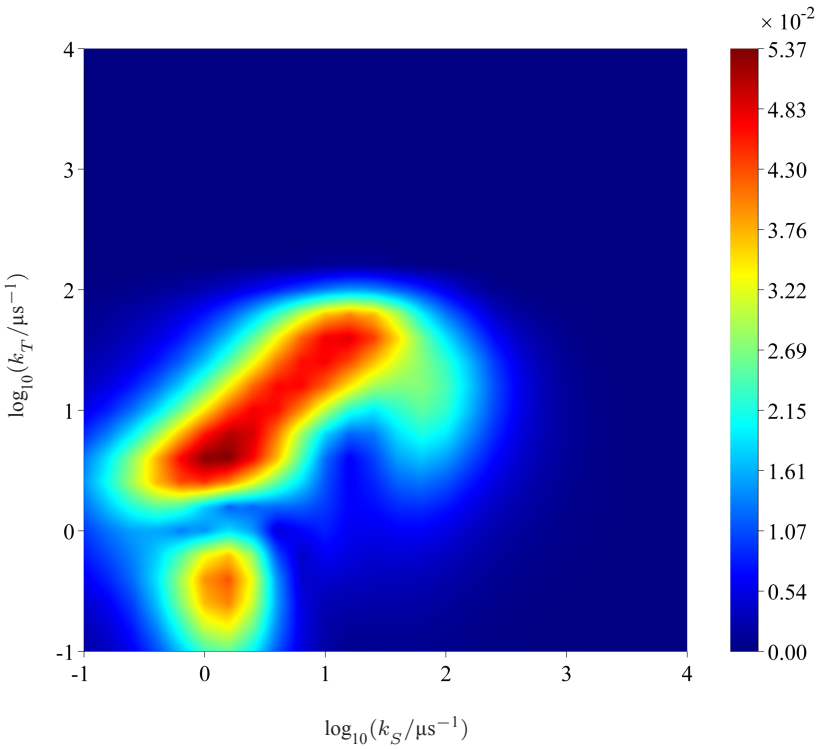

Figure 2.11: $\overline{\Delta\Delta\Phi_S^{\mathrm{LFE}}}$ of a singlet-born RP with one spin-1/2 nucleus ($a = 1\,\mathrm{mT}$) calculated using the four RPR models. A MARY curve is calculated at each combination of singlet rate constant, k_S, and triplet rate constant, k_T from the SY simulations at the 9 B_0 strengths (previously calculated for fig. 2.9). $\Delta\Phi_S^{\mathrm{LFE}}$ is the LFE of each of the MARY curves and $\overline{\Delta\Delta\Phi_S^{\mathrm{LFE}}}$ is the average difference of the LFE of the four RPR models. The colour of the plot represents the magnitude of the average LFE. The maximum is 0.054 and is found at $k_S = 1.58\,\mu\mathrm{s}^{-1}$, $k_T = 3.98\,\mu\mathrm{s}^{-1}$.

the time dependence of the density matrix is (eq. 1.45)

$$\begin{aligned}\hat{\rho}(t) &= e^{-\mathrm{i}\hat{H}t}\left(c_1\hat{\rho}_1 + c_2\hat{\rho}_2\right)e^{\mathrm{i}\hat{H}t} \\ &= c_1 e^{-\mathrm{i}\hat{H}t}\,\hat{\rho}_1\,e^{\mathrm{i}\hat{H}t} + c_2 e^{-\mathrm{i}\hat{H}t}\,\hat{\rho}_2\,e^{\mathrm{i}\hat{H}t}\end{aligned} \tag{2.58}$$

and the expectation value is (eq. 1.49)

$$\begin{aligned}\left\langle \hat{P}_S \right\rangle &= \mathrm{Tr}\left[\hat{P}_S(c_1\hat{\rho}_1 + c_2\hat{\rho}_2)\right] \\ &= c_1\mathrm{Tr}\left[\hat{P}_S\hat{\rho}_1\right] + c_2\mathrm{Tr}\left[\hat{P}_S\hat{\rho}_2\right] = c_1\left\langle \hat{P}_S \right\rangle_1 + c_2\left\langle \hat{P}_S \right\rangle_2.\end{aligned} \tag{2.59}$$

Therefore the quantum evolution of a mixed state is the weighted sum of the independent evolution of its constituent pure states. The SY or time evolution of an initially mixed state, calculated using any RPR model, should also be the weighted sum of the SY or time evolution of its constituent pure states.

Old Kominis model

If the initial state is a mixed state, the quantum jump equations in the old Kominis model are substituted by equation 2.59 and become

$$p_S = k_S c_1 \left\langle \hat{P}_S \right\rangle_1 \mathrm{d}t + k_S c_2 \left\langle \hat{P}_S \right\rangle_2 \mathrm{d}t \tag{2.60}$$

$$p_T = k_T c_1 \left\langle \hat{P}_T \right\rangle_1 \mathrm{d}t + k_T c_2 \left\langle \hat{P}_T \right\rangle_2 \mathrm{d}t. \tag{2.61}$$

The time dependence of the RP population is

$$\begin{aligned} n(t+\mathrm{d}t) &= n(t)[1 - p_S - p_T] \\ \frac{1}{n(t)}\frac{\mathrm{d}n}{\mathrm{d}t} &= -k_S c_1 \left\langle \hat{P}_S \right\rangle_1 - k_T c_1 \left\langle \hat{P}_T \right\rangle_1 - k_S c_2 \left\langle \hat{P}_S \right\rangle_2 - k_T c_2 \left\langle \hat{P}_T \right\rangle_2 \\ \ln n(t) &= -\int_0^t (k_S - k_T)(c_1 \left\langle \hat{P}_S \right\rangle_1 + c_2 \left\langle \hat{P}_S \right\rangle_2)\mathrm{d}\tau - k_T t \\ n(t) &= \exp\left[-(k_S - k_T)\int_0^t c_1 \left\langle \hat{P}_S \right\rangle_1 \mathrm{d}\tau\right] \\ &\quad \cdot \exp\left[-(k_S - k_T)\int_0^t c_2 \left\langle \hat{P}_S \right\rangle_2 \mathrm{d}\tau\right] \cdot \exp[-k_T t]. \end{aligned} \tag{2.62}$$

Equation 2.62 can be analysed using an exemplary mixed state,

$$\hat{\rho} = c_1 \left|S\right\rangle \left\langle S\right| + c_2 \left|T_{+1}\right\rangle \left\langle T_{+1}\right|.$$

If this mixed state is subjected to a high B_0 field spin Hamiltonian and $k_T = 0$, there is no singlet-triplet interconversion and the mixed state will only decay via the singlet reaction channel. Therefore $\left\langle \hat{P}_T(t) \right\rangle_2 = c_2$ and $\left\langle \hat{P}_S(t) \right\rangle_2 = 0$ at all times and the population is expected to decay to c_2. However, although the second term in equation 2.62 remains equal to one, the first term decays to zero. Therefore the total population according to equation 2.62, which is the product of the first and second terms, decays to zero irrespective of the unreactive T_{+1} state. So the old Kominis model fails to calculate the decay of the RP population correctly when the initial state is a mixed state (see fig. 2.5c and 2.6).

New Kominis model

In the new Kominis model, a function that accounts for the singlet-triplet coherence of the RP population, p_{coh} (eq. 2.16) is used. When the density matrix is in a mixed state, p_{coh} is not separable into the constituent parts of the mixed state. The equation of motion of the density matrix

in the new Kominis model also cannot be separated into the parts of a mixed state. Therefore the new Kominis model produces incorrect results, in a similar way to the old Kominis model, when the initial state is a mixed state (fig. 2.6).

2.7 Conclusion

In this chapter, the theoretical approaches and the predicted SYs of the four RPR models are compared. The only difference between the Haberkorn and the Jones-Hore model is the rate of the singlet-triplet decoherence: the singlet-triplet coherence in the Jones-Hore model decays at twice the rate in the Haberkorn model. The two Kominis models are different from the Haberkorn and the Jones-Hore models. The old Kominis model has a different description of the RP recombination - quantum jump equations are used - unlike the other models. On the other hand, the new Kominis model does not have the quantum jump equations, instead the singlet-triplet decoherence is dependent on a new function, p_{coh}, and the rates of decoherence are different for the reactive and the unreactive RPs.

There is no significant difference in the predicted SY of the four models except if the singlet and triplet rate constants are in the quantum Zeno regime. The LFE, obtained from a MARY spectrum, can also be used to compare the four models. However the difference in $\Delta\Phi_S^{\text{LFE}}$ is small and the largest difference is ~ 0.05 a.u., when the singlet and triplet rate constants are smaller than the hyperfine coupling constant.

The difference in the predicted SYs and the LFEs are mainly due to the different singlet-triplet decoherence terms used in the four RPR models. In a real RP system, the rate of spin relaxation is not known precisely as it is caused by stochastic magnetic field interactions. So spin relaxation is likely to influence the rate of decoherence and mask any difference in SYs or LFEs of the four models in a real RP system.

Since the differences between the models are small in a MARY-type experiment, it may be better to measure some other experimental quantities, for example, the T_2 relaxation time in an electron spin resonance experiment. This would provide some information about the rate of the

singlet-triplet decoherence but a simple RP system with no significant HFIs and low temperatures would be desirable as this would reduce the spin relaxation caused by random fields.

The two Kominis models produce incorrect results if a mixed initial state is used. Any pure state will evolve into a mixed-state over time, therefore the Kominis models are likely to produce incorrect results irrespective of the initial state used. There is only one published article [83] that directly argues against the old Kominis model and the general view in the Spin Chemistry community is that Kominis's arguments in his papers are fundamentally flawed [88–90]. In his 2009 paper, he stated that the quantum Zeno effect in RPR is 'masked by the phenomenological description' of the Haberkorn model. Contrary to this statement, the Haberkorn model is shown in this chapter to exhibit the quantum Zeno effect (fig. 2.4a) and the old Kominis model does not produce any quantum Zeno effect (fig. 2.4c). Due to these deficiencies, the two Kominis models should not be used to calculate product yields of a RPR.

Recently, experiments have been proposed [91,92] that are designed to distinguish the Haberkorn and the Jones-Hore models. However the experiments involve complex RP systems and complicated measurements, and they are beyond the scope of this chapter. So there is currently no experimental evidence that suggests new RPR models are needed or that the Haberkorn model is incorrect in any way.

The Haberkorn model is the established theoretical model that has been used to calculate SYs of RPRs in the past 40 years. The widely used exponential model is basically the Haberkorn model with equal singlet and triplet rate constants. There may be rare cases where the use of the faster rate of decoherence in the Jone-Hore model is justified, for instance a RP system that has the appropriate rate limits of the two-site model (fig. 2.2). However, in the majority of cases, the Haberkorn model would be suitable for the simulations and any difference from the Jones-Hore model would not be detectable.

Chapter 3

Photoselection and the radical pair mechanism in magnetoreception

Cryptochromes (CRY) are a newly discovered class of photoreceptors (§1.3.1) and hitherto the only molecules suggested as the magnetoreceptor in migratory birds [32,53,93]. The radical pair (RP) is formed initially by blue-light photoexcitation [50,94] of the fully oxidised flavin adenine dinucleotide (FAD), which is one of CRY's cofactors, to FAD^*. Three successive electron transfers occur along a chain of three tryptophans (Trp) from the protein surface to FAD^*; Protonation of $FAD^{\bullet -}$ may occur, and a RP comprised of $FADH^\bullet$ and $TrpH^\bullet$ is formed [50, 52, 95].

In vivo radio frequency (RF) radiation experiments performed on European robins strongly indicate that the underlying magnetoreception mechanism involves a radical pair reaction (RPR). These experiments also indicate that the lifetime of the radicals is of the order of μs and the counter radical to $FADH^\bullet$ has no HFIs [53]. However, the identity of this nuclear-spin-free radical, which will be called $Z^\bullet$, is not clear and there are some plausible suggestions, namely superoxide [54, 55]. Although the identity of the RP is unknown, the evidence from *in vivo* experiments points to CRY as the RP-forming magnetoreceptor.

Other experiments also indicate that the magnetoreception of robins is wavelength dependent and vision is involved in some way during the process. Robins are disoriented under red or yellow ambient light and they can only find their migratory direction under blue, green or white light

[96]. This result is consistent with the hypothesis that a RPR is involved in magnetoreception and CRY, a blue light sensitive protein, is the magnetoreceptor.

The current model for avian magnetoreception is described by Ritz *et al.* [32]. The authors suggest that magnetoreceptor cells are located in the retina in the eye of a bird and each cell contains identical receptor molecules. The sensory transduction pathway can be influenced by the response of the cell to the external magnetic field which is dependent on the direction and the strength of the external field. Therefore, in this model, the receptor cells should be ordered in some way so that cells at different locations would have correlated responses to the external field and directional information can be obtained.

The receptor cell response is the sum of the responses of all the receptor molecules within the cell and the response of an individual molecule depends on its orientation with respect to the external magnetic field. As a consequence, all molecules in the cell should be aligned; otherwise, the responses of randomly oriented molecules would average to zero. Under these conditions, a RPR would only function as an avian compass if both cells and molecules are immobile [32,97].

Photoreceptor cells in the avian retina are highly ordered [98,99]. Rods and cones, which are the main photoreceptor cells in the retina, are cylindrical and they are aligned along their long axes, perpendicular to the retina tangent. Other retinal cells, such as retinal ganglion cells, are also ordered to some extent. Therefore most cells in the retina have the necessary alignment to be magnetoreceptor cells potentially.

Rhodopsin and photopsins are the receptor proteins for visible light and they are found in the stacked membrane discs in the outer segments of the rods and cones. However, CRY is a small water-soluble protein and it is insoluble in membranes, so CRY is likely to be mobile within a cell. There are suggestions that CRY could be immobilised between membrane discs in the outer segments of rods and cones by attachment to the ordered membrane [49,100]. Another possibility is that CRY could be attached to cytoskeletal filaments in retinal ganglion cells [48]. There is so far no evidence to prove that CRY is immobile or aligned inside a cell. The lack of evidence for molecular alignment leads to objections to the plausibility of the cryptochrome-based RPR operating in avian magnetoreception [97].

One implied assumption of Ritz *et al.*'s model is that the formation of RPs is caused by

light. The absorption of light, the photoexcitation of the magnetoreceptor molecules, and the subsequent formation of RPs are assumed to be isotropic; the direction and the polarisation of the incoming light are not considered in the model. All magnetoreceptor molecules, at different positions in the retina and with different orientations, are assumed to absorb photons with the same probability. However, elementary photochemistry states that the absorption of a photon by any molecule depends on the relative orientation of the transition dipole moment of the molecule and the electric vector of the photon [101]. Therefore the formation of a RP, that precedes the RPR, is anisotropic, contrary to the assumption of Ritz *et al.*'s model.

It is possible that cells containing a collection of static, disordered magnetoreceptor molecules can give correlated responses that depends on the location of the cell and the direction of the external magnetic field. This is because the incoming light can only be absorbed by a subset of the disordered molecules which is determined by the direction of the electric vector of the photon. This anisotropic photoexcitation is know as photoselection [101]. In the next section, the model of photoselection in a RPR is described, then the theoretical retinal responses to magnetic fields including photoselection effects are presented.

3.1 Eye model

The avian eye is a globose ellipsoid and it has a marked asymmetry in the nasal-temporal plane [98]. This asymmetry contributes to the bird's static accommodation (the adjustment of the shape of the lens of the eye); some part of the visual field is emmetropic (long sighted) and the other part is myopic (short sighted). This allows the bird to keep both distant objects on the horizon and objects on the ground in focus simultaneously. The retina is asymmetrical with respect to the optical axis, so that the temporal visual field is always bigger than the nasal visual field.

The eye is assumed to be a sphere to simplify the mathematics and the retina covers the inner surface of a hemispherical section (fig. 3.1), similar to Ritz *et al.*'s model [32], which is a simplification of the asymmetric layout of the avian retina. This gives an optical visual field of 90°, however in reality the optical visual field is much greater than 90° in birds ($\sim 128^\circ$ in pigeon [98]). The eye is approximated to function as a pinhole camera and the pupil is the

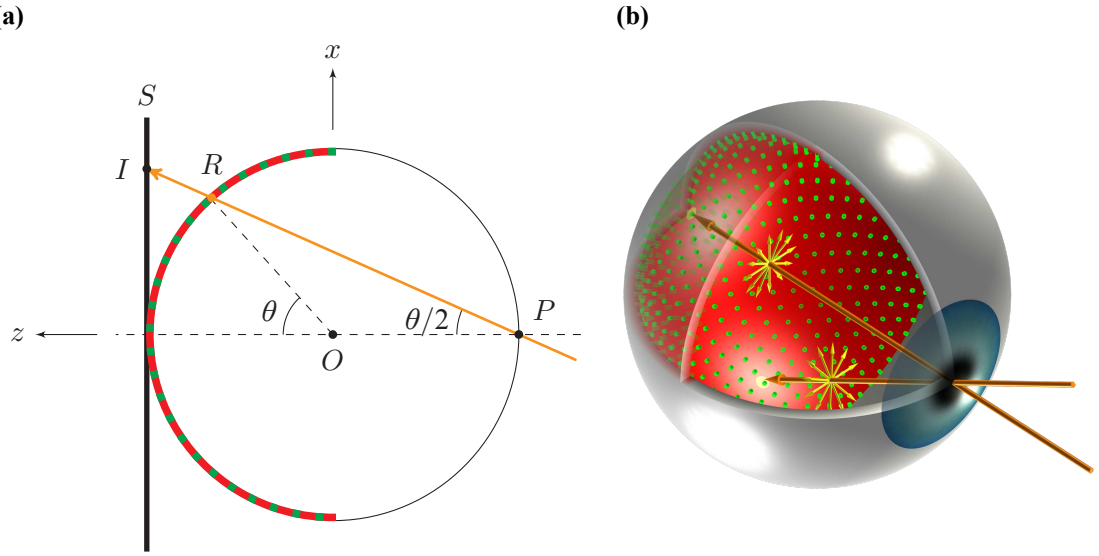

Figure 3.1: The model of the eye. (a) shows a vertical cross section through the centre, O, of the eye in the xz-plane and (b) shows a three-dimensional representation of the eye with a cut-out front-left quarter. O is also the origin of the retina axis system and the polar coordinates (θ, ϕ) locate each cell in the retina. The retina (red) is on the left hemisphere and the magnetoreceptor cells (green) are distributed uniformly in the retina ($0 \leq \theta \leq \pi/2$, $0 \leq \phi \leq 2\pi$). A light ray (orange) enters the eye through the pupil, P, at an angle $\theta/2$ with respect to the z-axis and strikes the retina at point R. A two-dimensional image of the retinal response is formed by projecting the retina onto a screen at S and the response at R is projected at I on the screen along the direction PR. The yellow arrows represent the different orientations of the polarisation of the incoming light.

pinhole on the optical axis, opposite to the retina. The magnetoreceptor cells are assumed to have cylindrical symmetry and align with their long axis normal to the retina. The magnetoreceptor molecules are contained in the magnetoreceptor cells and the cells are assumed to be distributed uniformly in the retina.

3.2 Singlet yield as spherical harmonics

3.2.1 Spherical harmonics

Spherical harmonics are functions that describe the angular part of the solutions to Laplace's equation, $\nabla^2\Phi = 0$. A spherical harmonic, $Y_l^m(\theta, \phi)$, is a single-valued, continuous, bounded, and complex function of spherical coordinates, (θ, ϕ), with $(0 \leq \theta \leq \pi)$ and $(0 \leq \phi \leq 2\pi)$. It is characterised by degree, l, which takes non-negative integer values $(0, 1, 2, \cdots)$ and order, m,

which takes integer values $(-l, -l+1, \cdots, 0, \cdots, l-1, l)$. The normalised spherical harmonic is defined as [102]

$$Y_l^m(\theta, \phi) = \sqrt{\frac{(2l+1)}{4\pi} \frac{(l-m)!}{(l+m)!}} \, P_l^m(\cos\theta) \, e^{im\phi} \tag{3.1}$$

where $P_l^m(x)$ are the associated Legendre polynomials [103]. The associated Legendre polynomial for a spherical harmonic with a negative order $-m$ is related to that with positive $+m$;

$$P_l^{-m}(x) = (-1)^m \frac{(l-m)!}{(l+m)!} \, P_l^m. \tag{3.2}$$

The factor $(-1)^m$ is a phase factor, known as the Condon-Shortley phase [103]. This factor alternates the phase of the spherical harmonic of successive order m and gives the following identity:

$$\left[Y_l^m\right]^* = (-1)^m \, Y_l^{-m}. \tag{3.3}$$

Equation 3.1 is normalised, so that

$$\int_0^{2\pi} \int_0^{\pi} \left[Y_l^m\right]^* \, Y_{l'}^{m'} \, \sin\theta \, \mathrm{d}\theta \, \mathrm{d}\phi = \delta_{ll'} \, \delta_{mm'}. \tag{3.4}$$

Spherical harmonics are important in quantum mechanics as they are the eigenfunctions of the orbital angular momentum operator. They describe the angular distribution of particles moving in a spherical field, for example, electrons moving around the nucleus. The degree, l, describes the orbital angular momentum (c.f. eq. 1.1) and order, m, is the projection of the orbital angular momentum on the quantisation axis (c.f. eq. 1.2).

3.2.2 Spherical harmonics expansion

Spherical harmonics are orthogonal functions and form an orthonormal basis set for any square-integrable function. Therefore any square-integrable function, $f(\theta, \phi)$, can be expressed as a linear combination of spherical harmonics,

$$f(\theta, \phi) = \sum_{l=0}^{\infty} \sum_{m=-l}^{l} f_l^m \, Y_l^m(\theta, \phi). \tag{3.5}$$

f_l^m is the expansion coefficient that corresponds to Y_l^m. The coefficients can be found by using the orthonormal property of the spherical harmonics (eq. 3.4),

$$f_l^m = \int_0^{2\pi} \int_0^{\pi} f(\theta, \phi) \, \left[Y_l^m\right]^* \, \sin\theta \, \mathrm{d}\theta \, \mathrm{d}\phi. \tag{3.6}$$

In reality, the coefficients are calculated more efficiently by discrete spherical harmonic transform, which is the discrete version of the continuous equation 3.6. Driscoll and Healy [104, 105] showed that the discrete spherical harmonic transform is similar to a Fourier transform. This is implemented in a `C` routine library, called `S2kit` [106], and this library is used in the following sections to find the spherical harmonic expansion of the singlet yield (SY).

3.2.3 Rotations

The rotation of a coordinate system is described by the Euler angles, (α, β, γ). The Euler rotation, in the z-y-z convention, is

$$R(\alpha, \beta, \gamma) = R_z(\gamma)\, R_y(\beta)\, R_z(\alpha). \tag{3.7}$$

R_y is a rotation around the y-axis and R_z is a rotation around the z-axis. The matrix representations of the two rotations are as follows:

$$R_y(\theta) = \begin{pmatrix} \cos\theta & 0 & \sin\theta \\ 0 & 1 & 0 \\ -\sin\theta & 0 & \cos\theta \end{pmatrix} \;,\; R_z(\phi) = \begin{pmatrix} \cos\phi & -\sin\phi & 0 \\ \sin\phi & \cos\phi & 0 \\ 0 & 0 & 1 \end{pmatrix}. \tag{3.8}$$

Both the coordinate system and the rotations are right-handed, which means that a positive rotation is clockwise along the positive axis direction. There are a number of ways to interpret Euler angles and Euler rotations [102]. In this thesis, the active transformation and extrinsic rotation, which is a rotation defined with respect to a global axes system, are used. One reason for this interpretation is that the rotation matrices used in this chapter are all defined extrinsically. An Euler rotation (fig. 3.2) transforms the coordinate axes (X, Y, Z) to the new positions (x', y', z') by:

(i) rotating around the Z-axis by α $(0 \leq \alpha \leq 2\pi)$;

(ii) rotating around the Y-axis by β $(0 \leq \beta \leq \pi)$;

(iii) rotating around the Z-axis by γ $(0 \leq \gamma \leq 2\pi)$.

An Euler rotation of the coordinate system transforms a spherical harmonic as [102]

$$R(\alpha, \beta, \gamma)\; Y_l^m(\theta, \phi) = \sum_{n=-l}^{l} \mathscr{D}^l_{n,m}(\gamma, \beta, \alpha)\; Y_l^n(\theta, \phi). \tag{3.9}$$

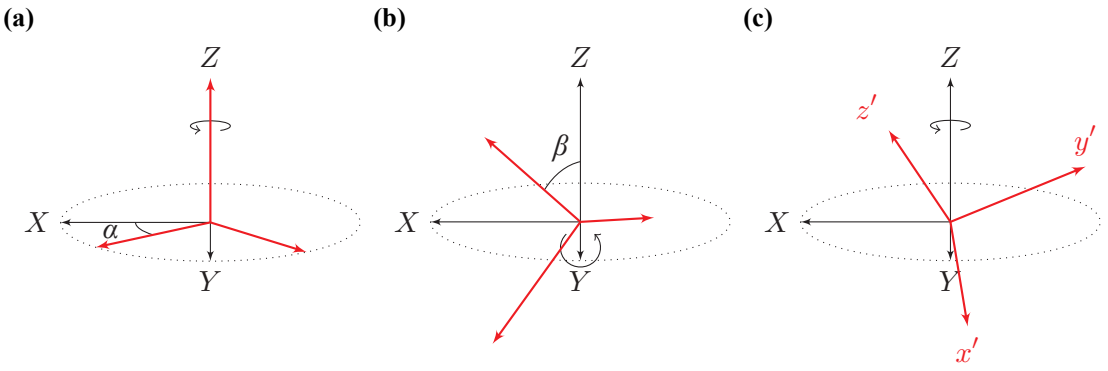

Figure 3.2: The z-y-z, extrinsic Euler rotation consists of three successive rotations around the global axes, (X, Y, Z): (a) a rotation around Z by α; (b) a rotation around Y by β; (c) a rotation around Z by γ. All rotations are right-handed. The axes in black are the global axes and the axes in red are the axes after each rotation.

Therefore the rotation of a spherical harmonic is the weighted sum of different orders of spherical harmonics with the same degree. $\mathscr{D}^l_{n,m}$ is the Wigner-D function and is defined as follows [102]:

$$\mathscr{D}^l_{n,m}(\gamma,\beta,\alpha) = e^{-in\gamma}\ \mathbf{d}^l_{n,m}(\beta)\ e^{-im\alpha}, \tag{3.10}$$

$$\begin{aligned}\mathbf{d}^l_{n,m}(\beta) =& \sqrt{(l+n)!(l-n)!(l+m)!(l-m)!} \\ &\times \sum_p (-1)^p \frac{(\cos\beta/2)^{2l-2p+n-m}\ (\sin\beta/2)^{2p-n+m}}{p!(l+n-p)!(l-m-p)!(m-n+p)!}.\end{aligned} \tag{3.11}$$

p runs over all integer values for all factorial arguments which are non-negative, therefore

$$\max(0, n-m) \leqslant p \leqslant \min(l+n, l-m).$$

3.2.4 Axis system

Different physical properties needed in the photoselection calculations are defined in different axis systems. The external magnetic field and the direction of the linear polarisation are defined in the retina frame. On the other hand, the HFIs and the transition dipole moment of the magneto-receptor molecule are defined in the molecular frame. All these different properties need to be defined in one common axis system and the molecular frame is chosen for this purpose.

The orientation of the molecule is defined with respect to the cell and the orientation of the cell is defined with respect to the retina. The axis systems of the retina, the cell, and the molecule are named as S_r, S_c, and S_m respectively (fig. 3.3). S_r is the global frame and the Euler angles

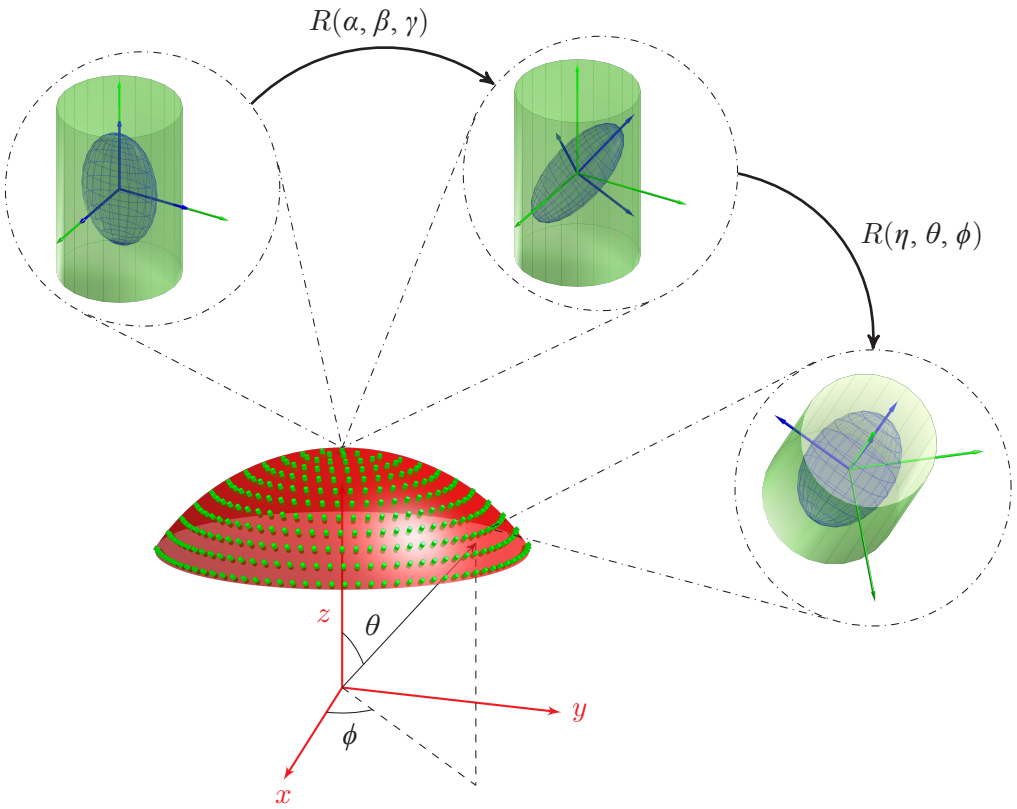

Figure 3.3: There are three axes system: retina (red), cell (green) and molecule (dark blue). An individual cell can be located by the spherical angles, (θ, ϕ). The Euler angles between the retina frame and the cell frame are (η, θ, ϕ). The Euler angles between the cell frame and the molecule frame are (α, β, γ).

of S_c with respect to S_r are (η, θ, ϕ). The angles (θ, ϕ) define the location of the cell in the retina and the angle η defines rotational orientation of the cell around the long axis, normal to the retina. (α, β, γ) define the Euler angles between S_c and S_m. The compositions of extrinsic rotations of the three axes systems are as follows:

$$S_c = R(\eta, \theta, \phi)\, S_r, \tag{3.12}$$

$$S_m = R(\eta, \theta, \phi)\, R(\alpha, \beta, \gamma)\, S_r. \tag{3.13}$$

3.2.5 Singlet yield in the retina frame

In the retina frame, the external magnetic field vector, $\vec{B}$, is defined by the spherical coordinates (ζ, δ),

$$\vec{B} = \begin{pmatrix} \sin\zeta\, \cos\delta \\ \sin\zeta\, \sin\delta \\ \cos\zeta \end{pmatrix} B \tag{3.14}$$

where B is the magnetic flux density. When the molecular frame coincides with the retina frame, the SY of a RPR can be described using (B, ζ, δ). The SY can be expanded in terms of spherical harmonics using equation 3.5,

$$\Phi_S(\vec{B}) = \Phi_S(B, \zeta, \delta) = \sum_{l=0,2,4,\cdots} \sum_{m=-l}^{l} a_l^m(B)\, Y_l^m(\zeta, \delta). \tag{3.15}$$

The coefficients, $a_l^m(B)$, can be found using equation 3.6. The SY is a real function, and using equation 3.3, the following identity is true:

$$\begin{aligned}
\Phi_S &= \Phi_S^* \\
\sum_l \sum_m a_l^m\ Y_l^m &= \sum_l \sum_m \left[a_l^m\right]^*\ \left[Y_l^m\right]^* \\
&= \sum_l \sum_m \left[a_l^m\right]^*\ (-1)^m\ Y_l^{-m} \\
&= \sum_l \sum_m \left[a_l^{-m}\right]^*\ (-1)^{-m}\ Y_l^m \\
\Rightarrow a_l^m &= (-1)^m\ \left[a_l^{-m}\right]^*.
\end{aligned} \tag{3.16}$$

Inversion symmetry

The spin Hamiltonian that is used later includes only the Zeeman interaction and the HFI. The Zeeman operator depends on the direction of the external magnetic field and the inversion of the field is equivalent to inversion of the axis system.

$$\hat{H}_{\text{Zee}}(-\vec{B}) = \hat{P}_r\, \hat{H}_{\text{Zee}}(\vec{B}) \tag{3.17}$$

where $\hat{P}_r$ is the inversion operator. Because the hyperfine tensor is symmetric, the HFI operator, H_{HFI}, is invariant under inversion:

$$\hat{P}_r\, H_{\text{HFI}} = H_{\text{HFI}}. \tag{3.18}$$

When the external field is inverted, the spin Hamiltonian changes to

$$\begin{aligned}
\hat{H}(-\vec{B}) &= H_{\text{Zee}}(-\vec{B}) + H_{\text{HFI}} \\
&= \hat{P}_r\, \hat{H}_{\text{Zee}}(\vec{B}) + \hat{P}_r\, H_{\text{HFI}} \\
&= \hat{P}_r\, \hat{H}(\vec{B}).
\end{aligned} \tag{3.19}$$

SYs are scalar values and they are invariant under any rotation of the axis system, therefore

$$\begin{aligned}\Phi_S(\vec{B}) &= \hat{P}_r\,\Phi_S(\vec{B}) \\ &= \Phi_S(-\vec{B}).\end{aligned} \tag{3.20}$$

The spherical harmonic transforms under inversion as [102]

$$\hat{P}_r\,Y_l^m = (-1)^l\,Y_l^m. \tag{3.21}$$

Only even values of l are needed for the SY spherical harmonic expansion in equation 3.15, since SY is invariant under the inversion of the external magnetic field.

Singlet yield rotation

The external field is defined in the retina frame with angles (ζ, δ) but the HFIs of the molecules are defined in the molecule frame. Using equation 3.9, the Euler rotations can be applied to the SY spherical harmonic expansion (eq. 3.15) to transform from the retina frame to the molecular frame;

$$\begin{aligned}\Phi_S &= \sum_{l=\text{even}}\sum_{m=-1}^{l} a_l^m(B)\,R(\eta,\theta,\phi)\,R(\alpha,\beta,\gamma)\,Y_l^m(\zeta,\delta) \\ \Phi_S &= \sum_{l=\text{even}}\sum_{m=-1}^{l} a_l^m(B)\sum_{n=-l}^{l}\mathscr{D}^l_{n,m}(\gamma,\beta,\alpha)\sum_{p=-l}^{l}\mathscr{D}^l_{p,n}(\phi,\theta,\eta)\,Y_l^p(\zeta,\delta).\end{aligned} \tag{3.22}$$

In equation 3.22, the $R(\alpha,\beta,\gamma)$ Euler rotation is applied first and $R(\eta,\theta,\phi)$ second (c.f. eq. 3.13). Now equation 3.22 can be used to calculate the SY of a magnetoreceptor molecule with orientation (α,β,γ), in a cell at (θ,ϕ) in the retina with cylindrical orientation (η), and the direction of the external magnetic field defined by (ζ,δ).

3.3 Probability of photoexcitation – photoselection

The orientation of the incoming light, $\vec{v}_r$, that strikes at retina position (θ,ϕ) is given by (fig. 3.1)

$$\vec{v}_r = R_z(\phi)\,R_y\left(\frac{\theta}{2}\right)\begin{pmatrix}0\\0\\1\end{pmatrix} = \begin{pmatrix}\sin(\frac{\theta}{2})\cos(\phi)\\ \sin(\frac{\theta}{2})\sin(\phi)\\ \cos(\frac{\theta}{2})\end{pmatrix}. \tag{3.23}$$

$\vec{v}_r$ is currently defined in the retina frame. The polarisation angle, ε, of the linearly polarised light is defined on the plane perpendicular to the direction of propagation. The $\varepsilon = 0$ polarisation vector, $\vec{e}_r^{\,0}$, is defined as the vector that is perpendicular to both the retina y-axis and $\vec{v}_r$,

$$\vec{e}_r^{\,0} = \begin{pmatrix} 0 \\ 1 \\ 0 \end{pmatrix} \times \vec{v}_r. \tag{3.24}$$

$\vec{e}_r^{\,0}$ is rotated around $\vec{v}_r$ to give the correct linear polarisation direction,

$$\vec{e}_r(\varepsilon) = R_{\text{vec}}(\vec{v}_r, \varepsilon)\, \vec{e}_r^{\,0} \tag{3.25}$$

where $R_{\text{vec}}(\vec{u}, \varphi)$ is the matrix for the right-handed rotation around the unit vector $\vec{u} = (u_x\, u_y\, u_z)$ by an angle of φ and it is defined as

$$R_{\text{vec}}(\vec{u},\varphi) = \begin{bmatrix} \cos\varphi + u_x^2(1-\cos\varphi) & u_x u_y(1-\cos\varphi) - u_z \sin\varphi & u_x u_z(1-\cos\varphi) + u_y \sin\varphi \\ u_y u_x(1-\cos\varphi) + u_z \sin\varphi & \cos\varphi + u_y^2(1-\cos\varphi) & u_y u_z(1-\cos\varphi) - u_x \sin\varphi \\ u_z u_x(1-\cos\varphi) - u_y \sin\varphi & u_z u_y(1-\cos\varphi) + u_x \sin\varphi & \cos\varphi + u_z^2(1-\cos\varphi) \end{bmatrix}. \tag{3.26}$$

The electric vector is transformed from the retina frame, $\vec{e}_r$, to the molecule frame, $\vec{e}_m$, by

$$\vec{e}_m = R(-\gamma, -\beta, -\alpha)\, R(-\phi, -\theta, -\eta)\, \vec{e}_r, \tag{3.27}$$

which is the inverse of the frame rotations (eq. 3.13).

The electric transition dipole moment (TDM), $\vec{\mu}_m$, of the magnetoreceptor molecule is defined in the molecule frame. If the angle between the TDM of the molecule and the electric vector of the incoming light is λ, the absorption probability, p, of the photoexcitation is proportional to $\cos^2\lambda$ [101], i.e. it is the square of the dot product of $\vec{\mu}_m$ and $\vec{e}_m$,

$$p(\alpha, \beta, \gamma, \eta, \theta, \phi, \varepsilon) = \left[\vec{\mu}_m \cdot \vec{e}_m\right]^2. \tag{3.28}$$

$\vec{\mu}_m$ is the unit vector along the direction of the TDM of the molecule. It is clear that if the TDM is perpendicular to the electric vector of the incoming light, the absorption probability is zero. Therefore molecules with TDMs that are aligned in the plane perpendicular to the linear polarisation vector do not absorb a photon (fig. 3.4a).

The absorption probability for unpolarised light, $\langle p \rangle_\varepsilon$, is the average of p over all values of ε,

$$\langle p \rangle_\varepsilon = \frac{1}{2\pi} \int_0^{2\pi} \left[\vec{\mu}_m \cdot \vec{e}_m\right]^2 \, \mathrm{d}\varepsilon. \tag{3.29}$$

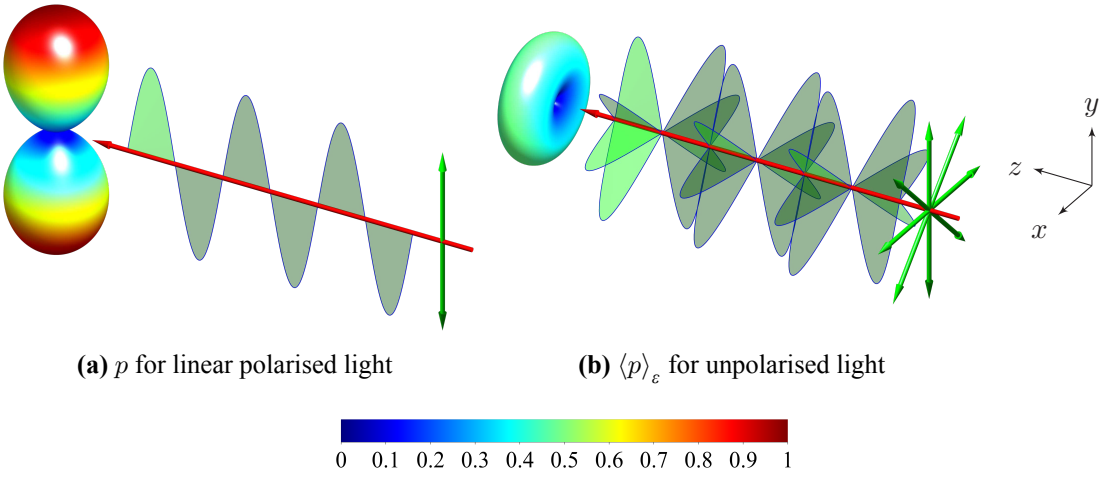

(a) p for linear polarised light **(b)** $\langle p \rangle_\varepsilon$ for unpolarised light

Figure 3.4: Surface plots of the absorption probabilities: (a) p for linear, y-axis polarised light, and (b) $\langle p \rangle_\varepsilon$ for unpolarised light. The vector from the centre to the surface represents the direction of the TDM of the molecule and the colour indicates the magnitude of the probability. The red arrows represent the direction of travel of the incoming light and the green arrows represent the oscillating planes of the electric field. The electric field is confined in the xy-plane. The maximum probability is 1 in polarised light when the TDM is parallel to the direction of the polarisation and 0 when the TDM lies in the xz-plane. The maximum probability is 0.5 in unpolarised light when the TDM lies in the xy-plane and 0 only when the TDM is parallel to the z-axis. Photoexcitation of the RP precursor by polarised and unpolarised light is anisotropic, hence photoselection occurs for the RP formation.

If the incoming light is unpolarised, only molecules with TDMs that are parallel to the direction of light propagation have zero absorption probability. The absorption probabilities for unpolarised light are significantly different to polarised light (fig. 3.4b). Some molecular orientations are unresponsive to polarised light but molecules with these same orientations can absorb unpolarised light. The probability of RP formation is assumed to be proportional to the absorption probability, p or $\langle p \rangle_\varepsilon$.

The FAD cofactor in CRY absorbs light at 450 nm and subsequently forms a RP. It is reported, from experimental and theoretical studies [107, 108], that the TDM for the 450 nm band lies in the plane of the isoalloxazine ring system (fig. 3.5).

Flavin species	Angle of TDM
Isoalloxazine [107]	75°
Flavin mononucleotide [108]	75°

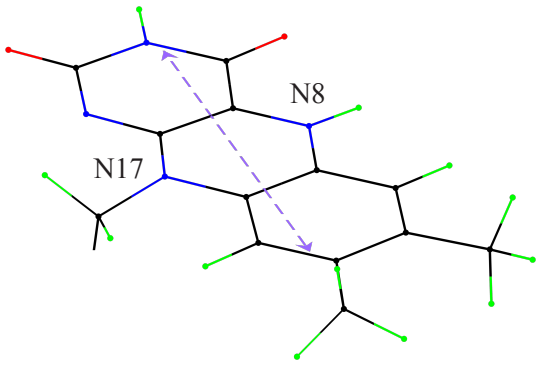

Figure 3.5: The angle of the transition dipole moment (TDM) of flavin species of the 450 nm band. The angle is measured with respect to the short molecular axis, N8 - N17. The purple double arrow represents the direction of the TDM of FAD at 450 nm.

3.4 Skylight polarisation

Radiation from the sun arrives at the Earth and it is scattered by particles in the atmosphere. This elastic scattering depends on the ratio of the size of the particle to the wavelength of the radiation. The wavelength of visible light is greater than the size of the atmospheric particles, therefore Rayleigh scattering applies.

The amount of Rayleigh scattering of a light beam depends on the wavelength λ; the scattered intensity is proportional to $1/\lambda^4$ [109]. Therefore blue light, which is shorter in wavelength, is scattered more than red light and this leads to the blue colour of the sky during the day. There would be no scattering of sunlight or diffuse skylight without an atmosphere, and the sky would be black during the day. The sunlight has to travel through a larger volume of atmosphere at twilight and most of the blue light is scattered, hence the sun and the sky appear red.

The sunlight arriving at the Earth is unpolarised and the absorption by the scattering particles is confined in the plane perpendicular to the direction of propagation (c.f. fig. 3.4b). The polarisation of the scattered photons is also confined in this plane. Photons scattered forward and backward will remain unpolarised but photons scattered 90° to the direction of propagation will be linearly polarised. Consequently, Rayleigh scattering of sunlight produces a polarisation pattern in the sky [110, 111].

The polarisation pattern is described by the Rayleigh sky model. The observed direction of the polarisation depends on the celestial position of the sun and the observation point. When

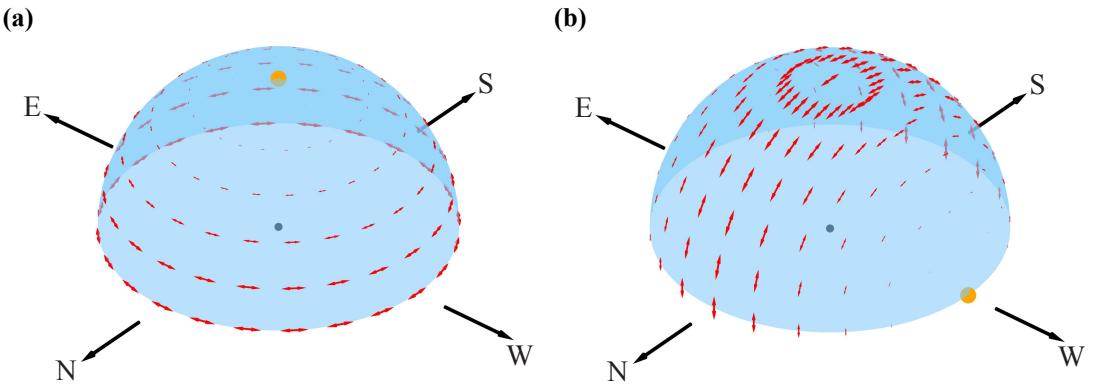

Figure 3.6: The skylight polarisation using the Rayleigh sky model when the sun is : (a) at the zenith at midday, (b) in the west at dusk. The blue dot in the middle represents the position of the observer and the orange dot represents the position of the sun. The blue surface represents the observable celestial hemisphere. The red double arrows represent the direction of the skylight polarisation relative to the horizon and the size of the arrows represents the degree of polarisation. The maximum degree of polarisation is found at an angular distance of 90° from the sun. The same polarisation pattern as (b) is produced when the sun is in the east at dawn.

the sun is at the zenith at midday, the maximum polarisation is on the horizon and the light is horizontally polarised (fig. 3.6a). When the sun is setting in the west at dusk, the maximum polarisation is on the south-zenith-north vertical circle and light is vertically polarised (fig. 3.6b). There are three detectable neutral points in the sky that have zero polarisation and they all lie on the circle going through the sun and the observer [112].

The Rayleigh sky model predicts that the degree of sky polarisation, δ_s, depends on the angular distance, γ_s, which is the angle between the observation direction and the sun direction on the scattering plane [113, 114],

$$\delta_s = \delta_s^{\max} \frac{\sin^2 \gamma_s}{\left(1 + \cos^2 \gamma_s\right)}. \tag{3.30}$$

The degree of polarisation is maximum when $\gamma_s = 90°$ (fig. 3.6), i.e. right-angle to the sun. The maximum degree of polarisation, $\delta_s^{\max}$, depends on the albedo of the surrounding environment. For an unreflective environment, $\delta_s^{\max}$ of blue light can be 72% [112] to 100% [113] under a clear sky.

The direction of polarisation predicted by the Rayleigh sky model is perpendicular to the scattering plane which is the plane that goes through the observer on the ground, the observation point in the sky, and the sun. Therefore the direction of the electric vector, $\vec{e}_{\text{sky}}$, of the incoming

skylight from a celestial point, $\vec{v}_{\text{obs}}$, is

$$\vec{e}_{\text{sky}} = \vec{v}_{\text{obs}} \times \vec{\mu}_{\text{sun}} \tag{3.31}$$

where $\vec{\mu}_{\text{sun}}$ is the position vector relative to the observer.

The skylight polarisation pattern was measured in a number of experiments and it was found that a large proportion, $\sim 70\%$ [114, 115], of the sky is in agreement with the Rayleigh sky model under clear conditions. When the clouds are sparsely distributed in the sky, the polarisation pattern continues underneath the clouds and $\sim 25\%$ of the sky follows the Rayleigh sky model [114,115]. Under heavily overcast conditions, δ_s^{max} drops to 5%, however the polarisation pattern was still detectable [116]. During the night, the moonlight also produces a polarisation pattern that is the same as a sun-lit sky [117].

Cue-conflict and cue-calibration experiments in the past 20 years have shown that migratory birds use the polarisation patterns near the horizon at sunrise and sunset to calibrate the magnetic compass [27, 118–121]. The polarisation patterns at sunrise and sunset persist for a relatively long time [122] and the directional information within the pattern at sunrise and sunset is easier to interpret than during day (fig. 3.6). This might explain why some migratory birds prefer to migrate during sunrise and sunset. There is also evidence indicating that migratory birds use the polarisation pattern as a backup compass [123].

3.5 Singlet yield anisotropy of CRY RPs

As discussed in this chapter's introduction, a flavin-containing protein, CRY, is the current candidate for the magnetoreception molecule. The flavin cofactor in CRY absorbs blue light, subsequent electron transfers occur and a RP is formed with flavin as one of the radicals. It is not clear whether the RP contains the protonated flavin radical, $\text{FADH}^{\bullet}$ or the negatively charged radical, $\text{FAD}^{\bullet-}$. Some types of cryptochrome do not have a proton close to the flavin for the protonation to occur and those that have suitable protons may not protonate $\text{FAD}^{\bullet-}$ fast enough for $\text{FADH}^{\bullet}$ to be magnetically sensitive. However, $\text{FAD}^{\bullet-}$ is expected to behave in a similar way to $\text{FADH}^{\bullet}$ in a RP.

Table 3.1: The list of nuclei included in the SY calculations of the two RPs. The positions of the nuclei can be found in figure 3.7.

	Radical		Radical	
Radical Pair	Acceptor	Nuclei	Donor	Nuclei
RP1	$FADH^{\bullet}$	N1, N8, N17, H28, H29, H30, H31, H38	$Z^{\bullet}$	None
RP2	$FADH^{\bullet}$	N8, N17, H30, H31, H37, H38, H39	$TrpH^{\bullet+}$	N9, H22, H23, H24, H25, H26, H27

It has been suggested that the counter radical has no or very small HFIs [124] and a RP that has all significant HFIs concentrated in one radical has a bigger SY anisotropy [53]. However, transient absorption experiments [125] and electron spin resonance (ESR) spectroscopy [95] showed that CRY forms a RP that comprises $FADH^{\bullet}$ and $TrpH^{\bullet+}$ after blue light illumination. The Trp involved in the CRY RP is the furthermost from FAD in the structurally conserved Trp triad.

The SY anisotropy of two RPs are calculated; RP1 consists of $FADH^{\bullet}$ and $Z^{\bullet}$ (no HFIs) and RP2 consists of $FADH^{\bullet}$ and $TrpH^{\bullet+}$. The strength of the external magnetic field, B_0, is taken to be 50 μT, which is roughly the strength of the Earth's magnetic field in northern Europe. The exponential model (eq. 1.54 and 1.55) is used to account for the RP recombination kinetics and the exponential rate constant, k, is 1 μs^{-1}, which is consistent with the estimated lifetime of the RP [93]. The initial state of the RP is taken to be singlet [51]. The relative orientation between $FADH^{\bullet}$ and $Z^{\bullet}$ in RP1 is inconsequential as $Z^{\bullet}$ contains no HFIs. However, the SY of RP2 depends on the relative orientation between $FADH^{\bullet}$ and $TrpH^{\bullet+}$.

The SY anisotropy of RP2 was previously calculated by Cintolesi *et. al.* [126] and the authors used the relative radical orientation from the X-ray crystal structure of *E. coli* DNA photolyase (PDB code: 1DNP [127]). In their calculation, four magnetic nuclei each for $FADH^{\bullet}$ and $TrpH^{\bullet+}$ were included. In this section's calculation of the RP2 SY anisotropy, the relative orientation between $FADH^{\bullet}$ and $TrpH^{\bullet+}$ is taken from the first animal CRY X-ray crystal structure, *Drosophila* CRY (dCRY, PDB code: 3TVS [128]). It is assumed that the relative orientation between FAD and Trp remains the same as the normal protein after RP formation. More magnetic nuclei will be included here and this would be an improvement compared to the previous calculation.

In RP1, eight nuclei are included (table 3.1) and these are chosen due to their large isotropic

hyperfine coupling constants. In RP2, seven nuclei each in $FADH^{\bullet}$ and $TrpH^{\bullet+}$ are included (table 3.1). No magnetic nuclei in the ribityl and amino acid side chains are included in RP2 because the geometry optimised positions that were used to calculate their hyperfine coupling constants do not match the positions in the dCRY crystal structure.

The HFI tensors of the nitrogen nuclei are highly axial, and their axes of symmetry are perpendicular to the isoalloxazine ring in $FADH^{\bullet}$ and the indole ring in $TrpH^{\bullet+}$. All HFI tensors of $FADH^{\bullet}$ (fig. 3.7a) and $TrpH^{\bullet+}$ (fig. 3.7b) used in the calculations are listed in appendix A.

3.5.1 SY anisotropy

The anisotropic part of the SY provides the relative directional information between the external field and the molecular frame. The anisotropic SY, Φ_S^{aniso}, is the difference between the SY (eq. 1.54) and its spherical average, $\langle \Phi_S \rangle$;

$$\Phi_S^{\text{aniso}}(\theta,\phi) = \Phi_S(\theta,\phi) - \langle \Phi_S(\theta,\phi) \rangle . \tag{3.32}$$

The spherical average of a function is the integral over all space;

$$\langle \Phi_S(\theta,\phi) \rangle = \frac{\int_0^{2\pi}\int_0^{\pi} \Phi_S(\theta,\phi)\, \sin\theta \,\mathrm{d}\theta\,\mathrm{d}\phi}{\int_0^{2\pi}\int_0^{\pi} \sin\theta \,\mathrm{d}\theta\,\mathrm{d}\phi}. \tag{3.33}$$

The anisotropic SY of RP1 (fig. 3.8a) has a high degree of rotational symmetry and the axis of symmetry is perpendicular to the isoalloxazine ring, which is the z-direction. The axis of symmetry also coincides with the axiality of the nitrogen HFIs on $FADH^{\bullet}$ (N1, N8, N17).

However, the shape of the anisotropic SY of RP2 (fig. 3.8b) is more complex and it has less rotational symmetry compared to RP1 because the HFIs of the two radicals are not aligned. There are two rough rotational symmetry axes; one axis corresponds to the nitrogen HFIs on $FADH^{\bullet}$ and the other axis corresponds to the single nitrogen HFI on $TrpH^{\bullet+}$. The anisotropy of RP2 is 100 times smaller than RP1 due to the presence of HFIs in both radicals.

3.5.2 Spherical harmonic expansion of the SY

One property of Wigner-D rotation of spherical harmonics (eq. 3.9) is that the quantity,

$$\sum_{m=-l}^{l} \left| a_l^m \right|^2 , \tag{3.34}$$

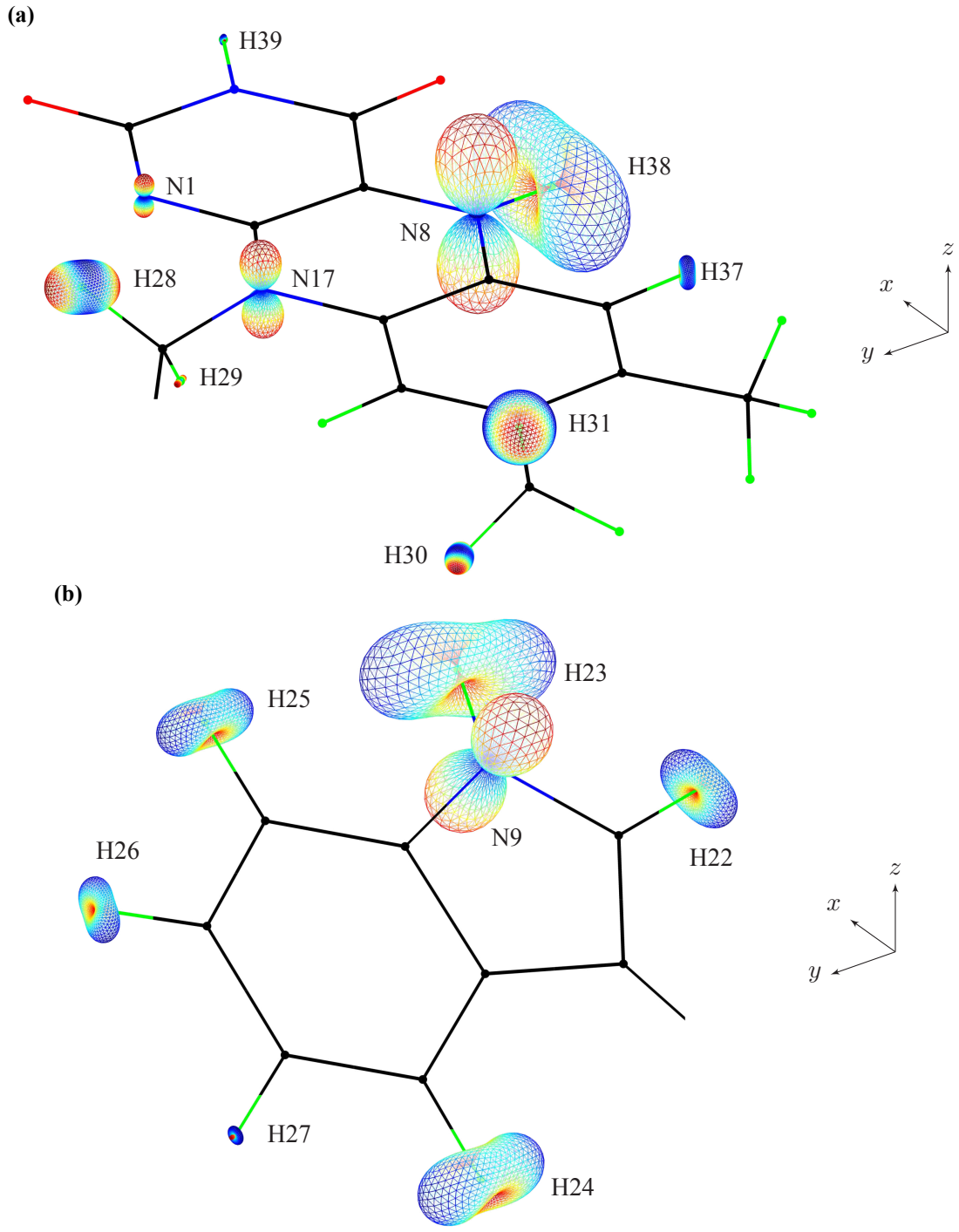

Figure 3.7: The three dimensional structure of (a) $FADH^{\bullet}$ and (b) $TrpH^{\bullet+}$. The mesh plots (appendix D) represent the magnitude and direction of the HFIs of the nuclei at the centre of the mesh plots. The colour codes for different atoms are: carbon, oxygen, hydrogen and nitrogen. Details of the geometries and HFIs can be found in appendix A. $FADH^{\bullet}$ and $TrpH^{\bullet+}$ are plotted in the same axis system and the relative orientation between the two molecules is taken from the X-ray crystal structure of dCRY (PDB code: 3TVS [128]).

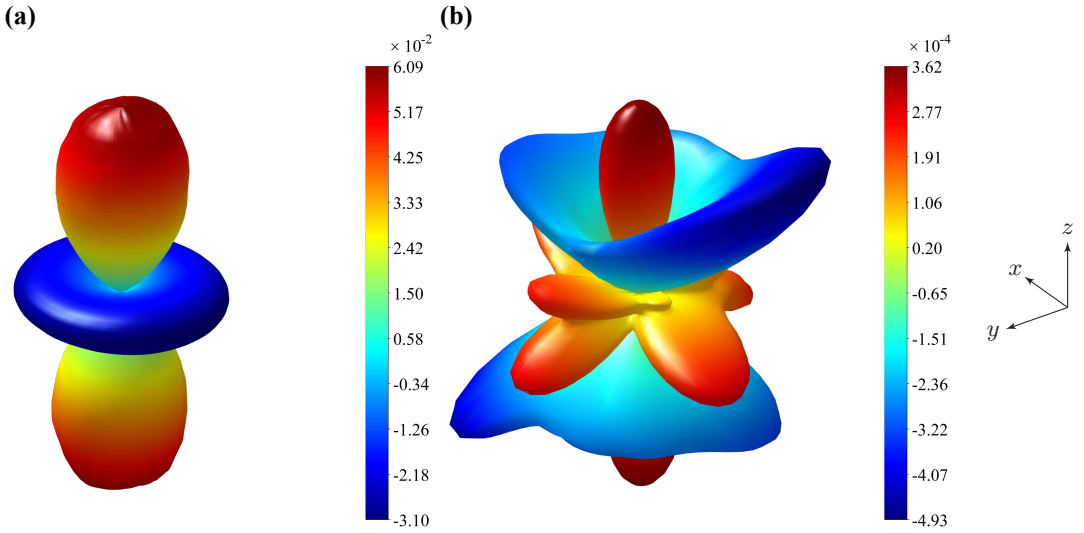

Figure 3.8: Anisotropic SY of (a) RP1 and (b) RP2. The nuclei included in the calculation can be found in table 3.1. The calculation is performed with exponential rate constant, $k = 1\ \mu s^{-1}$, $B_0 = 50\,\mu T$ and the initial state of the RP is singlet. The axis systems in (a) and (b) are the same as in figure 3.7. Given a position vector on the surface of the plot, the length of the vector (represented by the colour scale) is the anisotropic SY and the direction of the external magnetic field is parallel to the position vector.

remains unchanged under rotation for a given degree l. Therefore, the quantity,

$$A_l = \frac{2l+1}{4\pi} \sum_{m=-l}^{l} |a_l^m|^2 \tag{3.35}$$

is a measure of the contribution of a particular degree to the spherical harmonic expansion, Φ_S^{SHE}, of the SY.

The error of Φ_S^{SHE} is measured by the root mean square (RMS) of the difference between the spherical harmonic expansion and the actual SY,

$$\text{RMS(error)} = \sqrt{\frac{1}{n}\sum_{i=1}^{n} d_i^2} \quad \text{where} \quad d_i = \Phi_S - \Phi_{S,i}^{\text{SHE}}. \tag{3.36}$$

Y_0^0 is a constant, therefore a_0^0 is just the isotropic SY. The isotropic SYs of RP1 and RP2 are similar and RP2 has a lower directional sensitivity compared to RP1 because of the smaller anisotropic SY.

The $l = 2$ expansion gives less than 1% RMS error (fig. 3.9a) and the anisotropy of RP1 can be described by Y_2^0 with good agreement (fig. 3.10a). The spherical harmonic expansion with $l > 2$ gives no significant improvement and the spherical harmonic coefficients for $l > 2$ are small compared to the coefficients for $l = 2$.

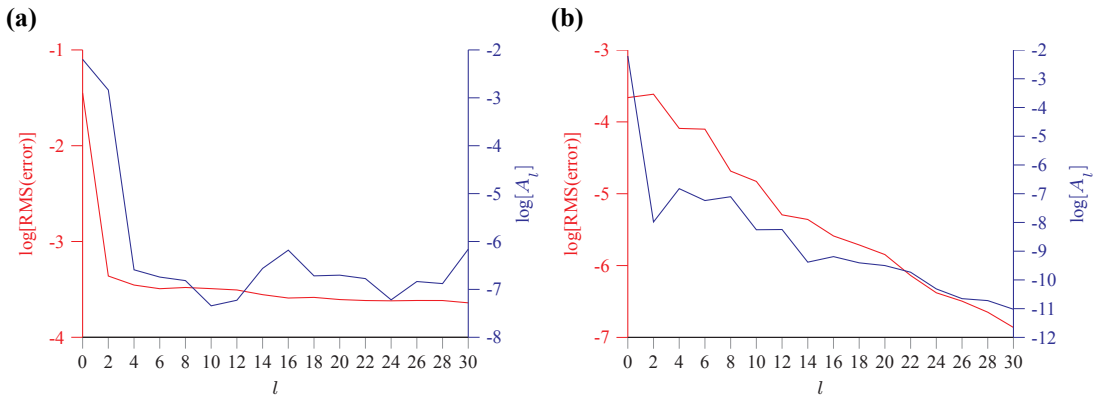

Figure 3.9: The error analysis of the spherical harmonic expansion of (a) RP1 and (b) RP2. The red line is the RMS(error) of Φ_S^{SHE} up to degree l. The blue line is A_l of the expansion coefficients of degree l.

The shape of the anisotropy of RP2 is more complex and higher degree spherical harmonics are needed for an accurate expansion. Spherical harmonic expansion up to $l = 16$ is needed to give 1% RMS error (fig. 3.9b). The biggest contribution to the spherical harmonic expansion of the RP2 anisotropy is the $l = 4$ spherical harmonics. The nine Y_4^m contribute to the complex shape of the RP2 anisotropy (fig. 3.10b).

The expansion coefficients for RP1 are in general bigger than for RP2 because the anisotropy of RP2 is smaller in magnitude. The spherical harmonic expansion coefficients of the SY of RP1 and RP2 are listed in appendix B.

3.6 Field dependence of magnetoreceptor signal

In this section, the field dependence of magnetoreceptor cells is investigated at five locations in the retina: centre, top, right, bottom, and left (fig. 3.11). These five points are representative of the overall retina response to the changing of the external field direction.

The direction of the Earth's magnetic field found in northern Europe is 66° downwards with a strength very close to 50 μT [129]. This is equivalent to $\zeta = -114°$ and $\delta = 0°$ when the eye is looking towards the horizon towards north. The field is then rotated around the x-axis of the retina frame in the right-handed direction by an angle, λ, so that a rotation of $\lambda = \pi/2$ is the same as pointing the eye from the north to the east.

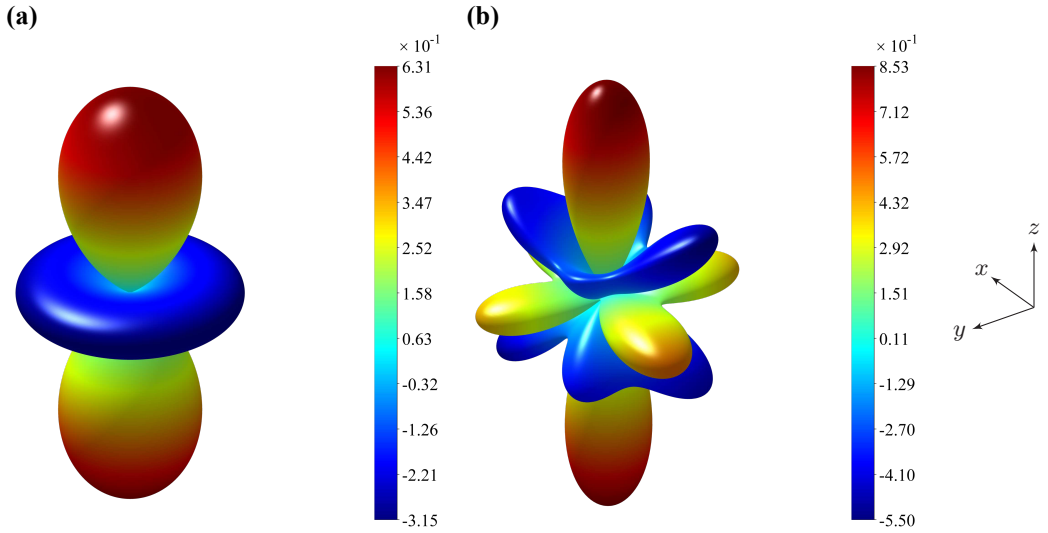

Figure 3.10: Spherical harmonic functions, (a) Y_2^0 and (b) $\sum_{m=-4}^{m=4} b_4^m\, Y_4^m$, where b_4^m are the scaled spherical harmonic coefficients of the RP2 anisotropy. The anisotropic SY of RP1 (fig. 3.8a) is almost identical to Y_2^0 and a_2^m coefficients have the biggest contribution to the spherical harmonic expansion of Φ_S^{aniso}. (b) has some of the complex shape of the anisotropic SY of RP2 (fig. 3.8b) and a_4^m coefficients are the biggest contributors to the spherical harmonic expansion of RP2 anisotropy.

The retina signal, S, produced by magnetoreceptor cells, is the product of the absorption probability (eq. 3.28) and the SY of the photo-excited RPs (eq. 3.22). The assumption here is that the signalling state is the singlet and the signal transduction is linear;

$$S = p(\alpha,\beta,\gamma,\eta,\theta,\phi,\varepsilon) \times \Phi_S(\alpha,\beta,\gamma,\eta,\theta,\phi,\zeta,\delta). \tag{3.37}$$

Only the anisotropic part of the SY is considered as it is the part that provides directional information and Y_0^0 is omitted. Φ_S in equation 3.37 is taken to be Y_2^0, which is the approximate shape of the anisotropic SY of RP1 (fig. 3.8a), such that

$$\Phi_S^{\text{RP1}} \approx \Phi_S^{(2,0)} = R(\eta,\theta,\phi)\, R(\alpha,\beta,\gamma)\, Y_0^2(\zeta,\delta) \tag{3.38}$$

$$\text{where} \quad Y_2^0(\zeta,\delta) = \frac{1}{4}\sqrt{\frac{5}{\pi}}\left(3\cos^2\zeta - 1\right).$$

The retina signal becomes

$$S' = p(\alpha,\beta,\gamma,\eta,\theta,\phi,\varepsilon) \times \Phi_S^{(2,0)}(\alpha,\beta,\gamma,\eta,\theta,\phi,\zeta,\delta) \tag{3.39}$$

The TDM of the magnetoreceptor molecule is taken to be $(1\,0\,0)$ in the molecular frame; the exact direction in the xy-plane is not important since Y_2^0 is cylindrically symmetric around the z-axis. This is similar to FAD in which the TDM is also in the xy-plane.

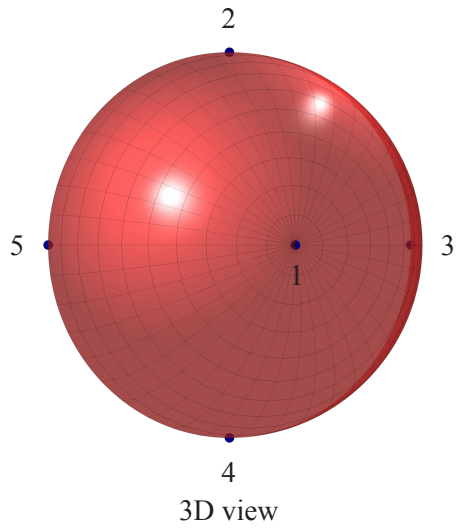

3D view

Position number	(θ, ϕ)
1	$(0, 0)$
2	$(\frac{\pi}{2}, 0)$
3	$(\frac{\pi}{2}, \frac{3\pi}{2})$
4	$(\frac{\pi}{2}, \pi)$
5	$(\frac{\pi}{2}, \frac{\pi}{2})$

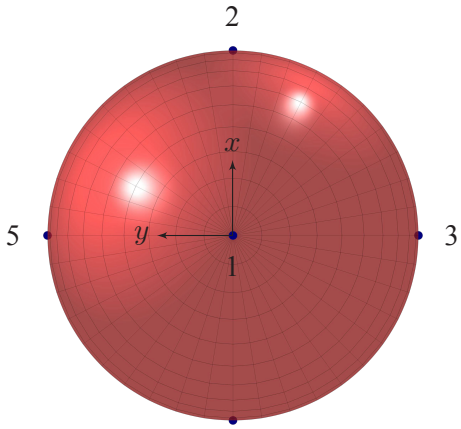

Back view

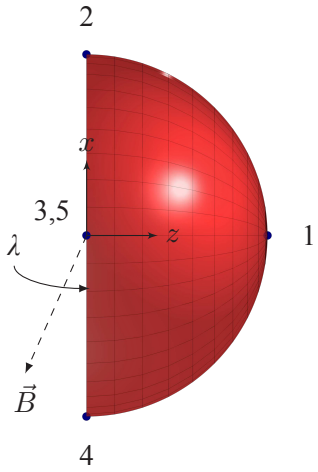

Side view

Figure 3.11: The locations of the five magnetoreceptor cells (blue dots) under investigation are numbered 1 to 5. The spherical polar angles, (θ, ϕ), with respect to the retina frame of the five positions can be found in the table. The direction of the external field, $\vec{B}$, is rotated around the x-axis and the x-rotation is defined by λ.

3.6.1 Unpolarised light

The retina signal is averaged over all 2π polarisation angles if the incoming light is unpolarised. Only the absorption probability of the retinal signal depends on ε, so the averaged absorption probability (eq. 3.29) is used for unpolarised light. The retinal signal for unpolarised light is

$$\left\langle S' \right\rangle_{\varepsilon} = \langle p \rangle_{\varepsilon} (\alpha, \beta, \gamma, \eta, \theta, \phi) \times \Phi_S^{(2,0)}(\alpha, \beta, \gamma, \eta, \theta, \phi, \zeta, \delta). \tag{3.40}$$

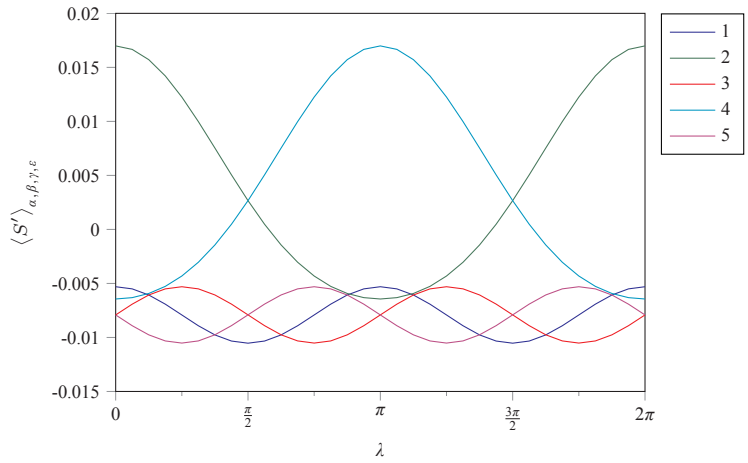

Figure 3.12: Averaged magnetoreceptor cell signal at five retina positions, 1 to 5. The incoming light is unpolarised and the molecules are randomly oriented. The signal is averaged over α, β, γ and ε. The angle λ is the x-rotation of the external magnetic field in the retina frame; $\lambda = 0$ is north, $\lambda = \pi/2$ is east, $\lambda = \pi$ is south and $\lambda = 3\pi/2$ is west. The external field angles are $\zeta = -114^\circ$ and $\delta = 0^\circ$.

Randomly oriented molecules

Currently, there is no evidence to prove that CRYs are immobilised and in this sub-section, the effects of randomly oriented magnetoreceptors are investigated. Molecules that are randomly oriented give rise to a signal that is averaged over α, β, and γ;

$$\left\langle S' \right\rangle_{\alpha,\beta,\gamma,\varepsilon}(\theta,\phi,\zeta,\delta) = \frac{1}{8\pi^2}\int_0^{2\pi}\int_0^{\pi}\int_0^{2\pi}\left\langle S' \right\rangle_{\varepsilon}\sin\beta\,\mathrm{d}\alpha\,\mathrm{d}\beta\,\mathrm{d}\gamma. \tag{3.41}$$

η can be effectively ignored after averaging over γ because η is a sequential z-axis rotation after γ.

The absorption probability of randomly oriented molecules averages to a constant value independent of the position of the cell. The SY also averages to the isotropic value for all cell positions and all external field directions if the molecules are randomly oriented. However, the averaged retina signal, $\left\langle S' \right\rangle$, which combines the absorption probability and the SY, is dependent on the cell position and the direction of the external field.

The cells at positions 1, 3 and 5 are in the same two-dimensional plane as the angle λ of the external field. The signals from these three positions are out of phase by $\pi/4$ to each other, however the angular distance between each position is $\pi/2$ (fig. 3.12). The smaller phase shift is

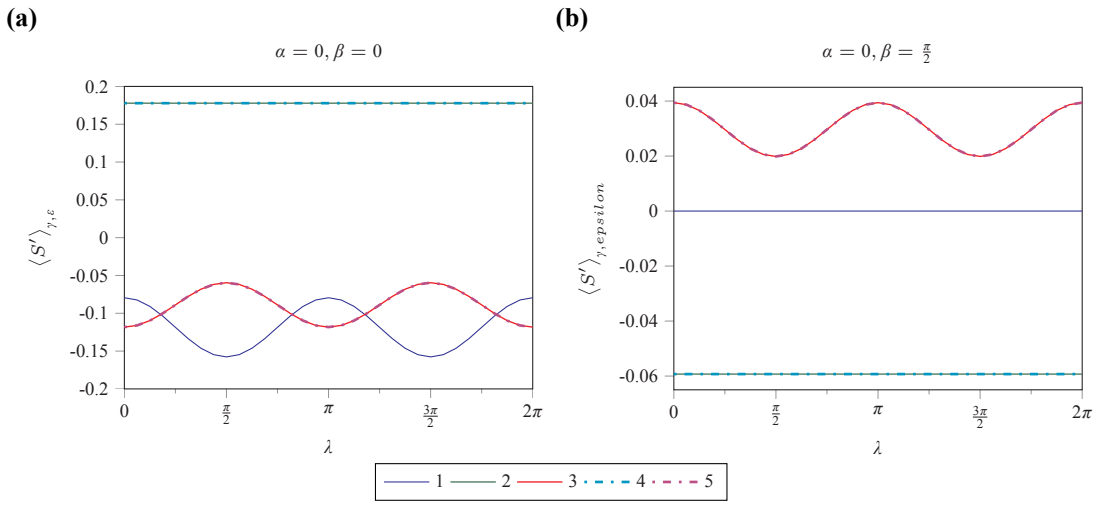

Figure 3.13: Averaged magnetoreceptor cell signal at five retina positions, 1 to 5. The incoming light is unpolarised and the molecules are partially oriented, $\alpha = 0$; in (a) $\beta = 0$ and in (b) $\beta = \pi/2$. The signal is averaged over γ. The angle λ is the x-rotation of the external magnetic field in the retina frame. The external field angles are $\zeta = -114^\circ$ and $\delta = 0^\circ$.

because the plane of light-propagation only rotates by $\pi/4$ between positions 1 and 3. The signals at positions 2 and 4 are out of phase by π and this is due to the inversion symmetry of the SY.

The signals' variations at the five positions with respect to the field direction are distinct. Therefore it is possible that randomly oriented molecules can provide directional information even if the incoming light is unpolarised. Potentially, the signals can also provide the angular distance between the current direction and the desired direction.

Partially oriented molecules

If the magnetoreceptor molecule is attached to the cell at two opposite points at the edge of the molecule, the molecule would be partially immobilised. The molecules would be aligned along the axis joining the two points and there would be no preferred orientation around this axis. In this case, $\alpha = 0$ and the retina signal is averaged over γ;

$$\langle S' \rangle_{\gamma,\varepsilon} (\alpha = 0, \beta, \theta, \phi, \zeta, \delta) = \frac{1}{2\pi} \int_0^{2\pi} \langle S' \rangle_{\varepsilon} \, \mathrm{d}\gamma. \tag{3.42}$$

When $\beta = 0$, the TDM lies tangential to the retina. The signals at positions 2 and 4 are now independent of the direction of the external field (fig. 3.13a) because the axis of symmetry for Y_2^0 at these two positions coincides with the rotation axis of the field. The signals at positions 1,

3 and 5 remain dependent on the direction of the field and the magnitude of the signal variation is about 20 times bigger than the signal given by randomly oriented molecules (fig. 3.12).

When $\beta = \pi/2$, the TDM lies perpendicular to the retina. The signal at position 1 is zero in this case because the plane of polarisation is perpendicular to the TDM. The signals at positions 2 and 4 are again independent of the external field (fig. 3.13b). At these two positions, the z-axis of the γ rotation coincides with the rotation plane of the external field and the signals are averaged to the same value for all λ. The magnitudes of the signal variation at position 3 and 5 are only 4 times bigger compared to the signal produced by randomly oriented molecules (fig. 3.12).

In general, partially oriented molecules produce a bigger variation in the signals when the eye sweeps across the horizon in the Earth's magnetic field. However the advantage is dependent on the orientation of the TDM with respect to the retina. When the TDMs of the molecules are aligned tangentially to the retina, the maximum variation is produced.

3.6.2 Polarised light

Although 100% polarised light rarely occurs in nature, light with different linear polarisation angles may be useful for *in vivo* orientation experiments. The absorption probability can be calculated for a particular polarisation angle (eq. 3.28) and the averaged signal, $\langle S' \rangle_{\alpha,\beta,\gamma}$, can be calculated using equation 3.41.

The polarisation vector points in the retina x-direction for $\varepsilon = 0$. The signals at positions 1, 3 and 5 are independent of the external field direction (fig. 3.14a) and this is because $\vec{e}_m$ is in the same direction as the rotation axis of the field. The signals are the same magnitude because $\vec{e}_m$ at each position is the same. The magnitude of the signal at positions 2 and 4 are 2 times bigger than the signals produced by unpolarised light (fig. 3.12).

When $\varepsilon = \pi/2$, the polarisation vector points in the retina y-direction. The signal variations at positions 1, 2 and 4 are the same (fig. 3.14b) because the polarisation vectors at these three positions are the same. The signals are out of phase by $\pi/4$ at positions 1 and 3 and similarly at positions 1 and 5. The angular distances between positions 1-3 and 1-5 are only $\pi/2$, however the

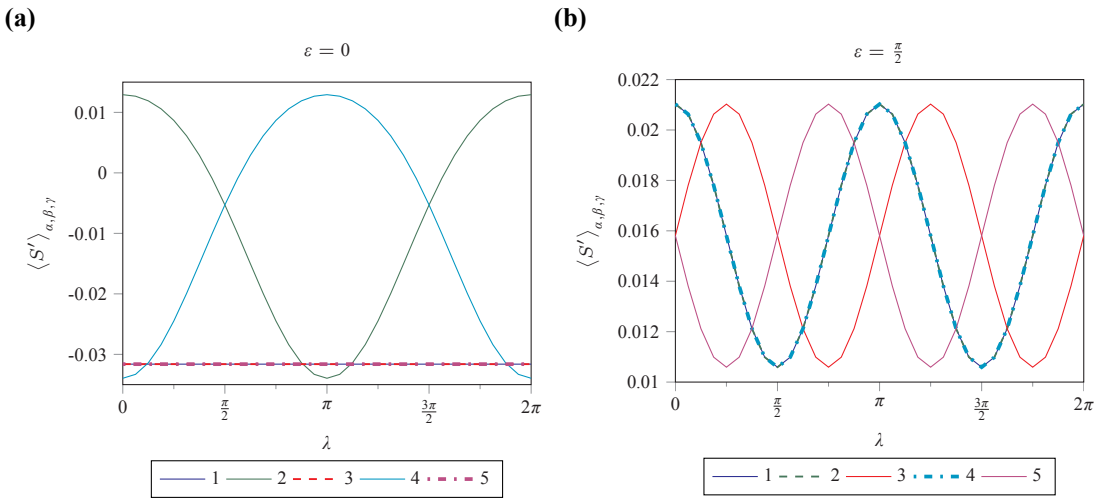

Figure 3.14: Averaged magnetoreceptor cell signal at five retina positions, 1 to 5. The incoming light is polarised; in (a) $\varepsilon = 0$ and in (b) $\varepsilon = \pi/2$. The signal is averaged over α, β and γ. The angle λ is the x-rotation of the external magnetic field in the retina frame. The external field angles are $\zeta = -114^\circ$ and $\delta = 0^\circ$.

polarisation vector rotates by $\pi/4$ between 1-3 and 1-5. The magnitudes of the signal are also 2 times bigger (fig. 3.14a) compared to the signals produced by unpolarised light (fig. 3.12).

Using polarised light improves the signal magnitudes compared to unpolarised light. Comparing figures 3.14a and 3.14b, the field direction dependence and signal magnitude at each position depends significantly on the direction of the polarisation vector. Potentially, a bird can recognise different polarisation angles because different retina patterns are produced when the angle of polarisation changes.

3.7 Retina patterns

The magnetoreceptor cells in the retina collectively produce a pattern of signal because each cell has a different orientation relative to the external field. An effective retinal compass should produce visual patterns that are different for different compass directions. As the bird scans across the horizon in the Earth's magnetic field, the pattern changes according to the direction of the line of vision. If the patterns vary gradually, it may be possible to determine the angular distance of the desired heading from the current direction. Since different directions produce different patterns, the bird can associate a particular pattern with a migration direction.

The signals from cells at each (θ, ϕ) location in the retina are projected onto a screen in order to represent the 3-dimensional pattern in 2-dimensions (fig. 3.1a and for projection details see appendix E). In this section, the retina patterns under unpolarised light and sky-polarised light are presented using the TDM of FAD (fig. 3.5), and the anisotropic SY of RP1 and RP2 (fig. 3.8). The CRYs are assumed to be randomly oriented.

3.7.1 Unpolarised light

The patterns for the eight compass directions are different (fig. 3.15) and the variation in the pattern is gradual. The north to southeast patterns are the inverted image of the south to northwest patterns. This is a result of the inversion symmetry of the SY. However, when there is no vertical component in the magnetic field in places near the equator, the patterns are identical when the retinal direction is inverted (such that north and south patterns are the same, east and west patterns are the same). In this case, other directional cues are needed to distinguish north-south and east-west.

The patterns of RP1 (fig. 3.15a) is very similar to the patterns of RP2 (fig. 3.15b), except that the positive and negative areas are interchanged. This is the result of the different signs of the RP1 and RP2 anisotropic SYs for the angles $2\pi/3 < \zeta < 4\pi/3$ (fig. 3.8). Although the anisotropic SY of RP1 is 100 times stronger than RP2, the retina patterns of RP1 are 860 times stronger than RP2 in magnitude. This is because the number of phase changes in the xz-plane of the anisotropic SY of the two RPs. The RP1 anisotropy has two phase changes and the RP2 anisotropy has four phase changes. The increased number of phase changes leads to a more effective spherical averaging of the retina signal.

3.7.2 Sky-polarised light

The patterns produced under sky-polarised light (fig. 3.16) are similar to the unpolarised patterns. The magnitudes of sky-polarised north and south patterns have increased by about 2 times compared to the unpolarised case but the east and west patterns remain the same. The improvements are only found in the north and south direction because the maximum degree of polarisation is found 90° away from the sun at the west.

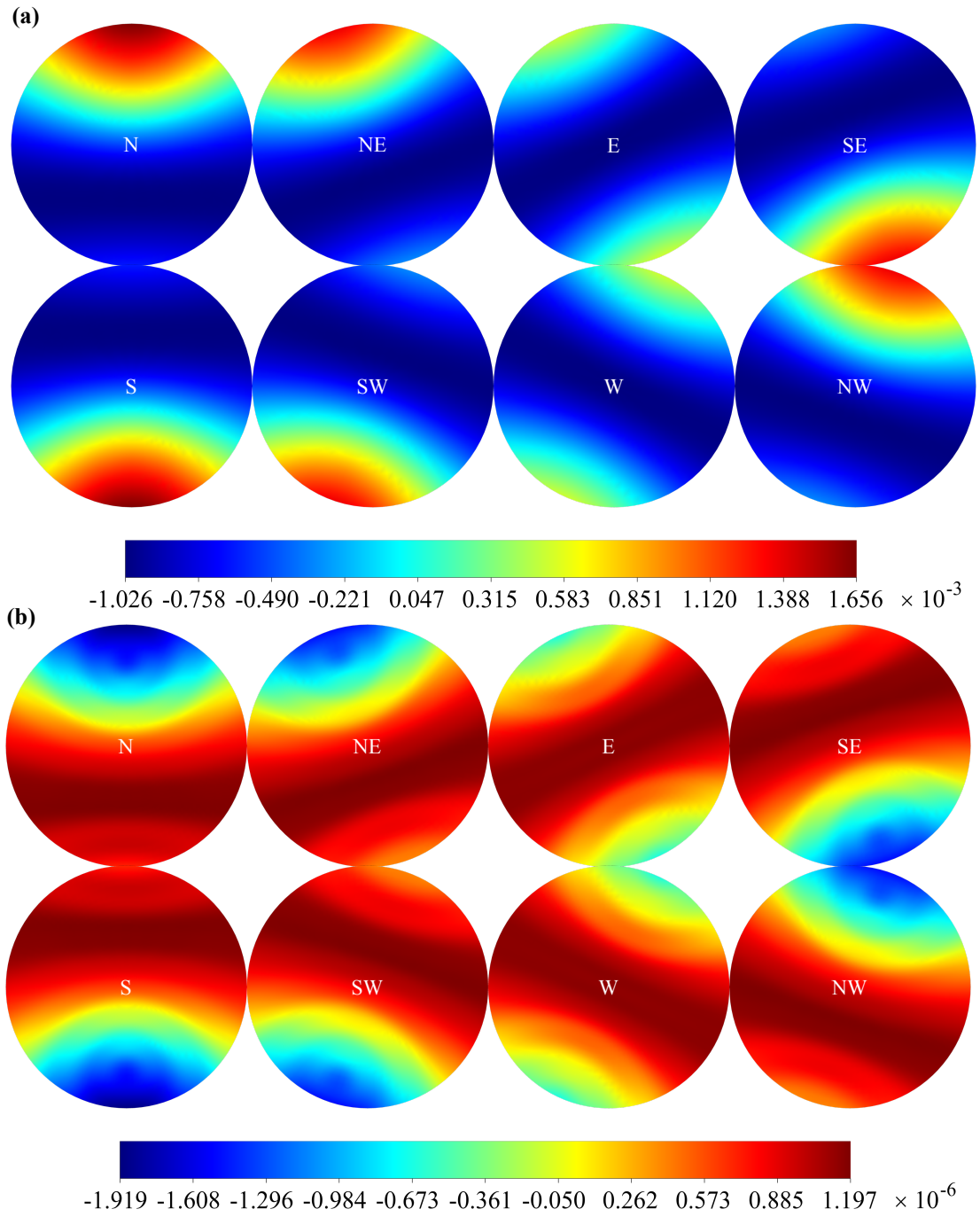

Figure 3.15: The visual patterns of randomly oriented (a): RP1 and (b): RP2. The eye is pointing at eight compass directions horizontally, indicated in the middle of each circle. The anisotropic SYs used are plotted in figure 3.8 and spherical harmonics up to $l = 16$ are used. The incoming light is unpolarised. The signals are averaged over α, β and γ. The external field angles are $\zeta = -114^\circ$ and $\delta = 0^\circ$, which describe the direction of the Earth's magnetic field in northern Europe.

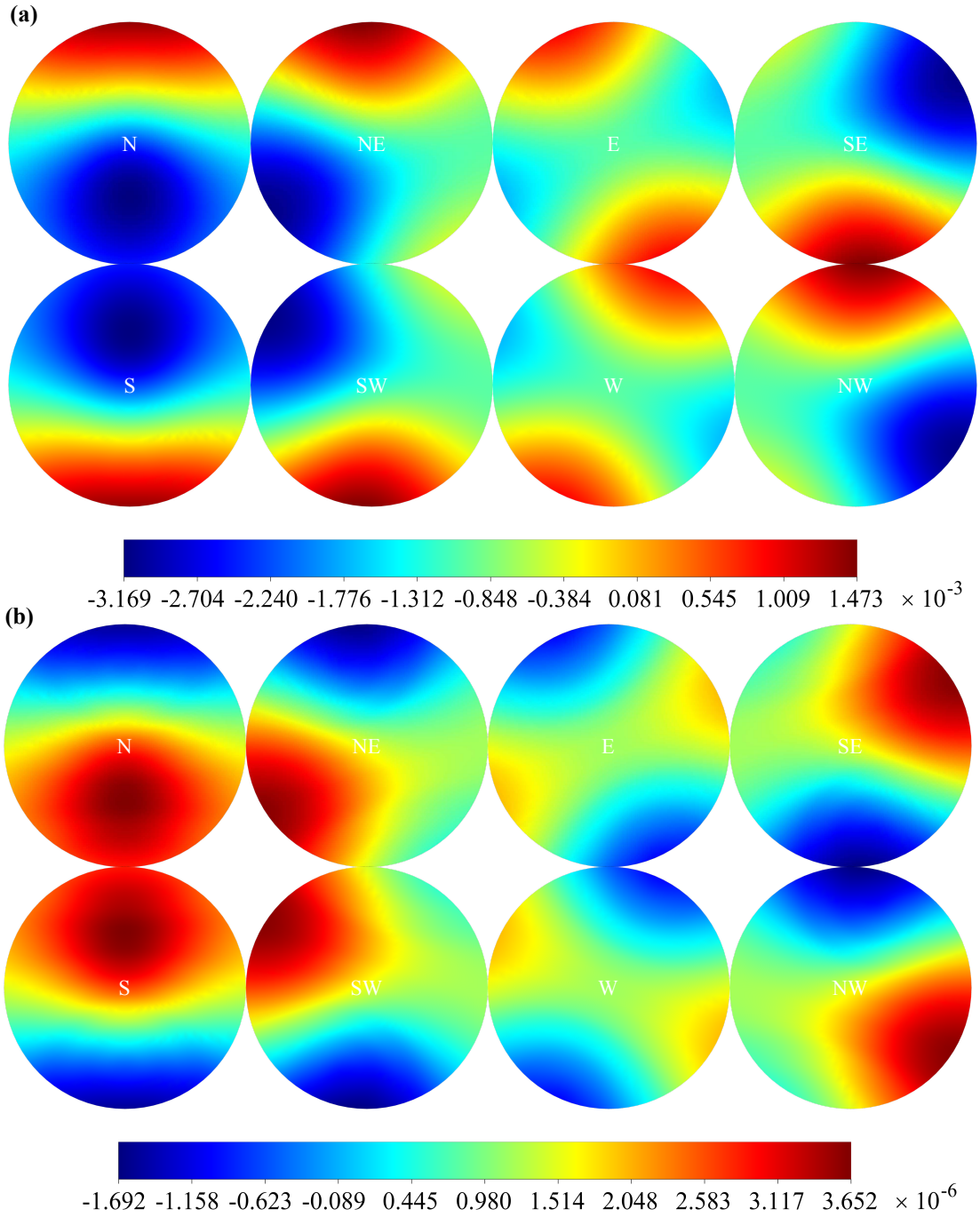

Figure 3.16: The visual patterns of randomly oriented (a): RP1 and (b): RP2. The eye is pointing at eight compass directions horizontally, indicated in the middle of each circle. The anisotropic SYs used are plotted in figure 3.8 and spherical harmonics up to $l = 16$ are used. The incoming light is polarised according to the Rayleigh sky model (eq. 3.31) and $\delta_s^{\max} = 0.7$. The sun is due west of the eye, i.e. along the positive y-axis. The same patterns are applicable when is the sun is due east as the polarisation pattern is the same during sunrise and sunset. The signals are averaged over α, β and γ. The external field angles are $\zeta = -114^\circ$ and $\delta = 0^\circ$, which describe the direction of the Earth's magnetic field in northern Europe.

Experiments show that some species of birds prefer to calibrate their compass during sunrise or sunset under a clear sky [119, 120]. If the RPR is the underlining mechanism for magnetoreception in birds, it may be easier to acquire north and south during sunset and sunrise because of the improved contrast of the retina patterns produced by sky-polarised light.

3.8 Conclusion

Randomly oriented molecules in magnetoreceptor cells in the retina can give a signal that depends on both the location of the cell in the retina and the direction of the external magnetic field. The geometry of the eye creates the variation of the polarisation vector at the retina and photoselection produces the anisotropic absorption probabilities. Photoselection is enhanced by polarised light or sky-polarised light but the presence of polarised light is not essential to the function of the magnetoreceptors.

The absorption probability and the SY combine to give the signal of a molecule in a particular orientation and in the case of randomly oriented molecules within a cell, the averaging over all molecular orientations gives a resultant cell signal that depends on the location of the cell with respect to the retina. Hence a collection of magnetoreceptor cells, ordered in a similar way to the rods and cones, on the retina can provide directional information even if the cells contain only randomly oriented molecules.

A previously assumed requirement of the RPR magnetoreception is the immobilisation and alignment of the magnetoreceptor molecules. In this chapter, this requirement is shown to be unnecessary for RPR magnetoreception, however the rotational motion of the molecules should still be slow in order to increase spin relaxation times [130].

The bird's eye is assumed to be spherical in this chapter but in reality it is ellipsoidal. This geometry creates a greater angular variation of the polarisation vector from the equator to the poles of the eye. Potentially this may lead to more distinguishable retina patterns because of the change in the absorption probabilities.

Since there is no evidence on the transduction mechanism, there are only speculations on the sensitivities of magnetoreceptor cells. The magnitude of the RP2 retina patterns are relatively

small but it can be increased by using a higher number of proteins in the cell. The distribution of the magnetoreceptor cells may not be uniform and a higher concentration of cells may be present at advantageous locations in the retina, similar to the fovea which is a region of enhanced visual acuity.

Chapter 4

Reaction yield detected magnetic resonance and γ–COMPUTE

Reaction yield detected magnetic resonance (RYDMR) is the study of the effects of the absorption of resonant electromagnetic radiation, under a static magnetic field, on the reaction kinetics of a RPR [22]. The term RYDMR was first used by Frankevich *et al.* in 1977 [131]. RYDMR can be viewed as a type of electron spin resonance (ESR) in which electromagnetic radiation at the characteristic resonant frequency is used to change the spin state of an electron. In RYDMR, the unpaired electron in a radical absorbs the radiation and this leads to the change of the spin multiplicity of the RP.

RYDMR is used when the direct detection, either via a free induction decay or transient absorption, of radical intermediates is difficult due to the short radical lifetimes and the low radical concentration. The resonant effects are observed indirectly via the detection of the products of the RPR. Usually the fluorescence of the singlet exciplex, formed from the singlet RP, is monitored and the amount of fluorescence represents the singlet product yield of the RPR.

Traditional RYDMR involves a strong magnetic field of around 0.3 T, and microwaves at 9.5 GHz and 0.1 mT [131]. At this static field strength, the dominant magnetic interaction is the Zeeman interaction, and T_{+1} and T_{-1} states are split in energy from the S and T_0 states (fig. 1.5b). Microwave radiation that matches the energy splitting reconnects the T_{+1} and T_{-1}

states to the S and T_0 states. Therefore more singlet-triplet interconversion occurs and the SY decreases, for a singlet-born RP, at the resonant frequency.

Recently RYDMR was observed in weak magnetic fields ($\leq$ 4 mT) [132–134] and radio frequency (RF) radiation was used instead in these experiments. HFIs and Zeeman interactions are similar in magnitude when the external field strength is less than 4 mT. The oscillating radiation now reconnects states with different singlet and triplet character that are split by HFIs and Zeeman interaction [135]. The result of the application of oscillating radiation to the RP system is qualitatively the same as in high field; at the resonant frequency, the SY decreases.

Off-resonant excitations can occur because generally there are multiple hyperfine transitions in a radical with several nuclei and there is also the lifetime-broadening of the radical energy levels [135]. The strength of the magnetic component of the radiation, B_1, determines the rate of singlet-triplet interconversion, and the lifetime of the RP should be longer than the reciprocal of the frequency of the oscillating field to observe a significant RYDMR effect.

RYDMR is an important diagnostic test for the RPR. Details of the radicals involved in the reaction can be found via RYDMR. Recent experiments on birds showed that they are disoriented by RF magnetic fields [35]. These experimental results support the involvement of RPs in avian magnetoreception. However, *in vitro* RYDMR experiments of relatively simple RP systems are still needed. Analysis of *in vitro* experiments with computed simulations can provide more information on the effects of RYDMR and perhaps better direct further *in vivo* experiments to discover more details about the RP involved in magnetoreception.

In this chapter, the algorithm that is used to calculate product yields in RYDMR experiments, γ–`COMPUTE`, is introduced and the modulation technique used in the RYDMR experiments is discussed. The RYDMR experimental data presented in sections §4.6 and §4.7 is collected by Dr. C. J. Wedge of the Timmel group in the University of Oxford. In section §4.8, the algorithm is used to analyse some Rotary-RYDMR experimental data collected by Ms Kelly-Anne Ferguson, also of the Timmel group. The same group conducted RYDMR experiments previously [136, 137] using a similar setup.

Table 4.1: Viscosities and dielectric constants of the solvents used in the RYDMR experiments [138].

	cyclohexanol	acetonitrile
viscosity, η (mPa s @ 298 K)	57.5	0.369
dielectric constant, ε (@ 293.2 K)	16.4	36.64

4.1 Experimental methods

The reagents were dissolved in a mixture of acetonitrile and cyclohexanol in a ratio of 1 : 9. The solution was continuously circulated in a loop through a quartz cuvette to reduce sample degradation. The cuvette is kept at room temperature. The RPs were generated in the cuvette by continuous ultraviolet ($\sim$350 nm) irradiation from a xenon arc lamp. The fluorescence signal from the exciplex is passed through an interference filter (100 nm bandwidth, centred at 548 nm) and is detected by a photomultiplier tube (PMT) perpendicular to the irradiation source. The recording was started after the lamp was switched on and after the fluorescence signals had reached a stable value.

Acetonitrile has a high dielectric constant (table 4.1); if only acetonitrile is used, it will increase the polarity of the solvent and stabilise the RP, hence there is no RP recombination and no fluorescence is observed. However, cyclohexanol has a high viscosity (table 4.1); if only cyclohexanol is used, the RP recombination rate will increase, because the radicals will separate slowly, and no significant RP concentration will be detected. The ratio 1 : 9 of acetonitrile to cyclohexanol solvent mixture was found to have the optimal RP formation and exciplex fluorescence, and have the largest magnetic field effect.

The static magnetic field of up to 4 mT was generated by two pairs of Helmholtz coils positioned at right angles to each other. The direction of the field was changed by varying the phase between the two sinusoidal voltages in each pairs of coils. The RF oscillating radiation is linearly polarised and fixed at 36 MHz. During the experiment, fluorescence signals were collected at various RF field strengths, and at different angles between the static field and RF field.

The effect of the RF field is weak compared to the background fluorescence. A modulation

technique was used to improve the signal-to-noise ratio. The full details of the modulation will be described in a later section. Phase-sensitive detection and a low-pass filter were used to select a component of the signal that oscillates at the modulation frequency, and any noise that oscillates at different frequencies was filtered. Therefore only the RF field effect was recorded.

4.1.1 Radical pair systems

The RYDMR experiments were conducted with four molecules (fig.4.1):

(i) pyrene (Py),

(ii) chrysene (Chr),

(iii) 1,3-dicyanobenzene (1,3-DCB), and

(iv) 1,4-dicyanobenzene (1,4-DCB).

Three separate RP systems were used in the experiments:

(a) Py-h_{10}/1,3-DCB,

(b) Chr-d_{12}/1,4-DCB, and

(c) Py-d_{10}/1,3-DCB.

Py and Chr are the electron donors, and 1,3-DCB and 1,4-DCB are the electron acceptors. The reactants were dissolved in a $1:9$ of acetonitrile:cyclohexanol solvent mixture. The solution used in Wedge's experiments contained 1 mM of Py and 20 mM DCB, and in Ferguson's experiments the solutions contained 0.4 mM of Py or Chr and 40 mM DCB.

Py absorbs ultraviolet light $(350\,\text{nm})$ and is excited from the ground state to the first singlet excited state. Py^* reacts with 1,3-DCB in the solution to form an exciplex. The exciplex fluoresces at ~ 548 nm and relaxes back to the ground state Py. The singlet RP is formed via an electron transfer within the exciplex. Singlet-triplet interconversion occurs in the RP and it is governed by all the magnetic interactions. The triplet RP forms the escape products, then the products return to the ground state. The intensity of the fluorescence is directly proportional to the SY of the RP. Other sources of luminescence, such as ^{T}Py, are omitted for simplicity (^{T}Py phosphoresces at different wavelength to the exciplex). The reaction between Chr and 1,4-DCB is assumed to be similar to Py/1,3-DCB and the exciplex, $^{S}\left\{^{\delta+}\text{Chr}\cdots\text{DCB}^{\delta-}\right\}$, also fluoresces at ~ 548 nm. A summary of the Py/1,3-DCB reaction scheme is shown in figure 4.2.

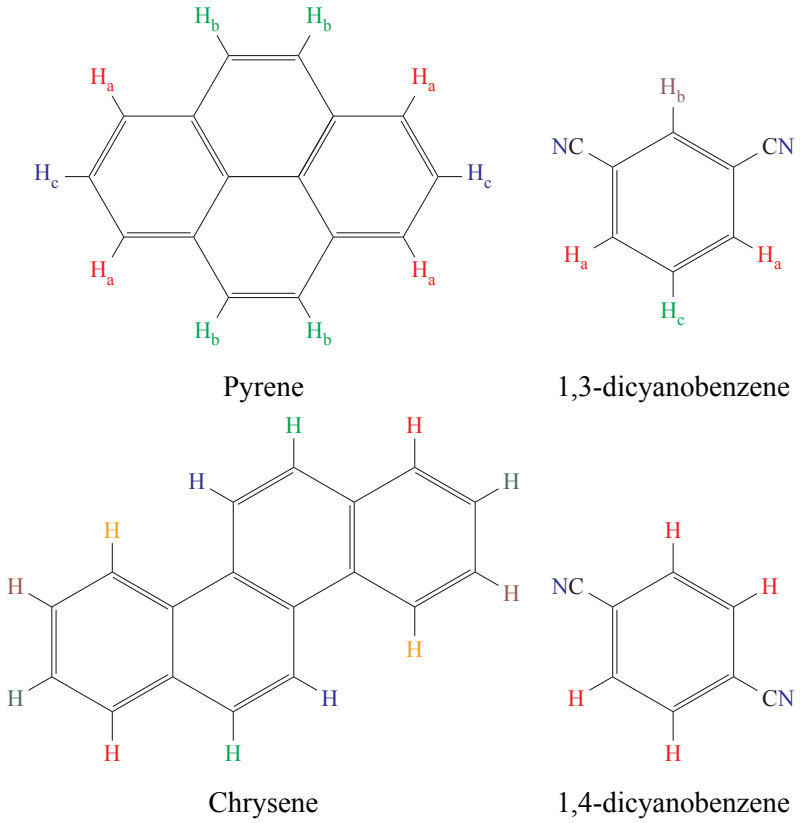

Figure 4.1: Chemical structure of the molecules used in the RYDMR experiments. Equivalent nuclei are labelled with the same colour.

Although these molecules and RPs have different properties to FAD and Trp, they are readily available and well understood. The isotropic hyperfine coupling constants of Py-$h_{10}^{\bullet+}$, Chr-$h_{12}^{\bullet+}$, 1,3-DCB$^{\bullet-}$, and 1,4-DCB$^{\bullet-}$ have been measured by ESR (table 4.2). The hyperfine coupling constants of the deuterated Chr-$d_{12}^{\bullet+}$ are estimated from the protonated version using the ratio of their gyromagnetic ratios γ_D/γ_H. It is assumed that there is no change in the molecular geometry and the electronic structure of Chr after deuteration.

4.2 Product yield of RYDMR experiments

Previously, simulations of RYDMR experiments have been done using an algorithm called γ–`COMPUTE` (Calculation Over one Modulation Period Using Time Evolution with γ-averaging) by Dr. C. T. Rodgers [124, 137, 143, 144]. The matrix dimensions of the operators increase exponentially with the number of nuclei included in the simulations. The computation time for square matrix multiplication is $O(n^3)$, where n is the matrix size. Therefore the number

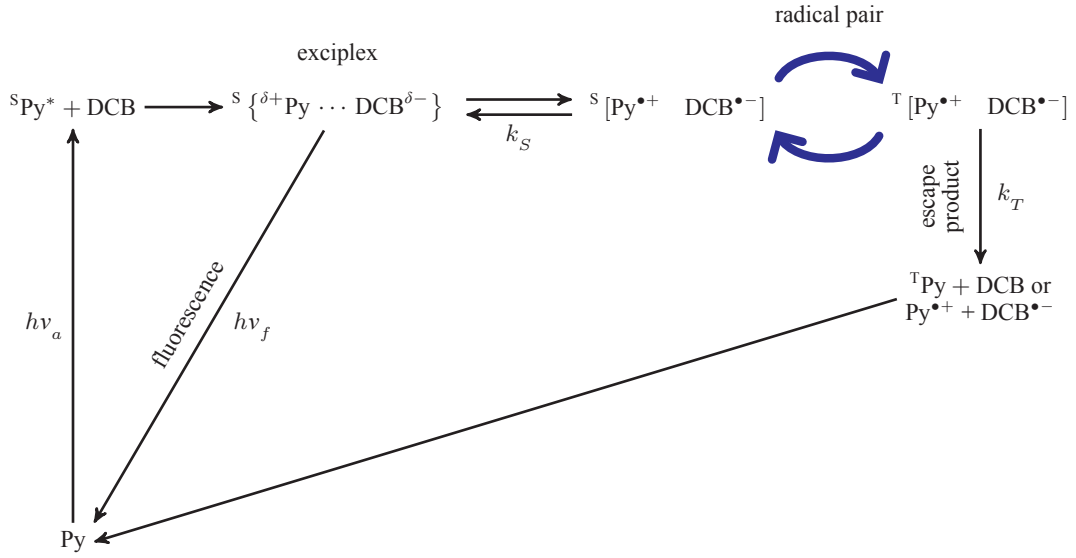

Figure 4.2: The reaction scheme of Py/1,3-DCB is adapted from Batchelor *et al.*'s paper [139]. The blue arrows represent the singlet-triplet interconversion in the RP. The Chr/1,4-DCB RP system is assumed to react via the same pathways. The escape products, ^{T}Py and DCB, are formed via a charge recombination and the free radicals, $Py^{\bullet+}$ and $DCB^{\bullet-}$, are formed via diffusive separation.

Table 4.2: Isotropic hyperfine coupling constants of the radicals involved in the RYDMR experiments. The coupling constants of Chr-$d_{12}^{\bullet+}$ are estimated using $a_D/a_H \approx \gamma_D/\gamma_H = 0.1535$. The locations of the known nuclei can be found in figure 4.2.

Radical	Nuclei	a / mT
Pyrene-$h_{10}^{\bullet+}$ [140]	$4 \times H_a$	0.538
	$4 \times H_b$	0.212
	$2 \times H_c$	0.118
Chrysene-$h_{12}^{\bullet+}$ [141]	$2 \times H$	0.556
	$2 \times H$	0.265
	$2 \times H$	0.181
	$2 \times H$	0.140
	$2 \times H$	0.070
Chrysene-$d_{12}^{\bullet+}$	$2 \times D$	0.085
	$2 \times D$	0.041
	$2 \times D$	0.028
	$2 \times D$	0.022
	$2 \times D$	0.011
1,3-$DCB^{\bullet-}$ [142]	$2 \times H_a$	0.829
	$1 \times H_b$	0.144
	$2 \times N$	0.102
	$1 \times H_c$	0.008
1,4-$DCB^{\bullet-}$ [142]	$4 \times H$	0.159
	$2 \times N$	0.181

of nuclei included in the simulations is limited by computer processing power and computer memory; multi-nuclei simulation requires exponentially more computing power and memory. It is necessary to keep the matrix dimensions as small as possible and this would enable the simulations to be calculated efficiently.

In Wedge *et al.*'s paper [144], the RYDMR simulations of the Py/1,3-DCB RP system included 8 hydrogens in Py and 3 hydrogens in 1,3-DCB. The simulations in Wedge *et al.*'s paper were performed with a single spin-space that contains both radicals. However, based on the assumptions that there are no dipolar or exchange interactions between the two electrons, the spin-space can be separated into two individual radical spin-spaces. Spin Hamiltonians and matrix operators can be constructed exclusively for each of the two radicals. A number of changes to the original γ–`COMPUTE` algorithm are needed to utilise the separate spin-spaces and these changes will be presented in the next section.

The motivation for using separate radical spin-spaces is to reduce computer memory usage and increase the computability of multi-nuclei simulations. The spin-space dimension of the Py/1,3-DCB system is $2048 \times 648 \approx 1.3 \times 10^6$ and the number of the non-zero matrix elements of the spin Hamiltonian is 1.2×10^7. In contrast, the total dimension of the separate spin-spaces of the RP system is only 2696, which is significantly smaller.

The separation of the spin-spaces is analogous to the block diagonalisation of the spin Hamiltonian. Although the result of the spin-space separation and block diagonalisation are the same, the subsequent algorithms for the two types of spin Hamiltonian are different. The separate spin-spaces enable the use of smaller matrices in the algorithm. Even when sparse-matrix algorithms are used, the block diagonalised, single spin-space matrices require longer computational time compared to the separate spin-spaces matrices.

4.2.1 Hamiltonian

The RPs in the RYDMR experiments are under the influence of three magnetic interactions: (i) the isotropic Zeeman interaction with the static magnetic field, B_0, (ii) the isotropic HFIs between the electron and the nuclei within the radical, and (iii) the linearly-polarised oscillating RF field of maximum strength, $B_1^{\max}$ and frequency, ν_{rf}. The spin Hamiltonian that governs the

coherent evolution of the density matrix is

$$\hat{H}(t,\gamma) = \sum_{i,N} a_{i,N}\, \hat{\vec{I}}_{i,N} \cdot \hat{\vec{S}}_N + B_0 \gamma_e \left(\hat{S}_x \cos\theta + \hat{S}_z \sin\theta \right) + B_1^{\max} \gamma_e \hat{S}_x \sin\left(2\pi \nu_{\mathrm{rf}} t + \gamma\right), \tag{4.1}$$

where $N = A, B$, $i =$ integer index for each nucleus.

The first and second terms in equation 4.1 are the operators for the isotropic HFIs and isotropic Zeeman interaction respectively. γ_e is the electron gyromagnetic ratio and θ is the angle between the static field and the RF field. When $\theta = 0$, the static field and the RF field are parallel. The third term in equation 4.1 is the operator for the Zeeman interaction with the RF field. γ is the initial phase of the RF field at $t = 0$.

Separate spin-space spin Hamiltonians, $\hat{H}_A$ and $\hat{H}_B$, of radical A and B are constructed using single-electron spin operators. The dimensions of each of the spin Hamiltonian are $2M_N \times 2M_N$, where M_N is the nuclear spin multiplicity of the radical N. It is assumed that the inter-radical separation is large enough such that dipolar and exchange interactions are negligible.

4.3 γ–COMPUTE

The simulation of a RYDMR experiment is mathematically similar to calculating a spectrum for magic angle spinning (MAS) NMR. MAS is used in solid state NMR and the sample is spun rapidly around an axis that is 54.74° to the direction of the static magnetic field. The spinning at this particular angle averages many of the anisotropic magnetic interactions to isotropic values. Additionally, the sample is subjected to RF pulses, which induce magnetic resonances. The spin systems are under the influence of a periodic spin Hamiltonian in both RYDMR and MAS NMR.

The powdered sample used in MAS contains crystals with random orientation and the magnetic resonance detected is the average of an ensemble of orientations. However, MAS only averages two out of three Euler angles that describe the crystal orientation with respect to the spinning axis. The third Euler angle, γ, in combination with the spinning frequency, affects the magnetic resonance frequency of the spin system [145].

COMPUTE (the predecessor of γ–COMPUTE) is an algorithm that calculates the dynamics of a spin system evolving under a periodic spin Hamiltonian [146] and it was designed to calculate NMR MAS spectra efficiently. It uses time-domain integration of the spin Hamiltonian over one full modulation period but the γ powder angle averaging is done separately.

γ–COMPUTE [147] is an improvement upon the original algorithm and the γ-averaging is integrated in the algorithm. It accumulates the discretised propagators over a full sinusoidal period, and using the symmetries of the periodic spin Hamiltonian, the γ-averaged spin Hamiltonian is calculated. This further reduces the computation time for MAS NMR spectra.

In the RYDMR experiments, RPs are created by continuous irradiation and they are exposed to a continuous RF field. RPs are created at any point during the RF field cycle. The RP spin evolution in a RYDMR simulation must be averaged over the full RF period ($0 \rightarrow 2\pi$). This averaging of the γ phase in continuous RYDMR is analogous to MAS NMR.

4.3.1 Symmetries

The spin Hamiltonian of the system is both time dependent and phase dependent due to the oscillating RF field. However it has two very useful symmetries:

$$\text{(i) periodicity, } \hat{H}(t,\gamma) = \hat{H}\left(t + \frac{m}{\nu_{\text{rf}}}, \gamma\right), \; m = \text{integer, and} \tag{4.2}$$

$$\text{(ii) time-shift, } \hat{H}(t,\gamma) = \hat{H}\left(t + \frac{\gamma}{2\pi\nu_{\text{rf}}}, 0\right). \tag{4.3}$$

The periodicity of the spin Hamiltonian means that the propagation of the spin system from $t = (0 \rightarrow T_p)$ can be divided into m full periods for $t = (0 \rightarrow {}^{m}/_{\nu_{\text{rf}}})$ and a partial period for $t = ({}^{m}/_{\nu_{\text{rf}}} \rightarrow T_p)$. Therefore the full period propagator, $U(0 \rightarrow {}^{1}/_{\nu_{\text{rf}}}, \gamma)$, and the partial period propagator, $U(0 \rightarrow T_p - {}^{m}/_{\nu_{\text{rf}}}, \gamma)$, are needed to calculate the density matrix at any time. The different initial phase is equivalent to a time-shift of the spin Hamiltonian and this allows the γ-averaging to be included in the calculation. Fourier transform of the periodic functions is used at a later stage to improve the efficiency of the SY calculation.

4.3.2 Discretisation

In general, the spin evolution propagator, U, with initial phase γ for a time dependent spin Hamiltonian from $0 \rightarrow t$ is [146]

$$U(0,t;\gamma) = \hat{T}\exp\left[-\mathrm{i}\int_0^t \hat{H}(t',\gamma)\,\mathrm{d}t'\right] \tag{4.4}$$

where $\hat{T}$ is an operator to order the infinitesimal propagators chronologically. The integral in equation 4.4 cannot be evaluated analytically but an approximate solution can be found by discretisation.

The RF time period, $T = 1/\nu_{\mathrm{rf}}$, is discretised into n-steps and the time t_j is discretised to

$$t_j = j\tau = j\cdot\frac{T}{n} = j\cdot\frac{1}{n\,\nu_{\mathrm{rf}}}, \tag{4.5}$$

where j is the time index. The integral in equation 4.4 is approximated to a series of exponential functions,

$$U(0,t;\gamma) \approx e^{-\mathrm{i}\,\tau\hat{H}(t_j,\gamma)}\cdot e^{-\mathrm{i}\,\tau\hat{H}(t_{j-1},\gamma)}\cdot\ldots\cdot e^{-\mathrm{i}\,\tau\hat{H}(t_1,\gamma)} \tag{4.6}$$

and the continuous spin Hamiltonian (eq. 4.1) is approximated to one that is piece-wise constant.

The RF phase, γ, is also discretised into n-steps with index p;

$$\gamma = p\cdot\frac{2\pi}{n}\ ,\ 0 \leqslant p \leqslant n-1. \tag{4.7}$$

A discretised propagator that has a time period of $(0 \rightarrow j\tau)$ and RF phase $\gamma = p\cdot 2\pi/n$ is represented by

$$\Gamma(j,p) = U\big(0, j\tau\,;\ p\cdot 2\pi/n\big) \tag{4.8}$$

and the propagator at the start of the RF period (*i.e.* $p = 0$) is

$$\Gamma(j) = \Gamma(j,0).$$

For a sufficiently large n, $\hat{H}(t,\gamma)$ varies negligibly with each time step τ and the propagator, $\Gamma(j,p)$, is approximated by

$$\Gamma(j,p) = \exp\left[-\mathrm{i}\tau\hat{H}\big(j-1/2,p\big)\right]\times\cdots\times\exp\left[-\mathrm{i}\tau\hat{H}\big(1/2,p\big)\right], \tag{4.9}$$

where the discretised spin Hamiltonian is represented by the indices j and p,

$$\hat{H}(j - 1/2, p) = \hat{H}\Big((j - 1/2)\tau\ ,\ p \cdot 2\pi/n\Big).$$

At $t = 0$, $\Gamma(0, p) = \mathbb{1}$. The discretised $\hat{H}$ is evaluated at the mid-point of each time step in order to reduce error. The order of the exponentials is essential to calculating the chronologically correct propagator. The chronology of equation 4.9 is from right to left.

Propagators with different RF phases can be written as the product of zero RF phase propagators, using the time-shift symmetry of the spin Hamiltonian (eq. 4.3). The propagator with a starting RF phase $\gamma = p \cdot 2\pi/n$ is

$$\Gamma(j, p) = \Gamma(j + p)\Gamma(p)^{\dagger}. \tag{4.10}$$

As the time-shift has shifted the time duration of the propagator forward by $p \cdot 2\pi/n$, an inverse propagator is needed to bring the propagator back to the correct time period. Since the spin Hamiltonian is Hermitian and the propagator is unitary, the inverse propagator is the conjugate transpose of the propagator, $\Gamma(p)^{\dagger}$.

Equation 4.10 can be expanded in terms of full period propagators and partial period propagators;

$$\Gamma(j, p) = \underbrace{\Gamma(j + p \bmod n)}_{\text{extra RF phase}} \times \underbrace{\Gamma(n)^m}_{\text{full period } n \text{ times}} \times \underbrace{\Gamma(p \bmod n)^{\dagger}}_{\text{inverse extra RF phase}}\ , 0 \leqslant p \leqslant n - 1, \tag{4.11}$$

$$\text{where} \quad m = \text{int}\left(\frac{j + p}{n}\right) - \text{int}\left(\frac{p}{n}\right). \tag{4.12}$$

The second term in equation 4.11 is the m full period propagators and the first term is the residue partial period propagator. The three propagators are represented in figure 4.3.

Because of the periodic nature of the propagator, the n propagators only need to be evaluated once, each one from $t = (0 \rightarrow j\tau)$ for one full modulation period. From this set of propagators, a propagator with initial RF phase γ for any discretised time period can be evaluated.

4.3.3 Average spin Hamiltonian

The zero RF phase average spin Hamiltonian, $\bar{H}$, is time independent and it summarises the time dependent spin evolution over one RF period [148]; the propagator for one RF period can be

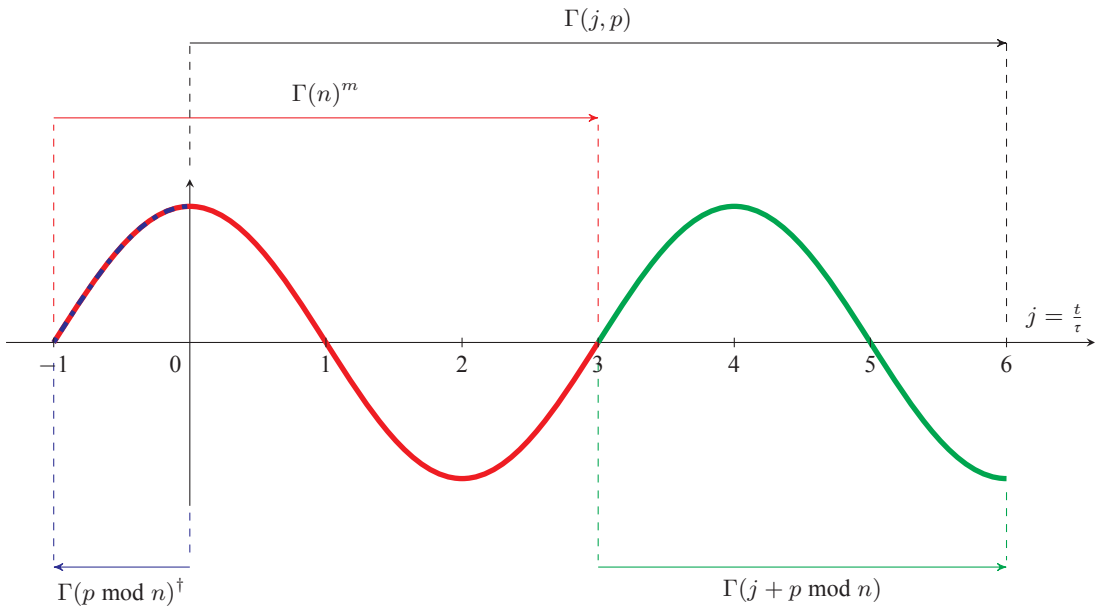

Figure 4.3: The sine curve represents the oscillating spin Hamiltonian. The black arrow represents a propagator $\Gamma(j,p)$. Blue, red, and green arrows represent the different time-discretised propagators used to generate $\Gamma(j,p)$. The chronological order of the three propagators is: blue, red, and green. The discretisation of the RF time period is $n = 4$ and the initial RF phase is $p = 1$.

written as

$$\Gamma(n) = \exp\left[-\mathrm{i}\bar{H}T\right]. \tag{4.13}$$

It is useful to diagonalise $\bar{H}$ using eigenvalue decomposition, so

$$\bar{H} = X\bar{\Omega}X^\dagger \tag{4.14}$$

where X is a unitary matrix containing the eigenvectors of $\bar{H}$ and $\bar{\Omega}$ is a diagonal matrix containing the eigenvalues of $\bar{H}$. The exact calculation of $\bar{H}$ is very difficult[3] as the spin Hamiltonian is time dependent and the spin Hamiltonian at different times do not commute. However the eigenvalues of $\bar{H}$ can be calculated from the discretised full period propagator, $\Gamma(n)$. The $\bar{H}$ eigenvalue transformation can be applied to $\Gamma(n)$ and it becomes

$$X^\dagger\Gamma(n)X = X^\dagger \exp\left[-\mathrm{i}\bar{H}T\right] X = \exp(-\mathrm{i}\bar{\Omega}T) = \Lambda. \tag{4.15}$$

[3] $\bar{H}$ can be calculated using the Campbell-Baker-Hausdorff series [149].

$\bar{H}$ shares the same eigenvectors with $\Gamma(n)$ and the eigenvalues matrix, Λ, is used to calculate $\bar{\Omega}$;

$$e^{-\mathrm{i}\bar{\omega}_i T} = \lambda_i \ , \text{ where } \bar{\omega}_i = \bar{\Omega}_{ii} \ , \ \lambda_i = \Lambda_{ii}, \tag{4.16}$$

$$\Rightarrow \bar{\omega}_i = \mathrm{i}\nu_{\mathrm{rf}} \ln \lambda_i - 2\pi\nu_{\mathrm{rf}} c_i. \tag{4.17}$$

The integer term, c_i, is a correction factor due to the 2π cyclic symmetry of the complex exponential, $\exp(x) = \exp(x + 2\pi\mathrm{i})$. This integer factor can be omitted and the omission is valid if $n\nu_{\mathrm{rf}}$ is bigger than the Nyquist rate (which will be explained in a later section).

A full period propagator with arbitrary starting RF phase can be written as products of zero phase propagators,

$$\begin{aligned}\Gamma(n,p) &= \Gamma(n+p)\Gamma(p)^\dagger = \Gamma(p)\Gamma(n)\Gamma(p)^\dagger \\ &= \Gamma(p)X\Lambda X^\dagger\Gamma(p)^\dagger = X_p\Lambda X_p^\dagger.\end{aligned} \tag{4.18}$$

Since both $\Gamma(p)$ and X are unitary, $X_p = \Gamma(p)X$ is also unitary. The eigenvalues for $\Gamma(n,p)$ are the same as $\Gamma(n)$ and the transition frequencies, $\bar{\omega}_i$, of the zero RF phase average spin Hamiltonian is the same as an average spin Hamiltonian with any other phase.

The description of γ–COMPUTE thus far in sections §4.3.1, §4.3.2, and §4.3.3 is essentially adapted from Rodgers's thesis [124] and the original γ–COMPUTE papers [146, 147]. The mathematics described in the following subsections will be the steps for spin-space separation in γ–COMPUTE.

4.3.4 Singlet probability

The singlet probability in Hilbert space (eq. 1.49) can be found for $t = j\tau$ and $\gamma = p \cdot 2\pi/n$ using the discretised propagator (eq. 4.8);

$$\left\langle \hat{P}^S(j\tau, p\cdot 2\pi/n) \right\rangle = \frac{1}{M}\mathrm{Tr}\left[\Gamma(j,p)\ \hat{P}^S\ \Gamma(j,p)^\dagger\ \hat{P}^S\right]. \tag{4.19}$$

Currently, the spin-space in equation 4.19 contains both radicals A and B. Since it is assumed that there are no interactions between the radicals (eq. 4.1), the spin-space can be separated into two spin-spaces, each containing one radical. The singlet projection operator and the spin

Hamiltonian can be written as Kronecker products of single-radical operators;

$$\hat{P}^S = \frac{1}{4}\mathbb{1} - \sum_q S_{Aq}\, S_{Bq}, \tag{4.20}$$

$$\text{where} \quad S_{Aq}\, S_{Bq} = S_{Aq} \otimes S_{Bq} \text{ and } q = x, y, z, \tag{4.21}$$

$$\hat{H}(j,p) = \hat{H}_A(j,p) \oplus \hat{H}_B(j,p). \tag{4.22}$$

$\oplus$ denotes a Kronecker sum. There are two Kronecker product identities that are useful,

$$(A \otimes B) \cdot (C \otimes D) = AC \otimes BD \text{ and} \tag{4.23}$$

$$e^{A \oplus B} = e^A \otimes e^B. \tag{4.24}$$

A propagator can expressed in terms of separate spin-space spin Hamiltonians and after simplifying the Kronecker products (eq. 4.23 and 4.24), the propagator becomes

$$\begin{aligned}
\Gamma(j,p) &= \exp\left[-\mathrm{i}\tau \left[\hat{H}_A\big(j - 1/2, p\big) \oplus \hat{H}_B\big(j - 1/2, p\big) \right] \right] \times \cdots \\
&\quad \times \exp\left[-\mathrm{i}\tau \left[\hat{H}_A\big(1/2, p\big) \oplus \hat{H}_B\big(1/2, p\big) \right] \right] \\
&= \exp\left[-\mathrm{i}\tau \hat{H}_A\big(j - 1/2, p\big) \right] \otimes \exp\left[-\mathrm{i}\tau \hat{H}_B\big(j - 1/2, p\big) \right] \times \cdots \\
&\quad \times \exp\left[-\mathrm{i}\tau \hat{H}_A\big(1/2, p\big) \right] \otimes \exp\left[-\mathrm{i}\tau \hat{H}_B\big(1/2, p\big) \right] \\
&= \Gamma_A(j,p) \otimes \Gamma_B(j,p)
\end{aligned} \tag{4.25}$$

where $\Gamma_N(j,p)$ is the propagator for radical N.

Equation 4.19 can be expanded using the singlet projection operator (eq. 4.20);

$$\begin{aligned}
\left\langle \hat{P}^S(j,p) \right\rangle &= \frac{1}{4M} \underbrace{\mathrm{Tr}\left[\Gamma(j,p)\, \Gamma(j,p)^\dagger \right]}_{=M} + \sum_{q,r} \Bigg[-\frac{1}{4M} \underbrace{\mathrm{Tr}\left[\Gamma(j,p)\, \Gamma(j,p)^\dagger\, S_{Ar}\, S_{Br} \right]}_{=0} \\
&\quad - \frac{1}{4M} \underbrace{\mathrm{Tr}\left[\Gamma(j,p)\, S_{Aq}\, S_{Bq}\, \Gamma(j,p)^\dagger \right]}_{=0} + \frac{1}{M} \mathrm{Tr}\left[\Gamma(j,p)\, S_{Aq}\, S_{Bq}\, \Gamma(j,p)^\dagger\, S_{Ar}\, S_{Br} \right] \Bigg] \\
\left\langle \hat{P}^S(j,p) \right\rangle &= \frac{1}{4} + \sum_{q,r} \frac{1}{M} \mathrm{Tr}\left[\Gamma(j,p)\, S_{Aq}\, S_{Bq}\, \Gamma(j,p)^\dagger\, S_{Ar}\, S_{Br} \right]
\end{aligned} \tag{4.26}$$

$$\text{where} \quad q, r = x, y, z.$$

Substituting equations 4.21 and 4.25 into equation 4.26 and simplifying the Kronecker products gives

$$\begin{aligned}\left\langle \hat{P}^S(j,p) \right\rangle &= \frac{1}{4} + \frac{1}{M}\sum_{q,r} \mathrm{Tr}\Big[\Gamma_A(j,p) \otimes \Gamma_B(j,p) \cdot S_{Aq} \otimes S_{Bq} \\ &\qquad \cdot \Gamma_A(j,p)^\dagger \otimes \Gamma_B(j,p)^\dagger \cdot S_{Ar} \otimes S_{Br}\Big] \\ &= \frac{1}{4} + \frac{1}{M}\sum_{q,r} \mathrm{Tr}\Big[\Gamma_A(j,p) \cdot S_{Aq} \cdot \Gamma_A(j,p)^\dagger \cdot S_{Ar} \\ &\qquad \otimes \Gamma_B(j,p) \cdot S_{Bq} \cdot \Gamma_B(j,p)^\dagger \cdot S_{Br}\Big] \\ &= \frac{1}{4} + \frac{1}{M}\sum_{q,r} \mathrm{Tr}\Big[\Gamma_A(j,p) \cdot S_{Aq} \cdot \Gamma_A(j,p)^\dagger \cdot S_{Ar}\Big] \\ &\qquad \cdot \mathrm{Tr}\Big[\Gamma_B(j,p) \cdot S_{Bq} \cdot \Gamma_B(j,p)^\dagger \cdot S_{Br}\Big]. \end{aligned} \tag{4.27}$$

The singlet probability is calculated from the product of the matrix traces in the spin-spaces of radical A and B. Now the radical A matrix trace, $T_A(j,p)$, in equation 4.27 is expanded using equations 4.11 and 4.18;

$$\begin{aligned} T_A(j,p) &= \mathrm{Tr}\Big[\Gamma_A(j,p) \cdot S_{Aq} \cdot \Gamma_A(j,p)^\dagger \cdot S_{Ar}\Big] \\ &= \mathrm{Tr}\Big[\Gamma_A(j+p \bmod n)\,[\Gamma_A(n)]^m\,\Gamma_A(p)^\dagger \cdot S_{Aq} \\ &\qquad \cdot \Gamma_A(p)\,[\Gamma_A(n)]^{m\dagger}\,[\Gamma_A(j+p \bmod n)]^\dagger \cdot S_{Ar}\Big] \\ &= \mathrm{Tr}\Big[\Gamma_A(j+p \bmod n) \cdot X_A\,[\Lambda_A]^m\,X_A^\dagger \cdot \Gamma_A(p)^\dagger \cdot S_{Aq} \\ &\qquad \cdot \Gamma_A(p) \cdot X_A\,[\Lambda_A]^{m\dagger}\,X_A^\dagger \cdot [\Gamma_A(j+p \bmod n)]^\dagger \cdot S_{Ar}\Big] \\ &= \mathrm{Tr}\Big[[\Lambda_A]^m \cdot S_{Aq}^T(p) \cdot [\Lambda_A]^{m\dagger} \cdot S_{Ar}^T(p+j)\Big] \end{aligned} \tag{4.28}$$

$$\text{where} \quad S_{Aq}^T(x) = X_A^\dagger \cdot \Gamma_A(x \bmod n)^\dagger \cdot S_{Aq} \cdot \Gamma_A(x \bmod n) \cdot X_A. \tag{4.29}$$

$S_{Aq}^T(x)$ depends on the n propagators, therefore it is a function with period n. This periodicity is very useful and the equation can be Fourier transformed. There are two transformations, $\Gamma_A(x \bmod n)$ and X_A, in equation 4.29. $\Gamma_A(x \bmod n)$ is a similarity transform that shifts the operators to the start of the RF cycle. X_A is a matrix containing the eigenvectors of radical A's average Hamiltonian, $\bar{H}_A$, and it transforms the operators into the eigenbasis of the zero RF phase $\bar{H}_A$.

The matrix trace in equation 4.28 can be written as a sum of the matrix elements, since Λ_A is diagonal, and the matrix trace becomes

$$T_A(j,p) = \sum_{a,b} e^{\mathrm{i}m\bar{\omega}^A_{ab}n\tau} \left[S^T_{Aq}(p)\right]_{ba} \left[S^T_{Ar}(j+p)\right]_{ab} \tag{4.30}$$

$$\text{where} \quad \bar{\omega}^A_{ab} = \bar{\omega}^A_a - \bar{\omega}^A_b \text{ and } \bar{\omega}^A_i = \bar{\Omega}^A_{ii}. \tag{4.31}$$

a and b are the matrix indices for the radical A operators and run from 1 to $2M_A$, which is the dimension of the spin-space of radical A.

The same factorisation (eq. 4.28) and expansion (eq. 4.30) are applicable to the radical B matrix trace, $T_B(j,p)$. The γ-averaging is now an average over the n-discretised RF periods, $p = 0 \rightarrow (n-1)$, to account for the continuous formation of RPs and the singlet probability simplifies to

$$\left\langle\left\langle \hat{P}^S(j) \right\rangle\right\rangle_\gamma = \frac{1}{4} + \frac{1}{Mn} \sum_{p=0}^{n-1} \sum_{q,r} \sum_{a,b} e^{\mathrm{i}m\bar{\omega}^A_{ab}n\tau} \left[S^T_{Aq}(p)\right]_{ba} \left[S^T_{Ar}(j+p)\right]_{ab} \cdot \sum_{c,d} e^{\mathrm{i}m\bar{\omega}^B_{cd}n\tau} \left[S^T_{Bq}(p)\right]_{dc} \left[S^T_{Br}(j+p)\right]_{cd}. \tag{4.32}$$

4.3.5 Discrete cross-correlation

Equation 4.32 is similar to a cross-correlation of two functions with period n and such a cross-correlation can be performed efficiently using Fourier transform. Now equation 4.32 is multiplied by a singular function, $\exp\left[\mathrm{i}\left(\bar{\omega}^A_{ab} + \bar{\omega}^B_{cd}\right)\left(j+p-(j+p)\right)\tau\right]$, and is substituted for the function m (eq. 4.12):

$$\begin{aligned}
\left\langle\left\langle \hat{P}^S(j) \right\rangle\right\rangle_\gamma &= \frac{1}{4} + \frac{1}{Mn} \sum_{p=0}^{n-1} \sum_{q,r} \sum_{a,b,c,d} \exp\left[\mathrm{i}\left(\bar{\omega}^A_{ab} + \bar{\omega}^B_{cd}\right)\left(\mathrm{int}\,(j+p/n) - \mathrm{int}\,(p/n)\right) n\tau\right] \\
&\qquad \cdot \left[S^T_{Aq}(p)\right]_{ba} \left[S^T_{Ar}(j+p)\right]_{ab} \left[S^T_{Bq}(p)\right]_{dc} \left[S^T_{Br}(j+p)\right]_{cd} \\
&\qquad \cdot \exp\left[\mathrm{i}\left(\bar{\omega}^A_{ab} + \bar{\omega}^B_{cd}\right)\left(j+p-(j+p)\right)\tau\right] \\
&= \frac{1}{4} + \frac{1}{Mn} \sum_{p=0}^{n-1} \sum_{q,r} \sum_{a,b,c,d} \exp\left[\mathrm{i}\left(\bar{\omega}^A_{ab} + \bar{\omega}^B_{cd}\right)\left(p - \mathrm{int}\,(p/n)\, n\right)\tau\right] \left[S^T_{Aq}(p)\right]_{ba} \left[S^T_{Bq}(p)\right]_{dc} \\
&\qquad \cdot \exp\left[-\mathrm{i}\left(\bar{\omega}^A_{ab} + \bar{\omega}^B_{cd}\right)\left(j+p - \mathrm{int}\,(j+p/n)\, n\right)\tau\right] \left[S^T_{Ar}(j+p)\right]_{ab} \left[S^T_{Br}(j+p)\right]_{cd} \\
&\qquad \cdot e^{\mathrm{i}\left(\bar{\omega}^A_{ab} + \bar{\omega}^B_{cd}\right)j\tau}
\end{aligned}$$

$$= \frac{1}{4} + \frac{1}{Mn} \sum_{q,r} \sum_{a,b,c,d} \sum_{p=0}^{n-1} \left[g^q_{abcd}(p) \right]^* g^r_{abcd}(j+p) \cdot e^{\mathrm{i}\left(\bar{\omega}^A_{ab} + \bar{\omega}^B_{cd}\right) j\tau} \tag{4.33}$$

$$\text{where} \quad g^q_{abcd}(x) = e^{-\mathrm{i}\left(\bar{\omega}^A_{ab} + \bar{\omega}^B_{cd}\right)(x \bmod n)\tau} \left[S^T_{Aq}(x) \right]_{ab} \left[S^T_{Bq}(x) \right]_{cd}.$$

The function, $g^q_{abcd}(x)$, has a period n and equation 4.33 contains the cross-correlation of the g-function (eq. F.3). Discrete Fourier transform (DFT) is applied to the cross-correlation of the g-functions (eq. F.4),

$$\mathrm{DFT}_\delta \left(\sum_{p=0}^{n-1} \left[g^q_{abcd}(p) \right]^* g^r_{abcd}(j+p) \right) = \left[G^q_{abcd}(\delta) \right]^* G^r_{abcd}(\delta) \tag{4.34}$$

$$\text{where} \quad G^q_{abcd}(\delta) = \mathcal{F}_\delta \left\{ g^q_{abcd}(x) \right\}. \tag{4.35}$$

The inverse DFT (eq. F.2) of equation 4.34 is substituted for the g-functions and equation 4.33 becomes

$$\left\langle \left\langle \hat{P}^S(j) \right\rangle \right\rangle_\gamma = \frac{1}{4} + \frac{1}{Mn} \sum_{q,r} \sum_{a,b,c,d} \frac{1}{n} \sum_{k=0}^{n-1} \left[G^q_{abcd}(\delta) \right]^* G^r_{abcd}(\delta)\, e^{2\pi\mathrm{i} \cdot \frac{j\delta}{n}}\, e^{\mathrm{i}\left(\bar{\omega}^A_{ab} + \bar{\omega}^B_{cd}\right) j\tau}. \tag{4.36}$$

4.3.6 Separate summation

In equation 4.36, the summation over (a, b, c, d) is serial and this method does not use the separate spin-space matrices efficiently. It will improve computation time greatly if equation 4.36 is rearranged so that the summation runs over (a, b) and (c, d) separately. Firstly, the G-functions (eq. 4.35) are expanded, so that

$$\begin{aligned} G^r_{abcd}(\delta) &= \sum_{\alpha=0}^{n-1} g^r_{abcd}(\alpha)\, e^{-\frac{2\pi\mathrm{i}}{n}\delta\alpha} \\ &= \sum_{\alpha=0}^{n-1} e^{-\mathrm{i}\bar{\omega}^A_{ab}(\alpha \bmod n)\tau} \left[S^T_{Ar}(\alpha) \right]_{ab} \cdot e^{-\mathrm{i}\bar{\omega}^B_{cd}(\alpha \bmod n)\tau} \left[S^T_{Br}(\alpha) \right]_{cd} \cdot e^{-\frac{2\pi\mathrm{i}}{n}\delta\alpha} \\ &= \mathcal{F}_\delta \left\{ g^{A,r}_{ab}(\alpha) \cdot g^{B,r}_{cd}(\alpha) \right\} \end{aligned} \tag{4.37}$$

$$\text{where} \quad g^{A,r}_{ab}(\alpha) = e^{-\mathrm{i}\bar{\omega}^A_{ab}(\alpha \bmod n)\tau} \left[S^T_{Ar}(\alpha) \right]_{ab}.$$

The convolution theorem (eq. F.6) can be used to separate the Fourier transform in equation 4.37 into two Fourier transforms (eq. F.7), one for each radical spin-space;

$$G^r_{abcd}(\delta) = \frac{1}{n} \mathcal{F}^{-1} \left\{ \mathcal{F}\{ \mathcal{F}\{ g^{A,r}_{ab}(\alpha) \} \} \cdot \mathcal{F}\{ \mathcal{F}\{ g^{B,r}_{cd}(\alpha) \} \} \right\}$$

$$= \frac{1}{n^2}\sum_{\beta=0}^{n-1}\mathcal{F}_\beta\left\{\ \mathcal{F}\{g_{ab}^{A,r}(\alpha)\}\ \right\}\cdot\mathcal{F}_\beta\left\{\ \mathcal{F}\{g_{cd}^{B,r}(\alpha)\}\ \right\}\cdot e^{\frac{2\pi \mathrm{i}}{n}\beta\delta}. \tag{4.38}$$

Now equation 4.38 is substituted for the two G-functions in equation 4.36 and the terms for the two sets of indices, (a,b) and (c,d), are gathered to give

$$\begin{aligned}
\left\langle\left\langle \hat{P}^S(j)\right\rangle\right\rangle_\gamma &= \frac{1}{4}+\frac{1}{Mn}\sum_{q,r}\sum_{a,b,c,d}\frac{1}{n}\sum_{\delta=0}^{n-1}\left[\frac{1}{n^2}\sum_{\beta=0}^{n-1}\mathcal{F}_\beta\left\{\mathcal{F}\{g_{ab}^{A,q}\}\right\}\mathcal{F}_\beta\left\{\mathcal{F}\{g_{cd}^{B,q}\}\right\}e^{\frac{2\pi \mathrm{i}}{n}\beta\delta}\right]^* \\
&\quad\cdot\frac{1}{n^2}\sum_{\gamma=0}^{n-1}\mathcal{F}_\gamma\left\{\mathcal{F}\{g_{ab}^{A,r}\}\right\}\mathcal{F}_\gamma\left\{\mathcal{F}\{g_{cd}^{B,r}\}\right\}e^{\frac{2\pi \mathrm{i}}{n}\gamma\delta}\cdot e^{\frac{2\pi \mathrm{i}}{n}j\delta}\cdot e^{\mathrm{i}\left(\bar{\omega}_{ab}^{A}+\bar{\omega}_{cd}^{B}\right)j\tau} \\
&= \frac{1}{4}+\frac{1}{Mn^6}\sum_{q,r}\sum_{a,b,c,d}\sum_{\delta,\beta,\gamma=0}^{n-1}\left[\mathcal{F}_\beta\left\{\mathcal{F}\{g_{ab}^{A,q}\}\right\}\right]^*\mathcal{F}_\gamma\left\{\mathcal{F}\{g_{ab}^{A,r}\}\right\}e^{\mathrm{i}\bar{\omega}_{ab}^{A}j\tau} \\
&\quad\cdot\left[\mathcal{F}_\beta\left\{\mathcal{F}\{g_{cd}^{B,q}\}\right\}\right]^*\mathcal{F}_\gamma\left\{\mathcal{F}\{g_{cd}^{B,r}\}\right\}e^{\mathrm{i}\bar{\omega}_{cd}^{B}j\tau}\cdot e^{-\frac{2\pi \mathrm{i}}{n}\beta\delta}\cdot e^{\frac{2\pi \mathrm{i}}{n}\gamma\delta}\cdot e^{\frac{2\pi \mathrm{i}}{n}j\delta} \\
&= \frac{1}{4}+\frac{1}{Mn^6}\sum_{q,r}\sum_{\beta,\gamma=0}^{n-1}\sum_{a,b}\left[\mathcal{F}_\beta\left\{\mathcal{F}\{g_{ab}^{A,q}\}\right\}\right]^*\mathcal{F}_\gamma\left\{\mathcal{F}\{g_{ab}^{A,r}\}\right\}e^{\mathrm{i}\bar{\omega}_{ab}^{A}j\tau} \\
&\quad\cdot\sum_{c,d}\left[\mathcal{F}_\beta\left\{\mathcal{F}\{g_{cd}^{B,q}\}\right\}\right]^*\mathcal{F}_\gamma\left\{\mathcal{F}\{g_{cd}^{B,r}\}\right\}e^{\mathrm{i}\bar{\omega}_{cd}^{B}j\tau}\cdot\sum_{\delta=0}^{n-1}e^{\frac{2\pi \mathrm{i}\delta}{n}(\gamma-\beta+j)}.
\end{aligned} \tag{4.39}$$

The most computatively intensive step in calculating the singlet probability is the summation over the matrix indices of the operators. Equation 4.39 takes advantage of the separate spin-space operators and the summation is performed separately over two sets of matrix indices of the two radical spin-spaces. Equation 4.39 offers significant reduction in computation time and allows the product yield simulation of larger spin systems.

4.3.7 Trigonometric interpolation

The singlet probability is needed at all times to calculate the SY. The singlet probability for the time in between the n-discretised points can be found using interpolation. The inverse DFT can be replaced with a trigonometric interpolant. In trigonometric interpolation, the discretised time index,

$$j = {}^{t}\!/_{\tau} = n\nu_{\mathrm{rf}}t, \tag{4.40}$$

is replaced by the continuous time variable, t. The summation of the DFT index, δ, also changes to $-n/2$ and $n/2-1$ in the interpolation; therefore the continuous singlet probability is

$$\left\langle\left\langle \hat{P}^S(t)\right\rangle\right\rangle_\gamma = \frac{1}{4} + \frac{1}{Mn^6}\sum_{q,r}\sum_{\beta,\gamma=0}^{n-1}\sum_{a,b}\left[\mathcal{F}_\beta\left\{\mathcal{F}\{g_{ab}^{A,q}\}\right\}\right]^*\mathcal{F}_\gamma\left\{\mathcal{F}\{g_{ab}^{A,r}\}\right\}e^{\mathrm{i}\bar{\omega}_{ab}^A t}$$
$$\cdot\sum_{c,d}\left[\mathcal{F}_\beta\left\{\mathcal{F}\{g_{cd}^{B,q}\}\right\}\right]^*\mathcal{F}_\gamma\left\{\mathcal{F}\{g_{cd}^{B,r}\}\right\}e^{\mathrm{i}\bar{\omega}_{cd}^B t}\cdot\sum_{\delta=-n/2}^{n/2-1}e^{\frac{2\pi\mathrm{i}\delta}{n}(\gamma-\beta+n\nu_{\mathrm{rf}}t)}. \quad (4.41)$$

This interpolation does not produce more error as $\left\langle \hat{P}^S(t)\right\rangle$ is band-limited. If n is large enough to satisfy the Nyquist rate (see section §4.3.10), the error is minimised.

4.3.8 Summary

These are the steps to calculate the singlet probability using γ–COMPUTE with separate radical spin-spaces:

1. form the separate spin Hamiltonians for radical A, $\hat{H}_A(t,0)$, and radical B, $\hat{H}_B(t,0)$, using the appropriate spin matrices at times $(\frac{\tau}{2}, \frac{3\tau}{2}, \cdots, \frac{(2n-1)\tau}{2})$;

2. calculate and store the two sets of propagators that correspond to times $(\tau, 2\tau, \cdots, n\tau)$ for radical A and B;

3. diagonalise the full RF period propagators, $\Gamma_A(n)$ and $\Gamma_B(n)$, to obtain the average spin Hamiltonians' eigenvectors, X_A and X_B, and eigenvalues, Λ_A and Λ_B;

4. take the complex logarithm of Λ_A and Λ_B to obtain $\bar{\omega}_a^A$ and $\bar{\omega}_c^B$, then calculate the energy differences, $\bar{\omega}_{ab}^A$ and $\bar{\omega}_{cd}^B$;

5. transform the spin operators S_{Aq} and S_{Bq} with $X_A, \Gamma_A(1,\cdots,n)$ and $X_B, \Gamma_B(1,\cdots,n)$ correspondingly;

6. use $S_{Aq}^T(1,\cdots,n), S_{Bq}^T(1,\cdots,n), \bar{\omega}_{ab}^A, \bar{\omega}_{cd}^B$ to calculate $g_{ab}^{A,q}(1,\cdots,n)$ and $g_{cd}^{B,q}(1,\cdots,n)$;

7. apply DFT twice on $g_{ab}^{A,q}(1,\cdots,n)$ and $g_{cd}^{B,q}(1,\cdots,n)$;

8. evaluate equation 4.41 using the Fourier transformed g-functions to calculate the singlet probability.

The modified algorithm (eq. 4.41), described from sections §4.3.4 to §4.3.7, was compared to the original γ–COMPUTE algorithm described in Rodgers's thesis [124] and both algorithm generated the same results under different input parameters.

4.3.9 Singlet product yield

It is assumed that the reaction is diffusion-controlled and the exponential model (eq. 1.53) is used for the encounter distribution function. Therefore the SY is

$$\left\langle \Phi_S \right\rangle_\gamma = k \int_0^\infty \left\langle \left\langle \hat{P}^S(t) \right\rangle \right\rangle_\gamma \cdot e^{-kt}\, \mathrm{d}t. \tag{4.42}$$

Equation 4.42 can be integrated analytically with γ–COMPUTE [124] but the summation over (a, b, c, d) would not be separable. Therefore equation 4.42 is solved numerically using separate spin-space summation.

The numerical SY can be calculated efficiently using an ODE solver, which usually uses adaptive time-steps. The number of adaptive time steps is about 150 for $k = 10\,\mu\mathrm{s}^{-1}$. It is more efficient to calculate the singlet probability at different time points (around 4500) when carrying out data-fitting, and then iterate (least squares) to find the best-fit rate constant for the experimental data.

4.3.10 Nyquist rate

$n\nu_{\mathrm{rf}}$ is the sampling rate of the periodic spin Hamiltonian and the propagator. It affects the accuracy of the singlet probability calculation (eq. 4.41) in three areas:

(i) the weighted sum over n different initial RF phases,

(ii) the trigonometric interpolation of the discretised time τ to continuous time t, and

(iii) the sampling rate of the g-function.

The weighted sum over the n initial RF phases in equation 4.32 is an approximation for the integral, $\int_0^{2\pi} \left\langle \hat{P}_S(t, \gamma) \right\rangle \mathrm{d}\gamma$. The error of the discretised summation decreases as n increases.

$\left\langle \hat{P}_S(t) \right\rangle$ is band-limited and the minimum sampling rate of a band-limited signal should exceed twice the maximum frequency [150]. This minimum sampling rate is know as the Nyquist

rate. The oscillating terms in $\left\langle \hat{P}_S(t) \right\rangle$ are $\exp[-\mathrm{i}\bar{\omega}^A_{ab}(\alpha \bmod n)\tau]$ and $\exp[-\mathrm{i}\bar{\omega}^B_{cd}(\beta \bmod n)\tau]$ (eq. 4.37), so the Nyquist rate for $\left\langle \hat{P}_S(t) \right\rangle$ is

$$n \geqslant 2\,\frac{\max\left(|\bar{\omega}^N_{ij}|\right)}{2\pi\nu_{\mathrm{rf}}} \tag{4.43}$$

where $N = A, B$ and $ij = ab, cd$. In equation 4.43, the numerator accounts for the maximum spin-evolution frequency of the average spin Hamiltonian and the denominator accounts for the periodicity of the spin Hamiltonian. The optimal n can be found by increasing n gradually until $\left\langle \hat{P}_S(t) \right\rangle$ converges.

4.3.11 Steady state fluorescence and γ–COMPUTE

The RYDMR experiments were done under continuous irradiation and the signals were recorded after the fluorescence had stabilised to a constant value. The ultraviolet lamp and the RF field were switched on at different times, therefore the initial generation of RPs was not synchronised with any particular point during the RF period and the initial RP population was generated under a spin Hamiltonian with an arbitrary γ-phase. In this subsection, it will be shown that the amount of steady state fluorescence in the RYDMR experiment is related to the product yield calculated by γ–COMPUTE and it is necessary to consider the reaction scheme of the RP again.

The reaction scheme of Py/1,3-DCB (figure 4.2) can be approximated by using only the essential species: exciplex (Ex), singlet RP ($^{\mathrm{S}}$RP), triplet RP ($^{\mathrm{T}}$RP), and ground state (GS) (fig. 4.4). The Ex is formed from the GS with a rate constant of k_1 by absorbing a photon at the excitation wavelength and the Ex forms the $^{\mathrm{S}}$RP with a rate constant of k_2. The RP is assumed to recombine in a diffusion-controlled manner with first order rate constant k. The $^{\mathrm{S}}$RP recombines to form the exciplex and the $^{\mathrm{T}}$RP recombines to form the ground state via other intermediates. The Ex fluoresces and relaxes to the GS with rate constant k_f and this fluorescence is measured by the PMT.

During the reaction cycle, $^{\mathrm{S}}$RPs are continuously formed from GS via the Ex, and at the same time $^{\mathrm{S}}$RPs and $^{\mathrm{T}}$RPs recombine to form their products. The time dependence of the Ex is

$$\frac{\mathrm{d}}{\mathrm{d}t}[\mathrm{Ex}] = k_1[\mathrm{GS}] + k[^{\mathrm{S}}\mathrm{RP}] - (k_2 + k_f)[\mathrm{Ex}]. \tag{4.44}$$

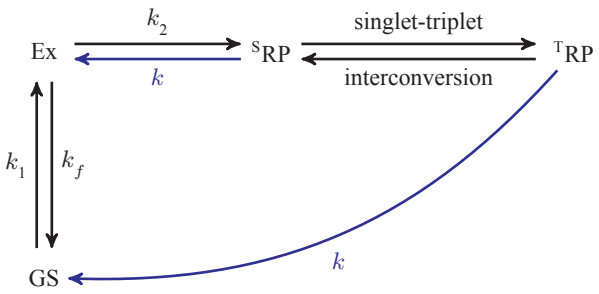

Figure 4.4: A simplified reaction scheme of Py/1,3-DCB (fig. 4.2): GS = ground state, Ex = exciplex, ^{S}RP = singlet RP, ^{T}RP = triplet RP. The diffusion-controlled RP recombination is coloured in blue.

When the fluorescence reaches steady state conditions, the amount of Ex is constant. Therefore

$$\frac{\mathrm{d}}{\mathrm{d}t}[\mathrm{Ex}] = 0$$

$$\Rightarrow \; (k_2 + k_f)[\mathrm{Ex}]_{\mathrm{ss}} = k_1[\mathrm{GS}]_{\mathrm{ss}} + k[^{\mathrm{S}}\mathrm{RP}]_{\mathrm{ss}}$$

$$[\mathrm{Ex}]_{\mathrm{ss}} = \frac{1}{k_2 + k_f}\left(k_1[\mathrm{GS}]_{\mathrm{ss}} + k[^{\mathrm{S}}\mathrm{RP}]_{\mathrm{ss}}\right) \tag{4.45}$$

where $[\ ]_{\mathrm{ss}}$ denotes the steady state concentration of a species. Hence in a continuous irradiation experiment, the amount of fluorescence, I_f, at steady state is

$$I_f = k_f[\mathrm{Ex}]_{\mathrm{ss}} = \frac{k_f}{k_2 + k_f}\left(k_1[\mathrm{GS}]_{\mathrm{ss}} + k[^{\mathrm{S}}\mathrm{RP}]_{\mathrm{ss}}\right). \tag{4.46}$$

It is assumed that once the ^{S}RP reacts to form the Ex, it would immediately fluoresce and form the GS. Therefore the rate of fluorescence is significant larger than the rate of ^{S}RP formation, *i.e.* $k_f \gg k_2$ and equation 4.46 becomes

$$\frac{k_f}{k_2 + k_f} \approx 1$$

$$I_f = k_1[\mathrm{GS}]_{\mathrm{ss}} + k[^{\mathrm{S}}\mathrm{RP}]_{\mathrm{ss}}. \tag{4.47}$$

The fluorescence is detected via a lock-in amplifier (LIA) and the workings of the LIA will be described in a later section (§4.5.1). The main benefit of the LIA is that it only detects fluorescence that is oscillating at the lock-in frequency. Therefore the LIA only detects the magnetic field sensitive part of the fluorescence, *i.e.* $[^{\mathrm{S}}\mathrm{RP}]$, and ignores other part of the fluorescence, $[\mathrm{GS}]_{\mathrm{ss}}$. As a result, equation 4.47 is further simplified to

$$I_f = k[^{\mathrm{S}}\mathrm{RP}]_{\mathrm{ss}}. \tag{4.48}$$

Next, the relationship between $[^{S}\mathrm{RP}]_{ss}$ and $\langle \Phi_S \rangle_\gamma$ is determined.

Steady state singlet RP population

The time dependence of $[^{S}\mathrm{RP}]$ is defined as

$$[^{S}\mathrm{RP}](t,\gamma) = \left\langle \hat{P}^S(t,\gamma) \right\rangle \cdot e^{-kt}. \tag{4.49}$$

Equation 4.49 combines the singlet probability with the exponential part of the exponential model (eq. 1.55). It is clear that RPs generated at different γ-phase have different time-dependence (fig. 4.5a) due to the time-dependent Hamiltonian (eq. 4.1).

The γ–COMPUTE algorithm calculates the time evolution of the singlet probability averaged over all γ-phases (eq. 4.41). In other words, $\left\langle [^{S}\mathrm{RP}] \right\rangle_\gamma (t)$, plotted in figure 4.5b is the average of the time-shifted curves in figure 4.5a over all γ-phases;

$$\left\langle [^{S}\mathrm{RP}] \right\rangle_\gamma (t) = \frac{1}{n} \sum_{\gamma=\gamma_1}^{\gamma_n} [^{S}\mathrm{RP}](t,\gamma) = \left\langle \left\langle \hat{P}^S(t) \right\rangle \right\rangle_\gamma \cdot e^{-kt}. \tag{4.50}$$

Under the continuous irradiation, RPs are generated continuously at different times within the RF period. This is illustrated in figure 4.6a; each dash-dotted line represents ^{S}RPs generated at different times after the ultraviolet lamp is switched on. Then the time evolution of the total ^{S}RP population during the experiment (black line in fig. 4.6a) is the average of the dash-dotted lines at time t. This average-sum of an infinite number of dash-dotted lines is equivalent to an integration over all times. The total ^{S}RP population reaches a steady state oscillation after $t_{ss} = 7/\nu_{RF}$. This oscillation has the same frequency as ν_{RF} and it is dependent on the γ-phase at $t = 0$.

However the oscillation of the total ^{S}RP population (red line in fig. 4.6b) is averaged by the LIA which only detects signals oscillating at the lock-in frequency. Therefore the LIA averages the fluorescence signal over the γ-phases (blue line in fig. 4.6b). Overall the steady state singlet RP population, $[^{S}\mathrm{RP}]_{ss}$, detected by the LIA is

$$[^{S}\mathrm{RP}]_{ss} = \frac{1}{n} \sum_{\gamma=\gamma_1}^{\gamma_n} \int_0^\infty [^{S}\mathrm{RP}](t,\gamma)\, \mathrm{d}t = \int_0^\infty \left\langle \left\langle \hat{P}^S(t) \right\rangle \right\rangle_\gamma \cdot e^{-kt}\, \mathrm{d}t. \tag{4.51}$$

Comparing the SY in figure 4.5b (calculated using eq. 4.41) and the steady state singlet population in figure 4.6b, it is clear that $[^{S}\mathrm{RP}]_{ss}$ is proportional to the SY calculated using the γ–COMPUTE

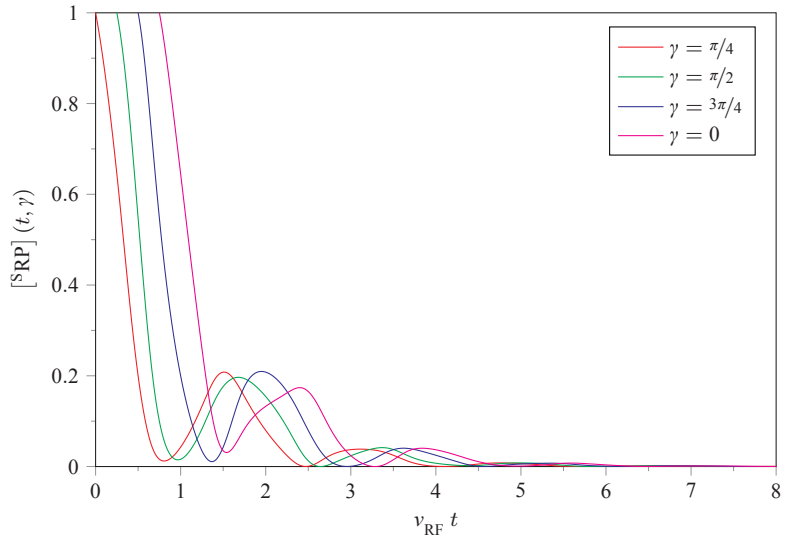

(a). Each curve represents RPs that are generated at different times with respect to the phase, γ, of the RF field. The RF phase at $t = 0$ is $\pi/4$. It is clear that the time evolution of the singlet population is dependent on γ.

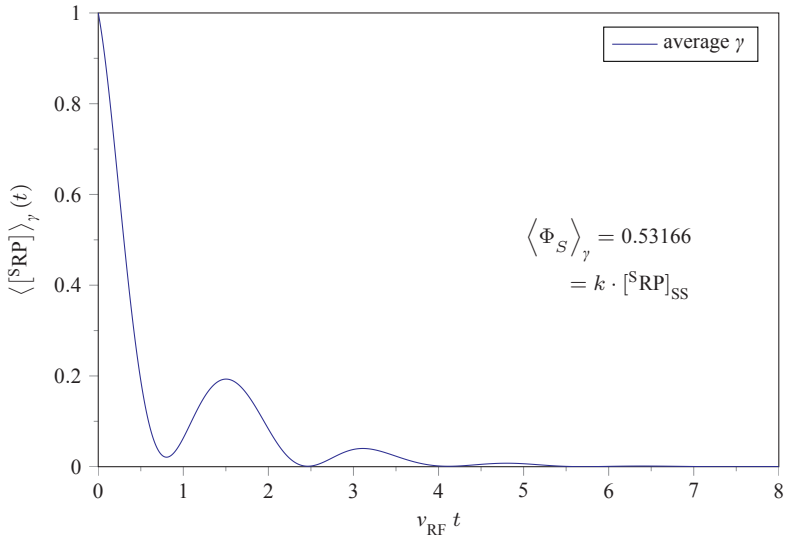

(b). The γ-averaged time evolution of the singlet population is calculated using γ–COMPUTE. The singlet yield is indicated in the graph.

Figure 4.5: The time evolution of the singlet population of a RP containing one spin-$1/2$ nucleus. The parameters of the simulation are as follows: $B_0 = 35\,\mu\text{T}$, $B_1^{\max} = 4\,\text{mT}$, $\nu_{RF} = 1\,\text{MHz}$, $\theta = \pi/4$, and the HFI tensor is $A_{xx} = 5\,\text{mT}$, $A_y = 5\,\text{mT}$ and $A_{zz} = 10\,\text{mT}$. The exponential model is used to account for the RP recombination and the rate constant is $k = 1\,\mu\text{s}^{-1}$.

algorithm (eq. 4.42) and the steady state fluorescence is

$$I_f = k[^{\mathrm{S}}\mathrm{RP}]_{\mathrm{ss}} = \left\langle \Phi_S \right\rangle_\gamma . \tag{4.52}$$

4.4 Equivalent nuclei

The molecules used in the RYDMR experiments, Py, Chr, 1,3-DCB, and 1,4-DCB, all have magnetically equivalent nuclei (fig. 4.1). The equivalence can be used to improve computation times by using matrix block diagonalisation and by increasing the matrix sparsity of the spin operators.

Firstly, a RP with two spin-1/2 nuclei, I_1, I_2, coupled to electron A is considered. The nuclear basis states, $\left| I_1, m_{I_1} \,;\, I_2, m_{I_2} \right\rangle$, for the system are

$$\left| \frac{1}{2}, +\frac{1}{2} \,;\, \frac{1}{2}, +\frac{1}{2} \right\rangle , \left| \frac{1}{2}, +\frac{1}{2} \,;\, \frac{1}{2}, -\frac{1}{2} \right\rangle ,$$
$$\left| \frac{1}{2}, -\frac{1}{2} \,;\, \frac{1}{2}, +\frac{1}{2} \right\rangle , \left| \frac{1}{2}, -\frac{1}{2} \,;\, \frac{1}{2}, -\frac{1}{2} \right\rangle .$$

The HFI Hamiltonian (eq. 1.12) for this system is

$$\hat{H}_{\mathrm{HFI}} = \hat{\vec{S}}_A \cdot \mathbf{A}_1 \cdot \hat{\vec{I}}_1 + \hat{\vec{S}}_A \cdot \mathbf{A}_2 \cdot \hat{\vec{I}}_2 . \tag{4.53}$$

The spin operators in this basis generally are dense matrices.

Since the two nuclei are equivalent and $\mathbf{A}_1 = \mathbf{A}_2 = \mathbf{A}$, equation 4.53 can be factorised into

$$\hat{H}_{\mathrm{HFI}} = \hat{\vec{S}}_A \cdot \mathbf{A} \cdot \left(\hat{\vec{I}}_1 + \hat{\vec{I}}_2 \right) = \hat{\vec{S}}_A \cdot \mathbf{A} \cdot \hat{\vec{I}}_{\mathrm{tot}} . \tag{4.54}$$

$\hat{\vec{I}}_{\mathrm{tot}}$ is the total coupled spin operator. The coupled spin number, I_{tot}, is calculated using the Clebsch-Gordan series [102, 151];

$$I_{\mathrm{tot}} = \left(I_1 + I_2 \right), \left(I_1 + I_2 - 1 \right), \cdots, \left| I_1 - I_2 \right| \tag{4.55}$$

The fully coupled nuclear basis states, $\left| I_1, I_2 \,;\, I_{\mathrm{tot}}, m_{I_{\mathrm{tot}}} \right\rangle$, for two spin-1/2 nuclei are

$$\left| \frac{1}{2}, \frac{1}{2} \,;\, 1, +1 \right\rangle , \left| \frac{1}{2}, \frac{1}{2} \,;\, 1, 0 \right\rangle ,$$
$$\left| \frac{1}{2}, \frac{1}{2} \,;\, 1, -1 \right\rangle , \left| \frac{1}{2}, \frac{1}{2} \,;\, 0, 0 \right\rangle .$$

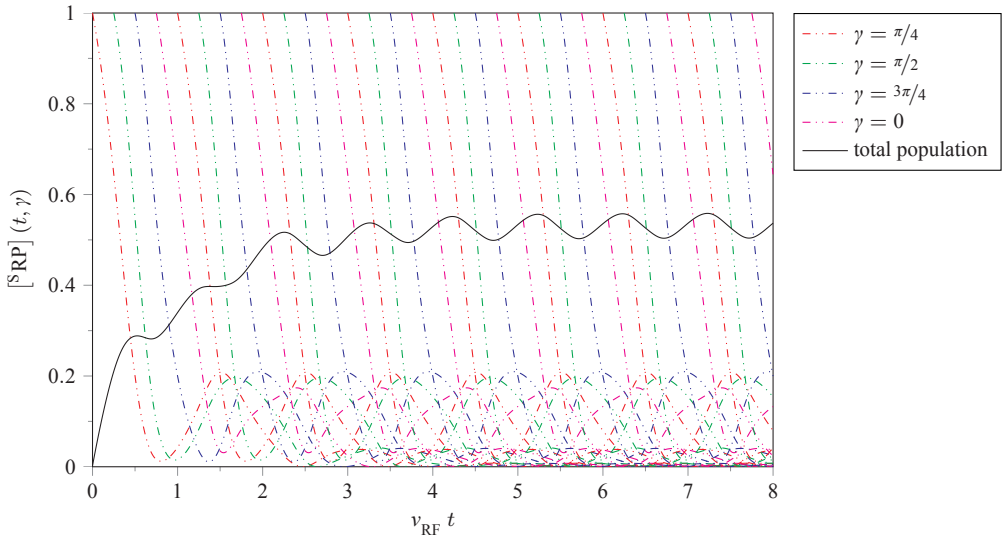

(a). The dash-dotted lines represent fractions of RP population generated at different times. The rate of RP generation is assumed to be the same at all times. The ultraviolet lamp is switched on at $t = 0$ and the RF phase at $t = 0$ is $\gamma = \pi/4$. The black solid line represents the total RP population calculated from the average of all the dash-dotted lines. This total RP population is directly proportional to the amount of fluorescence. The period of the oscillating total population is the same as the period of the RF field.

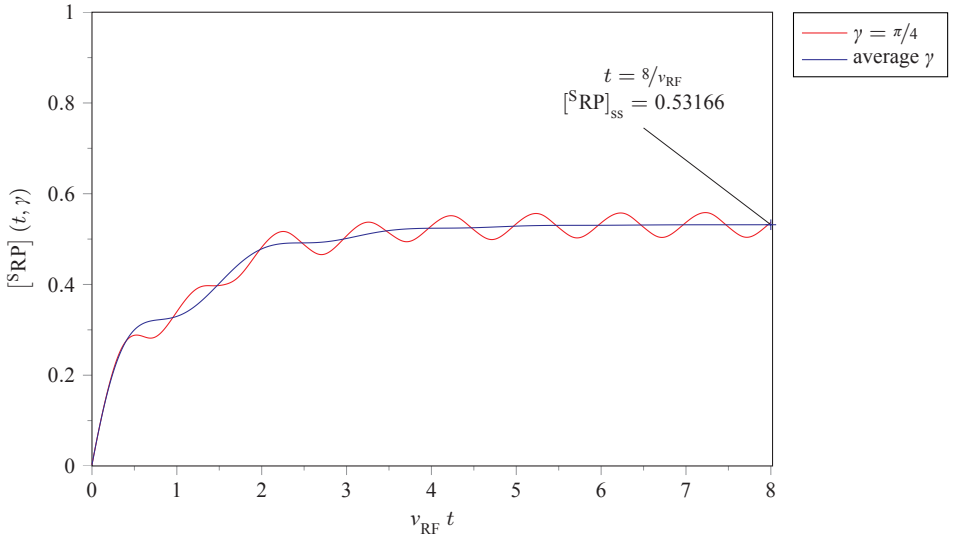

(b). The red line and the blue line represent the total RP populations. The time evolution of the red line has an initial RF-phase of $\pi/4$ and the blue line is averaged over all initial RF-phases. The oscillations of the red line are at ν_{RF} which is different to the frequency of the lock-in amplifier's phase-sensitive detection. Therefore the lock-in amplifier averages the oscillations in the RP population (red line) to a smooth curve (blue line). The steady state RP population is reached after $t = 7/\nu_{\mathrm{RF}}$ and it is the same as the SY calculated using γ–`COMPUTE` (4.5b).

Figure 4.6: The time evolution of the singlet population of a RP containing one spin-1/2 nucleus. The parameters of the simulation are as follows: $B_0 = 35\,\mu\mathrm{T}$, $B_1^{\max} = 4\,\mathrm{mT}$, $\nu_{\mathrm{RF}} = 1\,\mathrm{MHz}$, $\theta = \pi/4$, and the HFI tensor is $A_{xx} = 5\,\mathrm{mT}$, $A_y = 5\,\mathrm{mT}$ and $A_{zz} = 10\,\mathrm{mT}$. The exponential model is used to account for the RP recombination and the rate constant is $k = 1\,\mu\mathrm{s}^{-1}$.

In the fully coupled basis, the spin operators have block diagonal structure because $I_{\text{tot}} = 1$ and $I_{\text{tot}} = 0$ do not interact with each other and do not have cross-terms in the matrix. The block diagonal structure is preserved for all matrix operations: addition, multiplication, and matrix exponential.

In a radical that has more than two equivalent nuclei, each equivalent nuclear spin is coupled serially,

$$\hat{\vec{I}}_1 + \hat{\vec{I}}_2 = \hat{\vec{I}}_{12}\ ,\ \hat{\vec{I}}_{12} + \hat{\vec{I}}_3 = \hat{\vec{I}}_{123}\ ,\ \hat{\vec{I}}_{123} + \hat{\vec{I}}_4 = \hat{\vec{I}}_{1234}\ ,\ \text{etc.} \tag{4.56}$$

For example, the coupled spin numbers of a three spin-1/2 nuclei radical are

$$I_{12} = \{1, 0\}\ ,\ I_{\text{tot}} = \left\{\frac{3}{2}, \frac{1}{2}, \frac{1}{2}\right\}. \tag{4.57}$$

When there are multiple equivalent I_{tot} in the coupled basis, only one spin block is needed in the spin operators and a suitable multiple is applied to the matrix trace of that particular I_{tot} block in the singlet probability calculation. This will prevent the redundant repeated computation of the same I_{tot} blocks.

The transformation from the uncoupled basis to the fully coupled basis is effectively an analytical matrix block diagonalisation of the spin operators. Using spin operators in the fully coupled basis has substantial advantages, specifically lower memory usage and faster computation time, both due to the reduction in matrix size. Further reduction in computation time is found by removing zero elements in the g-functions and the corresponding elements in $\bar{\omega}^A_{ab}$ before the matrix index summations in equation 4.41. This removes operations that result in zero which do not contribute to the singlet probability. The matrix size reduction of the Py/1,3-DCB RP is summarised in table 4.3.

4.5 RYDMR and modulation

The oscillating field effect in a RYDMR experiment is small in comparison to the background noise, so the experiment was done with B_1 amplitude modulation. Phase-sensitive detection then removed all signals that oscillated at frequencies other than that at the modulation frequency. When B_1 field modulation was used, the PMT only recorded the changes in the fluorescence signals due to the B_1 field effect and this improved the signal-to-noise ratio.

Table 4.3: The matrix size of the g-functions for a pyrene radical and a 1,3-DCB radical. In the programmed algorithm of the calculation of the singlet probability, the cross multiplication for the indices, (q, r) and (β, γ) is also performed at the same time as the dot product of the g-functions. So the actual number of matrix elements involved in the matrix multiplications of one computation is $3n$ times the number stated in the table.

	Pyrene		1,3-DCB	
	Spin-space dimension	Matrix elements	Spin-space dimension	Matrix elements
Original	2048	$\sim 4.2 \times 10^6$	288	$\sim 8.3 \times 10^4$
Symmetry factorisation	648	$\sim 4.2 \times 10^5$	no reduction in size	
% reduction		90%	but increases sparsity	
Remove zero elements		$\sim 1.8 \times 10^5$		$\sim 5.2 \times 10^4$
% reduction		96%		37.5%

4.5.1 Lock-in amplifier

The lock-in amplifier (LIA) generates a reference cosine signal at an audio frequency (AF) of 331 Hz. A purpose-built mixing box then combines the RF signal from a RF generator with the AF signal from the LIA and the resultant signal generates the oscillating B_1 field in a set of small Helmholtz coils, separate from the B_0 field coils. The spin Hamiltonian (eq. 4.1) excludes the AF B_1 field as the AF component oscillates on a time scale that is significantly slower than the lifetime of the RP.

The fluorescence of the exciplex is detected by the PMT and the signal is fed to the LIA. The LIA then mixes the PMT signal with a cosine function oscillating at the reference AF. Then the mixed signal is passed through a low-pass filter, in which all oscillating components, except the signal that oscillates at the reference AF, are removed. The amplitude of the filtered signal is converted to a direct current and is recorded by a computer over the duration of the experiment.

4.5.2 Modulation pattern

The time dependence of the modulated B_1 field is

$$B_1(t) = B_1^{\max} \sin\left(2\pi\nu_{\text{rf}} t\right)\left(1 - M_d \sin^2\left(\pi\nu_{\text{af}} t\right)\right) \tag{4.58}$$

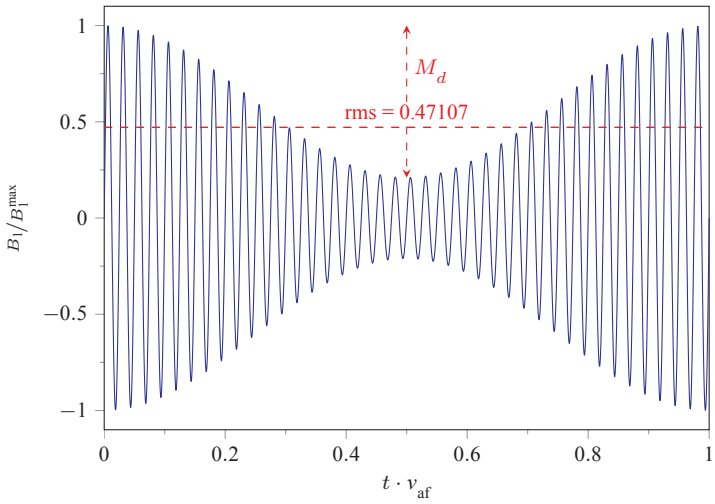

Figure 4.7: B_1 field strength over one AF cycle is generated by the Helmholtz coils according to equation 4.58. M_d is the fractional modulation depth and $M_d = 0.79$ in this figure. The root mean square (rms) strength is often the quoted value of the B_1 field. The ratio ν_{rf}/ν_{af} is 40 in this figure.

where ν_{rf} is the RF, ν_{af} is the AF, B_1^{max} is the peak strength of the B_1 field, and M_d is the fractional modulation depth (fig. 4.7).

The B_1 field strength is often quoted as the root mean square (rms) value, B_1^{rms}, of the oscillating field and it is

$$B_1^{rms} = B_1^{max} \cdot \sqrt{\nu_{rf} \int_0^{1/\nu_{rf}} B_1(t)^2 \, dt} \tag{4.59}$$

When γ–`COMPUTE` is used to simulate RYDMR experiments, B_1^{max} should be used, instead of B_1^{rms}. The rms value includes the amplitude change of the AF modulation which is only relevant in the fluorescence detection and the modulation period is too long to cause any resonance effect.

4.5.3 Lock-in amplifier output

There is no reason to expect the SY to be exponential, trigonometric, or any other function, with respect to B_1. Therefore the SY, at a particular B_0 field, can be written as a polynomial in terms of B_1. The simplest polynomial is a linear equation;

$$\langle \Phi_S \rangle_\gamma \left(B_1(t) \right) = c_1 B_1(t) + c_0, \tag{4.60}$$

where $c_0 = \Phi_S(0) = \Phi_S^0$. The time dependence of the B_1 field (eq. 4.58) can be simplified because the RF component has negligible effect on the LIA, so

$$B_1(t) = B_1^{\max}\left(1 - M_d \sin^2(\pi \nu_{\text{af}} t)\right). \tag{4.61}$$

The output signal, s, of the LIA is the integral of the product of equation 4.60 and the reference cosine function generated by the LIA over one modulation period;

$$s(B_1^{\max}) = \alpha \int_0^{1/\nu_{\text{af}}} \Phi_S(B_1(t))\, \cos(2\pi \nu_{\text{af}} t)\, \mathrm{d}t. \tag{4.62}$$

α is a constant that converts the exciplex fluorescence (eq. 4.52) to the output of the PMT. The output signal is simplified by substituting equations 4.60 and 4.61, and evaluating the integral gives

$$s = \frac{\alpha B_1^{\max} M_d}{4\nu_{\text{af}}}\, c_1. \tag{4.63}$$

Equation 4.63 is substituted for c_1 in equation 4.60 and the output signal in terms of the SY is

$$s = \frac{\alpha M_d}{4\nu_{\text{af}}}\left(\left\langle \Phi_S \right\rangle_\gamma \left(B_1^{\max}\right) - \Phi_S^0\right) = \frac{\alpha M_d}{4\nu_{\text{af}}}\, \Phi_S^{\text{diff}}(B_1^{\max}) \tag{4.64}$$

If the B_1 dependence of the SY is approximated by a linear function, the output signal is also linear in B_1.

However, it is clear from the experimental data (fig. 4.12) that the signal is not linear in B_1. Therefore the SY should be written as a higher order polynomial. For example, the SY can be written as a 4$^{\text{th}}$ order polynomial,

$$\left\langle \Phi_S \right\rangle_\gamma \left(B_1(t)\right) = c_4 B_1^4 + c_3 B_1^3 + c_2 B_1^2 + c_1 B_1 + \Phi_S^0. \tag{4.65}$$

The signal is calculated by evaluating the integral (eq 4.62) again with the 4$^{\text{th}}$ order polynomial (eq. 4.65), and the signal is

$$\begin{aligned} s = \alpha \Bigg[& c_4\, \frac{B_1^{\max 4}}{2}\left(-\frac{7M_d^4}{16} + \frac{15M_d^3}{8} - 3M_d^2 + 2M_d\right) + c_3\, \frac{B_1^{\max 3}}{4}\left(\frac{15M_d^3}{16} - 3M_d^2 + 3M_d\right) \\ & + c_2\, \frac{B_1^{\max 2}}{2}\left(M_d + \frac{M_d^2}{2}\right) + c_1\, \frac{B_1^{\max} M_d}{4}\Bigg]. \end{aligned} \tag{4.66}$$

The constant α now contains a multiple of the factor $1/\nu_{\text{af}}$. $1/\nu_{\text{af}}$ corresponds to a data collection time of one modulation period. A multiple of $1/\nu_{\text{af}}$ is needed if the data collection period is a

multiple of the modulation period. The signal should be recorded over a long period, relative to the modulation frequency, so that the error of not integrating over a multiple of the full modulation period is minimised.

The SY polynomial (eq. 4.65) and the signal function (eq. 4.66) have the same polynomial order, and the output signal function goes through the origin. The output signal polynomial can be written as

$$s = \kappa_4 B_1^{\max 4} + \kappa_3 B_1^{\max 3} + \kappa_2 B_1^{\max 2} + \kappa_1 B_1^{\max}. \tag{4.67}$$

Polynomial interpolation is applied to the experimental data to calculate the signal polynomial coefficients, $\{\kappa_4, \cdots, \kappa_1\}$. These coefficients, $\{\kappa_4, \cdots, \kappa_1\}$, are related to the SY polynomial coefficients, $\{c_4, \cdots, c_1\}$. For example, c_1 is related to κ_1 by

$$\alpha\, c_1 = \kappa_1 \frac{4}{M_d}.$$

Therefore $\{c_4, \cdots, c_1\}$ can be obtained from $\{\kappa_4, \cdots, \kappa_1\}$ and the demodulated output signal, s_{demod}, is calculated by using

$$\begin{aligned} s_{\text{demod}} &= \alpha \left(c_4 B_1^4 + c_3 B_1^3 + c_2 B_1^2 + c_1 B_1 \right) \\ &= \alpha\, \Phi_S^{\text{diff}} \end{aligned} \tag{4.68}$$

4.6 Interpolation of lock-in amplifier data

The RYDMR-B_0 spectrum of the Py-d_{10}/1,3-DCB system at various B_1 fields was recorded by Dr. C. Wedge (fig. 4.8). The modulation depth, M_d, was 88.5% and the modulation AF, ν_{af}, was 331 Hz. The data points were collected for 20 different B_1 strengths at different B_0 strengths.

Polynomial interpolation is essentially solving a set of simultaneous equations and the number of equations depends on the order of the polynomial, the number of data points, and other additional constraints. The polynomial coefficients can be found either directly using the inverse of the Vandermonde matrix or by iteration using least squares. A Vandermonde matrix is a $m \times n$ matrix containing the terms of a geometric progression in each row,

$$W = \begin{bmatrix} 1 & x_1 & x_1^2 & \cdots & x_1^{n-1} \\ \vdots & \vdots & \vdots & \ddots & \vdots \\ 1 & x_m & x_m^2 & \cdots & x_m^{n-1} \end{bmatrix}. \tag{4.69}$$

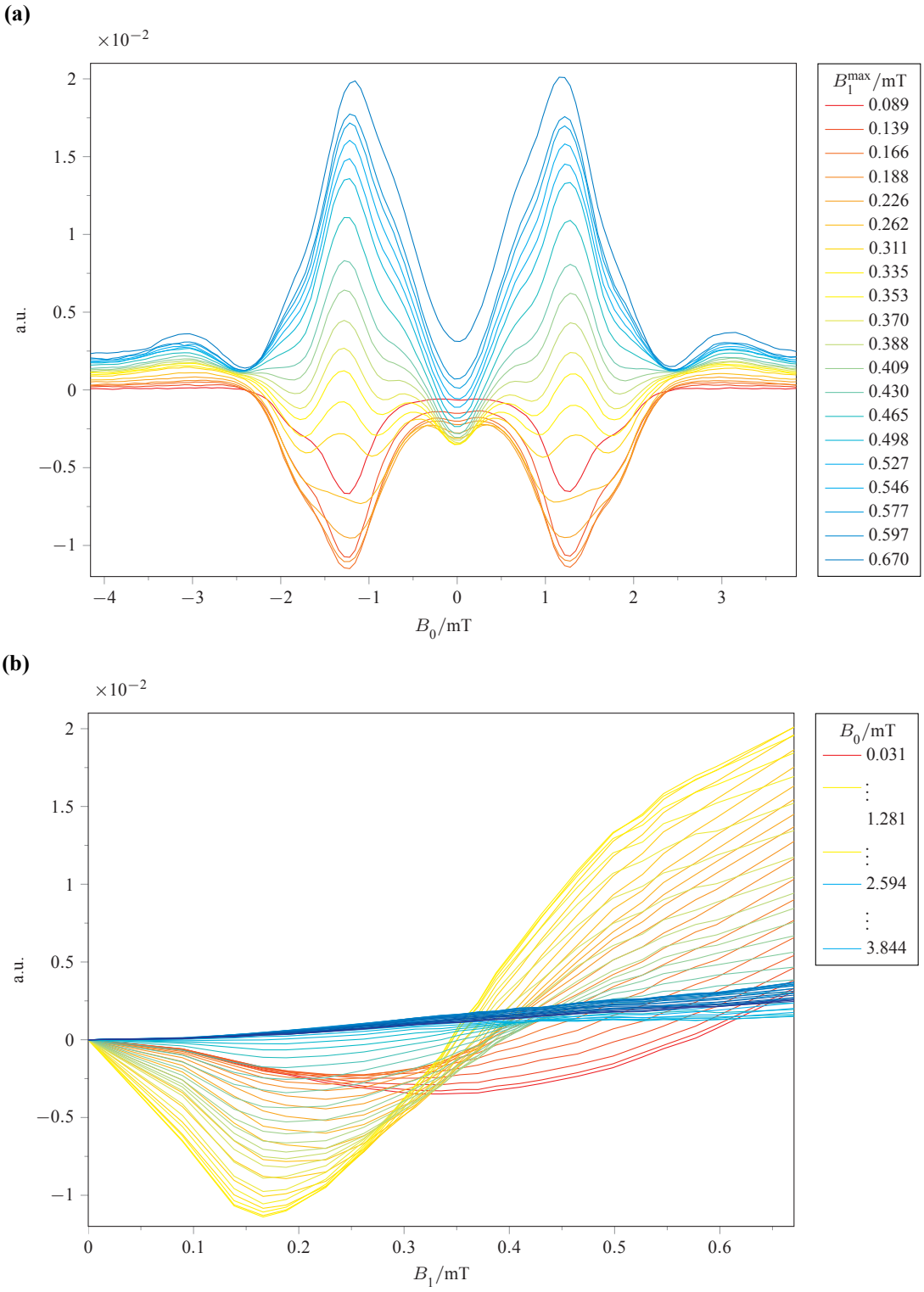

Figure 4.8: (a) is the RYDMR-B_0 spectrum of the Py-d_{10}/1,3-DCB system and the strength of the RF field, $B_1^{\max}$, is given in the legend. (b) is the RYDMR-B_1 spectrum of the Py-d_{10}/1,3-DCB system and the strength of the B_0 field is given in the legend. This legend is truncated for simplicity and the colour code varies gradually from red-yellow-cyan-blue. These are the raw data collected from the PMT.

The least squares method is used to find the polynomial coefficients in this chapter and the mathematics of the least squares interpolation will be discussed in detail in the next section.

There are two constraints to solving for the polynomial coefficients of the data; the first constraint is that the signal function has to go through the origin $(0, 0)$, and the second constraint is that the gradient at $(0, 0)$ is zero which ensures that the function is well-behaved at the origin. The second constraint implies that $c_1 = 0$.

The relative error (r.e.) of the polynomial interpolation of the data, s_{int}, is defined as the squared 2-norm error divided by the rms value of the signal, s^{rms}, at a particular B_0;

$$\text{r.e.} = \frac{\|s^{\text{int}} - s\|_2^2}{s^{\text{rms}}}. \tag{4.70}$$

There are 21 data points (including the origin) for each B_0 field and it is possible to use a 20^{th} order polynomial. However, it is inappropriate to use the 20^{th} order Vandermonde matrix because a polynomial interpolation of the maximum order is ill-conditioned. The resultant polynomial is ill-behaved, particularly at the edges of the interval.

The data is fitted to a 14^{th} order polynomial, s_{14}^{int}, to illustrate the unsuitability of a high order polynomial interpolation. All the data points are reproduced accurately (as the relative error is small, see fig. 4.9a) but the function is ill-behaved at the edges (fig. 4.9b). These oscillations at the edges of the interval is known as the Runge's phenomenon.

The higher order polynomial coefficients are larger than the original data by several orders of magnitude (fig. 4.10a). The large coefficients and the oscillation at the edges are indicative of an ill-conditioned problem. s_{demod} is dominated by the large coefficients and is meaningless due to the numerical errors (fig. 4.10b).

Generally, a lower order polynomial can be used to interpolate the data and then a well-behaved s_{demod} can be calculated. The problem is well-conditioned if the order n is chosen to be $n < 2\sqrt{m}$, where m is the number of data points [152]. The optimal order using this formula is $n < 9.17$ for 21 data points, and the data can be interpolated with a 10^{th} order polynomial with additional gradient constraints at the edges of the B_1 interval. The 10^{th} order polynomial fit, s_{10}^{int}, and Φ_S^{diff} (fig. 4.11a) are both well-behaved. However the coefficients, $\{c_5, \cdots, c_{10}\}$ (fig. 4.11b), are still large relative to the original data.

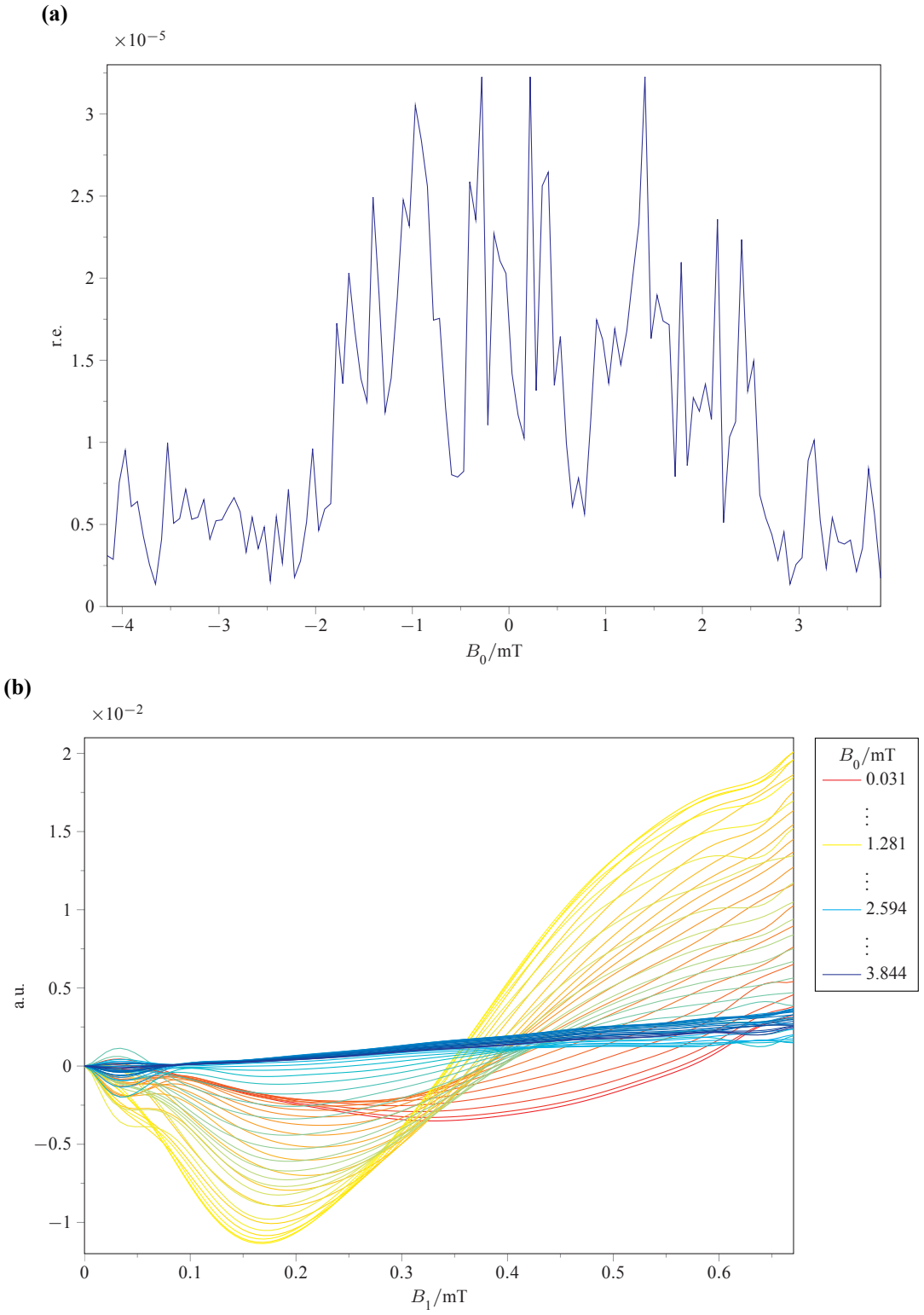

Figure 4.9: (a) is the relative error of s_{14}^{int} and (b) is s_{14}^{int}, which is the 14^{th} order polynomial interpolation of the original data (fig. 4.8a), plotted as a function of B_1. Comparing the figures 4.8b and 4.9b, it is clear that the high order polynomial interpolation suffers from the Runge's phenomenon at the edges, left of $B_1 = 0.1$ and right of $B_1 = 0.6$. The legend is truncated for simplicity and the colour code varies gradually from red-yellow-cyan-blue.

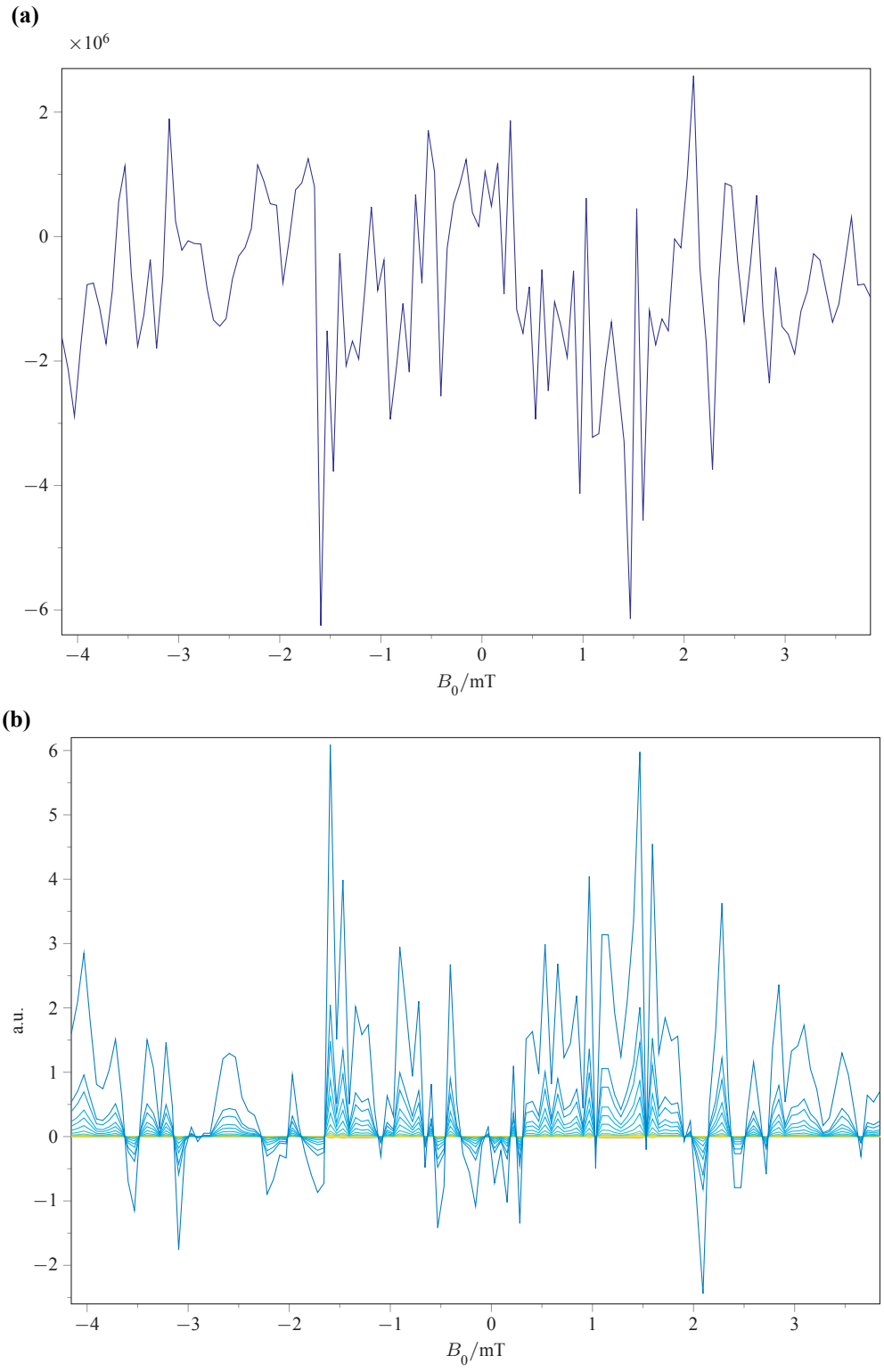

Figure 4.10: (a) is the magnitude of the coefficient, κ_{14}, of the 14$^{\text{th}}$ order polynomial interpolation s_{14}^{int} of the original data (fig. 4.8). The magnitude of the high order coefficients are significant bigger than the original data. (b) is the demodulated output signal, s_{demod}, for the various B_1 field strengths, which is calculated from the coefficients $\{c_1, \cdots, c_{14}\}$ and it is dominated by numerical error.

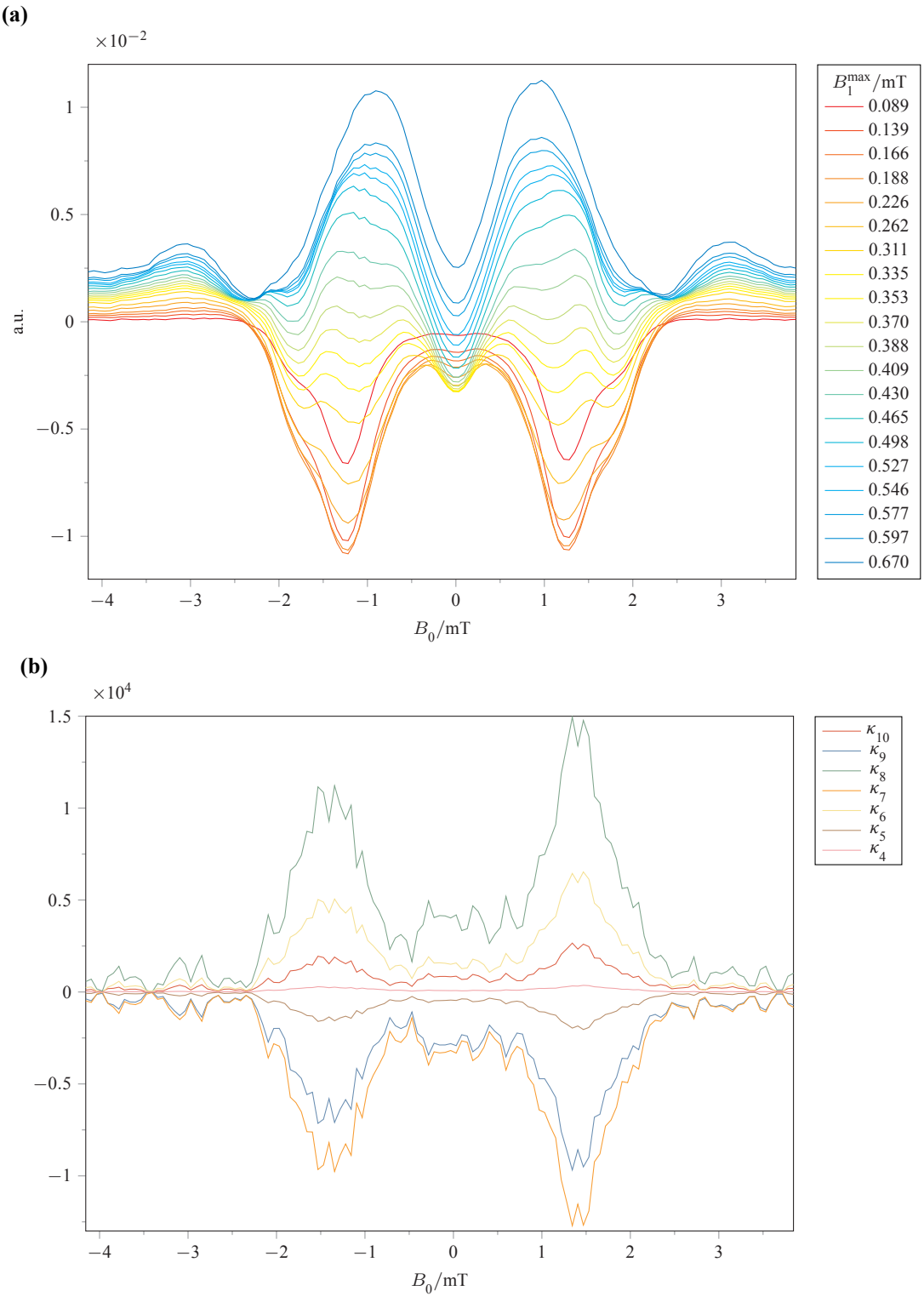

Figure 4.11: (a) is the demodulated output signal, s_{demod}, calculated from the 10^{th} order polynomial interpolation, s_{10}^{int}, coefficients of the original data (fig. 4.8). At the resonance field, $B_0 = 1.28\,\text{mT}$, the B_1 dependence is different to the experimental data in figure 4.8. (b) is the magnitude of the coefficients, $\{\kappa_{10}, \cdots, \kappa_4\}$, of s_{10}^{int}. Their magnitudes are still large compared to the original data.

4.6.1 B_1^0 and spin-locking

If the weak B_1 RF field is on resonance, it reconnects the singlet and $T_{\pm 1}$ triplet states, which are separated by the static B_0 field, and promotes singlet-triplet interconversion. Therefore the RYDMR SY is reduced compared to the SY under a static field only. However, as the strength of the B_1 field increases, the energy levels of $T_{\pm 1}$ triplet states start to move out of resonance with the S state. This effectively locks the RP in the singlet state (for a singlet-born RP) and this is known as spin-locking [153].

B_1^0 is the B_1 field strength where $\Phi_S^{\text{diff}}(B_1^0) = 0$, *i.e.* the RF field has no effect on the SY, and it marks the point where the spin-locking effect starts to dominate the RYDMR effect. B_1^0 can be found by calculating the roots to the Φ_S^{diff} polynomial.

Different order polynomials give different B_1^0 values, all of which are different from the B_1^0 obtained from the original data (fig. 4.12). Therefore obtaining B_1^0 from the raw, modulated experimental data is sometimes erroneous because it assumes that the SY dependence on B_1 is linear.

4.6.2 Improving polynomial interpolation

One way to minimise the error in high order polynomial interpolation is to collect data at specific points in the interpolation interval, such as points near the roots of the signal function and the zero gradients of the signal function.

More data points near the edge of the interval should minimise the Runge's phenomenon. Alternatively, the Chebyshev polynomial can be used to minimise the Runge's phenomenon but data have to be collected at the Chebyshev nodes.

It is difficult to control the power delivered to the small Helmholtz coils that generate the B_1 field and produce the desired field strengths precisely. It is better to perform polynomial interpolation with Tikhonov regularisation.

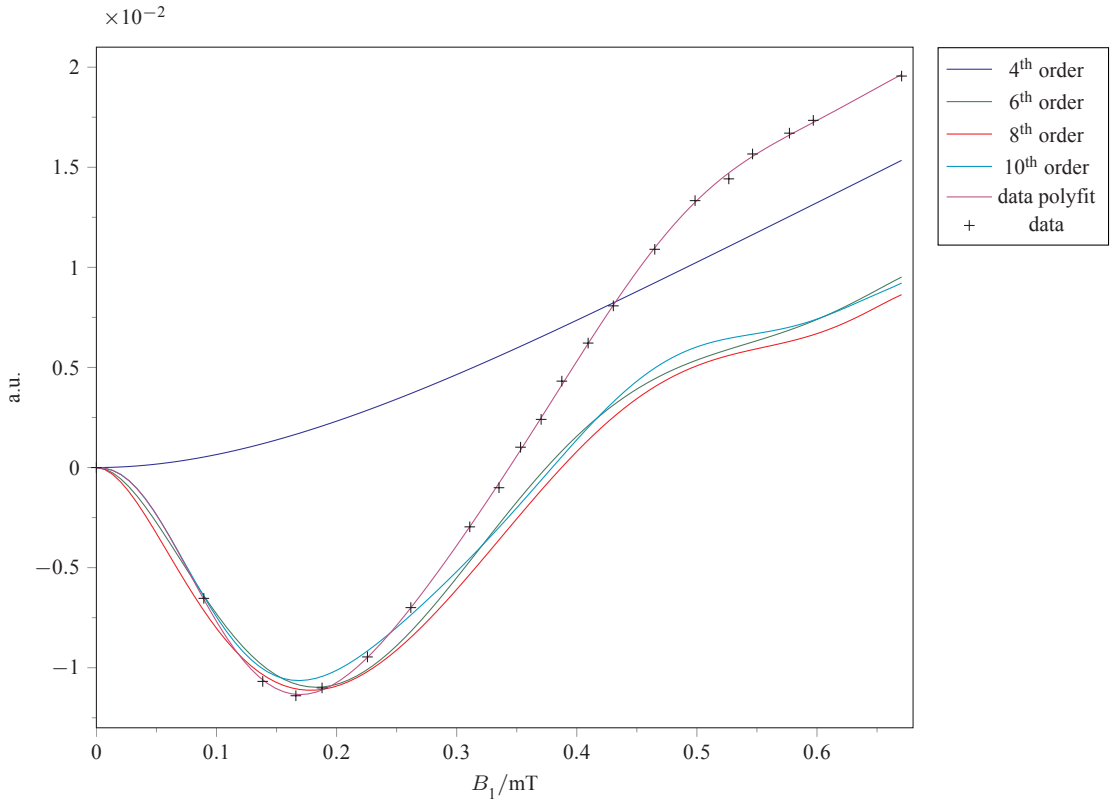

Figure 4.12: s_{demod} of various orders of polynomial interpolation is displayed as a function of B_1. B_1^0 is obtained by finding the roots to the polynomial function. —— is the polynomial fit to the original data (+), so $s = s_{\text{demod}}$ if $\Phi_S(B_1)$ is assumed to be linear. The roots for the different lines are: —— 0, —— 0.3747, —— 0.3874, —— 0.3795, —— 0.3438.

4.7 Polynomial interpolation with Tikhonov regularisation

When a small perturbation, such as experimental noise, is applied to an ill-posed problem, it usually produces a meaningless answer with a large range in magnitude and a large number of sign changes. The Runge's phenomenon occurs when high order polynomial interpolation is used because the Vandermonde matrix is ill-conditioned.

The condition of a high order polynomial interpolation can be improved by using Tikhonov regularisation. First, one needs to understand the link between an ill-conditioned Vandermonde matrix and an unreliable solution.

4.7.1 Ill-conditioned matrix

The coefficients of a polynomial that goes through or is near to multiple data points are calculated by solving a linear least squares problem involving the Vandermonde matrix (eq. 4.69);

$$\min \|Wx - d\|_2^2 \tag{4.71}$$

where x is the column vector containing the polynomial coefficients and d is the column vector containing the data points.

Equation 4.71 can be solved by the singular value decomposition (SVD) of W, which is

$$W = U\Sigma V^\dagger. \tag{4.72}$$

If W is a $m \times n$ matrix, then U is a $m \times m$ unitary matrix with m orthonormal column vectors, Σ is a $m \times n$ diagonal matrix with real non-negative singular values on the main diagonal, and V is a $n \times n$ unitary matrix with n orthonormal column vectors;

$$U = \begin{bmatrix} & & & \\ u_1 & u_2 & \cdots & u_m \\ & & & \end{bmatrix}, \Sigma = \begin{bmatrix} \sigma_1 & 0 & \cdots & 0 \\ 0 & \sigma_2 & \cdots & 0 \\ \vdots & \vdots & \ddots & \vdots \\ 0 & 0 & \cdots & \sigma_n \\ 0 & 0 & \cdots & 0 \end{bmatrix}, V = \begin{bmatrix} & & & \\ v_1 & v_2 & \cdots & v_n \\ & & & \end{bmatrix}. \tag{4.73}$$

If $m \geqslant n$, the SVD can be written as

$$W = \sum_{i=1}^{n} u_i \, \sigma_i \, v_i^\dagger. \tag{4.74}$$

The singular values are listed in Σ in descending order, such that

$$\sigma_1 \geqslant \sigma_2 \geqslant \cdots \geqslant \sigma_n \geqslant 0. \tag{4.75}$$

The condition number of W is σ_1/σ_n. The condition number of an ill-conditioned matrix is large and generally the elements in u_i and v_i that correspond to the smaller singular values have more sign changes.

The pseudoinverse of W is

$$W^+ = V\Sigma^+ U^\dagger \tag{4.76}$$

where $^+$ denotes the pseudoinverse. Σ^+ is formed by replacing all non-zero elements with their reciprocals and transposing the resulting matrix. The linear least squares problem of equation 4.71 can be solved by using the pseudoinverse, W^+, such that the least squares solution is

$$x_{\text{lsq}} = \sum_{i=1}^{n} \frac{u_i^\dagger d}{\sigma_i} v_i. \tag{4.77}$$

In a well-posed problem, the discrete Picard condition

$$\sum_{i=1}^{n} \left| \frac{u_i^\dagger d}{\sigma_i} \right|^2 < \infty \tag{4.78}$$

is satisfied and the dot product, $u_i^\dagger d$, in the numerator of the summation series decays to zero faster than σ_i [154]. In an ill-posed problem, the dot product decays slower than the singular value and x_{lsq} is dominated by the smallest σ_i in the sum. Therefore the solution has many sign changes and is large in magnitude.

4.7.2 Tikhonov regularisation

The condition of the Vandermonde matrix can be improved by incorporating more information about the solution into the matrix, then a useful and stable solution can be calculated from the improved problem. This is known as regularisation.

Different types of additional information of the solution can be included in the problem. The most popular is the Tikhonov regularisation which minimises the 2-norm of some function of the solution. When Tikhonov regularisation is added, the least squares problem becomes

$$\min \left(\|Wx - d\|_2^2 + \|\lambda L x\|_2^2 \right) \tag{4.79}$$

where L is a suitably chosen Tikhonov matrix and λ is the regularisation parameter. The second term describes the prior knowledge of the solution. The explicit regularised solution is

$$x_{\text{reg}} = \left(W^T W + \lambda^2 L^T L \right)^{-1} W^T d. \tag{4.80}$$

Usually L is chosen to be the identity matrix and in this case, the second term in equation 4.79 minimises the 2-norm of the solution and constraints the magnitude of the solution. A difference operator for the first or second derivative can also be used as the Tikhonov matrix to ensure the smoothness of the solution.

λ controls the weight given to the minimisation of the second term in equation 4.79. A large λ biases the minimisation towards the second term but the solution may not be related to the data as the regularised problem is shifted too far away from the original problem. However, a small λ may be too small to regularise the problem sufficiently and to improve the condition of the problem. The optimal value of λ can be found using the L-curve, which depends on the problem, the data, and the Tikhonov matrix.

4.7.3 L-curve

The L-curve is a way of displaying information about the regularised solution as a function of the regularisation parameter [155, 156]. The L-curve is a function of the regularisation norm, $\|\lambda Lx\|_2^2$, against the residual norm, $\|Wx - d\|_2^2$ and it is named after the shape of the function in a plot. The L-curve is used to determine the optimal compromise between the minimisation of the two norms.

Different values of λ give different values of the residual norm and regularisation norm (fig. 4.13). A small λ equals to a small amount of regularisation. In this case, the residual norm is small and the regularisation norm is big; this corresponds to the top of the L-curve. When λ is big and there is too much regularisation, the residual norm is big and the regularisation norm is small. The large λ values are located on the right of the L-curve.

In between of the two extremes, the optimal λ can be found at the corner of the L-curve and gives a reasonable balance between finding a solution that fits the data and a solution close to the prior knowledge.

4.7.4 Maximum order polynomial interpolation

The original Py-d_{10}/1,3-DCB RYDMR data can be interpolated with a 20^{th} order polynomial with Tikhonov regularisation. The value of the regularisation parameter is determined using a L-curve for each B_0 field, because the L-curve of different B_0 fields are different. The Φ_S^{diff} is reconstructed from the polynomial coefficients (fig. 4.14a).

The s_{demod} calculated using regularisation and maximum order of polynomial (fig. 4.14a) has more clearly defined peaks for strong B_1 fields at the resonance B_0 field ($\sim 1.28\,\text{mT}$) com-

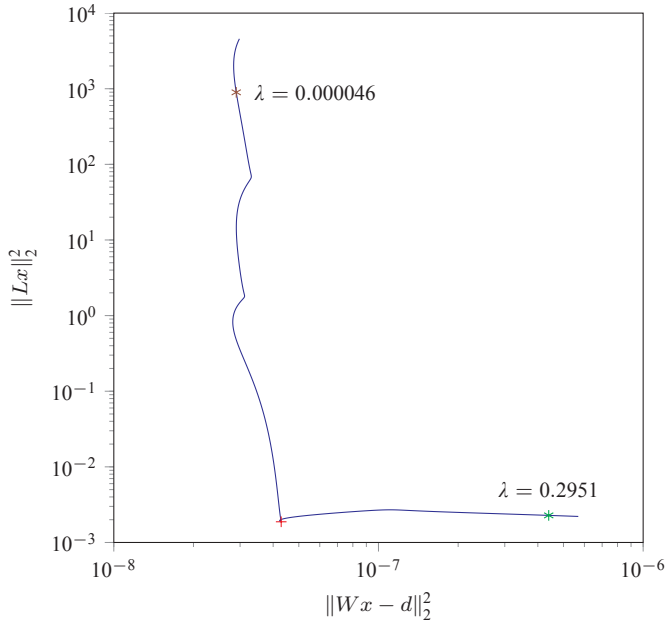

Figure 4.13: The L-curve of the 21$^{\text{th}}$ order polynomial interpolation of the Py-d$_{10}$/1,3-DCB system at $B_0 = 3.03125\,\text{mT}$. The large λ values (*) are located on the right of the L-curve and the small λ values (*) are located at the top of the L-curve. The corner of the L-curve is indicated with +, where $\lambda = 0.00955$.

pared to the s_{demod} calculated without regularisation and 10$^{\text{th}}$ order polynomial (fig. 4.11a). Furthermore, the polynomial coefficients (fig. 4.14b) are significantly smaller and are similar in magnitude to the original data.

4.7.5 Importance of demodulation

Using the demodulated signal (fig. 4.14a), the effect of the B_1-amplitude-modulated detection can be examined. $\Phi_S(B_1)$ functions of different static fields are polynomials of different degrees. $\Phi_S(B_1)$ near the Larmor resonance frequency ($B_0 = 1.28\,\text{mT}$) is approximately a cubic function (fig. 4.15a) whereas $\Phi_S(B_1)$ at higher static field strengths, $B_0 > 3\,\text{mT}$, is more or less linear (fig. 4.15b).

The modulated signal detected at a particular B_0 field by the PMT can be calculated by substituting the demodulated signal function, which is proportional to Φ_S^{diff}, into equation 4.62 and evaluating the subsequent integral numerically. The effects of different modulation depth can be seen in figure 4.15. The shape of the output signal as a function of B_1 is dependent on the modulation depth when $B_0 < 2\,\text{mT}$ (fig. 4.15a). All the output signals of different

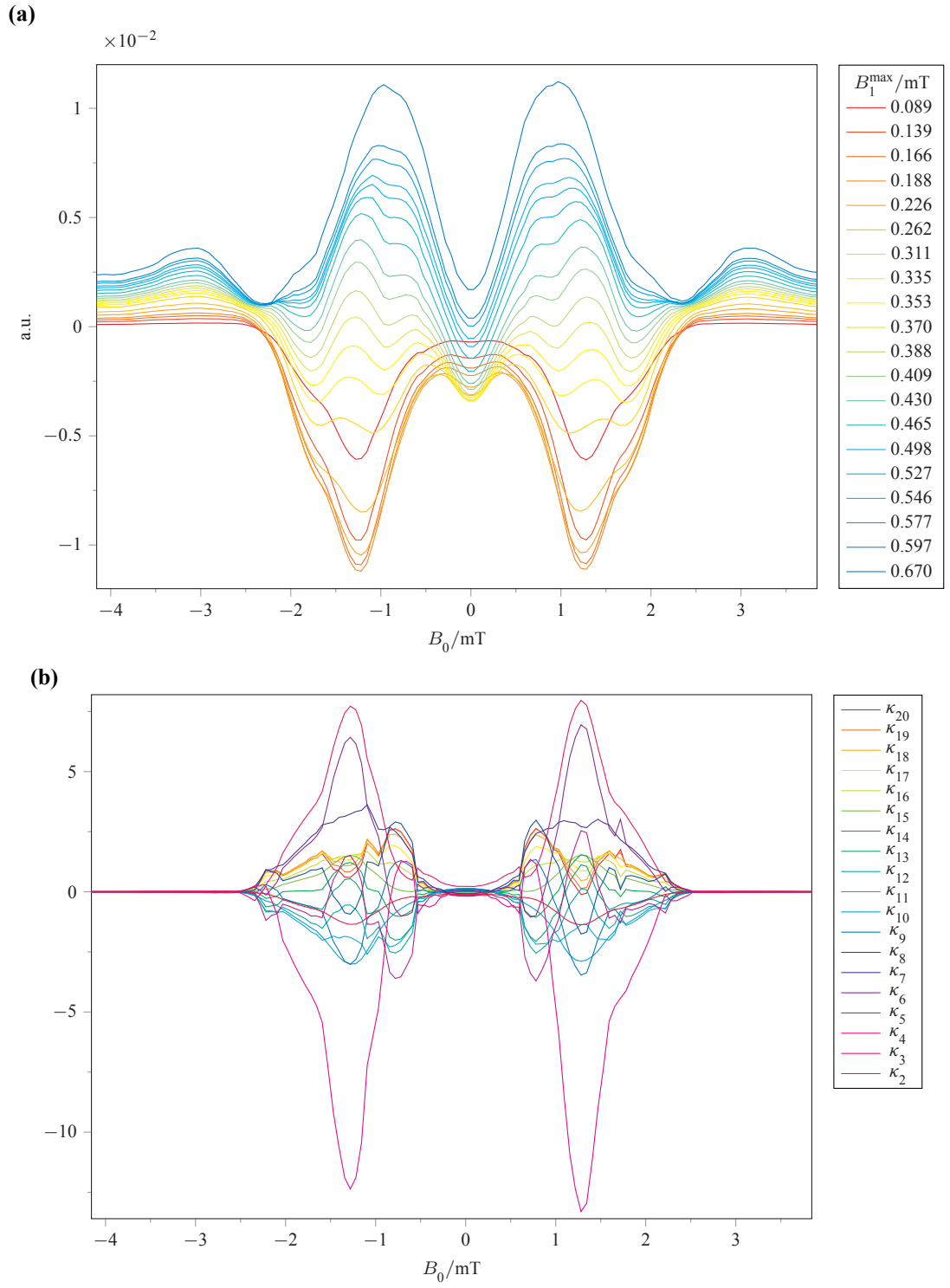

Figure 4.14: 20$^{\text{th}}$ order polynomial interpolation with Tikhonov regularisation of the Py-d$_{10}$/1,3-DCB RYDMR data. (a) is s_{demod} calculated from the 20 polynomial coefficients. λ for each B_0 field is different due to the different L-curve at each field. (b) gives the magnitudes of the polynomial coefficients, $\{\kappa_{20}, \cdots, \kappa_2\}$. Compared to figure 4.11b, the coefficients are significantly smaller and closer to the magnitude of the original data (fig. 4.8).

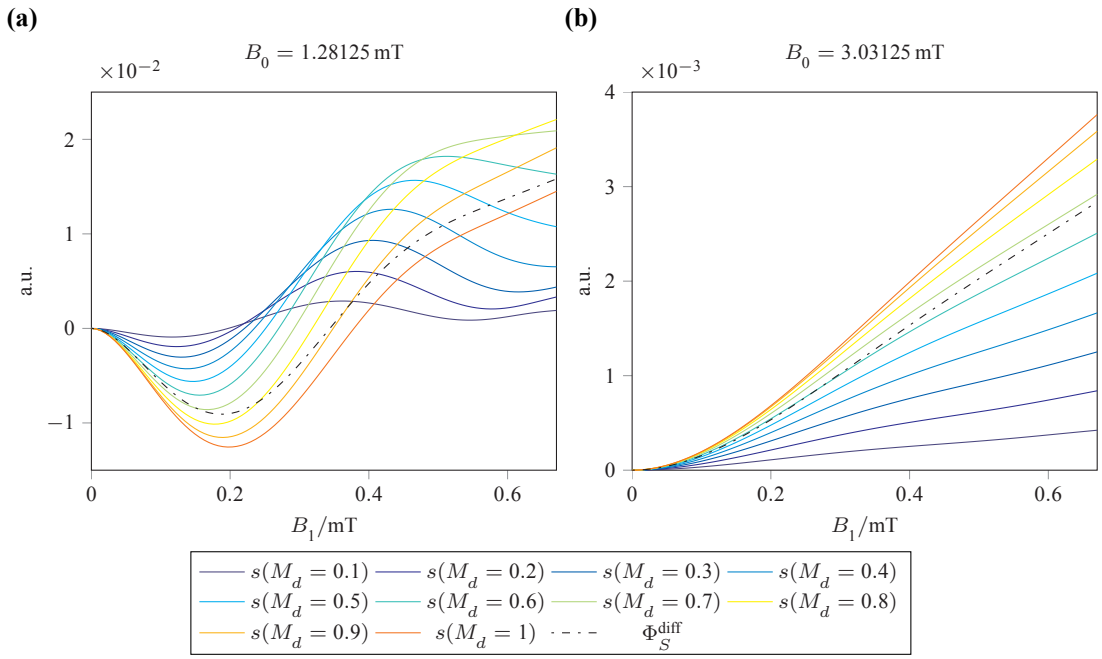

Figure 4.15: Comparison of the modulated signals of different modulation depths, M_d, detected by the PMT to the true Φ_S^{diff} function. ·-·-· in (a) and (b) are the demodulated signal, s_{demod} $(= \alpha\Phi_S^{\mathrm{diff}})$, of the RYDMR spectrum of Py-d_{10}/1,3-DCB at $B_0 = 1.28125\,\mathrm{mT}$ and $B_0 = 3.03125\,\mathrm{mT}$, taken from figure 4.14a.

modulation depths are different to the true Φ_S^{diff} function. However, when $B_0 > 3\,\mathrm{mT}$, the output signal function is a simpler near-linear function for all modulation depths (fig. 4.15b). As the modulation depth is increased, only the gradient of s increases but the shape of the function remains unchanged.

Therefore demodulation is essential in the analysis of B_1-amplitude-modulated RYDMR experiments. $\Phi_S(B_1)$ should not be approximated as linear, especially when B_0 is close to the Larmor resonance field ($\sim 1.28\,\mathrm{mT}$). Assuming equation 4.60 to be valid across the full range of B_0 field strengths, and hence assuming the raw spectrum to be proportional to Φ_S^{diff}, will lead to erroneous interpretations as the detected signal is dependent on the modulation depth.

4.8 Rotary-RYDMR simulation

Rotary-RYDMR investigates the effects of changing the angle, θ, between the static and oscillating magnetic fields. The reactants are in solution and all anisotropic interactions are averaged, therefore only the signals from $0^\circ - 90^\circ$ are unique as the fluorescence signals from the four

quadrants of a circle are mirror images of each other. The fluorescence signals of two systems, Py-h_{10}/1,3-DCB and Chr-d_{12}/1,4-DCB, were recorded by K.-A. Ferguson.

Koptyug's vector model [153] of spin-locking approximates the two electron spins in a RP as vector quantities. In the rotating frame of one of the spins, the model predicts that an oscillating magnetic field applied parallel to the static field does not produce a spin-locking effect. This is because the precession axis of the second electron spin remains the same if the RF field is applied parallel to the static field. The model also predicts that there is no RYDMR effect for a RF field that is parallel to the static field. In reality, a RF field that is parallel to the static field produces a weaker RYDMR effect than a perpendicular RF field of the same strength. The vector model fails to describe the effect of a parallel RF field.

4.8.1 Data fitting

γ–`COMPUTE` is used for the simulation and the number of discretised steps, n, of the RF period is 32 for all simulations. The exponential model (eq. 1.53) is used for the simulation, and the singlet and triplet reaction rates are the same.

The B_1 modulation depth used was 88% and 7 B_1^{max} field strengths were used. With only 7 B_1 points, a large λ is needed for the polynomial interpolation to obtain the 7$^{\text{th}}$ order polynomial interpolation, s_7^{int}, and the demodulated output signal, s_{demod} (fig. 4.17 and 4.18).

s_{demod} is fitted to Φ_S^{diff} with two parameters, k, the first order reaction rate constant, and α, the scaling factor. Both k and α are assumed to be independent to the B_1 field strength, and the two values are found via a global fit of all the data at the different B_0 and B_1 field strengths.

The signals recorded for the stronger B_1 fields are bigger in magnitude than the low field signals, and this skews the global least squares search to a better fit at high B_1 fields. So an averaged squared-difference, χ^2, is used in the least squares search; the difference, σ, and the average difference-squared, χ^2, are defined as

$$\sigma(B_1) = \sum_{B_0} \sum_{\theta} \left[\alpha \, \Phi_S^{\text{diff}}\left(\theta, B_0, B_1\right) - s_{\text{demod}}\left(\theta, B_0, B_1\right) \right], \tag{4.81}$$

$$\chi^2 = \frac{1}{7} \sum_{B_1} \left[\frac{\sigma_{\text{rms}}\left(B_1\right)}{s_{\text{demod}}^{\text{rms}}\left(B_1\right)} \right]^2 . \tag{4.82}$$

4.8.2 Py-h_{10}/1,3-DCB

All 16 magnetic nuclei in Py and 1,3-DCB (table 4.2) are used in the simulation of the Py-h_{10}/1,3-DCB RYDMR-B_0 spectra (fig. 4.18). The positions of the RYDMR troughs for both B_1 fields that are parallel and perpendicular to the B_0 field occur at similar B_0 fields, around 1.28 mT, in both the experimental data (fig. 4.16) and the simulations (fig. 4.18).

The RYDMR troughs gradually disappear due to the spin-locking effect as the 90° B_1 field strength is increased. The RYDMR troughs for 0° B_1 fields gradually increase in magnitude and shift to the right of the resonance field strength, $B_0 = 1.28$ mT, as the B_1 field strength increases. No spin-locking effect is observed for any parallel B_1 fields.

The agreement between the γ–COMPUTE simulations and the s_{demod} is poor. For the 0° B_1 fields, the simulations (fig. 4.19c) underestimate the signals at $B_0 < 1$ mT and $B_1 > 0.3$ mT compared to the demodulated signal (fig. 4.19a) but the magnitude of the RYDMR effect around the resonance field strength, $B_0 \approx 1.8$ mT, in the simulations is similar to the data.

For the 90° B_1 fields, the simulations (fig. 4.19d) also underestimate the signals at $B_0 <$ 1 mT and $B_1 > 0.3$ mT compared to the data (fig. 4.19b) and the spin-locking effect, which occurs at $B_1 > 0.6$ mT near the resonance field strength $B_0 \approx 1$ mT, in the simulation compares very poorly to the data.

γ–COMPUTE simulations of the Py-h_{10}/1,3-DCB system were calculated previously in Wedge's thesis [157]. The old simulations included four hydrogens on the Py and two hydrogens on the 1,3-DCB which is about 40% of the magnetic nuclei of the RP system. However, the old simulations (fig. 4.19e and 4.19f) are very similar to the new simulations (fig. 4.19c and 4.19d), which includes all the magnetic nuclei, and both set of simulations differ from the experimental data.

A different dynamic probability factor, the simplified Noyes probability distribution of first re-encounter $t^{-3/2}$ [22], was trialled in an attempt to improve the γ–COMPUTE simulations of this system. The Noyes function describes the secondary solvent cage effect and is also widely used to describe the diffusive reaction of the RPs. However, the change of the dynamic probability factor gave no improvements. This RP system contains charged radicals in a fairly viscous solvent and

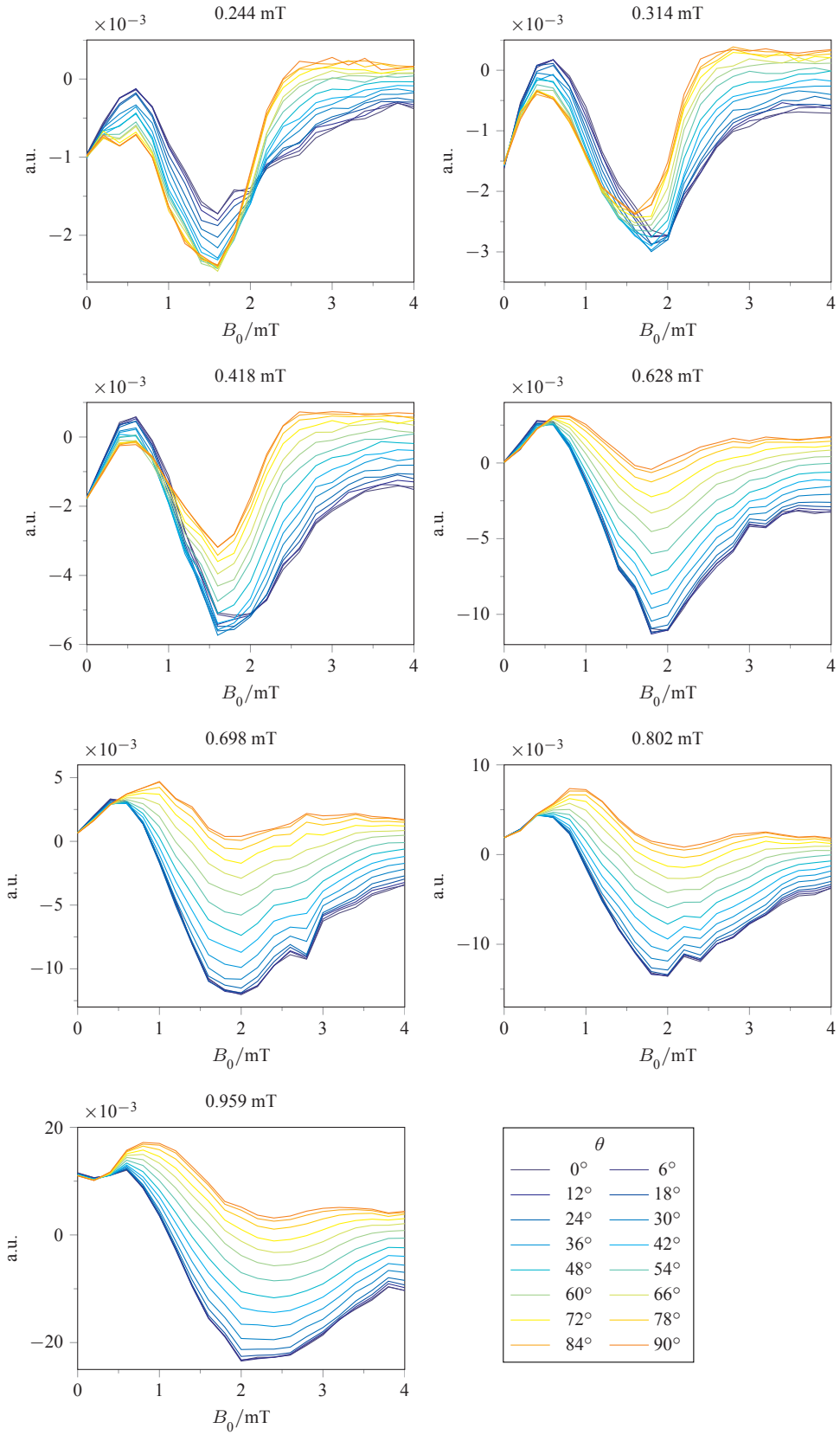

Figure 4.16: The rotary-RYDMR experimental data of Py-h_{10}/1,3-DCB. The $B_1^{\max}$ field strength is stated at the top of each plot.

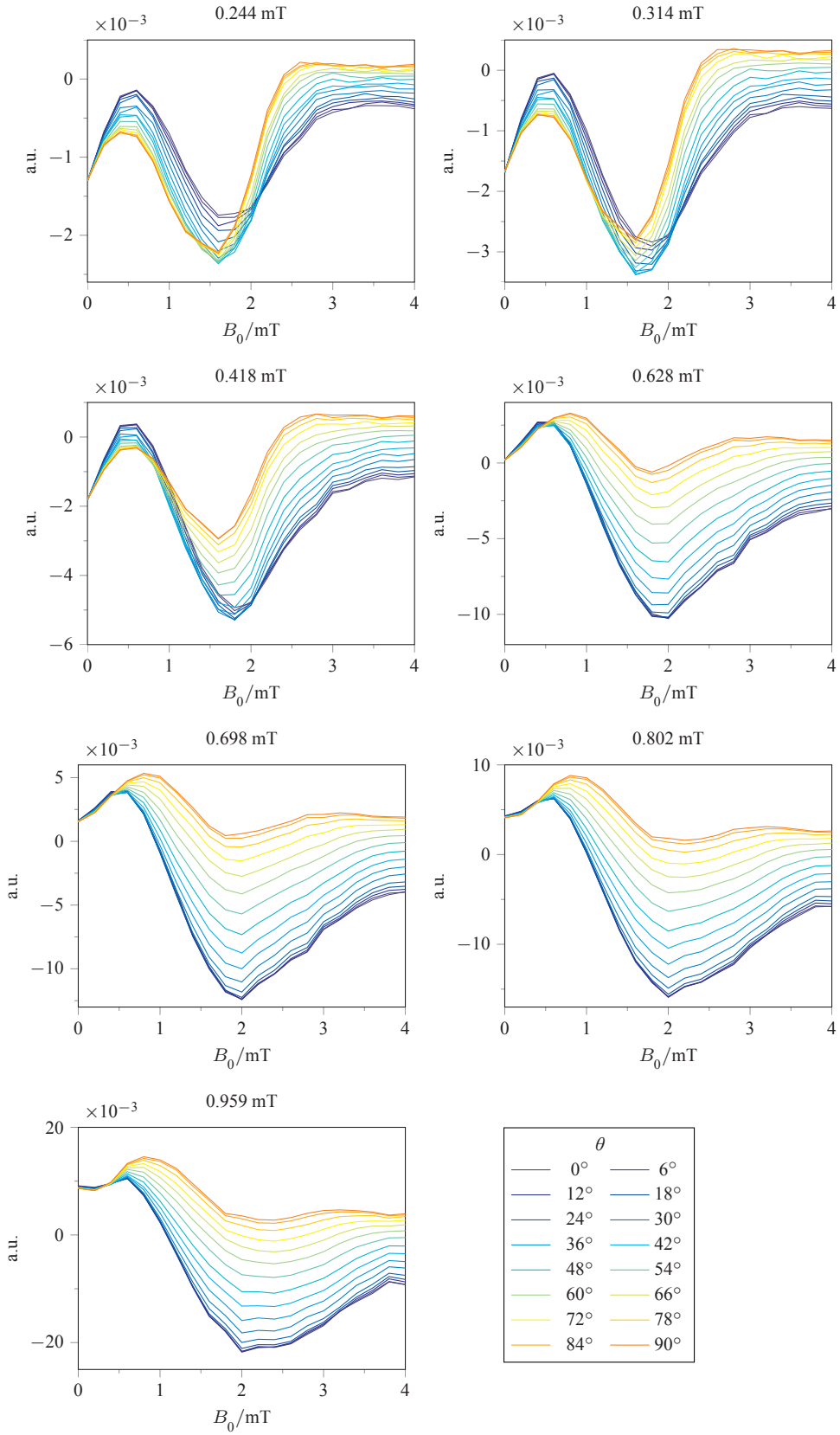

Figure 4.17: s_{demod} of the rotary-RYDMR experimental data of Py-h_{10}/1,3-DCB using s_7^{int}; $\lambda = 0.02$. The $B_1^{\max}$ field strength is stated at the top of each plot.

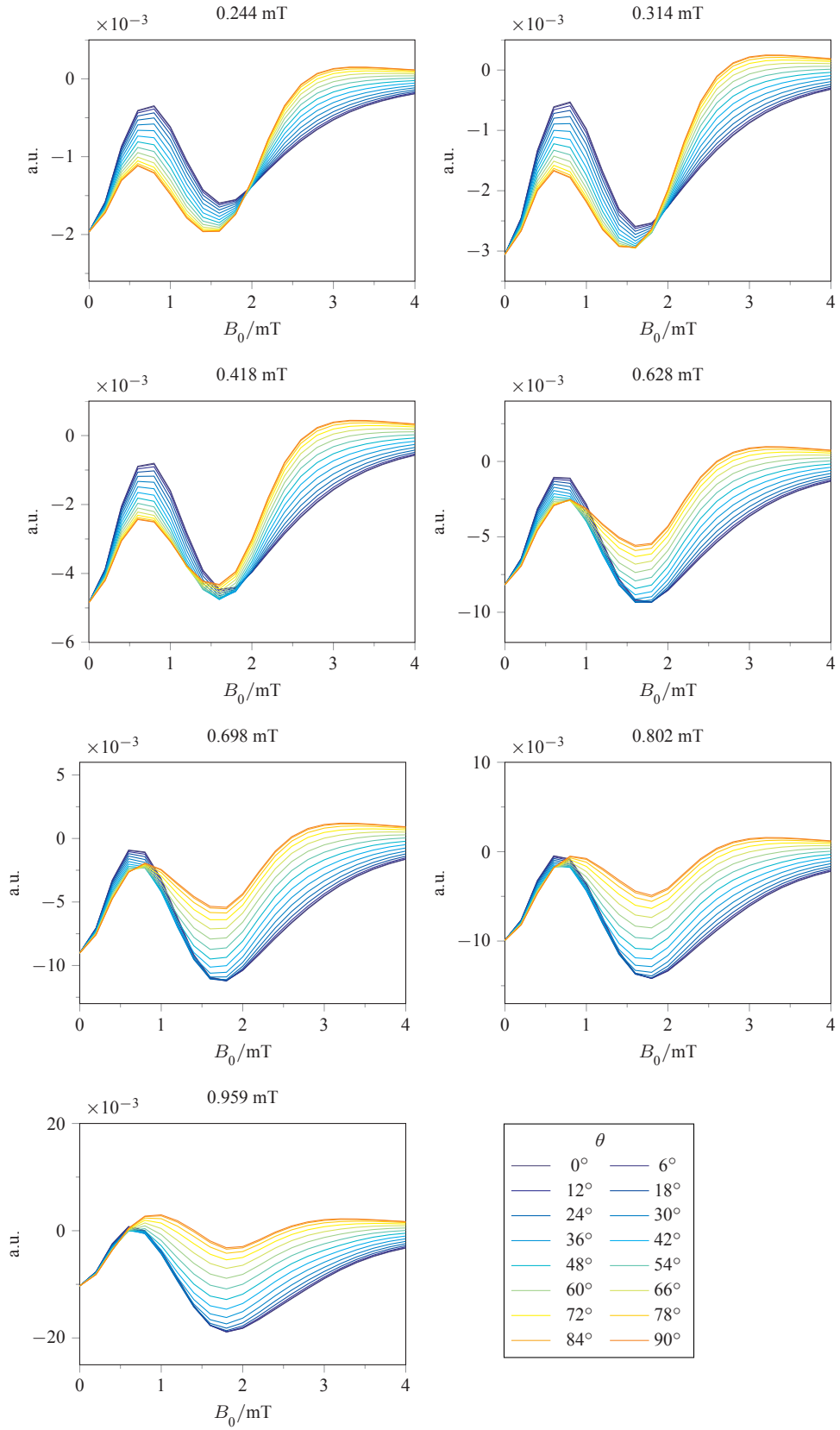

Figure 4.18: Φ_S^{diff}, the simulation of the rotary-RYDMR experimental data of Py-h_{10}/1,3-DCB using γ–COMPUTE; $n = 32$, $k = 90\,\mu s^{-1}$, $\alpha = 1.2$ and $\chi^2 = 0.564$. The $B_1^{\max}$ field strength is stated at the top of each plot.

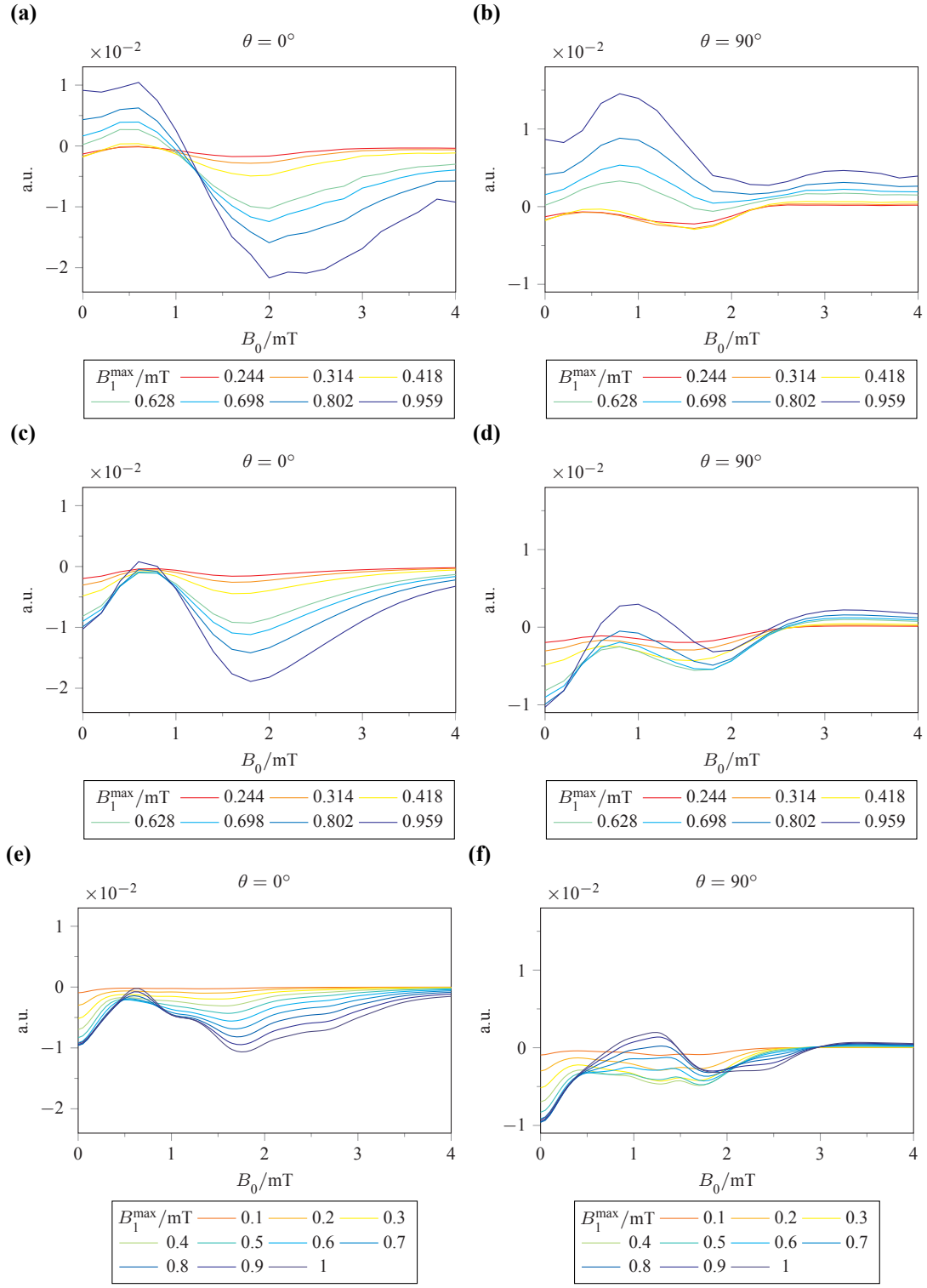

Figure 4.19: RYDMR spectra of the Py-h_{10}/1,3-DCB system. (a) and (b) are s_{demod} (fig. 4.17) of the rotary-RYDMR experimental data. (c) and (d) are Φ_S^{diff} (fig. 4.18), the new simulation of the RYDMR experimental data using a least difference-squared best-fit; $n = 32$, $k = 90\,\mu\text{s}^{-1}$, $\alpha = 1.2$, $\chi^2 = 0.564$, and all magnetic nuclei were included. (e) and (f) are the old γ–COMPUTE simulation, adapted from Wedge's thesis [157, fig. 4.53]; $n = 64$, $k = 40\,\mu\text{s}^{-1}$, $\alpha = 20$. The old simulation was only a calculation, not a best-fit, and it included the nuclei: $\text{Py}^{\bullet+}$ 0.538 mT (4H) and 1,3-$\text{DCB}^{\bullet-}$ 0.829 mT (2H). The angle, θ, between B_0 and B_1 is stated on the top of each spectrum.

the exponential model should be adequate to describe the re-encounter statistics of the radicals [22].

Py is a polycyclic aromatic hydrocarbon with extensive π-bonds above and below the molecular plane, and it is known to form an excimer under the right conditions [158]. The excimer, Py_2^*, is formed from an excited pyrene, Py^*, and a ground-state Py. However, two ground-state Py molecules are not bound. The excimer was found to fluoresce at $\sim$480 nm [159].

The excimer was shown to form a dimer radical cation, $Py_2^{\bullet+}$, after an electron transfer to 1,2-dicyanobenzene (1,2-DCB) [160]. The HFIs of the $Py_2^{\bullet+}$ radical were measured via an ESR spectrum [161, 162] and the hyperfine coupling constants of the dimer radical were found to be half those of the monomer radical ($Py_2^{\bullet+}$: 0.2659 mT (8H), 0.1096 mT (8H), 0.0575 mT (4H) [162]).

In Förster's paper [159], he reported the relative amount of fluorescence of Py^* and Py_2^* at different Py concentrations in benzene at 20°C. When the Py concentration was 1.2 mM, equal amounts of Py^* and Py_2^* fluorescence were measured. In comparison, the Py concentration used in the RYDMR experiments presented in this chapter was 0.4 mM in a relatively viscous solvent. At 0.4 mM Py, about 20% of the fluorescence was ascribed to Py_2^* according to Förster's experiment [159].

Therefore it is very likely that a significant amount of Py_2^* was formed in the RYDMR experiment and the RYDMR data may contain the magnetic field effects of two RPs, $Py^{\bullet+}$/1,3-$DCB^{\bullet-}$ and $Py_2^{\bullet+}$/1,3-$DCB^{\bullet-}$, as the bandwidth of the PMT includes the wavelength of Py_2^* fluorescence. Then the difference between the γ–`COMPUTE` simulations and the RYDMR data may be due to the difference between the HFIs of $Py^{\bullet+}$ and $Py_2^{\bullet+}$.

4.8.3 Chr-d_{12}/1,4-DCB

In the Chr-d_{12}/1,4-DCB system, as the strength of the B_1 field increases, both the RYDMR effect and the spin-locking effect increase. The magnitudes of the spectra increase as the B_1 field increases. However, the data collected at $B_1 = 0.802$ mT are smaller in magnitude than expected by about 30% (fig. 4.20). It is not clear why this should be; perhaps a sample of different concentration was used, or the duration of the data collection was different to the other

B_1 fields but these are only conjectures [163]. Nevertheless, the Tikhonov regularisation in the polynomial interpolation compensated for this error and the noise in s_{demod} is reduced (fig. 4.21).

In the simulation (fig. 4.22), all 6 magnetic nuclei in 1,4-DCB and 6 nuclei with the biggest hyperfine interactions (three pairs of deuteriums: 0.085 mT, 0.041 mT, 0.028 mT) in Chr were included. Only 6 of the 10 deuteriums were included in the simulation because $I = 1$ for deuterium and the spin-space of the deuterated molecule is bigger.

The simulation is in good agreement with the experimental data over all the B_1 fields. The positions and magnitudes of both the RYDMR effect and spin-locking effect in the simulation agree with the experimental data.

The shift and broadening of the RYDMR troughs, in the parallel RF field spectra, occur at a slower rate with respect to B_1 field strength, compared to the Py system. Also a smaller RYDMR effect is observed for the perpendicular RF fields, compared to the Py system, because of the smaller hyperfine coupling constants in Chr-d_{12}/1,4-DCB [157].

4.9 Conclusion

RYDMR experiments are usually performed with B_1 modulation to increase the signal-to-noise ratio. The fluorescence signals collected by the PMT need to be demodulated to obtain the true fluorescence produced by the exciplex. In previous reports on RYDMR experiments [143, 144], the raw output signals were interpreted as proportional to Φ_S^{diff} and no demodulation was implemented. However this interpretation assumes that the SY is a linear function of B_1, and the assumption is not valid for the whole range of B_1 fields and it may lead to incorrect interpretations of the RYDMR spectra.

Polynomial interpolation with Tikhonov regularisation is used in this chapter to calculate the demodulated fluorescence signal, $s_{\text{demod}} = \alpha\Phi_S^{\text{diff}}$. The regularisation parameter can be chosen to coincide with the expected experimental error and to further reduce the noise present in the spectrum.

The first order rate constants obtained from the data fitting of the Py and Chr systems, 90 μs^{-1} and 69 μs^{-1} respectively, are similar to the rate constants found in other references [136, 144].

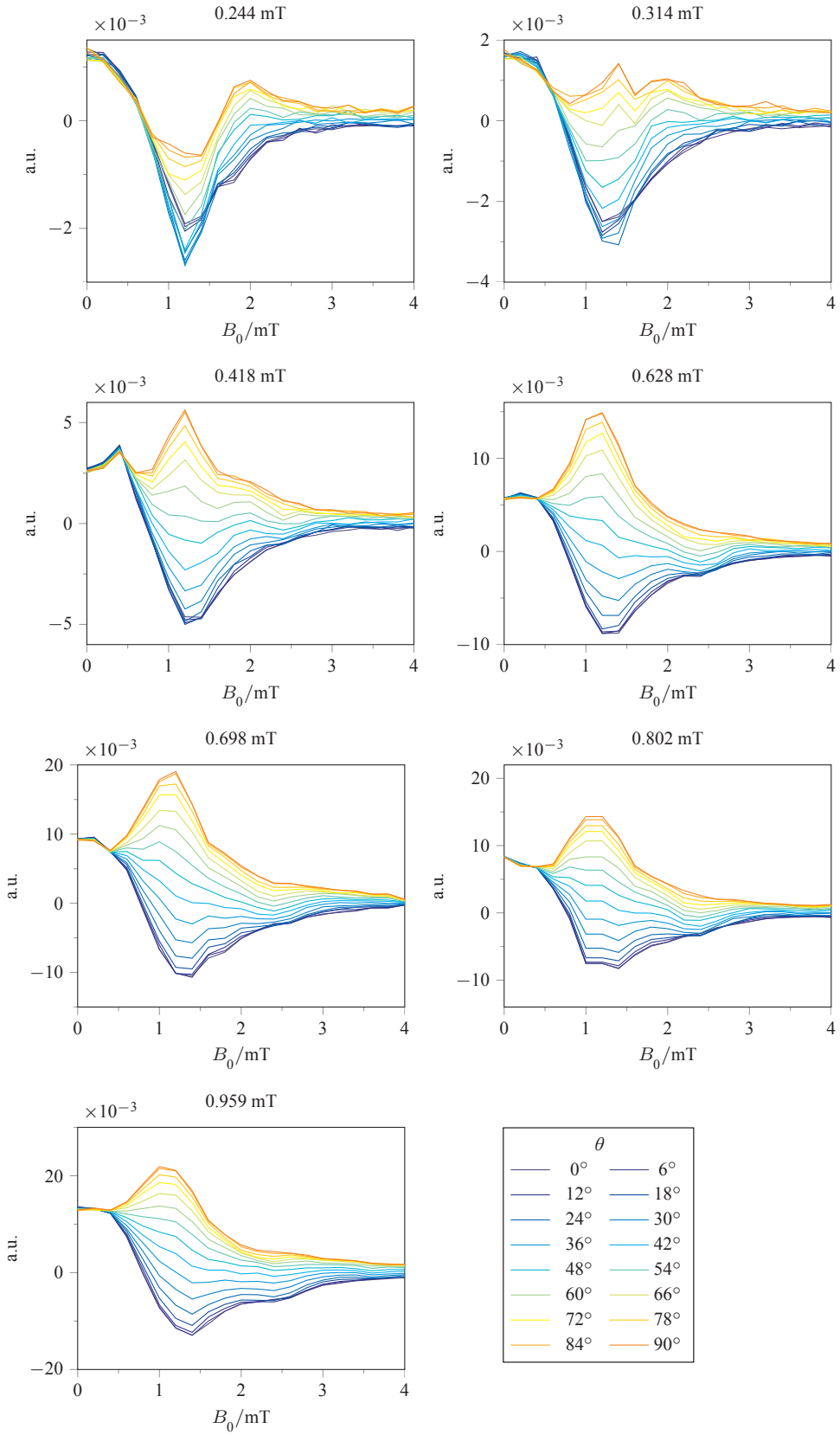

Figure 4.20: The rotary-RYDMR experimental data of Chr-d_{12}/1,4-DCB. The $B_1^{\max}$ field strength is stated at the top of each plot.

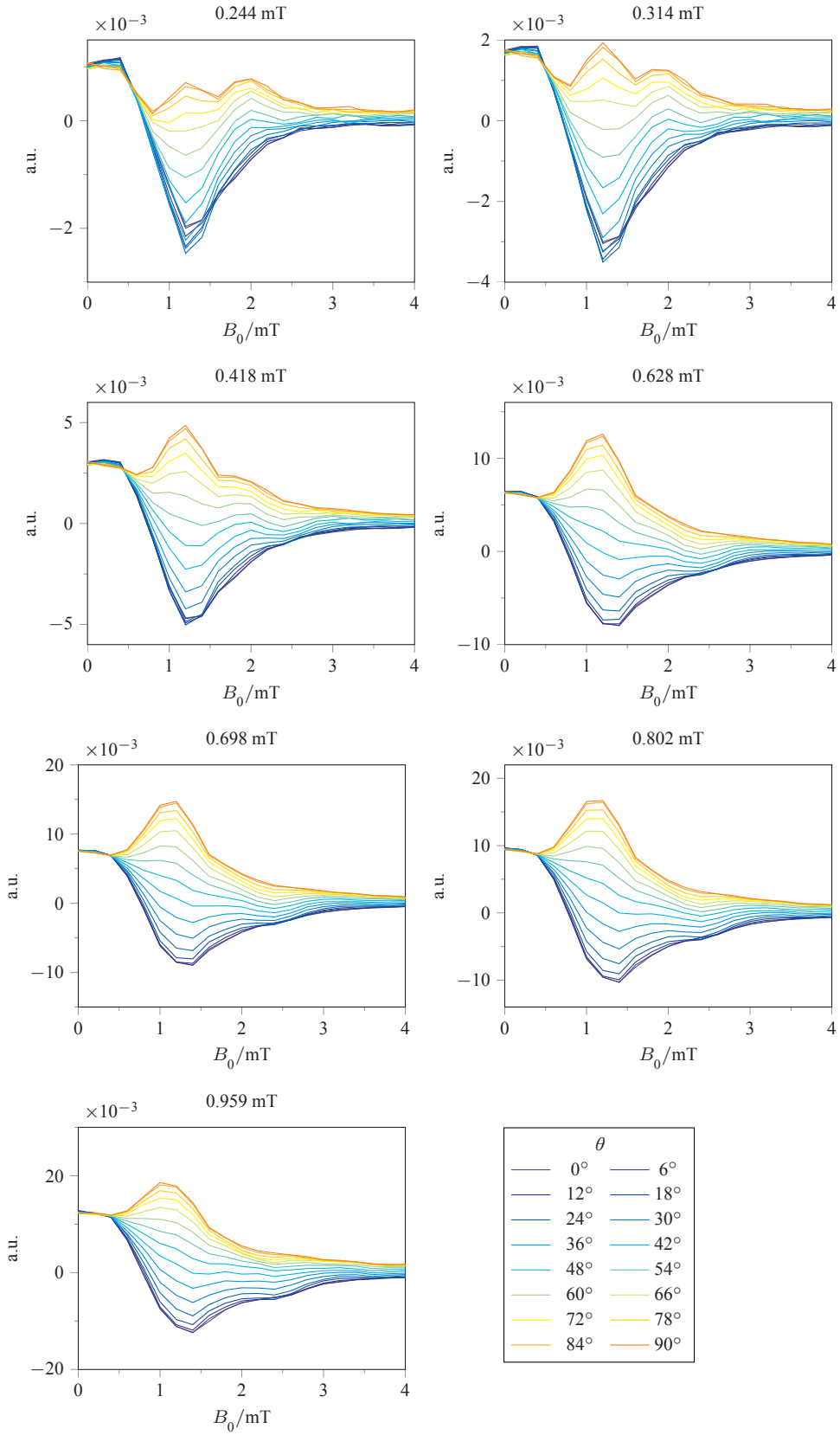

Figure 4.21: s_{demod}, of the rotary-RYDMR experimental data of Chr-d_{12}/1,4-DCB using s_7^{int}; $\lambda = 0.02$. The B_1^{max} field strength is stated at the top of each plot.

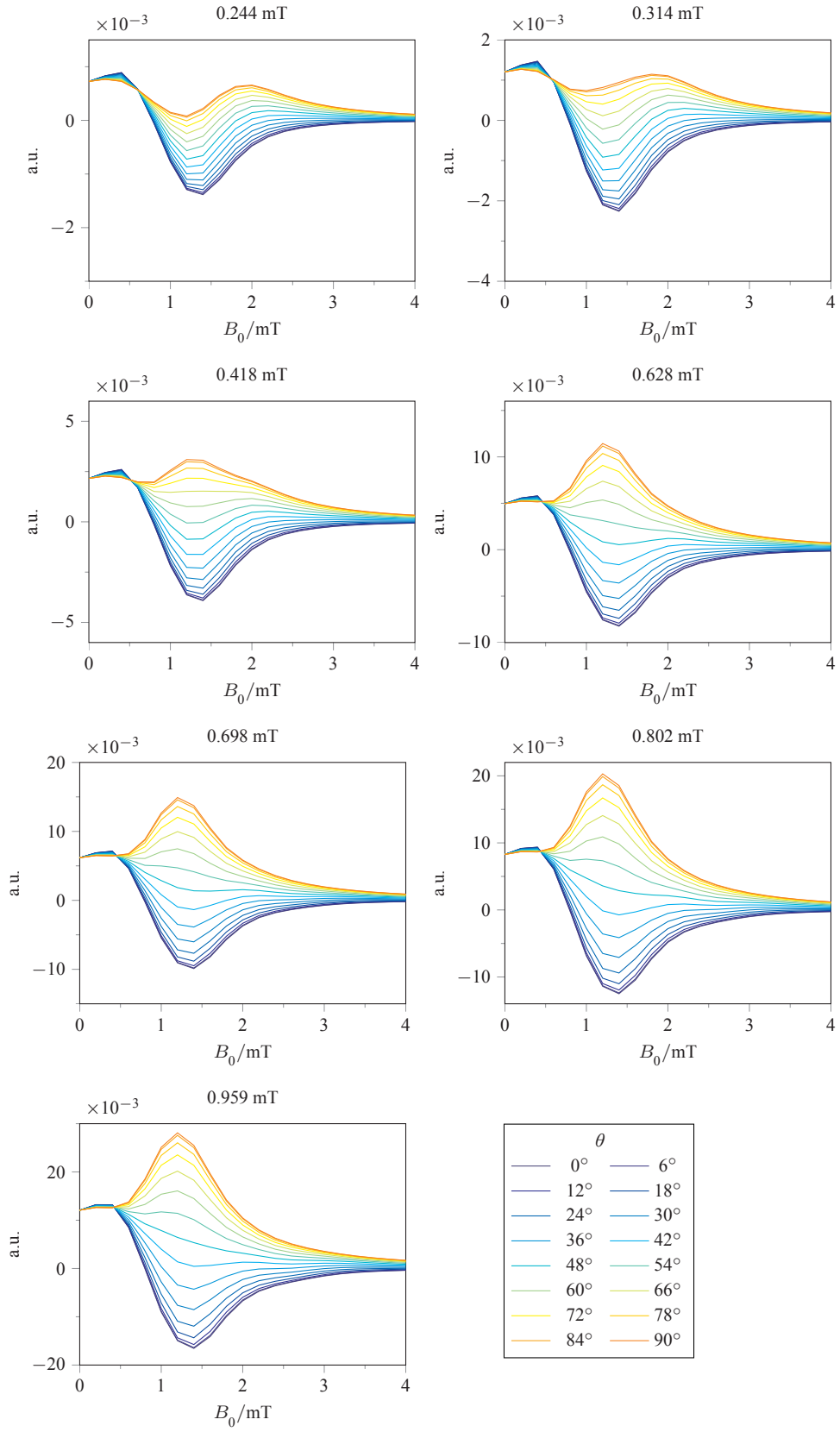

Figure 4.22: Φ_S^{diff}, the simulation of the rotary-RYDMR experimental data of Chr-d_{12}/1,4-DCB using γ–COMPUTE; $n = 32$, $k = 69\,\mu s^{-1}$, $\alpha = 0.779$ and $\chi^2 = 0.0964$. The B_1^{max} field strength is stated at the top of each plot.

The two rate constants are obtained using the exponential model and represent the rate of re-encounter for each RP system. As Chr is a longer molecule than Py, it is expected to have a slower rate of diffusion and smaller re-encounter frequency, which is consistent with the rate constants obtained from the data fitting.

In the Chr system, there is good agreement between the experimental data and the simulation, in which only 75% of the magnetic nuclei were used. However, there is poor agreement between the experimental data and the simulation in the Py system, even though all magnetic nuclei are included. It is very likely that there was a significant amount of the Py excimer formed during the RYDMR experiments and this may explain the inconsistencies between the simulation and the experimental data. Further experiments with varying Py concentrations combined with γ–COMPUTE simulations of the $Py_2^{\bullet+}$/1,3-$DCB^{\bullet-}$ RP would be desirable and the results would reveal whether the Py_2^* excimer was involved in the RYDMR experiments.

Previous γ–COMPUTE simulations of the Py-h_{10}/1,3-DCB system were constrained by computer hardware and only 40% of the magnetic nuclei were included. As described in the chapter, the γ–COMPUTE algorithm was modified and the new algorithm uses separate spin-space operators which requires less computer memory. Comparing the new simulations in this chapter and the previous simulations in Wedge's thesis [157], the inclusion of all the magnetic nuclei in the Py-h_{10}/1,3-DCB simulations does not change the RYDMR spectra significantly. Furthermore, only the biggest nuclei were needed to simulate the RYDMR spectra of the Chr system. Therefore it appears that it is unnecessary to include all the small HFIs in the simulation. Nonetheless, the new algorithm would be very useful for RP systems that have multiple nuclei with similar hyperfine couplings and more nuclei can be included in the simulation.

The RYDMR experiments of two RP systems, analysed in this chapter, demonstrated the effects of the application of the RF magnetic field at different direction relative to the static magnetic field. In particular, the spin-locking phenomenon is shown to be a suitable test for RP involvement in magnetoreception. As the strength of the RF field, applied near the Larmor resonance frequency perpendicular to the static field, gradually increases from zero, the bird is expected to be disoriented. This is because the product yields of the RP magnetoreceptors are altered due to the RYDMR effect. However, the spin-locking effect will eventually nullify the

RYDMR effect when the RF field strength reaches B_1^0. The bird's response is also expected to be dependent on the relative direction of the RF field to the static field; if a B_1^0-strength RF field is applied parallel to the static field, the bird is again expected to be disoriented. These *in vivo* RYDMR experiments can be analysed using the modified γ–`COMPUTE` algorithm presented in this chapter with a more realistic and complex RP system, such as a portion of the cryptochrome-FAD-tryptophan RP.

Appendix A

Hyperfine coupling tensors

A.1 $TrpH^{\bullet+}$

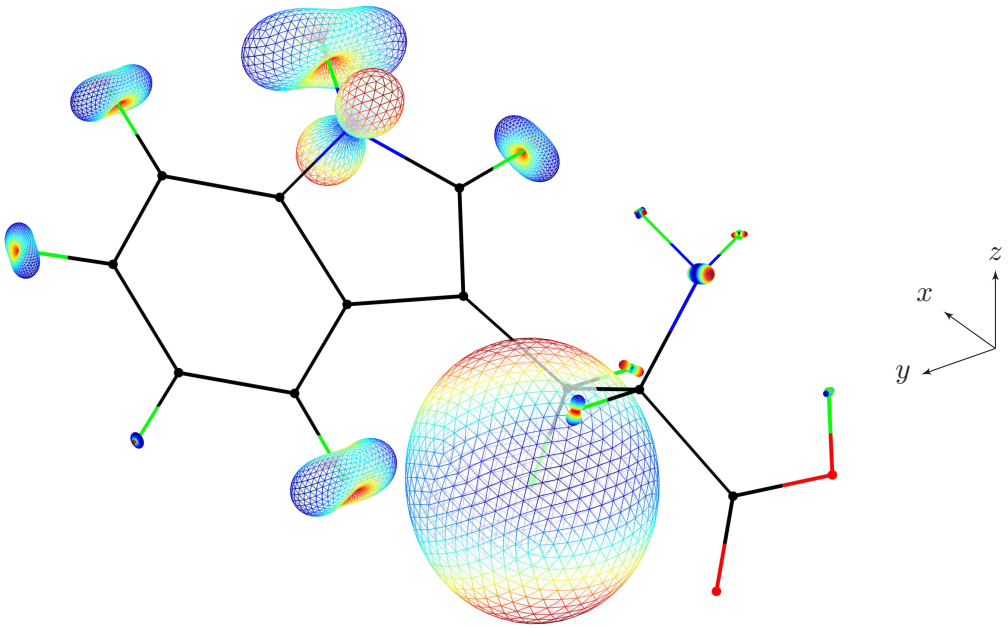

Figure A.1: 3D structure of $TrpH^{\bullet+}$ and the HFI representations. The colour codes for different atoms are: carbon, oxygen, hydrogen and nitrogen. The mesh plots (eq. D.1) represent the magnitudes and directions of the HFI (table A.1) of the nuclei, which are at the centre of the mesh plots. The geometry and HFIs are calculated by I. Kuprov using `Gaussian03`. The geometry was optimised in vacuum.

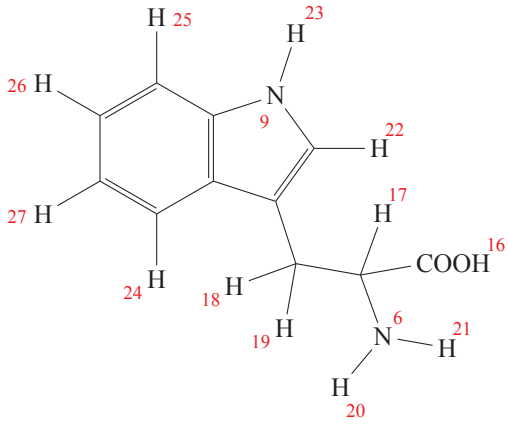

Figure A.2: The chemical structure of $TrpH^{\bullet+}$. The numbers in red are the `Gaussian` numbers of the magnetic nuclei.

Table A.1: HFIs of $TrpH^{\bullet+}$ calculated by I. Kuprov. The HFIs were calculated using UB3LYP correlation functions with EPR-III basis set in `Gaussian03`. The positions of magnetic nuclei can be found in figure A.2.

Classical Number	Gaussian Number	A_{xx}/μT	A_{yy}/μT	A_{zz}/μT	Principal axes		
Nα	N6	124.1	125.8	189.6	-0.4074 0.6015 0.6872	0.6837 0.6997 -0.2072	0.6055 -0.3854 0.6963
N1	N9	-63.6	-53	1081.2	0.3223 0.9172 0.2343	0.9353 -0.3468 0.0710	-0.1463 -0.1963 0.9696
HO	H16	-100.1	-16.4	-2.3	0.2440 0.1105 0.9635	0.8599 0.4346 -0.2676	-0.4483 0.8938 0.0110
Hα	H17	-202.3	-53.7	-23.3	-0.0934 0.9368 -0.3372	0.5119 0.3357 0.7908	0.8540 -0.0988 -0.5108
Hβ	H18	1498.1	1559	1756.7	0.2968 0.8180 -0.4928	-0.3935 0.5749 0.7174	0.8701 -0.0190 0.4925
Hβ	H19	-30.1	0.4	166.8	0.3333 -0.2430 0.9110	0.0783 0.9700 0.2301	0.9396 0.0053 -0.3423
HαN	H20	-88.8	-35.7	93.3	0.2188 -0.6701 0.7093	0.9709 0.2219 -0.0899	-0.0971 0.7083 0.6992
HαN	H21	-38.5	9.3	99.1	-0.4432 -0.2267 0.8673	0.1417 0.9376 0.3175	0.8852 -0.2636 0.3834
H2	H22	-471.6	-369.9	7.5	0.9190 0.2782 0.2793	-0.3028 0.0442 0.9520	-0.2525 0.9595 -0.1249
H1	H23	-1082.6	-705.4	-6.9	0.7540 0.2344 -0.6136	0.6319 0.0808 0.7852	-0.2336 0.9688 0.0830
H4	H24	-740	-536	-187.9	0.5359 0.2657 0.8014	0.8279 0.0205 -0.5604	-0.1653 0.9638 -0.2089
H7	H25	-558.2	-423.1	-109.7	0.5779 0.2498 0.7769	0.7959 0.0378 -0.6042	-0.1803 0.9676 0.1769
H6	H26	-356.8	-257.7	-10.4	-0.6290 0.2463 0.7374	0.7659 0.0335 0.6421	0.1335 0.9686 -0.2097
H5	H27	-103.2	-101.6	84.8	-0.5521 0.6964 0.4585	0.4130 -0.2493 0.8760	0.7243 0.6730 -0.1499

A.2 FADH•

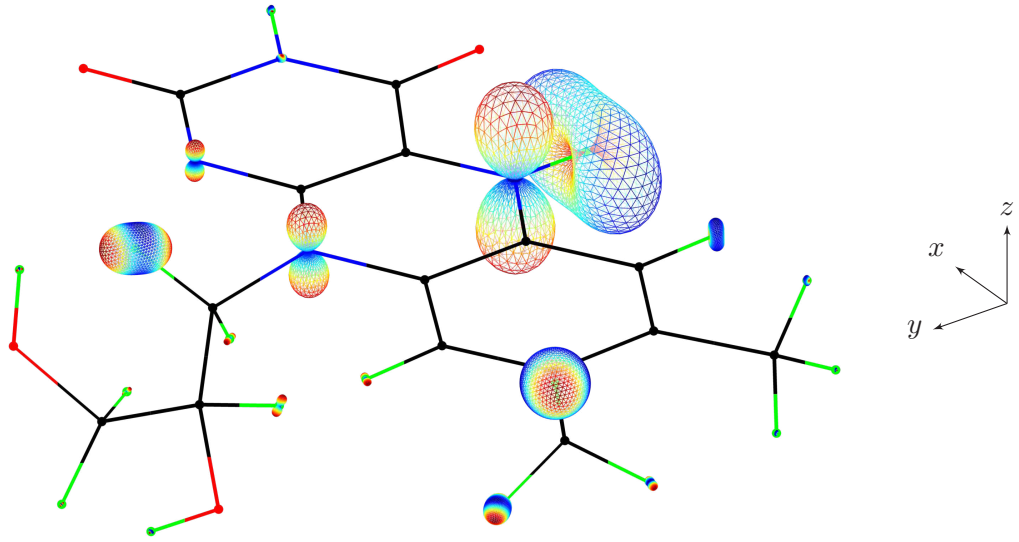

Figure A.3: 3D structure of FADH• and the HFI representations. The colour codes for different atoms are: carbon, oxygen, hydrogen and nitrogen. The mesh plots (eq. D.1) represent the magnitudes and directions of the HFI (table A.2) of the nuclei, which are at the centre of the mesh plots. The geometry and HFIs are calculated by Weber *et. al.* [164, model 2]. The starting structure for the geometry optimisation is the X-ray crystal structure of FAD *E. coli* DNA photolyase (PDB code: 1DNP [127]). The optimisation was done at the semiempirical PM3 level. The positions of isoalloxazine atoms were optimised and the position of the ribityl side chain was kept unchanged.

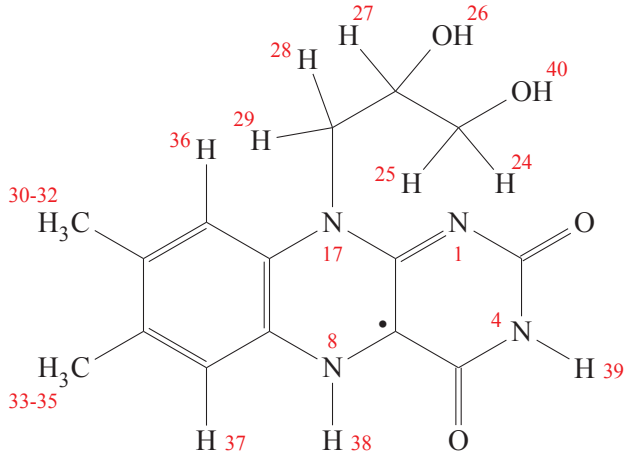

Figure A.4: The chemical structure of FADH•. The numbers in red are the `Gaussian` numbers of the magnetic nuclei.

Table A.2: HFIs of $FADH^{\bullet}$ calculated by Weber *et. al.* [164, model 2]. The HFIs were calculated using UB3LYP correlation functions with EPR-II basis set in `Gaussian98`. The positions of magnetic nuclei can be found in figure A.4.

Classical Number	Gaussian Number	A_{xx}/μT	A_{yy}/μT	A_{zz}/μT	Principal axes		
N1	N1	33.2	37.8	300.4	0.7387 -0.6699 -0.0745	0.6586 0.6937 0.2916	-0.1437 -0.2645 0.9536
N3	N4	-72.5	-60.1	-44.8	-0.2436 0.9398 -0.2397	0.9036 0.3097 0.2959	-0.3523 0.1445 0.9246
N5	N8	-104.9	-99.6	1382.6	0.4380 0.8981 -0.0384	0.8655 -0.4097 0.2883	-0.2432 0.1595 0.9568
N10	N17	-30.5	-22.2	687.2	0.9703 0.2383 -0.0419	-0.2207 0.9426 0.2506	0.0992 -0.2340 0.9672
H3'C	H24	-18.3	-11.8	32.5	0.2459 0.9146 -0.3210	-0.3671 0.3943 0.8424	0.8971 -0.0893 0.4328
H3'C	H25	-4.9	3.5	73.4	0.4675 0.7722 -0.4302	-0.2610 0.5856 0.7674	0.8446 -0.2465 0.4754
H2'O	H26	-42.7	-31.8	36.5	0.9825 0.1863 0.0079	0.0100 -0.0952 0.9954	-0.1862 0.9779 0.0954
H2'C	H27	-5.4	44.9	151.3	0.9767 -0.1935 -0.0930	-0.0650 -0.6796 0.7307	0.2046 0.7076 0.6763
H1'	H28	328.2	356.6	484.9	-0.1902 0.9156 -0.3542	0.3965 0.4017 0.8255	0.8981 0.0165 -0.4395
H1'	H29	-14.0	-9.3	119.0	0.2539 0.9028 0.3470	0.1826 -0.3971 0.8994	0.9498 -0.1650 -0.2657
H8α	H30	169.4	177.9	228.7	-0.0734 0.8302 0.5526	0.0830 -0.5471 0.8330	0.9938 0.1070 -0.0288
H8α	H31	457.4	465.2	522.5	-0.5928 0.3401 0.7300	0.8047 0.2856 0.5205	-0.0314 0.8960 -0.4430
H8α	H32	52.8	54.8	117.1	0.0600 -0.3504 0.9347	-0.3224 0.8794 0.3504	0.9447 0.3224 0.0602
H7α	H33	-28.6	-21.8	23.1	-0.1364 0.3148 0.9393	0.4011 0.8845 -0.2382	0.9058 -0.3442 0.2469
H7α	H34	-68.7	-59.6	-20.2	0.1703 0.2716 0.9472	0.14889 0.9431 -0.2972	0.9741 -0.1916 -0.1201
H7α	H35	-39.9	-35.0	12.1	-0.1297 0.2057 0.9700	0.3522 0.9240 -0.1488	0.9269 -0.3223 0.1923
H9	H36	-0.9	25.6	121.4	-0.0545 -0.5012 0.8636	0.2631 0.8271 0.4967	0.9632 -0.2543 -0.0868
H6	H37	-218.0	-201.6	-54.4	-0.0362 0.7948 -0.6059	0.2937 0.5879 0.7537	0.9552 -0.1507 -0.2546
H5	H38	-1385	-937.2	14.3	0.9819 -0.0348 -0.1861	0.1883 0.2850 0.9398	-0.0203 0.9579 -0.2864
H3	H39	-75.5	-44.7	46.0	-0.0680 -0.2088 0.9756	0.2708 0.9373 0.2194	0.9602 -0.2791 0.0072
H3'O	H40	-38.2	-16.4	43.8	-0.0859 0.8553 -0.5109	-0.0037 0.5125 0.8587	0.9963 0.0757 -0.0408

Appendix B

Singlet yield spherical harmonic expansion

The spherical harmonic expansion of the singlet yield of RP1 and RP2 (for nuclei used, see table 3.1) is done using `S2kit` [106] up to $l = 30$ with a bandwidth of 32. The spherical harmonic expansions of the SY of RP1 and RP2 are plotted in figure B.1. The expansion coefficients up to $l = 12$ are listed in tables B.1 and B.2. Only coefficients with $m \geqslant 0$ are listed because $a_l^m = (-1)^m \left[a_l^{-m}\right]^*$ for real functions. The RMS error of the spherical expansion for RP1 is 2.289×10^{-4} and RP2 is 1.376×10^{-7}.

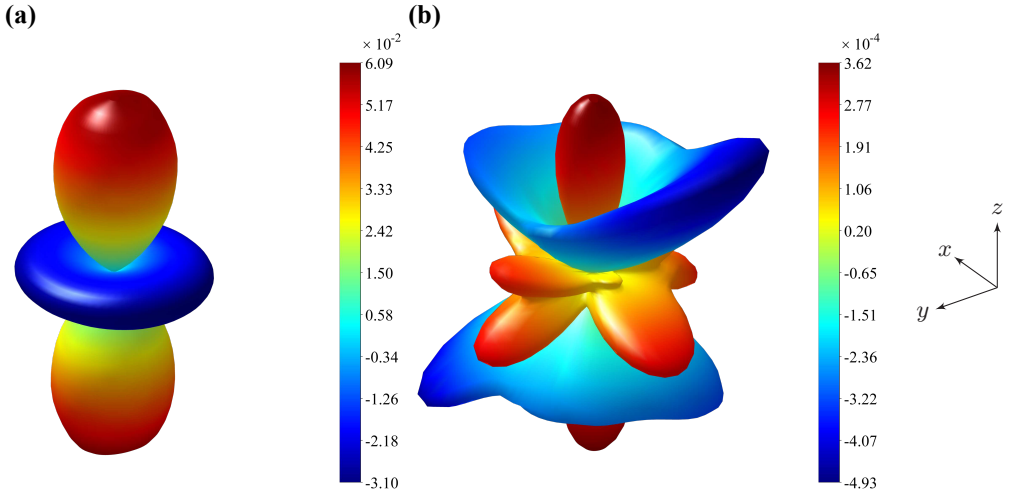

Figure B.1: The spherical harmonic expansions of the SY, Φ_S^{SHE}, of (a) RP1 and (b) RP2. The SY is expanded up to $l = 30$. The RMS(error) of the expansions (compared to Φ_S, fig. 3.7) are: (a) 2.29×10^{-4}, (b) 1.38×10^{-7}.

Table B.1: Spherical harmonic expansion coefficients of RP1

(a) Real coefficients

m \ l	0	2	4	6	8	10	12
0	1.002	9.576×10^{-2}	3.397×10^{-4}	3.423×10^{-4}	2.426×10^{-4}	-3.396×10^{-5}	-5.415×10^{-5}
1		-1.325×10^{-3}	2.380×10^{-5}	2.982×10^{-6}	3.181×10^{-5}	5.767×10^{-5}	4.990×10^{-6}
2		-1.416×10^{-3}	-3.241×10^{-4}	-9.012×10^{-5}	-1.459×10^{-5}	3.725×10^{-5}	4.751×10^{-5}
3			6.812×10^{-5}	5.623×10^{-5}	3.352×10^{-5}	4.136×10^{-6}	-1.779×10^{-6}
4			1.061×10^{-4}	5.302×10^{-5}	1.460×10^{-5}	2.814×10^{-5}	1.096×10^{-5}
5				1.139×10^{-6}	-1.482×10^{-5}	-1.004×10^{-5}	1.096×10^{-5}
6				9.214×10^{-7}	4.046×10^{-6}	-6.110×10^{-6}	-2.794×10^{-5}
7					2.351×10^{-6}	1.102×10^{-5}	9.194×10^{-6}
8					1.266×10^{-5}	-5.585×10^{-6}	-5.383×10^{-6}
9						7.526×10^{-6}	5.803×10^{-6}
10						5.026×10^{-6}	6.471×10^{-6}
11							-4.894×10^{-6}
12							-8.237×10^{-7}

(b) Imaginary coefficients

m \ l	0	2	4	6	8	10	12
0	0	0	0	0	0	0	0
1		-2.747×10^{-3}	1.308×10^{-4}	-2.105×10^{-5}	-5.565×10^{-5}	1.481×10^{-5}	3.600×10^{-5}
2		4.083×10^{-4}	1.817×10^{-4}	6.787×10^{-5}	-1.280×10^{-5}	-1.876×10^{-6}	-1.260×10^{-5}
3			1.383×10^{-4}	7.715×10^{-5}	7.289×10^{-5}	2.085×10^{-5}	-5.705×10^{-8}
4			-3.961×10^{-5}	-2.011×10^{-5}	-1.425×10^{-5}	-2.394×10^{-5}	-2.013×10^{-7}
5				-1.464×10^{-5}	-1.644×10^{-5}	-1.507×10^{-5}	-9.149×10^{-6}
6				-1.544×10^{-5}	-3.066×10^{-7}	-1.002×10^{-5}	2.556×10^{-5}
7					6.099×10^{-6}	7.405×10^{-6}	7.734×10^{-6}
8					1.521×10^{-5}	2.570×10^{-6}	1.075×10^{-5}
9						6.176×10^{-6}	-7.485×10^{-7}
10						-1.421×10^{-7}	9.633×10^{-6}
11							6.862×10^{-6}
12							2.591×10^{-6}

Table B.2: Spherical harmonic expansion coefficients of RP2

(a) Real coefficients

m \ l	0	2	4	6	8	10	12
0	0.9890	-1.961×10^{-4}	5.177×10^{-4}	2.275×10^{-4}	-1.984×10^{-4}	6.388×10^{-6}	3.554×10^{-5}
1		-9.158×10^{-5}	3.220×10^{-5}	-3.866×10^{-8}	1.365×10^{-6}	-1.195×10^{-5}	5.685×10^{-6}
2		-6.633×10^{-5}	-5.277×10^{-5}	1.211×10^{-5}	3.308×10^{-7}	-1.365×10^{-5}	2.720×10^{-6}
3			-3.789×10^{-5}	1.093×10^{-5}	-1.348×10^{-5}	4.938×10^{-6}	3.514×10^{-7}
4			6.460×10^{-5}	1.108×10^{-5}	-1.628×10^{-5}	1.352×10^{-5}	-7.529×10^{-7}
5				-8.198×10^{-6}	-5.090×10^{-6}	9.860×10^{-6}	-1.009×10^{-6}
6				-7.191×10^{-6}	-1.047×10^{-6}	4.031×10^{-6}	-5.819×10^{-8}
7					2.383×10^{-6}	-2.976×10^{-7}	9.648×10^{-7}
8					2.027×10^{-6}	-2.905×10^{-7}	-3.353×10^{-7}
9						-2.113×10^{-7}	2.483×10^{-8}
10						-5.773×10^{-7}	1.091×10^{-6}
11							-7.868×10^{-7}
12							8.108×10^{-7}

(b) Imaginary coefficients

m \ l	0	2	4	6	8	10	12
0	0	0	0	0	0	0	0
1		1.344×10^{-5}	2.991×10^{-5}	2.255×10^{-5}	-3.318×10^{-5}	7.681×10^{-7}	4.762×10^{-6}
2		2.460×10^{-5}	3.660×10^{-5}	-7.111×10^{-6}	2.231×10^{-7}	5.597×10^{-6}	1.176×10^{-6}
3			1.817×10^{-5}	-3.991×10^{-6}	7.888×10^{-6}	7.798×10^{-7}	2.133×10^{-7}
4			8.837×10^{-6}	3.067×10^{-6}	7.615×10^{-6}	-1.109×10^{-5}	-2.663×10^{-7}
5				-7.600×10^{-7}	8.572×10^{-6}	-1.184×10^{-5}	-1.926×10^{-7}
6				6.690×10^{-6}	3.390×10^{-7}	-4.553×10^{-6}	1.468×10^{-6}
7					-1.035×10^{-6}	-2.918×10^{-6}	-5.424×10^{-7}
8					-2.105×10^{-6}	3.162×10^{-7}	-3.579×10^{-6}
9						9.244×10^{-7}	-8.538×10^{-7}
10						7.901×10^{-7}	-3.367×10^{-7}
11							-6.784×10^{-7}
12							-7.860×10^{-8}

Appendix C

Associated Legendre function

The spherical harmonics depend on the unnormalised associated Legendre function,

$$P_l^m(x) = (-1)^{-m} \left(1 - x^2\right)^{m/2} \frac{\mathrm{d}^m}{\mathrm{d}x^m} \left(P_l(x)\right) \tag{C.1}$$

$P_l(x)$ is the Legendre function,

$$P_l(x) = 2^l \sum_{k=0}^{l} x^k \binom{l}{k} \binom{\frac{l+k-1}{2}}{l} \tag{C.2}$$

The functions with negative m are defined in terms of the functions with positive m;

$$P_l^{-m} = (-1)^{-m} \frac{(l-m)!}{(l+m)!} P_l^m \tag{C.3}$$

The factor $(-1)^{-m}$ is a phase factor, which is known as the Condon-Shortley phase factor.

Appendix D

Hyperfine interaction representation

The hyperfine interaction of a nucleus is represented by a mesh plot centred on the nucleus. The distance, r, from the centre to the mesh at the spherical angles, (θ, ϕ), is calculated by

$$r = a + \begin{pmatrix} \sin\theta\cos\phi & \sin\theta\sin\phi & \cos\theta \end{pmatrix} \begin{pmatrix} T_{11} & T_{12} & T_{13} \\ T_{21} & T_{22} & T_{23} \\ T_{31} & T_{32} & T_{33} \end{pmatrix} \begin{pmatrix} \sin\theta\cos\phi \\ \sin\theta\sin\phi \\ \cos\theta \end{pmatrix} \tag{D.1}$$

where a is the isotropic hyperfine coupling constant and T_{ij} is the ij-th element of the anisotropic hyperfine coupling tensor, `T`.

Appendix E

Retina projection

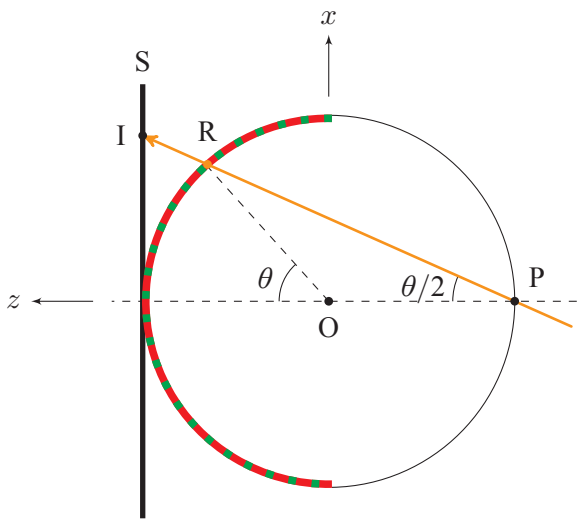

The retina response is viewed from the back of the retina, $i.e.$ in the negative z direction. The stereographic projection will be used. The projection transforms the three dimensional spherical polar coordinates, (r, θ, ϕ), to the two dimensional polar coordinates, (r', θ'). The eye is chosen to be a unit sphere therefore $r = 1$.

$$r' = 2 - \tan\frac{\theta}{2} \tag{E.1}$$

$$\theta' = \phi \tag{E.2}$$

Appendix F

Fourier transform

F.1 Forward discrete Fourier transform

$$X(k) = \mathcal{F}_k\{x\} = \sum_{j=0}^{N-1} x(j) e^{-2\pi \mathrm{i} \cdot \frac{jk}{N}} \tag{F.1}$$

F.2 Inverse discrete Fourier transform

$$x(j) = \mathcal{F}_k^{-1}\{X\} = \frac{1}{N} \sum_{k=0}^{N-1} X(k) e^{2\pi \mathrm{i} \cdot \frac{jk}{N}} \tag{F.2}$$

F.3 Discrete cross-correlation

For two functions with period N, their discrete cross-correlation is defined as

$$(f \star g)[n] = \sum_{m=0}^{N-1} f^*[m] g[n+m] \tag{F.3}$$

This has a convenient Fourier transform;

$$\mathcal{F}\{f \star g\} = [\mathcal{F}\{f\}]^* \mathcal{F}\{g\} \tag{F.4}$$

F.4 Convolution theorem

The discrete convolution of two functions is defined as

$$(f * g)[n] = \sum_{m=0}^{N-1} f[m]g[n-m] \tag{F.5}$$

This has a convenient Fourier transform;

$$\mathcal{F}\{f * g\} = \mathcal{F}\{f\} \cdot \mathcal{F}\{g\} \tag{F.6}$$

The reverse is also true;

$$\begin{aligned}\mathcal{F}\{f \cdot g\} &= \mathcal{F}\{f\} * \mathcal{F}\{g\} \\ &= \frac{1}{N}\mathcal{F}^{-1}\{\ \mathcal{F}\{\ \mathcal{F}\{f\} * \mathcal{F}\{g\}\ \}\ \} \\ &= \frac{1}{N}\mathcal{F}^{-1}\{\ \mathcal{F}\{\ \mathcal{F}\{f\}\ \} \cdot \mathcal{F}\{\ \mathcal{F}\{g\}\ \}\ \}\end{aligned} \tag{F.7}$$

F.5 Consecutive discrete Fourier transform

$$\boldsymbol{G}(\alpha) = \mathcal{F}_{\alpha}\{\ \mathcal{F}\{g\}\ \} \tag{F.8}$$

The consecutive discrete Fourier transform is equivalent to a rearrangement of the sequence of the indices in the g-function.

$$\boldsymbol{G}(\alpha) = \begin{cases} Ng(N-\alpha) & \text{for} \quad 0 < \alpha \leq (N-1) \\ g(\alpha) & \text{for} \quad \alpha = 0 \end{cases} \tag{F.9}$$

Proof :

$$\begin{aligned}\frac{1}{N}\boldsymbol{G}(-N+\alpha) &= \frac{1}{N}\sum_{k=0}^{N-1}\sum_{j=0}^{N-1} g(j)\ e^{-2\pi \mathrm{i}\frac{k}{N}(j+N-\alpha)} \\ &= \frac{1}{N}\sum_{k=0}^{N-1}\sum_{j=0}^{N-1} g(j)\ e^{-2\pi \mathrm{i}\frac{jk}{N}} e^{+2\pi \mathrm{i}\frac{ak}{N}} e^{-2\pi \mathrm{i}k} \\ &= \frac{1}{N}\sum_{k=0}^{N-1} \mathcal{F}_k\{g(j)\} e^{+2\pi \mathrm{i}\frac{ak}{N}} \overbrace{e^{-2\pi \mathrm{i}k}}^{=1} \\ &= \frac{1}{N}\sum_{k=0}^{N-1} G(k) e^{+2\pi \mathrm{i}\frac{ak}{N}}\end{aligned}$$

$$
\begin{aligned}
&= \mathcal{F}_{\alpha}^{-1}\{G(k)\} \\
&= g(\alpha) \\
\Rightarrow \boldsymbol{G}(\alpha) &= Ng(N-\alpha) \qquad \square
\end{aligned} \tag{F.10}
$$

Bibliography

[1] Thomson, J.J., "Cathode rays", *Philosophical Magazine*, **44**: 293, 1897.

[2] Millikan, R.A., "ON THE ELEMENTARY ELECTRICAL CHARGE AND THE AVOGADRO CONSTANT", *Physical Review*, **2**: 109–143, 1913.

[3] Gerlach, W.; Stern, O., "Das magnetische Moment des Silberatoms", *Zeitschrift für Physik A Hadrons and Nuclei*, **9**: 353–355, 1922.

[4] Phipps, T.E.; Taylor, J.B., "THE MAGNETIC MOMENT OF THE HYDROGEN ATOM", *Physical Review*, **29**: 309–320, 1927.

[5] Zeeman, P., "THE EFFECT OF MAGNETISATION ON THE NATURE OF LIGHT EMITTED BY A SUBSTANCE", *Nature*, **55**: 347, 1897.

[6] Uhlenbeck, G.E.; Goudsmit, S., "Spinning Electrons and the Structure of Spectra", *Nature*, **117**: 264–265, 1926.

[7] Pauli, W., "Exclusion principle and quantum mechanicsc", *Nobel Lecture*, 1946.

[8] Dirac, P.A.M., "The Quantum Theory of the Electron", *Proceedings of the Royal Society of London. Series A*, **117**(778): 610–624, 1928.

[9] Dirac, P.A.M., "A Theory of Electrons and Protons", *Proceedings of the Royal Society of London. Series A*, **126**(801): 360–365, 1930.

[10] Frisch, R.; Stern, O., "Über die magnetische Ablenkung von Wasserstoffmolekülen und das magnetische Moment des Protons. I", *Zeitschrift für Physik A Hadrons and Nuclei*, **85**: 4–16, 1933.

[11] Stern, O., “The method of molecular rays”, *Nobel Lecture*, 1946.

[12] Kellogg, J.M.B.; Rabi, I.I.; Ramsey, N.F.; Zacharias, J.R., “The Magnetic Moments of the Proton and the Deuteron. The Radiofrequency Spectrum of H_2 in Various Magnetic Fields”, *Physical Review*, **56**: 728–743, 1939.

[13] Purcell, E.M.; Torrey, H.C.; Pound, R.V., “Resonance Absorption by Nuclear Magnetic Moments in a Solid”, *Physical Review*, **69**: 37–38, 1946.

[14] Bloch, F.; Hansen, W.W.; Packard, M., “The Nuclear Induction Experiment”, *Physical Review*, **70**: 474–485, 1946.

[15] Kaptein, R., “CHEMICALLY INDUCED DYNAMIC NUCLEAR POLARIZATION IN FIVE ALKYL RADICALS”, *Chemical Physics Letters*, **2**(4): 261–267, 1968.

[16] Lawler, R.G., “Chemically Induced Dynamic Nuclear Polarization”, *Journal Of The American Chemical Society*, **89**(21): 5519–5521, 1967.

[17] Fischer, H.; Bargon, J., “Chemically Induced Dynamic Nuclear Polarization during Thermal Decomposition of Peroxides and Azo Compounds”, *Accounts Of Chemical Research*, **2**(4): 110–114, 1969.

[18] Kaptein, R., “Chemically Induced Dynamic Nuclear Polarization. VIII. Spin Dynamics and Diffusion of Radical Pairs”, *Journal Of The American Chemical Society*, **94**(18): 6251–6262, 1972.

[19] Kaptein, R., “Simple Rules for Chemically Induced Dynamic Nuclear Polarization”, *Journal Of The Chemical Society D - Chemical Communications*, **0**(14): 732–733, 1971.

[20] Fessenden, R.W.; Schuler, R.H., “Electron Spin Resonance Studies of Transient Alkyl Radicals”, *Journal of Chemical Physics*, **39**(9): 2147–2195, 1963.

[21] Kaptein, R.; Oosterhoff, J.L., “CHEMICALLY INDUCED DYNAMIC NUCLEAR POLARIZATION II: (Relation with anomalous ESR spectra)”, *Chemical Physics Letters*, **4**(4): 195–197, 1969.

[22] Steiner, U.E.; Ulrich, T., "Magnetic Field Effects in Chemical Kinetics and Related Phenomena", *Chemical Reviews*, **89**(1): 51–147, 1989.

[23] Maeda, K.; Henbest, K.B.; Cintolesi, F.; Kuprov, I.; Rodgers, C.T.; Liddell, P.A.; Gust, D.; Timmel, C.R.; Hore, P.J., "Chemical compass model of avian magnetoreception", *Nature*, **453**(7193): 387–390, 2008.

[24] Papi, F.; Luschi, P., "PINPOINTING 'ISLA META□: THE CASE OF SEA TURTLES AND ALBATROSSES", *Journal of Experimental Biology*, **199**(1): 65–71, 1996.

[25] Gill, R.E.; Tibbitts, T.L.; Douglas, D.C.; Handel, C.M.; Mulcahy, D.M.; Gottschalck, J.C.; Warnock, N.; McCaffery, B.J.; Battley, P.F.; Piersma, T., "Extreme endurance flights by landbirds crossing the Pacific Ocean: ecological corridor rather than barrier?", *Proceedings of the Royal Society B: Biological Sciences*, **276**(1656): 447–457, 2009.

[26] Brower, L.P., "Monarch butterfly orientation: missing pieces of a magnificent puzzle", *Journal of Experimental Biology*, **199**(1): 93–103, 1996.

[27] Muheim, R.; Phillips, J.B.; Åkesson, S., "Polarized Light Cues Underlie Compass Calibration in Migratory Songbirds", *Science*, **313**(5788): 837–839, 2006.

[28] Wiltschko, R.; Wiltschko, W., "AVIAN NAVIGATION", *The Auk*, **126**(4): 717–743, 2009.

[29] Wiltschko, W., "THE INFLUENCE OF MAGNETIC TOTAL INTENSITY AND INCLINATION ON DIRECTIONS PREFERRED BY MIGRATING EUROPEAN ROBINS", in S.R. Galler; K. Schmidt-Koenig; G.J. Acobs; R.E. Belleville, eds., "Animal Orientation and Navigation", pp. 569–578, NASA Scientific and Technical Publications, 1970.

[30] Wiltschko, R.W.; Wiltschko, R., "Magnetic Compass of European Robins", *Science*, **176**(4030): 62–64, 1972.

[31] Schulten, K.; Swenberg, C.E.; Weller, A., "Biomagnetic Sensory Mechanism Based on Magnetic Field Modulated Coherent Electron Spin Motion", *Zeitschrift Für Physikalische Chemie*, **111**(1): 1–5, 1978.

[32] Ritz, T.; Adem, S.; Schulten, K., "A Model for Photoreceptor-Based Magnetoreception in Birds", *Biophysical Journal*, **78**(2): 707–718, 2000.

[33] Wiltschko, W.; Munro, U.; Ford, H.; Wiltschko, R., "Red-light disrupts magnetic orientation of migratory birds", *Nature*, **364**(6437): 525–527, 1993.

[34] Wiltschko, W.; Wiltschko, R., "Migratory orientation of European Robins is affected by the wavelength of light as well as by a magnetic pulse", *Journal Of Comparative Physiology A-sensory Neural And Behavioral Physiology*, **177**(3): 363–369, 1995.

[35] Thalau, P.; Ritz, T.; Stapput, K.; Wiltschko, R.; Wiltschko, W., "Magnetic compass orientation of migratory birds in the presence of a 1.315 MHz oscillating field", *Naturwissenschaften*, **92**(2): 86–90, 2005.

[36] Cashmore, A.R.; Jarillo, J.A.; Wu, Y.J.; Liu, D.M., "Cryptochromes: Blue Light Receptors for Plants and Animals", *Science*, **284**(5415): 760–765, 1999.

[37] Sancar, A., "Structure and Function of DNA Photolyase and Cryptochrome Blue-Light Photoreceptors", *Chemical Reviews*, **103**(6): 2203–2237, 2003.

[38] Lin, C.T.; Todo, T., "The cryptochromes", *Genome Biology*, **6**(5), 2005.

[39] Hitomi, K.; Okamoto, K.; Daiyasu, H.; Miyashita, H.; Iwai, S.; Toh, H.; Ishiura, M.; Todo, T., "Bacterial cryptochrome and photolyase: characterization of two photolyase-like genes of *Synechocystis* sp. PCC6803", *Nucleic Acids Research*, **28**(12): 2353–2362, 2000.

[40] Ahmad, M.; Cashmore, A.R., "*HY4* gene of *A. thaliana* encodes a protein with characteristics of a blue-light photoreceptor", *Nature*, **366**(6451): 162–166, 1993.

[41] Emery, P.; So, W.V.; Kaneko, M.; Hall, J.C.; Rosbash, M., "CRY, a *Drosophila* Clock and Light-Regulated Cryptochrome, Is a Major Contributor to Circadian Rhythm Resetting and Photosensitivity", *Cell*, **95**(5): 669–679, 1998.

[42] Miyamoto, Y.; Sancar, A., "Vitamin B2-based blue-light photoreceptors in the retinohypothalamic tract as the photoactive pigments for setting the circadian clock in mammals",

Proceedings Of The National Academy Of Sciences Of The United States Of America, **95**(11): 6097–6102, 1998.

[43] Hsu, D.S.; Zhao, X.; Zhao, S.; Kazantsev, A.; Wang, R.P.; Todo, T.; Wei, Y.F.; Sancar, A., "Putative Human Blue-Light Photoreceptors hCRY1 and hCRY2 Are Flavoproteins", *Biochemistry*, **35**(44): 13871–13877, 1996.

[44] Lin, C.; Robertson, D.E.; Ahmad, M.; Raibekas, A.A.; Jorns, M.S.; Dutton, P.L.; Cashmore, A.R., "Association of Flavin Adenine Dinucleotide with the *Arabidopsis* Blue Light Receptor CRY1", *Science*, **269**(5226): 968–970, 1995.

[45] Thresher, R.J.; Vitaterna, M.H.; Miyamoto, Y.; Kazantsev, A.; Hsu, D.S.; Petit, C.; Selby, C.P.; Dawut, L.; Smithies, O.; Takahashi, J.S.; Sancar, A., "Role of Mouse Cryptochrome Blue-Light Photoreceptor in Circadian Photoresponses", *Science*, **282**(5393): 1490–1494, 1998.

[46] Gegear, R.J.; Casselman, A.; Waddell, S.; Reppert, S.M., "Cryptochrome mediates light-dependent magnetosensitivity in *Drosophila*", *Nature*, **454**(7207): 1014–1018, 2008.

[47] Bailey, M.J.; Chong, N.W.; Xiong, J.; Cassone, V.M., "Chickens' Cry2: molecular analysis of an avian cryptochrome in retinal and pineal photoreceptors", *FEBS letters*, **513**(2-3): 169–174, 2002.

[48] Mouritsen, H.; Janssen-Bienhold, U.; Liedvogel, M.; Feenders, G.; Stalleicken, J.; Dirks, P.; Weiler, R., "Cryptochromes and neuronal-activity markers colocalize in the retina of migratory birds during magnetic orientation", *Proceedings Of The National Academy Of Sciences Of The United States Of America*, **101**(39): 14294–14299, 2004.

[49] Nießner, C.; Denzau, S.A.; Gross, J.C.; Peichl, L.; Bischof, H.J.; Fleissner, G.; Wiltschko, W.; Wiltschko, R., "Avian Ultraviolet/Violet Cones Identified as Probable Magnetoreceptors", *PLoS ONE*, **6**(5): e20091, 2011.

[50] Liedvogel, M.; Maeda, K.; Henbest, K.; Schleicher, E.; Simon, T.; Timmel, C.R.; Hore, P.J.; Mouritsen, H., "Chemical Magnetoreception: Bird Cryptochrome 1a Is Excited by Blue Light and Forms Long-Lived Radical-Pairs", *PLoS ONE*, **2**(10): e1106, 2007.

[51] Weber, S.; Biskup, T.; Okafuji, A.; Marino, A.R.; Berthold, T.; Link, G.; Hitomi, K.; Getzoff, E.D.; Schleicher, E.; Norris, Jr., J.R., "Origin of Light-Induced Spin-Correlated Radical Pairs in Cryptochrome", *Journal Of Physical Chemistry B*, **114**(45): 14745–14754, 2010.

[52] Biskup, T.; Hitomi, K.; Getzoff, E.D.; Krapf, S.; Koslowski, T.; Schleicher, E.; Weber, S., "Unexpected Electron Transfer in Cryptochrome Identified by Time-Resolved EPR Spectroscopy", *Angewandte Chemie International Edition*, **50**(52): 12647–12651, 2011.

[53] Ritz, T.; Wiltschko, R.; Hore, P.J.; Rodgers, C.T.; Stapput, K.; Thalau, P.; Timmel, C.R.; Wiltschko, W., "Magnetic Compass of Birds Is Based on a Molecule with Optimal Directional Sensitivity", *Biophysical Journal*, **96**(8): 3451–3457, 2009.

[54] Solov'yov, I.A.; Schulten, K., "Magnetoreception through Cryptochrome May Involve Superoxide", *Biophysical Journal*, **96**(12): 4804–4813, 2009.

[55] Hogben, H.J.; Efimova, O.; Wagner-Rundell, N.; Timmel, C.R.; Hore, P.J., "Possible involvement of superoxide and dioxygen with cryptochrome in avian magnetoreception: Origin of Zeeman resonances observed by *in vivo* EPR spectroscopy", *Chemical Physics Letters*, **480**(1-3): 118–122, 2009.

[56] Taylor, B.N.; Mohr, P.J., "NIST Reference on Constants, Units, and Uncertainty", 2011, `http://physics.nist.gov/cuu/index.html`.

[57] Weil, J.A.; Bolton, J.R., *Electron Paramagnetic Resonance: Elementary Theory and Practical Applications*, Wiley, 2007, ISBN 9780470084977.

[58] McConnell, H.M., "Indirect Hyperfine Interactions in the Paramagnetic Resonance Spectra of Aromatic Free Radicals", *The Journal of Chemical Physics*, **24**(4): 764–766, 1956.

[59] Pedersen, J.B.; Freed, J.H., "Some theoretical aspects of chemically induced dynamic nuclear polarization", *The Journal of Chemical Physics*, **61**(4): 1517–1525, 1974.

[60] McLauchlan, K.A.; Steiner, U.E., "The spin-correlated radical pair as a reaction intermediate", *Molecular Physics*, **73**(2): 241–263, 1991.

[61] Levitt, M.H., *Spin Dynamics: Basics of Nuclear Magnetic Resonance*, Wiley, 2 edition, 2008, ISBN 9780470517123.

[62] Slichter, C.P., *Principles of Magnetic Resonance*, Springer Series in Solid-State Sciences, Springer, 1996, ISBN 9783540501572.

[63] Goldman, M., "Formal Theory of Spin-Lattice Relaxation", *Journal of Magnetic Resonance*, **149**(2): 160–187, 2001.

[64] Lindblad, G., "On the generators of quantum dynamical semigroups", *Communications in Mathematical Physics*, **48**: 119–130, 1976.

[65] Deutch, J.M., "Theory of Chemically Induced Dynamic Polarization in Thin Films", *The Journal of Chemical Physics*, **56**(12): 6076–6081, 1972.

[66] Timmel, C.R.; Till, U.; Brocklehurst, B.; Mclauchlan, K.A.; Hore, P.J., "Effects of weak magnetic fields on free radical recombination reactions", *Molecular Physics*, **95**(1): 71–89, 1998.

[67] Kubo, R., "Stochastic Theories Of Randomly Modulated Systems", *Journal Of The Physical Society Of Japan*, **S 26**: 1–5, 1969.

[68] Kubo, R., "A stochastic theory of line shape", *Advances in Chemical Physics*, **15**: 101–127, 1969.

[69] Freed, J.H.; Bruno, G.V.; Polnaszek, C.F., "Electron Spin Resonance Line Shapes and Saturation in the Slow Motional Region", *The Journal of Physical Chemistry*, **75**(22): 3385–3399, 1971.

[70] Pedersen, J.B.; Christensen, M., "The Backward Stochastic Liouville Equation", *J. Phys. Chem. B*, **108**(27): 9516–9523, 2004.

[71] Hogben, H.J.; Krzystyniak, M.; Charnock, G.T.P.; Hore, P.J.; Kuprov, I., "*Spinach* - A software library for simulation of spin dynamics in large spin systems", *Journal Of Magnetic Resonance*, **208**(2): 179–194, 2011.

[72] Haberkorn, R., "Density matrix description of spin-selective radical pair reactions", *Molecular Physics*, **32**(5): 1491–1493, 1976.

[73] Kominis, I.K., "Quantum Theory of Radical-Ion-Pair Recombination: A New Physical Paradigm for Low-Magnetic-Field Effects", *arXiv:0805.3081 [quant-ph]*, 2008.

[74] Kominis, I.K., "Quantum Zeno Effect Explains Magnetic-Sensitive Radical-Ion-Pair Reactions", *arXiv:0806.0739 [quant-ph]*, 2009.

[75] Kominis, I.K., "En Route to Quantum Biology: Non-trivial Quantum Effects in Radical-Ion-Pair Reactions", in "SCM 2009 Programme and Abstracts", Spin Chemistry Meeting 2009, 2009.

[76] Kominis, I.K., "Quantum Zeno effect explains magnetic-sensitive radical-ion-pair reactions", *Physical Review E*, **80**(5): 056115, 2009.

[77] Kominis, I.K., "Radical-ion-pair reactions are the biochemical equivalent of the optical double-slit experiment", *Physical Review E*, **83**(5): 056118, 2011.

[78] Jones, J.A.; Hore, P.J., "Spin-selective reactions of radical pairs act as quantum measurements", *Chemical Physics Letters*, **488**(1-3): 90–93, 2010.

[79] Kominis, I.K., "Erratum: Quantum Zeno effect explains magnetic-sensitive radical-ion-pair reactions [Phys. Rev. E 80, 056115 (2009)]", *Physical Review E*, **81**(2): 029901 (E), 2010.

[80] Breuer, H.P.; Petruccione, F., *The Theory of Open Quantum Systems*, Oxford University Press, 2002, ISBN 0198520638.

[81] Il'ichov, L.V.; Anishchik, S.V., "Should recombinations of radical pairs be considered as accompanied by measurements?", *arXiv:1003.1793 [quant-ph]*, 2010.

[82] Fano, U., "Description of States in Quantum Mechanics by Density Matrix and Operator Techniques", *Reviews of Modern Physics*, **29**: 74–93, 1957.

[83] Ivanov, K.L.; Petrova, M.V.; Lukzen, N.N.; Maeda, K., "Consistent Treatment of Spin-Selective Recombination of a Radical Pair Confirms the Haberkorn Approach", *Journal of Physical Chemistry A*, **114**(35): 9447–9455, 2010.

[84] Shushin, A.I., "The effect of the spin exchange interaction on snp and rydmr spectra of geminate radical pairs", *Chemical Physics Letters*, **181**(2-3): 274–278, 1991.

[85] Maeda, K., "Reaction dynamics of the model chemical compass and quantum measurement", in "SCM 2011 Programme and Abstracts", Spin Chemistry Meeting, 2011, noordwijk, The Netherlands.

[86] Jones, J.A.; Maeda, K.; Hore, P.J., "Reaction operators for spin-selective chemical reactions of radical pairs", *Chemical Physics Letters*, **507**(4-6): 269–273, 2011.

[87] Misra, B.; Sudarshan, E.C.G., "The Zeno's paradox in quantum theory", *J. Math. Phys.*, **18**(4): 756–763, 1977.

[88] Shushin, A.I., "Effect of state-selective reactive decay on the evolution of quantum systems", *J. Chem. Phys.*, **133**(4): 044505–7, 2010.

[89] Purtov, P.A., "To the theory of Zeno chemical effect: The exactly solvable model", *Chemical Physics Letters*, **496**(4-6): 335–338, 2010.

[90] Maeda, K.; Wedge, C.J.; Storey, J.G.; Henbest, K.B.; Liddell, P.A.; Kodis, G.; Gust, D.; Hore, P.J.; Timmel, C.R., "Spin-selective recombination kinetics of a model chemical magnetoreceptor", *Chemical Communications*, **47**(23): 6563–6565, 2011.

[91] Maeda, K., "Personal communication", 2013, ePR data of CPF triads.

[92] Bagryansky, V.A.; Borovkov, V.I.; Molin, Y.N., "On the verification of different approaches describing spin-selective radical recombination", *Chemical Physics Letters*, **570**(0): 141–146, 2013.

[93] Rodgers, C.T.; Hore, P.J., "Chemical magnetoreception in birds: The radical pair mechanism", *Proceedings Of The National Academy Of Sciences Of The United States Of America*, **106**(2): 353–360, 2009.

[94] Liu, B.; Liu, H.; Zhong, D.; Lin, C., "Searching for a photocycle of the cryptochrome photoreceptors", *Current Opinion in Plant Biology*, **13**(5): 578–586, 2010.

[95] Biskup, T.; Schleicher, E.; Okafuji, A.; Link, G.; Hitomi, K.; Getzoff, E.D.; Weber, S., "Direct Observation of a Photoinduced Radical Pair in a Cryptochrome Blue-Light Photoreceptor", *Angewandte Chemie International Edition*, **48**(2): 404–407, 2009.

[96] Wiltschko, W.; Wiltschko, R., "Light-dependent magnetoreception in birds: the behaviour of European robins, *Erithacus rubecula*, under monochromatic light of various wavelengths and intensities", *Journal of Experimental Biology*, **204**(19): 3295–3302, 2001.

[97] Kirschvink, J.L.; Winklhofer, M.; Walker, M.M., "Biophysics of magnetic orientation: strengthening the interface between theory and experimental design", *Journal of The Royal Society Interface*, **7**(Suppl 2): S179–S191, 2010.

[98] Zeigler, H.P.; Bischof, H.J., eds., *Vision, brain, and behavior in birds*, A Bradford book, Massachusetts Institute of Technology, 1993, ISBN 9780262240369.

[99] Sturkie, P.D.; Whittow, G.C., *Sturkie's Avian Physiology*, Academic Press Inc, 1999, ISBN 9780080542089.

[100] Solov'yov, I.A.; Mouritsen, H.; Schulten, K., "Acuity of a Cryptochrome and Vision-Based Magnetoreception System in Birds", *Biophysical Journal*, **99**(1): 40–49, 2010.

[101] Braslavsky, S.E., "GLOSSARY OF TERMS USED IN PHOTOCHEMISTRY 3rd EDITION (IUPAC Recommendations 2006)", *Pure and Applied Chemistry*, **79**(3): 293–465, 2007.

[102] Varchalovitch, D.A.; Moskalev, A.N.; Khersonskii, V.K., *Quantum Theory of Angular Momentum: Irreducible Tensors, Spherical Harmonics, Vector Coupling Coefficients, 3 nj Symbols*, World Scientific Publishing Company, Incorporated, 1988, ISBN 9971509962.

[103] Arfken, G.B.; Weber, H.J.; Harris, F.E., *Mathematical Methods For Physicists*, Elsevier Science, sixth edition, 2005, ISBN 9780120598762.

[104] Driscoll, J.R.; Healy, D.M.J., "Asymptotically Fast Algorithms for Spherical and Related Transforms", in "30th Annual Symposium on Foundations of Computer Science, 1989", pp. 344–349, 1989.

[105] Driscoll, J.R.; Healy, D.M.J., "Computing Fourier Transforms and Convolutions on the 2-Sphere", *Advances in Applied Mathematics*, **15**(2): 202–250, 1994.

[106] Kostelec, P.J.; Rockmore, D.N., "S2kit: A lite version of SpharmonicKit", 2004, `http://www.cs.dartmouth.edu/~geelong/sphere/`.

[107] Climent, T.; González-Luque, R.; Merchán, M.; Serrano-Andrés, L., "Theoretical Insight into the Spectroscopy and Photochemistry of Isoalloxazine, the Flavin Core Ring", *The Journal of Physical Chemistry A*, **110**(50): 13584–13590, 2006.

[108] Eaton, W.A.; Hofrichter, J.; Makinen, M.W.; Andersen, R.D.; Ludwig, M.L., "Optical Spectra and Electronic Structure of Flavine Mononucleotide in Flavodoxin Crystals", *Biochemistry*, **14**(10): 2146–2151, 1975.

[109] Rayleigh, L., "On the Transmission of Ligld through an Atmosphere containing Small Particles in Suspenslon, and on the Origin of the Blue of the Sky", *Philosophical Magazine Series 5*, **47**(287): 375–384, 1899.

[110] Tyndall, J., "On the Blue Colour of the Sky, the Polarization of Skylight, and on the Polarization of Light by Cloudy matter generally", *Proceedings of the Royal Society of London*, **17**: 223–233, 1868.

[111] Strutt, J.W., "On the Light from the Sky, its Polarization and Colour", *Philosophical Magazine Series 4*, **41**(271): 107–120, 1871.

[112] Gàl, J.; Horvàth, G.; Meyer-Rochow, V.B.; Wehner, R., "Polarization patterns of the summer sky and its neutral points measured by full-sky imaging polarimetry in Finnish La-

pland north of the Arctic Circle", *Proceedings of the Royal Society of London. Series A: Mathematical, Physical and Engineering Sciences*, **457**(2010): 1385–1399, 2001.

[113] Brines, M.L.; Gould, J.L., "SKYLIGHT POLARIZATION PATTERNS AND ANIMAL ORIENTATION", *Journal Of Experimental Biology*, **96**: 69–91, 1982.

[114] Pomozi, I.; Horvàth, G.; Wehner, R., "How the clear-sky angle of polarization pattern continues underneath clouds: full-sky measurements and implications for animal orientation", *Journal Of Experimental Biology*, **204**(17): 2933–2942, 2001.

[115] Suhai, B.; Horvath, G., "How well does the Rayleigh model describe the E-vector distribution of skylight in clear and cloudy conditions? A full-sky polarimetric study", *Journal Of The Optical Society Of America A-optics Image Science And Vision*, **21**(9): 1669–1676, 2004.

[116] Hegedüs, R.; Åkesson, S.; Horváth, G., "Polarization patterns of thick clouds: overcast skies have distribution of the angle of polarization similar to that of clear skies", *Journal of the Optical Society of America A*, **24**(8): 2347–2356, 2007.

[117] Gàl, J.; Horvàth, G.; Barta, A.; Wehner, R., "Polarization of the moonlit clear night sky measured by full-sky imaging polarimetry at full Moon: Comparison of the polarization of moonlit and sunlit skies", *J. Geophys. Res.*, **106**(D19): 22647–22653, 2001.

[118] Phillips, J.B.; Moore, F.R., "Calibration of the sun compass by sunset polarized-light patterns in a migratory bird", *Behavioral Ecology And Sociobiology*, **31**(3): 189–193, 1992.

[119] Cochran, W.; Mouritsen, H.; Wikelski, M., "Migrating Songbirds Recalibrate Their Magnetic Compass Daily from Twilight Cues", *Science*, **304**(5669): 405–408, 2004.

[120] Muheim, R.; Moore, F.R.; Phillips, J.B., "Calibration of magnetic and celestial compass cues in migratory birds - a review of cue-conflict experiments", *Journal of Experimental Biology*, **209**(1): 2–17, 2006.

[121] Muheim, R., "Behavioural and physiological mechanisms of polarized light sensitivity in birds", *Philosophical Transactions of the Royal Society B: Biological Sciences*, **366**(1565): 763–771, 2011.

[122] Cronin, T.W.; Warrant, E.J.; Greiner, B., "Celestial polarization patterns during twilight", *Applied Optics*, **45**(22): 5582–5589, 2006.

[123] Munro, U.; Wiltschko, R., "The role of skylight polarization in the orientation of a day-migrating bird species", *Journal Of Comparative Physiology A-sensory Neural And Behavioral Physiology*, **177**(3): 357–362, 1995.

[124] Rodgers, C.T., *Magnetic Field Effects in Chemical Systems*, Ph.D. thesis, University of Oxford, UK, 2007.

[125] Giovani, B.; Byrdin, M.; Ahmad, M.; Brettel, K., "Light-induced electron transfer in a cryptochrome blue-light photoreceptor", *Nature Structural Biology*, **10**(6): 489–490, 2003.

[126] Cintolesi, F.; Ritz, T.; Kay, C.W.M.; Timmel, C.R.; Hore, P.J., "Anisotropic recombination of an immobilized photoinduced radical pair in a 50-μT magnetic field: a model avian photomagnetoreceptor", *Chemical Physics*, **294**(3): 385–399, 2003.

[127] Park, H.W.; Kim, S.T.; Sancar, A.; Deisenhofer, J., "Crystal structure of DNA photolyase from *Escherichia coli*", *Science*, **268**(5219): 1866–1872, 1995.

[128] Zoltowski, B.D.; Vaidya, A.T.; Top, D.; Widom, J.; Young, M.W.; Crane, B.R., "Structure of full-length *Drosophila* cryptochrome", *Nature*, **480**(7377): 396–399, 2011.

[129] NOAA, "Magetic field calculators", `http://www.ngdc.noaa.gov/geomag-web/`.

[130] Lau, J.C.S.; Wagner-Rundell, N.; Rodgers, C.T.; Green, N.J.B.; Hore, P.J., "Effects of disorder and motion in a radical pair magnetoreceptor", *Journal Of The Royal Society Interface*, **7**(2): S257–S264, 2010.

[131] Frankevich, E.L.; Pristupa, A.I.; Lesin, V.I., "MAGNETIC RESONANCE OF SHORT-LIVED TRIPLET EXCITON PAIRS DETECTED BY FLUORESCENCE MODULATION AT ROOM TEMPERATURE", *Chemical Physics Letters*, **47**(2): 304–308, 1977.

[132] Woodward, J.R.; Jackson, R.J.; Timmel, C.R.; Hore, P.J.; McLauchlan, K.A., "Resonant radiofrequency magnetic field effects on a chemical reaction", *Chemical Physics Letters*, **272**(5-6): 376–382, 1997.

[133] Stass, D.V.; Woodward, J.R.; Timmel, C.R.; Hore, P.J.; McLauchlan, K.A., "Radiofrequency magnetic field effects on chemical reaction yields", *Chemical Physics Letters*, **329**(1-2): 15–22, 2000.

[134] Woodward, J.; Timmel, C.; McLauchlan, K.; Hore, P., "Radio Frequency Magnetic Field Effects on Electron-Hole Recombination", *Physical Review Letters*, **87**(7): 077602, 2001.

[135] Timmel, C.R.; Hore, P.J., "Oscillating magnetic field effects on the yields of radical pair reactions", *Chemical Physics Letters*, **257**(3-4): 401–408, 1996.

[136] Henbest, K.B.; Kukura, P.; Rodgers, C.T.; Hore, P.J.; Timmel, C.R., "Radio Frequency Magnetic Field Effects on a Radical Recombination Reaction: A Diagnostic Test for the Radical Pair Mechanism", *Journal of the American Chemical Society*, **126**(26): 8102–8103, 2004.

[137] Rodgers, C.T.; Henbest, K.B.; Kukura, P.; Timmel, C.R.; Hore, P.J., "Low-Field Optically Detected EPR Spectroscopy of Transient Photoinduced Radical Pairs", *Journal Of Physical Chemistry A*, **109**(23): 5035–5041, 2005.

[138] Haynes, W.M., ed., *CRC Handbook of Chemistry and Physics*, CRC Handbook of Chemistry and Physics, CRC Press, 93 edition, 2012, ISBN 9781439880494.

[139] Batchelor, S.N.; Kay, C.W.M.; McLauchlan, K.A.; Shkrob, I.A., "Time-Resolved and Modulation Methods in the Study of the Effects of Magnetic Fields on the Yields of Free-Radical Reactions", *Journal of Physical Chemistry*, **97**(50): 13250–13258, 1993.

[140] Lewis, I.C.; Singer, L.S., "Electron Spin Resonance of Radical Cations Produced by the Oxidation of Aromatic Hydrocarbons with $SbCl_5$", *Journal of Chemical Physics*, **43**(8): 2712–2727, 1965.

[141] Ohya-Nishiguchi, H., "Both Oxidation and Reduction of Aromatic Hydrocarbons by an Electrolysis Cell Designed for Low-temperature ESR Studies", *Bulletin of the Chemical Society of Japan*, **52**(7): 2064–2068, 1979.

[142] Rieger, P.H.; Fraenkel, G.K., "Spin-Density Distribution in Nitrile Anion Radicals", *Journal of Chemical Physics*, **37**(12): 2795–2810, 1962.

[143] Rodgers, C.T.; Wedge, C.J.; Norman, S.A.; Kukura, P.; Nelson, K.; Baker, N.; Maeda, K.; Henbest, K.B.; Hore, P.J.; Timmel, C.R., "Radiofrequency polarization effects in zero-field electron paramagnetic resonance", *Physical Chemistry Chemical Physics*, **11**(31): 6569–6572, 2009.

[144] Wedge, C.J.; Rodgers, C.T.; Norman, S.A.; Baker, N.; Maeda, K.; Henbest, K.B.; Timmel, C.R.; Hore, P.J., "Radiofrequency polarization effects in low-field electron paramagnetic resonance", *Physical Chemistry Chemical Physics*, **11**(31): 6573–6579, 2009.

[145] Levitt, M.H., "Why Do Spinning Sidebands Have the Same Phase?", *Journal of Magnetic Resonance*, **82**(2): 427–433, 1989.

[146] Eden, M.; Lee, Y.; Levitt, M., "Efficient Simulation of Periodic Problems in NMR. Application to Decoupling and Rotational Resonance", *Journal Of Magnetic Resonance Series A*, **120**(1): 56–71, 1996.

[147] Hohwy, M.; Bildsøe, H.; Jakobsen, H.J.; Nielsen, N.C., "Efficient Spectral Simulations in NMR of Rotating Solids. The γ-COMPUTE Algorithm", *Journal of Magnetic Resonance*, **136**(1): 6–14, 1999.

[148] Ernst, R.R.; Bodenhausen, G.; Wokaun, A., *Principles of Nuclear Magnetic Resonance in One and Two Dimensions*, International Series of Monographs on Chemistry, Clarendon Press, Oxford, 1987, ISBN 9780198556473.

[149] Rossmann, W., *Lie Groups: An Introduction Through Linear Groups*, Oxford Mathematics, Oxford University Press, 2006, ISBN 9780199202515.

[150] Marks, R.J.I., *Handbook of Fourier Analysis & Its Applications*, Oxford University Press, 2009, ISBN 0195335929.

[151] Brink, D.M.; Satchler, G.R., *Angular momentum*, Clarendon Press, third edition, 1993, ISBN 0198517599.

[152] Dahlquist, G.; Björck, Å., *Numerical Methods*, Prentice-Hall series in automatic computation, Prentice-Hall, 1974.

[153] Koptyug, A.V.; Saik, V.O.; Animisov, O.A.; Molin, Y.N., "SPIN-LOCKING IN CONCENTRATION-NARROWED OD ESR SPECTRA", *Chemical Physics*, **138**(1): 173–178, 1989.

[154] Hansen, P.C., "THE DISCRETE PICARD CONDITION FOR DISCRETE ILL-POSED PROBLEMS", *BIT Numerical Mathematics*, **30**(4): 658–672, 1990.

[155] Hansen, P.C., "ANALYSIS OF DISCRETE ILL-POSED PROBLEMS BY MEANS OF THE L-CURVE", *SIAM Review*, **34**(4): 561–580, 1992.

[156] Hansen, P.C.; O'Leary, D.P., "THE USE OF THE L-CURVE IN THE REGULARIZATION OF DISCRETE ILL-POSED PROBLEMS", *SIAM Journal on Scientific Computing*, **14**(6): 1487–1503, 1993.

[157] Wedge, C.J., *Radiofrequency Magetic Field Effects on Radical Pair Recombination Reactions*, Ph.D. thesis, University of Oxford, UK, 2010.

[158] Stevens, B.; Hutton, E., "Radiative Life-time of the Pyrene Dimer and the Possible Role of Excited Dimers In Energy Transfer Processes", *Nature*, **186**(4730): 1045–1046, 1960.

[159] Förster, T., "Excimers", *Angewandte Chemie International Edition*, **8**(5): 333–343, 1969.

[160] Tsuchida, A.; Tsujii, Y.; Ohoka, M.; Yamamoto, M., "Laser Photolysis Studies on the Intramolecular Dimer Radical Cations Formed in 1,3-DIpyrenylpropanes", *Journal of Physical Chemistry*, **95**(15): 5797–5802, 1991.

[161] Cooper, J.T.; Forbes, W.F., "Organic and biological spectrochemical studies. XXVII. Electron spin resonance spectra of the pyrene monomer and dimer cation radicals", *Canadian Journal of Chemistry*, **46**(7): 1158–1160, 1968.

[162] Howarth, O.W.; Fraenkel, G.K., "Electron Spin Resonance Spectra of Monomeric and Dimeric Cation Radicals", *Journal of Chemical Physics*, **52**(12): 6258–6267, 1970.

[163] Ferguson, K.A., "Personal communication", 2012, rYDMR experiments.

[164] Weber, S.; Möbius, K.; Richter, G.; Kay, C.W.M., "The Electronic Structure of the Flavin Cofactor in DNA Photolyase", *Journal of the American Chemical Society*, **123**(16): 3790–3798, 2001.